



January 2022

## Rock Physics Based Velocity-Porosity Correlations Developed For Estimation Of The Elastic Properties Of The Bakken Formations Of The Williston Basin, North Dakota

Lynn D. Helms

Follow this and additional works at: <https://commons.und.edu/theses>

---

### Recommended Citation

Helms, Lynn D., "Rock Physics Based Velocity-Porosity Correlations Developed For Estimation Of The Elastic Properties Of The Bakken Formations Of The Williston Basin, North Dakota" (2022). *Theses and Dissertations*. 4342.

<https://commons.und.edu/theses/4342>

This Dissertation is brought to you for free and open access by the Theses, Dissertations, and Senior Projects at UND Scholarly Commons. It has been accepted for inclusion in Theses and Dissertations by an authorized administrator of UND Scholarly Commons. For more information, please contact [und.common@library.und.edu](mailto:und.common@library.und.edu).

**Rock Physics Based Velocity-Porosity Correlations Developed for  
Estimation of the Elastic Properties of the Bakken Formations of the  
Williston Basin, North Dakota**

by

**Lynn D. Helms**

Bachelor of Science in Engineering from South Dakota School of Mines and Technology, 1986  
Master of Petroleum Engineering, University of North Dakota, 2020

A Dissertation

Submitted to the Graduate Faculty

of the

University of North Dakota

In fulfillment of the requirements

for the degree of

Doctor of Philosophy

Grand Forks, North Dakota

August 2022

This thesis, submitted by Lynn Helms in partial fulfillment of the requirements for the Degree of Ph.D. from the University of North Dakota, has been read by the Faculty Advisory Committee under whom the work has been done and is hereby approved.

---

Dr. Vamegh Rasouli

---

Dr. Hui Pu

---

Dr. Minou Rabiei

---

Dr. Brian Tande

This dissertation is being submitted by the appointed advisory committee as having met all of the requirements of the School of Graduate Studies at the University of North Dakota and is hereby approved.

---

Christopher Nelson  
Dean of the Graduate School

---

Date

## PERMISSION

Title: Rock Physics Based Velocity-Porosity Correlations Developed for Estimation of the Elastic Properties of the Bakken Formations of the Williston Basin, North Dakota

Department: Petroleum Engineering

Degree: Doctor of Philosophy

In presenting this thesis in partial fulfillment of the requirements for a graduate degree from the University of North Dakota, I agree that the library of this University shall make it freely available for inspection. I further agree that permission for extensive copying for scholarly purposes may be granted by the professor who supervised my thesis work or, in his absence, by the chairperson of the department or the dean of the Graduate School. It is understood that any copying or publication or other use of this thesis or part thereof for financial gain shall not be allowed without my written permission. It is also understood that due recognition shall be given to me and to the University of North Dakota in any scholarly use which may be made of any material in my thesis.

Lynn Helms  
July 18, 2022

## Table of Contents

ABSTRACT .....	xii
<b>Chapter 1 Research Statement and Thesis Outline .....</b>	<b>1</b>
1.1 Introduction .....	1
1.2 Research Objectives .....	4
1.3 Methodology .....	5
1.4 Research Significance.....	5
1.5 Thesis Structure .....	6
1.6 Summary .....	7
<b>Chapter 2 Study Area and Input Data .....</b>	<b>8</b>
2.1 Introduction .....	8
2.2 Texture and Pore Systems.....	19
2.3 Summary .....	25
<b>Chapter 3 Geology and Rock Properties of The Bakken Formation .....</b>	<b>26</b>
3.1 Bakken Formation Stratigraphy and Lithofacies .....	26
3.2 Rock Physics Models.....	35
3.2.1 Pore Fluid Models.....	36
3.2.2 Voigt-Reuss-Hill Model.....	37
3.2.3 Hashin-Shtrikman Model .....	37
3.2.4 Kuster and Toksoz (K-T) Inclusion Model .....	38
3.2.5 Differential Effective Medium (DEM) .....	39
3.2.6 Backus Averaging Theory.....	40
3.3 Example Rock Physics Models of the Bakken .....	41
3.4 Summary .....	47
<b>Chapter 4 DEM-Based Velocity-Porosity Correlations.....</b>	<b>48</b>
4.1 Superimposed Modeling .....	48
4.2 Minerals and Fluid Properties .....	50
4.3 Porosity-Velocity Relationship from DEM Model.....	51
4.4 Relationship of Coefficients <b>Cs</b> and <b>ARs</b> .....	56

4.5	Relationship of Constants A, B and C with $S_o$ .....	58
4.6	Relationship of Constants a's, m's and n's with $S_w$ .....	58
4.7	Summary of Correlations.....	59
4.8	Rock Velocity Averaging .....	67
4.9	Summary .....	70
<b>Chapter 5 Case Study Examples .....</b>		<b>71</b>
5.1	Well #17015, Nesson State .....	71
5.2	Case Studies from Grenora Oilfield, Williams County.....	94
5.2.1	Petrophysical ELAN for Wells from Grenora Oilfield, Williams County.....	94
5.2.2	Shear Velocity ( $V_s$ ) Estimation .....	98
5.2.3	Well #17946, Trigger 1-31H.....	99
5.2.3.1	Minerals Composition in Well #17946.....	99
5.2.3.2	Fluids Saturation in Well #17946.....	101
5.2.3.3	Shear Velocity Estimation in Well #17946.....	102
5.2.3.4	Density, Velocities, and Pore's AR prediction in Well #17946.....	103
5.2.4	Well #20552, Muller 1-21-16H.....	106
5.2.4.1	Mineral Composition in Well #20552 .....	106
5.2.4.2	Fluids Saturation in Well #20552.....	108
5.2.4.3	Shear Velocity Estimation in Well #20552.....	109
5.2.4.4	Density, Velocities, and Pore AR Prediction in Well #20552 .....	111
5.2.5	Well #20844, Rasmussen 1-21-16H .....	113
5.2.5.1	Minerals Composition in Well #20844.....	113
5.2.5.2	Fluids Saturation in Well #20844.....	115
5.2.5.3	Shear Velocity Estimation in Well #20844.....	116
5.2.5.4	Density, Velocities, and Pore's AR Prediction in Well #20844 .....	117
5.3	Summary .....	120
<b>Chapter 6 Conclusions and Recommendations .....</b>		<b>121</b>
6.1	Conclusions .....	121
6.2	Recommendations .....	126
<b>Appendix A.....</b>		<b>128</b>
<b>Appendix B.....</b>		<b>136</b>

**REFERENCES .....152**

## List of Figures

<b>Figure 1.1.</b> The Bakken formation occurs in most of western North Dakota and northeastern Montana (Polzin, 2017). .....	2
<b>Figure 1.2.</b> The sequence stratigraphy of the Bakken formation (Egenhoff, 2017). .....	2
<b>Figure 2.1.</b> Map of the study areas (Sorensen et al., 2014), where the data were taken for rock physics modeling in this work. ....	9
<b>Figure 3.1.</b> Example of generalized stratigraphy of the Bakken Formation (Modified from Barnes et al., 2020). .....	27
<b>Figure 3.2.</b> Bulk mineral chemostratigraphy through the Bakken Formation (Barnes et al., 2020). .....	28
<b>Figure 3.3.</b> A general classification of shale lithofacies showing six different shale lithofacies (Bhattacharyaa and Carr, 2019). .....	29
<b>Figure 3.4.</b> Regular thin section and Secondary X-ray Emission Spectroscopy images showing five different shale lithofacies, corresponding to Figure 2.5 (Bhattacharyaa and Carr, 2019). .....	30
<b>Figure 3.5.</b> Example of integrated well logs in one of the Bakken wells with identified lithofacies (Bhattacharyaa and Carr, 2019). .....	31
<b>Figure 3.6.</b> Example mineralogical features, TOC, and conventional well log response of the five shale lithofacies of the Bakken (Bhattacharyaa and Carr, 2019). .....	32
<b>Figure 3.7.</b> Location of Dunn County in the Williston Basin, North Dakota (Raimi and Newell, 2016). ..	33
<b>Figure 3.8.</b> Bakken lithofacies assigned in Well #16333 (left) and Well #16766 (right) in Dunn County (Sorensen et al., 2010). .....	33
<b>Figure 3.9.</b> Bakken lithofacies assigned in Well #16766 in Dunn County (Sorensen et al., 2010). .....	35
<b>Figure 3.10.</b> Comparison of compressional (left) and shear (right) velocities parallel (top) and perpendicular (bottom) to the shale laminations for patchy versus homogeneous fluid (Harju, 2022). .....	43
<b>Figure 3.11.</b> Compressional (left) and shear (right) velocities models for MB clastic formation (Harju, 2022). .....	45
<b>Figure 3.12.</b> Compressional (top) and shear (bottom) velocities of MB carbonates based on DEM critical porosity of 1.0 and K-T model for patchy (left) and homogeneous fluid (right), Harju (2022). Red and blue dots are, respectively, lab data corresponding to limestone and dolomite from Bakken reported by Sayers (2008). .....	46
<b>Figure 4.1.</b> DEM model compressional ( $V_p$ ), (left) and shear ( $V_s$ ), (right) velocity versus porosity for calcite fully saturated with gas with different pore's aspect ratios. ....	53
<b>Figure 4.2.</b> Exponential fits to the DEM model data (from Figure 4.1) present a good agreement for both compressional ( $V_p$ ), (left) and shear ( $V_s$ ), (right) velocity data for calcite fully saturated with gas. ....	53
<b>Figure 4.3.</b> Exponential fits to the DEM model data for compressional ( $V_p$ ), (left) and shear ( $V_s$ ), (right) velocity data for calcite fully saturated with oil. ....	54
<b>Figure 4.4.</b> Exponential fits to the DEM model data for compressional ( $V_p$ ), (left) and shear ( $V_s$ ), (right) velocity data for calcite fully saturated with oil. ....	54
<b>Figure 4.5.</b> The vertices of the triangle correspond to the velocity of the rock saturated with a single-phase fluid of water, oil or gas. The edges represent the two-phase fluid saturations. Any point inside the triangle represents three-phase fluid with the saturation percentages represented by the distance to each vertex. ....	54
<b>Figure 4.6.</b> The effect of fluid type mixing (Brie coefficient, $e$ ) on velocity response for calcite with two phase fluids of water and oil with different saturations and assuming crack type pores ( $AR=0.01$ ). ..	55



<b>Figure 4.7.</b> Second orders polynomial fits well to the coefficients $C_0$ with respect to pore's aspect ratios ( $AR$ ) as a function of water, oil and gas saturations for calcite. This is for the case of $AR < 0.1$ .....	56
<b>Figure 4.8.</b> Examples showing that power equations show a good fit for changes of coefficients $C_1$ , when $AR < 0$ , and coefficients $C_0$ and $C_1'$ for both cases of $AR < 0$ and with respect to pore aspect ratios ( $AR$ ) as a function of water, oil and gas saturations for calcite. ....	57
<b>Figure 4.9.</b> Examples of relationships between correlation constants A, B and C with oil saturation, $S_o$ , when $AR < 0$ , and for three water saturations of 25%, 50% and 75%. ....	58
<b>Figure 4.10.</b> Examples of relationships between constants a's, m's and n's with water saturation, $S_w$ , when $AR < 0$ . ....	59
<b>Figure 4.11.</b> Comparison of (compressional (left) and shear (right) velocity versus porosity relationship from DEM model versus developed correlations for calcite (top) and kerogen (bottom) fully saturated with gas and with different pore's aspect ratios.....	68
<b>Figure 4.12.</b> Comparison of velocity-porosity relationship from the DEM model (Harju, 2022) versus developed correlations for the Middle Bakken carbonate formation. Compressional (left) and shear (right) velocities.....	69
<b>Figure 4.13.</b> Comparison of velocity-porosity relationship from K-T model (Harju, 2022) versus developed correlations for the Middle Bakken clastic formation. Compressional (left) and shear (right) velocities.....	70
<b>Figure 4.14.</b> Comparison of velocity-porosity relationship from K-T model (Harju, 2022) versus developed correlations for the Middle Bakken shale formation. Compressional (left) and shear (right) velocities. ....	70
<b>Figure 5.1.</b> Location of Well #17015, Nesson State (Sorensen et al., 2011).....	72
<b>Figure 5.2.</b> Petrophysical logs of Well #17015, Nesson State. ....	72
<b>Figure 5.3.</b> Volume fractions of minerals in Well #17015 from ECS log. ....	73
<b>Figure 5.4.</b> Velocity prediction for Well #17015. DEM model versus correlations, based on Harju's (2022) assumptions. ....	75
<b>Fig. 5.5.</b> Pore's aspect ratios ( $AR$ ) estimated corresponding to $V_p$ (left) and $V_s$ (right) and total porosity (from Harju, 2022).....	76
<b>Figure 5.6.</b> Lab data from Well #17015, showing a linear correlation between water and gas saturation. ....	80
<b>Figure 5.7.</b> Water, oil and gas saturation predicted for Well #17015, Nesson State. ....	80
<b>Figure 5.8.</b> $V_p$ (left) and $V_s$ (right) velocity estimation from DEM model and correlations considering variable water saturations.....	81
<b>Figure 5.9.</b> Pores' aspects ratio ( $AR$ ) prediction from Harju (2022) (blue) with constant fluid saturations assumption versus developed correlations with varying fluid saturations (black), corresponding to $V_p$ (left) and $V_s$ (right).....	82
<b>Figure 5.10.</b> Estimation of TOC level in UB and LB shale in Well #17015 using Passey, Schmoker, and Hester method.....	85
<b>Figure 5.11.</b> Impact of adding kerogen in UB and LB shale on velocity prediction from correlations for Well #17015 using Passey (top) and Schmoker (bottom) methods. ....	86
<b>Figure 5.12.</b> $V_p$ (left) and $V_s$ (right) velocity estimation from DEM model and correlations versus measured log data considering variable water saturations and variable Kerogen fraction, dry illite and total porosity as the inclusion volume.....	87
<b>Figure 5.13.</b> Modeled densities for the Bakken assuming dry and wet illite and with and without addition of Kerogen.....	88

<b>Figure 5.14.</b> Pore's aspect ratios corresponding to $V_p$ and $V_s$ , estimated from new DEM (black and red curves) and previous (blue and green curves) modeling. ....	89
<b>Figure 5.15.</b> Ternary plots of change of $V_p$ (left column) and $V_s$ (right column) for the Middle Bakken carbonate formation as a function of three-phase fluid saturation, due to change of porosity from 5% to 10% and 15%, from top to the bottom. Pore aspect ratio is $AR=0.01$ .....	92
<b>Figure 5.16.</b> Ternary plots of change of $V_p$ (left column) and $V_s$ (right column) for the Middle Bakken carbonate formation as a function of three-phase fluid saturation, due to change of pore aspect ratio from 0.05 (interparticle), (top) to 0.15 (intergranular), (bottom). Porosity is 5%. ....	93
<b>Figure 5.17.</b> The output of the Petrophysical ELAN for Well #17946 in Grenora field. ....	97
<b>Figure 5.18.</b> The output of the Petrophysical ELAN for Well #20552 in Grenora field. ....	97
<b>Figure 5.19.</b> The output of the Petrophysical ELAN for Well #20844 in Grenora field. ....	98
<b>Figure 5.20.</b> Minerals composition of Well #17946 in Grenora field, calibrated with XRD data.....	100
<b>Figure 5.21.</b> Lab data from Well #17946, showing a linear correlation between water and oil saturation. ....	101
<b>Figure 5.22.</b> Water, oil, and gas saturation predicted for well #17946. ....	102
<b>Figure 5.23.</b> Shear velocity ( $V_s$ ) prediction from compressional velocity using Greenberg-Castagna relation, in well #17946. ....	103
<b>Figure 5.24.</b> $V_p$ (left) and $V_s$ (right) velocity estimation from DEM model and correlations versus measured log data in well #17946. ....	104
<b>Figure 5.25.</b> Estimated (red) versus measured (green) bulk density ( $\rho_b$ ) (left) and $AR$ 's prediction from both $V_p$ (black) and $V_s$ (red) (right) in Well #17946. ....	105
<b>Figure 5.26.</b> Minerals composition of Well #17946 in Grenora field, calibrated with XRD data.....	107
<b>Figure 5.27.</b> Lab data from Well #20552 shows a logarithmic relation between water and oil saturations. ....	108
<b>Figure 5.28.</b> Water, oil, and gas saturation predicted for well #20552. ....	109
<b>Figure 5.29.</b> Shear velocity ( $V_s$ ) prediction from compressional velocity using Greenberg-Castagna relation, in well #20552. ....	110
<b>Figure 5.30.</b> $V_p$ (left) and $V_s$ (right) velocity estimation from DEM model and correlations versus measured log data in well #20552. ....	111
<b>Figure 5.31.</b> Estimated (red) versus measured (green) bulk density ( $\rho_b$ ) (left) and $AR$ s prediction for both $V_p$ (black) and $V_s$ (red) (right) in well #20552. ....	112
<b>Figure 5.32.</b> Mineral composition of Well #20844, calibrated with XRD and TOC data. ....	114
<b>Figure 5.33.</b> Lab data from Well #20844, showing linear relationships between water and oil saturation in the MB (left) and UB and LB shales (right). ....	115
<b>Figure 5.34.</b> Water, oil, and gas saturation predicted for well #20844. ....	116
<b>Figure 5.35.</b> Shear velocity ( $V_s$ ) prediction from compressional velocity using Greenberg-Castagna relation, in Well #20844.....	117
<b>Figure 5.36.</b> $V_p$ (left) and $V_s$ (right) velocity estimation from DEM model and correlations versus measured log data in Well #205844.....	118
<b>Figure 5.37.</b> Estimated (red) versus measured (green) bulk density ( $\rho_b$ ) (left) and pore $AR$ prediction from both $V_p$ (black) and $V_p$ (red) (right) in Well #20844. ....	119
<b>Figure A.1.</b> Images and brief description for Lithofacies L1 to L7 in NDIC Well No. 8850. Depths shown indicate the depth from which each sample was obtained (continued). ....	128
<b>Figure A.2.</b> (continued). Images and brief description for Lithofacies L1 to L7 in NDIC Well No. 9001. Depths shown indicate the depth from which each sample was obtained.....	131

**Figure A.3.** Images and a brief description of lithofacies characterized by the EERC in NDIC Well No. 20552. Depths shown indicate the depth from which each sample was obtained (continued)..... 132

**Figure A.4.** Images and a brief description of lithofacies characterized by the EERC in NDIC Well No. 20844. Depths shown indicate the depth from which each sample was obtained (continued)..... 134

**List of Tables**

**Table 2.1.** Summary of Petrographic Properties for Rival Field Samples (Smith et al., 2013). ..... 14

**Table 2.2.** Summary of UCS Geomechanical Testing for the Rival Area (Smith et al., 2013). ..... 15

**Table 2.3.** Data from samples of the Grenora Area Cores (Smith et al., 2013). ..... 18

**Table 2.4.** Summary of Confined Triaxial Testing of Grenora Area Core Plugs (Smith et al., 2013). ..... 18

**Table 2.5.** List of sixteen samples from Well Trigger No. 1-31H (Well #17946) in Grenora field analyzed by both thin section and XRD (NDIC, 2019). ..... 20

**Table 2.6.** XRD data for 16 samples from Well Trigger No. 1-31H (Well #17946) in Grenora field (NDIC, 2019). ..... 20

**Table 2.7.** Point-count data for 16 samples from Well Trigger No. 1-31H (Well #17946) in Grenora field (NDIC, 2019). ..... 21

**Table 2.8.** Examples of lithology and petrographic description of two samples from Well Trigger No. 1-31H (NDIC Well #17946) in Grenora field (NDIC, 2019). ..... 22

**Table 2.9.** Examples of lithology and petrographic description of two samples from Well Muller No. 1-21-16H (NDIC Well #20552) in Grenora field (NDIC, 2021a). ..... 23

**Table 2.10.** Examples of lithology and petrographic description of two samples from Well Rasmussen No. 1-21-16H (NDIC Well #20844) in Grenora field (NDIC, 2021a). ..... 24

**Table 3.1.** Bulk organic carbon and mineralogical mean and range statistics for the Bakken formation members (After Barnes et al. (2020)). ..... 29

**Table 3.2.** Rock Physics Classifications (After Saberi, 2017). ..... 36

**Table 3.3.** Shape factors for sphere and penny shaped cracks (Schon, 2011). ..... 38

**Table 3.4.** Summary of UB and LB Shale Mineralogy (wt%) (Sorensen, et al., 2010). Clay minerals are bolded. .... 42

**Table 3.5.** Summary of MB clastic Mineralogy (wt%) (Sorensen, et al., 2010). Clay minerals are bolded. .... 42

**Table 3.6.** Summary of MB carbonate Mineralogy (wt%) (Sorensen, et al., 2010). Clay minerals are bolded. .... 42

**Table 4.1.** Bulk moduli ( $K$ ), shear moduli ( $\mu$ ), density ( $\rho$ ) and compressional ( $V_p$ ) and shear ( $V_s$ ) velocities of minerals used in this study for modeling (Harju, 2022). ..... 50

**Table 4.2.** Bulk moduli ( $K$ ), density ( $\rho$ ) and equivalent velocity ( $V_p$ ) of pore fluids (Harju, 2022). ..... 51

**Table 4.3.** Constants  $p$ ,  $q$  and  $r$  for **calcite** to estimate velocities as function of fluid saturations and pore’s aspect ratio using the DEM based developed correlations. .... 61

**Table 4.4.** Constants  $p$ ,  $q$  and  $r$  for **Quartz** to estimate velocities as function of fluid saturations and pore’s aspect ratio using the DEM based developed correlations. .... 62

**Table 4.5.** Constants  $p$ ,  $q$  and  $r$  for **Dolomite** to estimate velocities as function of fluid saturations and pore’s aspect ratio using the DEM based developed correlations. .... 63

**Table 4.6.** Constants  $p$ ,  $q$  and  $r$  for **Illite** to estimate velocities as function of fluid saturations and pore’s aspect ratio using the DEM based developed correlations. .... 64

<b>Table 4.7.</b> Constants p, q and r for <b>Anhydrite</b> to estimate velocities as function of fluid saturations and pore's aspect ratio using the DEM based developed correlations. ....	65
<b>Table 4.8.</b> Constants p, q and r for <b>Kerogen</b> to estimate velocities as function of fluid saturations and pore's aspect ratio using the DEM based developed correlations. ....	66
<b>Table 4.9.</b> Comparison of the velocity prediction based on the DEM model and correlations for calcite for some case examples. ....	67
<b>Table 5.1.</b> modified Simendoux input parameter to predict water saturation. ....	79
<b>Table 5.2.</b> Workflow of estimating kerogen level in the Bakken shale using Passey method. ....	84
<b>Table 5.3.</b> Input data to calculate water saturation using Simandoux model in 3 wells of Grenora field. .	95
<b>Table 5.4.</b> Regression coefficients for pure lithologies (Castagna et al., 1993). ....	99
<b>Table B.1.</b> Trigger No. 1-31H, NDIC Well #17946 (Regenerated from NDIC Well report, 2019).....	136
<b>Table B.2.</b> Muller No. 1-21-16H, NDIC Well #20552 (Regenerated from NDIC Well report, 2021a) ..	144
<b>Table B.3.</b> Rasmussen No. 1-21-16H, NDIC Well #20844 (Reproduced from NDIC Well report, 2021b) .....	148

## **Acknowledgements**

I would like to acknowledge the enormous contributions of my friend and colleague John Harju.

**Dedicated to** my loving family Sally, Nathan, Anjel, and Paul Helms.

## **ABSTRACT**

Oil production from the Bakken Shale in North Dakota has benefitted from significant technological advancements since its beginning approximately two decades ago. Most of the advancements resulted from better characterization of shales, which are very heterogeneous and their properties vary at different scales. The need for costly operations such as drilling long laterals and multi-stage hydraulic fracturing for production from these unconventional reservoirs, signifies the importance of understanding the physical and mechanical properties of these formations in order to reduce the risk margins and improve project economics at different phases of the life of the field. Rock physics is a relatively new discipline that has been used in shale reservoirs to integrate petrophysical, geomechanical and seismic measurements.

Rock physics models are predictive tools used to estimate the velocity, or elastic properties of formations, based on strong theoretical foundations, as opposed to some of the simple empirical correlations that have been developed for specific regional formations. While the basic rock physics models use simplified assumptions and involve less input, more complex models, such as inclusion-based models, estimate velocity-porosity relation as function of different parameters including pore fluid saturation and type, cementation, confining pressure and diagenesis. The downside is that these models require performing tedious calculations and in some cases solving complex differential equations. These models may also differ depending on the type of formation, for example, in the Bakken, separate models may be used for the upper Bakken and lower Bakken shales (UBS, LBS) compared to the clastic or carbonate formations in the Middle Bakken (MB) member.

In this research study, we developed velocity-porosity correlations for the Bakken formation. These models were developed based on large volumes of data from simulation of many cases using the differential effective medium (DEM) theory, a commonly used rock physics model. DEM models were developed for single mineral rocks, i.e. rocks composed of only one mineral, with different porosities. The pores were then modeled with three phase fluid (water, oil and gas) at different saturation levels and finally, different pore aspect ratios were assumed to simulate crack, interparticle, intergranular and moldic type pore geometries. The correlations constants were extracted for different key minerals in the Bakken, including quartz, calcite, dolomite, anhydrite, illite and kerogen. Having the volume fraction of minerals from lab-based XRD or Elemental Capture Spectroscopy (ECS) logs, linear averaging was applied to estimate the velocity and elastic properties of the formations.

The correlations were applied to several wells in the Bakken and also compared with the existing lab data, which showed a good agreement with the DEM model. The simplicity of using the correlations, that can be developed in an excel spreadsheet and using a single approach for different type of formations, offers a great advantage for their applications.



# CHAPTER 1

## Research Statement and Thesis Outline

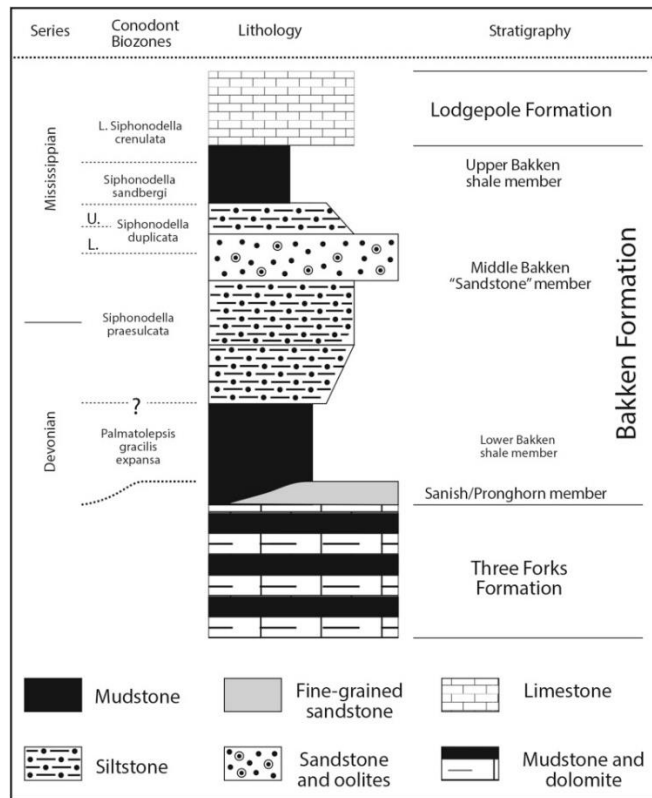
### 1.1 Introduction

The Bakken Formation is currently the most productive oil-producing formation in the Williston Basin and one of the most productive tight oil plays in North America. In the U.S. portion of the Williston Basin, it occurs in North Dakota and Montana, while in Canada, it occurs in Saskatchewan and Manitoba (Figure 1.1). Daily oil production in the North Dakota portion of the Bakken has been as high as 1.5 million barrels and estimates of total oil in place across the entire Bakken Formation range from 100 to 900 billion barrels. While the hydrocarbon resource within the Bakken Formation is tremendous, the Bakken is considered to be an unconventional oil play because it is typically characterized by very low porosity (<10%) and permeability (<0.1 mD).

With respect to stratigraphy, the Devonian–Mississippian-age Bakken Formation in the Williston Basin typically consists of three members: the Upper (UB), Middle (MB), and Lower (LB) Bakken (see Figure 1.2). In some locations, the lower shale is underlain by a unit with variable lithology referred to as the Pronghorn Member. Lithologically, the upper and lower members of the Bakken are dominated by shales rich in organic carbon that act as the source rock for oil reservoirs in the Middle Bakken and Pronghorn Members.



**Figure 1.1.** The Bakken formation occurs in most of western North Dakota and northeastern Montana (Polzin, 2017).



**Figure 1.2.** The sequence stratigraphy of the Bakken formation (Egenhoff, 2017).

The lithology of the Middle Bakken varies widely from clastic (including shales, silts, and sandstones) to carbonates, with five distinct lithofacies typically being identified in the North Dakota portion of the Williston Basin, although in some areas, there may be more than five and in other areas fewer. The physical and mechanical properties of the various Bakken members and lithofacies are a key component of their ability to serve as productive oil reservoirs, as those properties dictate the size, frequency, pattern, and orientation of fracture networks (natural and artificial) at both the micro- and macroscale (Sorensen et al., 2014).

Considering the complex lithology of the Bakken, a good knowledge of physical and mechanical properties of different Bakken members is essential in order to optimize development, completion, stimulation and production from this formation. The significant heterogeneity and anisotropy of the Bakken members, makes it necessary to study different areas of the Bakken separately, and difficult to generalize the findings from one Bakken field to other areas.

The idea of this study was to develop some simple correlations to estimate the elastic properties of different Bakken members. The correlations were developed based on the well-known and frequently used rock physics model of Differential Effective Medium (DEM). This is an inclusion-based approach that models wave velocity and attenuation based on scattering theory and approximate the rock as an elastic block of mineral perturbed by holes (porosity). The DEM model considers the effect of pore geometry, fluid type and mineralogy in estimation of the rock's elastic properties. The details of some of the rock physics models, including DEM will be discussed in the following Chapters and it will be shown that the use of some of these models, including DEM, is not straightforward and requires the use of extensive calculations and software aids. Also, different models are proposed depending on the type of formation. However, the developed

correlations provide an alternative approach to estimate the velocity and elastic properties of the formations in a much simpler way.

The developed correlations will then be applied to several wells in the Bakken to examine their applicability in several case studies. In particular, the data from a well in Mountrail County, and some wells from the Grenora oil field of Williams County will be used in this study.

The following sections present the objectives, methodology, significance, and structure of this Ph.D. thesis.

## **1.2 Research Objectives**

The objectives of this project include the followings:

- Review of the geology and mineralogy of the Bakken formation in the studied areas and the results of published lab data including the XRD, SEM and thin sections of different Bakken members. Also, a summary of the physical and mechanical properties of the Bakken formation obtained from lab testing will be presented. These data will be used as the input for rock physics modeling in this study.
- A summary review of the inclusion-based rock physics models that have been used for shale, carbonate, and clastic formations and in specific with reference to the Bakken formation. Some of the advantages and shortcomings of the main models will be presented briefly.
- Introduce the concept of the mixing model to predict the velocity and elastic properties of rocks based on the integration of the correlations developed for single phase rocks with dominant mineral constituents in the medium.
- Develop the DEM model for single mineral rocks, with different saturations of three phase fluid (water, oil and gas), and with pores of different geometries, i.e. aspect ratio (*AR*). The

models will be presented for the dominant minerals that are observed in the Bakken, i.e. Calcite, Dolomite, Quartz, Illite and Anhydrite, as well as several other minerals.

- Use the mixing model to estimate the rock's velocity and elastic properties in different Bakken formations and compare the results with the published reports and data to assess the applicability of the developed correlations. This will be done at both lab and log scales with examples in different Bakken oilfields.

### **1.3 Methodology**

The methodology that will be used in this study to fulfill the objectives of this research comprises the accumulation of a data inventory, comprehensive review of literature and communication with researchers who work in the same area for exchange of technical knowledge and peer review of the results of the project. Calculations of rock physics models will be developed in the excel sheets. Various commercial software including Techlog will be used for log-based rock physics modeling and geomechanical analysis. Validation of the results will be performed by comparison against the lab data reported by previous researchers working on the Bakken.

### **1.4 Research Significance**

To the best of the author's knowledge, this is the first work that presents simplified correlations which are based on robust rock physics theories. One set of correlations can be used regardless of the formation types, which make their use simple and easy. While the applications are most suitable for the Bakken formation, they can be used to get a reasonable estimate of elastic properties in other formations as well.

The formation's velocity and elastic parameters are the key inputs to any geomechanical studies for the purposed of field development, completion and stimulation design and production.

Therefore, the use of simplified correlations presented in this work offers a great advantage to optimize field development, completion and stimulation design, and well production by better characterization of the formations' physio-mechanical properties.

## **1.5 Thesis Structure**

This thesis consists of six Chapters.

Chapter 1 provides the overall scope of this Ph.D. dissertation by introducing briefly the problem that will be studied in this research and the importance of studying the topic for applications in the oil and gas industry. In this Chapter the objectives of the research, the methodology that is used and some significance of this work are also presented.

In Chapter 2 the general geology of the Bakken formation in the Williston Basin with specific focus on the fields that were targeted for data collection and use in this study will be presented. A summary of geology, mineralogy, and mechanical properties of the Bakken members obtained from different core sampling will be presented in this Chapter.

Chapter 3 will provide a short summary of the inclusion-based rock physics models. Also, some of the past literature with respect to rock physics modeling of carbonates, clastic and shale formations will be presented with specific reference to the Bakken formation.

Chapter 4 presents the methodology that was used to develop the DEM based correlations for estimation of rock velocity. The idea of the mixing model will be discussed in this Chapter and some basic applications of the proposed correlations will be presented.

Chapter 5 presents the results of the applications of the developed correlations in estimation of velocity in four wells in the Bakken to examine the range of applicability of the models.

Chapter 6 presents the main conclusions of this study and some of the recommendations for future work as a continuation of this research.

## **1.6 Summary**

This Chapter briefly highlighted the importance of estimation of the elastic properties of the formations for applications at different stages of field development in oil and gas fields. The importance of using rock physics models was highlighted and the idea of developing new correlations based on the DEM inclusion-based rock physics model for estimation of formations' elastic properties was discussed. Also, the main objectives of this study, the methodology used, the significance of this work and the structure of this Ph.D. dissertation were presented.

In the next Chapter, the geology of the study area will be presented and various data that are used as part of the analysis in this work will be reviewed.

# CHAPTER 2

## Study Area and Input Data

### 2.1 Introduction

In this Chapter a review of the fields and the wells from which the data were extracted and used in this study is given. A summary of the data related to the mineralogical and geomechanical characterization of the Bakken formation is also presented. The material in this Chapter is mainly taken from the report of the Energy and Environmental Research Center (EERC) which was a study on the potential of CO<sub>2</sub> injectivity into the Bakken (Smith, 2013). Figure 1 shows the map of the study area. This includes the Bailey and Murphy Creek oil fields of Dunn County, the Rival oil field of Burke County, and the Grenora oil field of Williams County. The data from these fields are mainly taken from the report of the Energy and Environmental Research Center (Sorensen et al., 2014) which studied the potential of CO<sub>2</sub> injectivity into the Bakken formation. The Bailey and Murphy Creek areas are thermally mature whereas Rival and Grenora areas are thermally immature portions of the Bakken.

Five wells from which the samples were tested belong to two geographic areas proximal to the Rival Field in northwestern North Dakota near the Saskatchewan border and the Grenora Field on the border between North Dakota and Montana. NDIC Well Numbers 9001 and 8850 were sampled from the Rival area, and NDIC Well Numbers 17946, 20552, and 20844 were sampled from the Grenora area. The locations of these wells relative to the Rival and Grenora oilfields,



respectively, are shown in Figures 2.2 and 2.3. As the log data for the two wells in Rival area were not available, only the three wells in Grenora field were studied in this research work. However, the summary for the Rival field is also presented in this Chapter due to its proximity to Grenora field and that it provides valuable information for future use by others working in this topic.

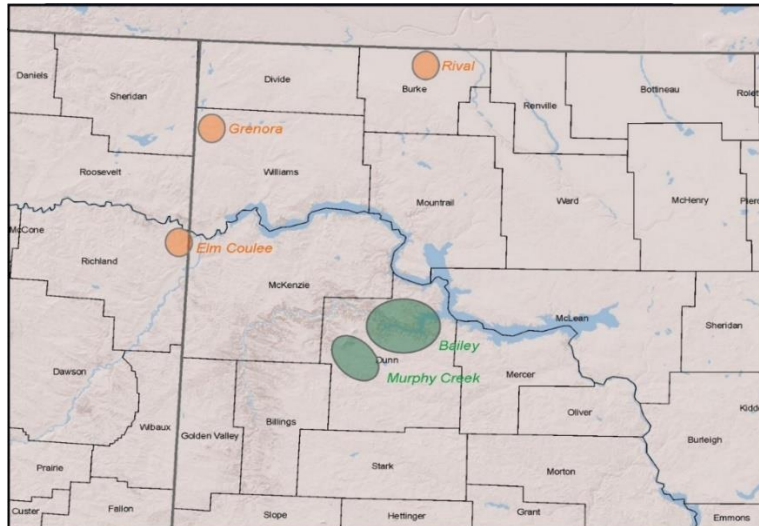


Figure 2.1. Map of the study areas (Sorensen et al., 2014), where the data were taken for rock physics modeling in this work.

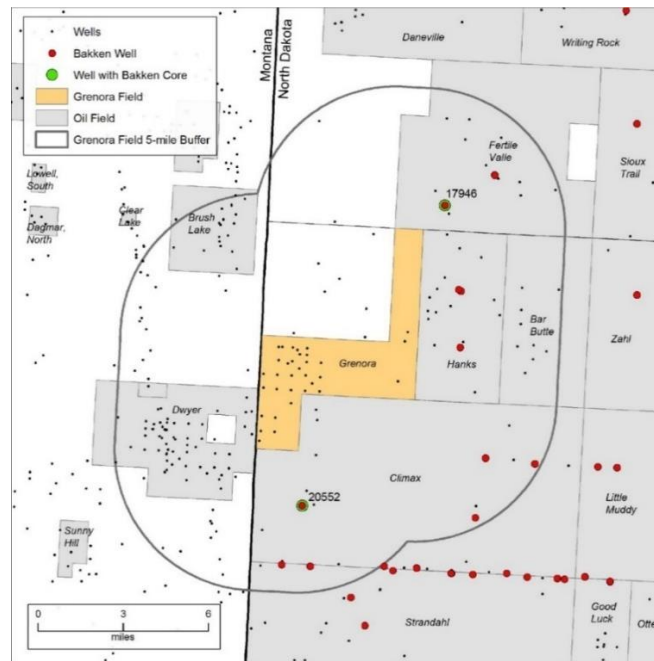


Figure 2.2. Location of wells sampled near the Grenora Field (Sorensen et al., 2014).

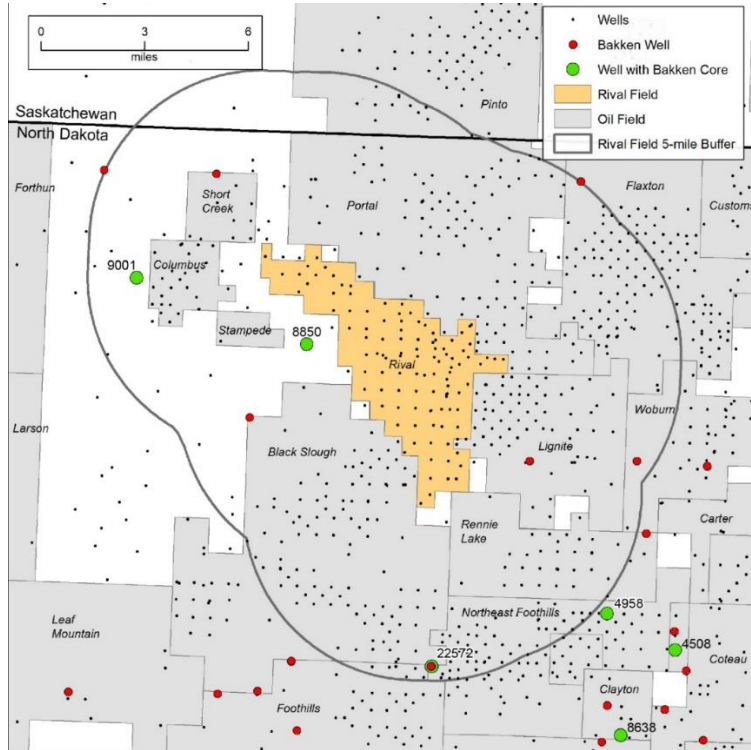


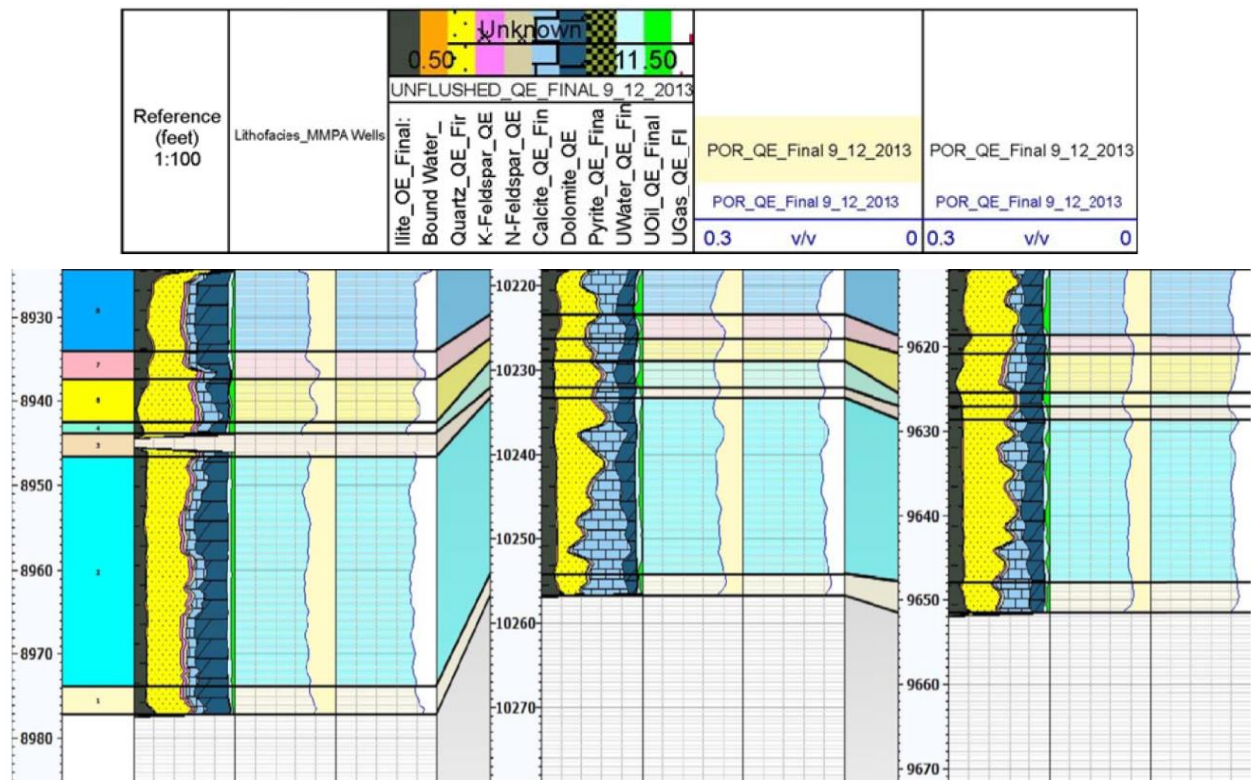
Figure 2.3. Location of wells sampled near the Rival Field (Sorensen et al., 2014).

Doing comprehensive rock physics modeling requires a wide range of input data. The typical information that are needed to be collected from different type of lab experiments include:

- Optical microscopy and thin-section analysis,
- X-ray fluorescence (XRF) for bulk chemical analysis,
- X-ray diffraction (XRD) for bulk mineral analysis,
- Scanning electron microscopy (SEM) to provide high-magnification images of rock samples for analysis of microfractures, rock fabric, and determination of minerals,
- Energy-dispersive spectroscopy (EDS) to provide quantitative elemental analysis and determination of minerals,
- Porosity determination through the use of a helium gas porosimeter, and

- Geomechanical testing of core plugs, including elastic properties such as Young’s modulus, Poisson’s ratio, and strength parameters including uniaxial compressive strength (UCS), cohesion and friction angle.

Figure 2.4 shows a cross section of the Bakken from three wells in the Grenora study area. Both NDIC-20844 and NDIC-17946 have seven lithofacies that appear to be somewhat correlative, with some subtle differences in fabric and mineralogy. Generally speaking, the Middle Bakken in the Grenora area appears to be significantly more dolomitic than in the Rival area. The lithofacies in the Grenora area appear to be generally more variable than was observed in the Rival and Dunn County areas. This variability and lack of an easily correlatable, thick, laminated zone makes the selection of a suitable horizontal drilling target more challenging.

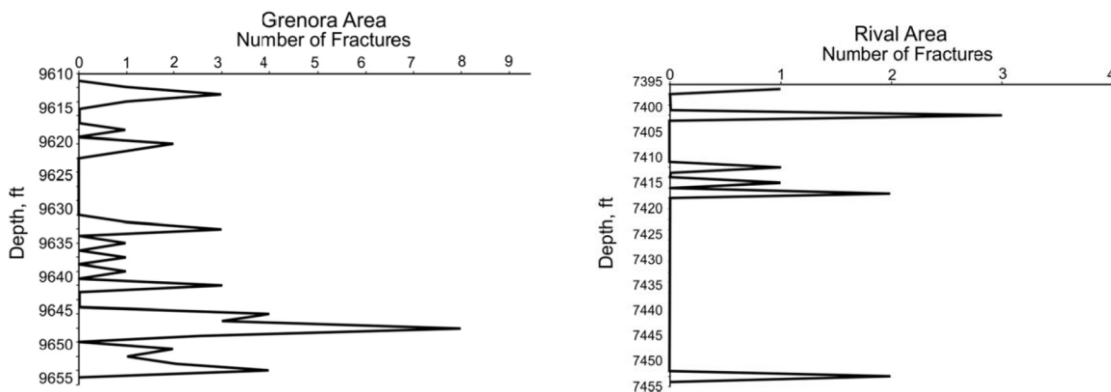


**Figure 2.4.** Cross section showing the thickness of Middle Bakken lithofacies in the Grenora study area. The well logs shown, from left to right, represent NDIC-17946, NDIC-20844, and NDIC-20552, respectively (Sorensen et al., 2014).

The presence of dolomite also facilitates the development of fractures as dolomite tends to fracture more easily than calcite. The presence of structure and dolomite may be linked. The existence of a fracture network caused by structure or tectonic activity along the Brockton–Froid fault (which runs near the Grenora Field) may have facilitated fluid migration through the Bakken. Such fluid migration may have supported diagenesis, creating dolomite rhombs and further enhanced natural fracturing of the formation (Sorensen et al., 2014). Figure 2.5 presents fracture intensity in the Grenora and Rival areas.

In both wells in the Rival Field, seven distinct lithofacies were identified through macroscopic description of the core. Figures A.1 to A.4 in Appendix A provide the depth, a brief lithology classification, and images obtained from macroscopic photography, thin-section, and SEM analyses for portions of the core representing each lithofacies in each Rival area well. The lithofacies are designated L1 at the base of the MB (contact on the LB Shale) to L7 at the top of the MB (contact on the Upper Bakken Shale). These designations were used strictly to orient the reader within the context of the relative stratigraphic position within the core.

Figure 2.6 presents a summary overview of the characteristics of the MB lithofacies observed in the Grenora and Rival areas.



**Figure 2.5.** Fracture intensity in Grenora (left) and Rival (right) areas (Sorensen et al., 2014).

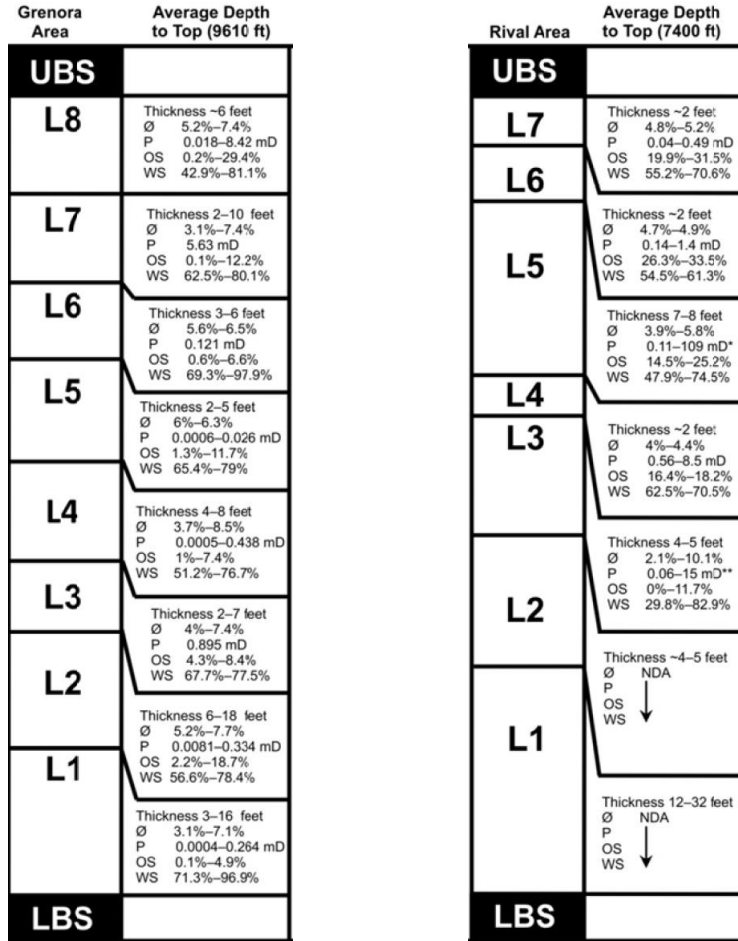


Figure 2.6. Lithofacies in Grenora (left) and Rival (right) areas (Sorensen et al., 2014).

Table 2.1 presents a summary of the key observations and data regarding porosity, grain density, and dominant mineral phases identified for each sample collected from the Rival area cores. Table 2.2 provides a summary of triaxial geomechanical testing results of the samples, including elastic and strength properties. These are important information that will be used to calibrate the rock physics and geomechanical models that will be constructed in this study and presented in the following Chapters.

With respect to this study, key observations for the Rival area characterization include the following:

- In both wells, the lithofacies appear to be fairly correlative.

- Both wells have a relatively thick argillaceous siltstone at the base (L1). The primary difference between the two wells is that L1 in Well #8850 exhibits a more massive character in contrast to a more bioturbated L1 in Well #9001.

**Table 2.1.** Summary of Petrographic Properties for Rival Field Samples (Smith et al., 2013).

Sample #	Well #	Depth (ft)	Grain Density (gr/cc)	Porosity (%)	XRD Dominant Mineral Phase*
116978	8850	7397.50	2.763	6.68	Q (41.3), D (24.7), KF (11.9)
116979	8850	7400.80	2.748	6.11	Q (42.1), D (35.5)
116980	8850	7407.30	2.706	6.84	Q (41.4), K-F (19.6), D (19.0)
116981	8850	7410.00	2.741	3.67	Q (35.6), D (20.0), C (19.1), K-F (12.5)
116982	8850	7412.50	2.728	9.88	Q (63.0), D (19.1)
116983	8850	7420.00	Not tested	Not tested	Q (66.3), D (17.5), C (11.2)
116984	8850	7450.00	Not tested	Not tested	Q (41.9), C (22.5), D (13.2), K-F (12.0)
116988	9001	7381.00	2.761	6.11	D (35.7), Q (32.4), KF (11.2)
116989	9001	7382.70	2.749	5.11	D (36.9), Q (36.5), KF (10.2)
116990	9001	7385.30	2.735	6.74	Q (34.8), D (24.2), KF (16.1), I (11.8)
116991	9001	7392.40	2.758	6.55	Q (38.1), D (35.1), KF (13.3)
116992	9001	7394.80	2.738	8.70	Q (56.0), D (24.6), KF (10.1)
116993	9001	7399.00	Not tested	Not tested	Q (56.8), C (35.9)
116994	9001	7409.20	Not tested	Not tested	Q (54.7), D (21.2)

\* Quartz (Q), Dolomite (D), Potassium Feldspar (K-F), Illite (I), and Calcite (C) listed in order of prevalence based on XRD relative weight percentage. Only mineral phases greater than 10% are considered to be dominant mineral phases.

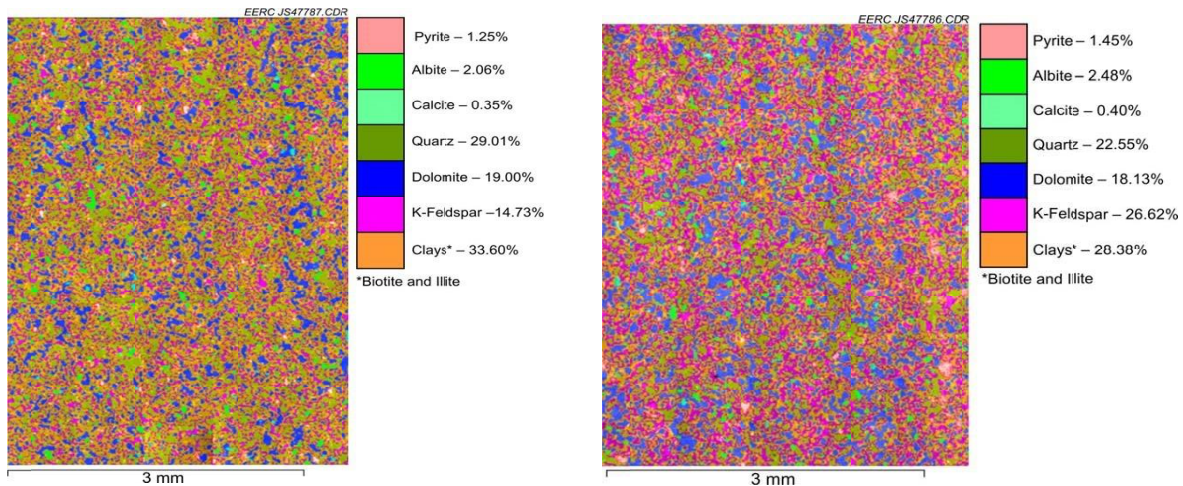
- In both wells, L2 is a calcite-rich siltstone, L3 is a bioturbated siltstone and L4 is a 2- to 3-foot-thick laminated dolomitic siltstone.
- Examination by UV fluorescence indicated no presence of microfractures in L4 in either well.
- Figure 2.7 shows SEM-based mineral maps of portions of thin sections from samples in two wells. Specifically, L4 in Well #9001 appears to have nearly twice as much feldspar as L4 in Well #8850. Of particular note are the clay particles (orange) lining the perimeter of both quartz

(olive) and dolomite (dark blue) grains. In certain areas of this sample, calcite is shown to be diagenetically altered to dolomite around the perimeter of the grain.

- Both wells show L5 to be a bioturbated siltstone, L6 to be a thin dolostone, and L7 to be a more massive dolostone.
- Geomechanically, L4, L6, and L7 displayed similar peak stress properties, while L1 appears to be significantly weaker. This could be attributed to the less dolomitic nature of L1 compared to the other lithofacies.

**Table 2.2.** Summary of UCS Geomechanical Testing for the Rival Area (Smith et al., 2013).

Sample No.	NDIC Well No.	Depth, ft	Peak Stress, psi	Young's Modulus, MPa
116981	8850	7410.0	21252.0	408.1
116983	8850	7420.0	22913.8	437.3
116984	8850	7450.0	22977.1	448.8
116988	9001	7381.0	19339.4	408.5
116989	9001	7382.7	20706.7	409.1
116991	9001	7392.4	19171.5	372.4
116994	9001	7409.2	13122.6	343.1



**Figure 2.7.** SEM mineral map of a portion of a thin section from L4 in NDIC Well #8850 (left) and Well #9001(right) in Rival Field (Sorensen et al., 2014).

The results of porosity, mineralogy and geomechanical testing of samples taken from Grenora area are presented in Table 2.3 and 2.4, respectively. Well #20552 is the closest, located approximately 1 mile south of the Grenora oilfield and as opposed to other two wells which have seven lithofacies, it contains eight identifiable lithofacies (from L1 at the base to L8 at the top of the MB).

In Well #20552, L1 is a massive to bioturbated fossiliferous siltstone. Lithofacies L2 through L7 alternate between bioturbated siltstone and laminated siltstone, with the laminated zones generally being thinner than the bioturbated zones. L5 through L7 appear to become more dolomitized as one moves up the core, until finally at the top of the Middle Member of the Bakken, L8 appears as a dolomitic siltstone. As with the evaluation of Rival cores, these designations are not necessarily correlative to similar MB lithofacies designations that are commonly used throughout published literature on Bakken stratigraphy. Here, they are strictly used to orient the reader within the context of the relative stratigraphic position within the cores that were evaluated in the Grenora area.

With respect to this study, some of the key observations for the Grenora area characterization include the followings:

- Both wells #20844 and #17946 have seven lithofacies that appear to be somewhat correlative, with some subtle differences in fabric and mineralogy. Figures A.3 and A.4 in Appendix provide a series of images depicting the specific lithofacies analyzed in this evaluation. These samples were chosen to fill gaps in previously conducted core analyses.
- In general, the Middle Bakken in the Grenora area appears to be significantly more dolomitic than in the Rival area.



- The lithofacies in the Grenora area appear to be generally more variable than those observed in the Rival area and which have been observed in other productive areas of the Bakken (e.g., the Dunn County and Parshall–Sanish areas). This variability and the lack of an easily correlatable, thick, laminated zone make the choice of a suitable horizontal drilling target more challenging.
- The cores from the Grenora area are notably more fractured than those from the Rival area. This may be due to the presence of structure, which is known to occur in the Grenora area.
- The core from the Grenora wells exhibits a higher degree of macroscopic fracture intensity (Sorensen and others, 2013) than was observed in the Rival area core. This characteristic was also generally observed in the UV photographs of thin sections from Grenora.
- Analysis of thin sections from Grenora area wells showed the presence of microfractures throughout many of the lithofacies, particularly those with laminations. However, in most cases, SEM analysis of these microfractures showed little evidence of mineralization or clay filling, suggesting that they may not have been naturally created in situ. The lack of naturally occurring microfractures in the Grenora area core may be related to the thermally immature nature of the Bakken in this area. Thermally mature rocks have experienced greater stresses due to the expulsion of oil from kerogen and, therefore, may be expected to have a greater number of microfractures.

**Table 2.3.** Data from samples of the Grenora Area Cores (Smith et al., 2013).

Sample #	Well #	Depth (ft)	Grain Density (gr/cc)	Porosity (%)	XRD Dominant Mineral Phase*
117009	20552	9613.0	2.729	3.03	Q (28.8), C (27.7), D (27.6)
117010	20552	9616.0	Not tested	Not tested	D (35.3), Q (34.5), K-F (13.2)
117012	20552	9622.0	2.727	3.12	C (45.8), Q (29.0), D (15.8)
117013	20552	9623	2.76	6.27	Q (38.2), D (38.2)
117014	20552	9624.0	2.717	5.20	Q (54.6), D (19.6), C (16.8)
117016	20552	9646.5	2.729	6.61	Q (44.1), D (19.0), K-F (12.8)
117021	20844	10217.0	2.750	8.01	Q (35.4), D (31.7)
117023	20844	10227.02	2.757	7.73	Q (39.2), D (32.3), K-F (10.7)
117026	20844	10237.0	2.716	3.07	Q (37.8), C (34.7), D (11.5)
117027	20844	10245.0	2.733	3.38	Q (46.0), D (20.2), K-F (12.0)
117030	20844	10256.0	2.726	7.18	C (75.5), Q (16.2)

\* Quartz (Q), Dolomite (D), Potassium Feldspar (K-F), and Calcite (C) listed in order of prevalence based on XRD relative weight percentage. Only mineral phases greater than 10% are considered to be dominant mineral phases; a complete listing of minerals associated with each sample is found in Appendix B.

**Table 2.4.** Summary of Confined Triaxial Testing of Grenora Area Core Plugs (Smith et al., 2013).

Sample No.	NDIC Well No.	Depth (ft)	Maximum Confining Pressure (psi)	Peak Strength (psi)	Young's Modulus ( $10^6$ psi)	Poisson's Ratio
117000	17946	8956.5	5025	42862	3.484	0.207
117001	17946	8964.5	5031	45020	3.437	0.221
117002	17946	8968.5	5031	44249	3.493	0.179
117004	17946	8977.0	5037	44578	3.494	0.213
117009	20552	9613.0	5391	45621	4.190	0.255
117012	20552	9622.0	5399	51841	4.001	0.252
117013	20552	9623.0	5399	51750	3.783	0.195
117014	20552	9624.0	5398	50118	3.768	0.268
117016	20552	9646.5	5413	46610	3.552	0.184
117023	20844	10227.0	5739	46490	3.306	0.171
117026	20844	10237.0	5745	43391	4.175	0.251
117027	20844	10245.0	3410	37051	3.935	0.232

## 2.2 Texture and Pore Systems

The published results of petrographic analysis of conventional core samples for the three study wells (NDIC Well reports, 2019, 2021a, b) in the Grenora field were used in this study to cross validate the prediction of the pore's aspect ratio ( $AR$ ) from the rock physics models that are presented in Chapter 5.

The previous studies were with the objective to evaluate the composition and diagenetic features of selected samples, with particular focus on pore types, fractures, dolomitization, clay composition, and cementation. This was accomplished through thin section point-count descriptions and XRD analysis (bulk and clay) of the core samples.

A list of the sixteen samples from Well #17946 analyzed by both thin section and XRD, including depth, lithology, tests performed, and core analysis data are presented in Table 2.5. XRD data is provided in Table 2.6 and point-count data is presented in Table 2.7. An example of the lithology and petrographic as well as SEM descriptions and photomicrographs are provided in Table 2.8 for two samples, with the list for all samples being presented in Table B.1 in the Appendix B. The sixteen samples analyzed by thin section and XRD are from the Middle Bakken Formation and range in depth from 8934.00-8980.10 feet. The twenty additional samples analyzed by XRD are from the Sanish and Three Forks Formations and range in depth from 9002.50-9021.40 feet (NDIC Well#17946 Report, 2019).

Tables 2.9 and 2.10 present, respectively, examples of lithology and pore system descriptions for two samples in wells Well Muller No. 1-21-16H (NDIC Well #20552) and Well Rasmussen No. 1-21-16H (NDIC Well #20844). The information for all samples examined from these two wells can be found in Tables B.2 and B.3 of the Appendix B, respectively.

**Table 2.5.** List of sixteen samples from Well Trigger No. 1-31H (Well #17946) in Grenora field analyzed by both thin section and XRD (NDIC, 2019).

Sample ID	Depth (ft):	Thin Section	XRD	Porosity (%)	Permeability (md)	Grain Density (g/cc)	Lithology	Grain Size (mm)	Sorting	Classification (Folk, 1980)
4	8934.00	X	X	1.9	0.0003	2.74	Calcareous Silty Shale	N/A	N/A	-
7	8940.00	X	X	3.3	0.0005	2.73	Argillaceous Sandstone	0.069	moderately well	Feldspathic Litharenite
8	8942.00	X	X	8.5	0.060	2.80	Slightly Argillaceous Sandstone	0.092	moderate	Subarkose
9	8943.00	X	X	8.4	0.004	2.72	Argillaceous Sandstone	0.087	moderate	Subarkose
10	8943.60	X	X	1.1	0.001	2.70	Sandstone	0.115	moderately well	Litharenite
11	8943.80	X	X	8.1	1.55	2.71	Sandstone	0.114	moderately well	Litharenite
12	8943.90	X	X	5.9	0.32	2.70	Slightly Argillaceous Sandstone	0.130	moderately well	Sublitharenite
13	8944.20	X	X	10.2	2.15	2.70	Slightly Argillaceous Sandstone	0.120	moderately well	Sublitharenite
14	8944.40	X	X	3.8	0.004	2.70	Slightly Argillaceous Sandstone	0.139	well	Sublitharenite
15	8944.90	X	X	1.5	0.001	2.71	Sandstone	0.109	moderately well	Litharenite
20	8950.00	X	X	5	0.048	2.72	Argillaceous Siltstone	0.062	moderately well	-
24	8958.25	X	X	7.5	0.002	2.73	Argillaceous Siltstone	0.061	moderately well	-
25	8960.10	X	X	7.6	0.003	2.74	Argillaceous Siltstone	0.062	moderately well	-
30	8970.00	X	X	7.9	0.004	2.73	Argillaceous Siltstone	0.059	moderately well	-
34	8978.15	X	X	5.9	0.343	2.73	Argillaceous Siltstone	0.046	moderately well	-
35	8980.10	X	X	3.2	0.0003	2.72	Argillaceous Siltstone	0.038	moderately well	-

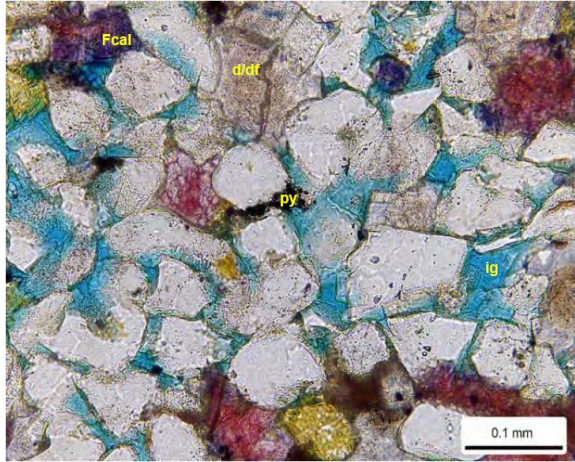
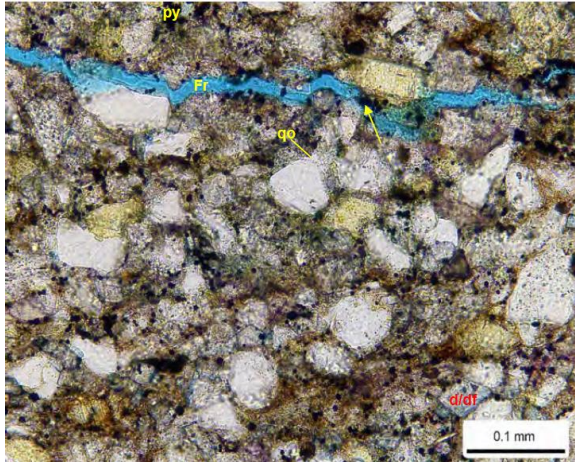
**Table 2.6.** XRD data for 16 samples from Well Trigger No. 1-31H (Well #17946) in Grenora field (NDIC, 2019).

Sample ID	Depth (ft):	Whole Rock Mineralogy (Weight %)									Clay Abundance (Weight %)				
		Quartz	K-Feldspar	Plagioclase	Calcite	Dolomite	Siderite	Anhydrite	Pyrite	Total Clay	Illite / Smectite	Illite & Mica	Kaolinite	Chlorite	% Smectite in I/S
4	8934.00	21	2	3	46	17	0	0	2	9	0	7	Tr	2	-
7	8940.00	26	2	2	49	12	0	0	1	8	0	7	Tr	1	-
8	8942.00	60	4	4	4	20	0	0	1	6	0	5	Tr	1	-
9	8943.00	56	7	2	6	19	0	0	Tr	9	0	8	Tr	1	-
10	8943.60	33	1	1	60	1	0	0	1	3	0	2	0	1	-
11	8943.80	67	2	1	18	7	0	0	2	3	1	2	0	Tr	10-15
12	8943.90	49	2	1	41	4	0	0	1	2	Tr	2	0	Tr	10-15
13	8944.20	61	9	2	15	9	0	0	1	3	Tr	3	0	Tr	10-15
14	8944.40	50	4	1	37	4	0	0	1	3	1	2	0	Tr	10-15
15	8944.90	31	1	Tr	64	1	0	0	1	2	Tr	2	0	Tr	10-15
20	8950.00	46	3	11	16	12	0	0	Tr	11	2	8	Tr	1	10-15
24	8958.25	44	7	7	5	20	0	0	2	14	1	11	Tr	2	10-15
25	8960.10	55	3	4	5	23	0	0	1	9	1	7	Tr	1	10-15
30	8970.00	48	4	4	6	20	0	0	1	16	1	13	Tr	2	10-15
34	8978.15	42	3	5	19	13	0	0	1	16	1	13	Tr	2	10-15
35	8980.10	43	2	4	23	8	0	0	1	18	0	15	Tr	3	-

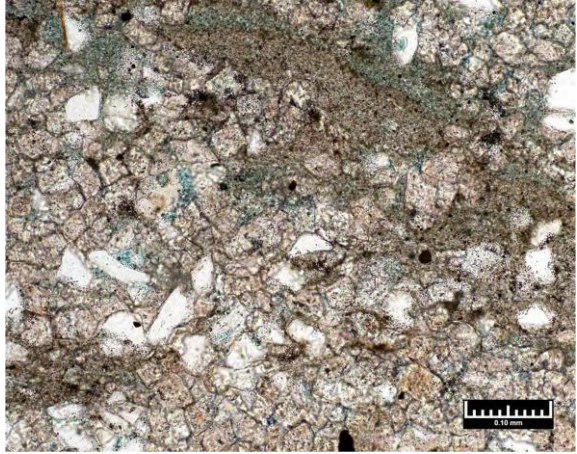
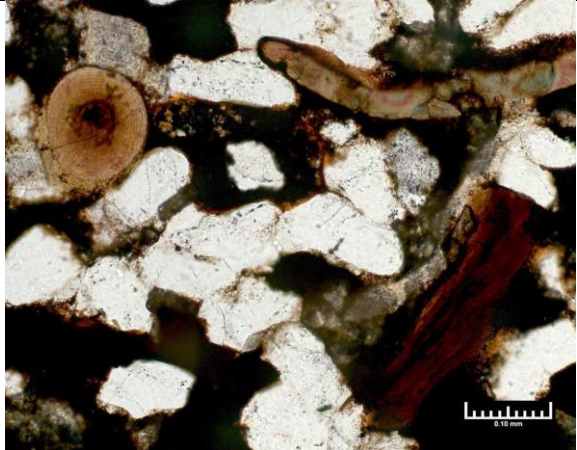
Table 2.7. Point-count data for 16 samples from Well Trigger No. 1-31H (Well #17946) in Grenora field (NDIC, 2019).

Sample Number:	Depth (ft):	Texture		Framework Grains																	Matrix			Authigenic Minerals										Porosity				
		Grain Size (mm):	Sorting:	Monocrystalline quartz	Polycrystalline quartz	Potassium feldspar	Plagioclase	Volcanic rock fragment	Metamorphic rock fragment	Calcareous Grains	Argillaceous rock fragments	Chert	Muscovite	Heavy minerals	Echinoderms	Bryozoans	Brachiopods	Skeletal grains-undifferentiated	Ooids	Organic Matter	Replacement - ferroan calcite	Total Framework Constituents	Clay matrix	Carbonate matrix	Total detrital matrix	Syntaxial quartz overgrowths	Potassium feldspar overgrowths	Ferroan dolomite	Dolomite	Calcite	Ferroan calcite	Anhydrite	Pyrite	Titanium oxides	Total authigenic minerals	Intergranular	Intragranular	Total porosity
4	8934.00	N/A	N/A	18.4	0.0	1.2	0.4	0.0	0.0	1.6	0.0	0.0	0.4	0.0	0.0	0.0	0.0	0.0	tr	0.0	22.0	13.6	33.6	47.2	0.8	0.0	0.0	23.6	2.4	0.0	0.0	0.0	4.0	0.0	30.8	0.0	0.0	0.0
7	8940.00	0.069	moderately well	22.8	0.0	2.8	0.8	0.4	0.0	5.2	3.2	0.0	0.4	0.0	0.0	0.0	0.0	0.0	0.4	0.0	36.0	10.8	0.0	10.8	2.4	0.0	0.0	13.6	35.6	0.0	0.0	1.6	0.0	53.2	0.0	0.0	0.0	
8	8942.00	0.092	moderate	43.6	0.0	4.8	3.2	0.8	0.0	2.4	1.2	0.0	0.0	0.0	0.0	0.0	0.4	0.0	0.8	tr	57.2	5.2	0.0	5.2	2.0	0.4	3.2	23.6	0.8	1.6	0.0	1.6	0.4	33.6	3.6	0.4	4.0	
9	8943.00	0.087	moderate	44.8	0.0	6.0	1.6	0.4	0.0	2.0	2.0	0.0	0.8	0.4	0.0	0.0	0.0	0.0	0.8	0.4	59.2	12.4	0.0	12.4	2.0	0.4	2.0	14.8	1.6	0.4	0.0	2.8	0.0	24.0	3.6	0.8	4.4	
10	8943.60	0.115	moderately well	34.8	0.0	2.4	0.4	1.2	0.0	10.4	0.4	0.8	0.0	0.0	0.8	0.0	2.8	0.0	0.4	0.0	54.4	0.0	0.0	0.0	0.8	0.0	0.0	1.2	42.0	0.0	0.0	1.6	0.0	45.6	0.0	tr	0.0	
11	8943.80	0.114	moderately well	52.4	0.0	2.8	1.2	0.0	0.0	12.4	1.6	0.0	0.8	0.0	0.0	1.6	0.0	0.0	0.8	0.4	74.0	0.4	0.0	0.4	2.8	0.0	0.8	7.6	2.4	0.4	0.0	2.4	0.0	16.4	9.2	0.0	9.2	
12	8943.90	0.130	moderately well	39.6	0.0	2.4	0.0	0.4	0.0	7.6	1.2	0.0	0.0	0.0	0.4	0.0	0.4	0.0	tr	0.8	52.8	1.2	0.0	1.2	2.4	tr	3.6	6.0	29.6	0.4	0.0	1.2	0.0	43.2	2.8	0.0	2.8	
13	8944.20	0.120	moderately well	48.8	0.0	6.0	0.8	0.4	0.4	8.0	0.4	0.0	0.0	0.0	0.0	0.4	0.0	0.0	0.0	0.0	65.2	2.0	0.0	2.0	2.8	0.4	4.4	8.0	6.4	0.0	0.8	1.6	0.0	24.4	8.4	0.0	8.4	
14	8944.40	0.139	well	50.4	0.8	4.0	0.8	0.0	0.0	7.2	1.2	0.0	0.0	tr	0.4	0.0	0.4	0.0	0.4	0.8	66.4	1.2	0.0	1.2	2.8	0.0	1.2	4.0	21.2	0.0	0.0	0.8	0.0	30.0	2.4	0.0	2.4	
15	8944.90	0.109	moderately well	25.6	0.0	2.4	0.0	0.4	0.0	11.6	0.4	0.0	0.0	0.0	3.2	0.4	3.6	0.4	0.8	0.4	49.2	0.0	0.0	0.0	0.4	0.0	0.0	2.0	45.6	0.0	0.0	2.4	0.0	50.4	0.0	0.4	0.4	
20	8950.00	0.062	moderately well	37.2	0.0	4.8	3.2	1.2	0.0	0.8	0.4	0.0	0.8	0.0	0.0	0.0	0.0	0.0	0.8	0.0	49.2	11.2	0.0	11.2	tr	0.0	8.4	8.4	21.2	0.0	0.0	1.6	0.0	39.6	0.0	0.0	0.0	
24	8958.25	0.061	moderately well	38.4	0.0	3.6	2.8	1.2	0.0	0.8	0.0	0.0	0.4	0.0	0.0	0.0	0.4	0.0	0.4	0.0	48.0	18.8	0.0	18.8	5.6	0.0	13.2	8.4	0.4	0.0	0.0	5.2	0.4	33.2	0.0	0.0	0.0	
25	8960.10	0.062	moderately well	32.4	0.0	3.2	3.6	2.0	0.0	0.8	0.0	0.4	0.4	0.0	0.0	0.0	0.0	0.0	0.0	0.4	43.2	17.6	0.0	17.6	7.6	0.8	6.0	17.2	0.0	2.0	0.0	4.4	0.4	38.4	0.4	0.4	0.8	
30	8970.00	0.059	moderately well	32.8	0.0	5.2	1.6	1.6	0.0	1.2	0.0	0.0	1.6	0.4	0.0	0.0	tr	0.4	0.0	0.0	44.8	21.2	0.0	21.2	6.4	0.0	6.8	19.6	0.8	tr	0.0	0.4	0.0	34.0	tr	0.0	0.0	
34	8978.15	0.046	moderately well	31.2	0.0	4.4	1.2	0.0	0.0	3.6	0.0	0.0	0.8	0.8	tr	0.0	tr	0.0	0.0	0.8	42.8	33.2	4.8	38.0	0.4	0.0	0.0	14.0	1.2	0.0	0.0	3.2	0.0	18.8	0.0	0.0	0.0	
35	8980.10	0.038	moderately well	34.8	0.0	1.6	2.4	1.6	0.0	1.2	0.0	0.0	0.8	0.0	0.4	0.0	0.4	0.0	0.0	0.0	43.6	28.0	10.4	38.4	0.8	0.0	0.0	10.0	3.6	0.0	0.0	3.2	0.4	18.0	0.0	0.0	0.0	

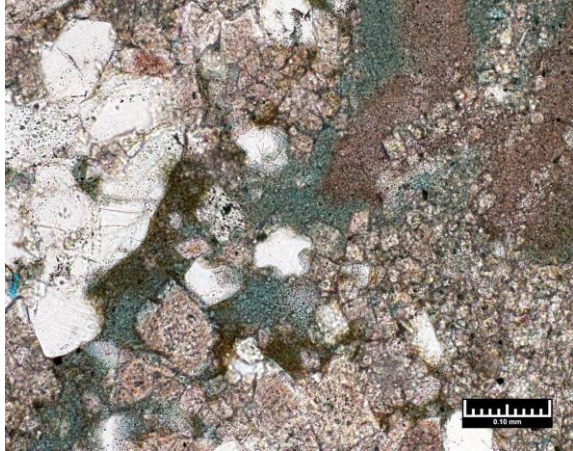
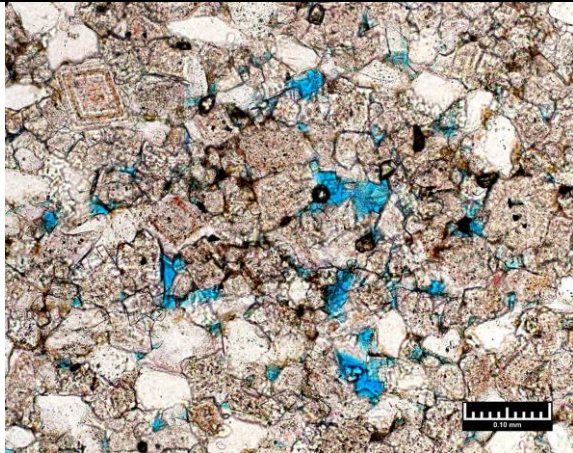
**Table 2.8.** Examples of lithology and petrographic description of two samples from Well Trigger No. 1-31H (NDIC Well #17946) in Grenora field (NDIC, 2019).

Sample Number	Sample Depth (ft)	Porosity (%)	Permeability (md)
11	8943.80	8.1	1.55
<b>Lithology:</b> Sandstone			
<b>Petrographic Description</b> This very fine-grained sandstone is moderately well sorted. Monocrystalline quartz grains are abundant and calcareous grains are common. Other grains found in minor to trace amounts include potassium feldspar, plagioclase, argillaceous rock fragments, muscovite, and brachiopod fragments. Dolomite (d/df) is found in moderate amounts as replaced grains and as intergranular cement. The intergranular cement has a patchy distribution. Some of the dolomite is slightly ferroan. Other minor cements include pyrite (py), calcite, ferroan calcite (Fcal), and syntaxial quartz overgrowths. Intergranular pores (ig) are observed in moderate amounts.			
Sample Number	Sample Depth (ft)	Porosity (%)	Permeability (md)
25	8960.10	7.6	0.003
<b>Lithology:</b> Argillaceous Siltstone			
<b>Petrographic Description</b> This argillaceous siltstone contains faint clay-rich laminations. Monocrystalline quartz grains are abundant. Other grains found in minor to trace amounts include potassium feldspar, plagioclase, volcanic rock fragments, chert, muscovite, and calcareous grains. Detrital clay matrix is abundant. Dolomite cement/replacement (d/df) is abundant. Much of the dolomite is slightly ferroan. Syntaxial quartz overgrowths (qo) are observed in moderate amounts. Pyrite framboids (py) are dispersed throughout the matrix. Potassium feldspar overgrowths are rare. Tiny intergranular pores are found in trace amounts. Secondary intragranular pores are rare. Pyrite (arrow) appears to have precipitated in the fracture (Fr), suggesting the fracture may be natural.			

**Table 2.9.** Examples of lithology and petrographic description of two samples from Well Muller No. 1-21-16H (NDIC Well #20552) in Grenora field (NDIC, 2021a).

Sample Number	Sample Depth (ft)	Porosity (%)	Klink. Perm. @ 2600 psi (md)
1-96	9676.50	3.9%	0.0017
<p><b>Lithology:</b> Slightly argillaceous, silty/sandy dolostone</p>			
<p><b>Pore System</b>                      Dominantly subequal amounts of poorly developed very small intercrystalline/intergranular pores that are erratically distributed, occurring between dolomite crystals and/or siliciclastic grains, and micropores that mostly occur within altered/partially leached argillaceous rip-up clasts and also within clays present in dolomite intercrystalline areas and small dolomitic grains; a very minor amount of small secondary intraparticle pores result from the partial leaching of siliciclastic grains (mostly feldspar)</p>			
Sample Number	Sample Depth (ft)	Porosity (%)	Klink. Perm. @ 2600 psi (md)
1-83	9663.50	5.5%	NA (fractured)
<p><b>Lithology:</b> Organic-rich, phosphatic, dolomitic, pyritic, argillaceous, very fine-grained sandstone to sandy dolostone, with thin silty/sandy shale laminations</p>			
<p><b>Pore System</b>                      Trace intraparticle pores within phosphatic fragments</p>			

**Table 2.10.** Examples of lithology and petrographic description of two samples from Well Rasmussen No. 1-21-16H (NDIC Well #20844) in Grenora field (NDIC, 2021a).

Sample Number	Sample Depth (ft)	Porosity (%)	Klink. Perm. @ 2600 psi (md)
1-105	10277.40	8.1	4.8 (fractured)
<p><b>Lithology:</b> Interbedded/interlaminated dolomitic, very fine-grained sandstone, silty/sandy dolostone, and slightly dolomitic mudstone to silty/sandy mudstone</p>			
<p><b>Pore System</b> Erratically distributed pores that generally appear isolated; the sandstone contains minor intergranular/intercrystalline pores are very sparsely scattered, and micropores the occur within compacted argillaceous clasts; dolostones contain micropores in argillaceous clasts and in remnant detrital clays that occur between replacement dolomite crystals, as well as rare intercrystalline pores</p>			
Sample Number	Sample Depth (ft)	Porosity (%)	Klink. Perm. @ 2600 psi (md)
1-115	10287.50	4.5	0.0020
<p><b>Lithology:</b> Sandy dolostone</p>			
<p><b>Pore System</b> Dominantly erratically small intercrystalline/intergranular pores occur between dolomite crystals or between dolomite crystals and siliciclastic grains; a minor amount of micropores are observed within some argillaceous intraclasts; rare secondary pores that appear to result from the dissolution of feldspar grains</p>			



### **2.3 Summary**

In this Chapter, the location of the fields and wells of study were presented. Mineralogical testing data and geomechanical data are the main inputs to the rock physics-based correlations that will be developed in the following Chapters. It was observed that the Bakken formation is very heterogeneous, hence, defining one generalized model to be used for the entire formation may not be practical.

In the next Chapter, a review of the geology of the Bakken will be provided, with specific reference to the application of this study. A review of the rock physics models will also be presented.

# CHAPTER 3

## Geology and Rock Properties of The Bakken Formation

In the first part of this Chapter, a summary related to the geology of the Bakken formation is presented. This will be with a reference to the petrophysical and geological characteristics of the three Bakken members, as this information will be needed for the modeling that will be developed in this study.

The second part of the Chapter will present a brief overview of the rock physics models. The DEM inclusion-based model is the basis for developing the correlations in this research study.

### **3.1 Bakken Formation Stratigraphy and Lithofacies**

Figure 3.1 shows an example of generalized stratigraphy of the Bakken formation. In this Figure seven potential lithofacies that typically are seen in the Bakken are listed with some description of the mineralogy of each facies. The Bakken Formation is made up of a series of complex lithofacies with variable distribution and properties. The Bakken Formation is a subsurface unit extending across southern Manitoba and Saskatchewan, northeastern Montana and north-western North Dakota. It has three distinctive stratigraphic successions of three members. The Lower Bakken black shale (LB), the Middle Bakken dolomitic siltstone to sandstone (MB) and the Upper Bakken

black shale (UB). Deposition took place through the Late Devonian – Early Carboniferous in the Williston Basin, a shallow intracratonic setting at the southernmost end of the Western Canada Sedimentary Basin (Barnes et al., 2020). Understanding the presence and nature of fractures within and across the various lithofacies is critical to developing an accurate model of a Bakken reservoir and predicting the effectiveness of various oil and gas operations.

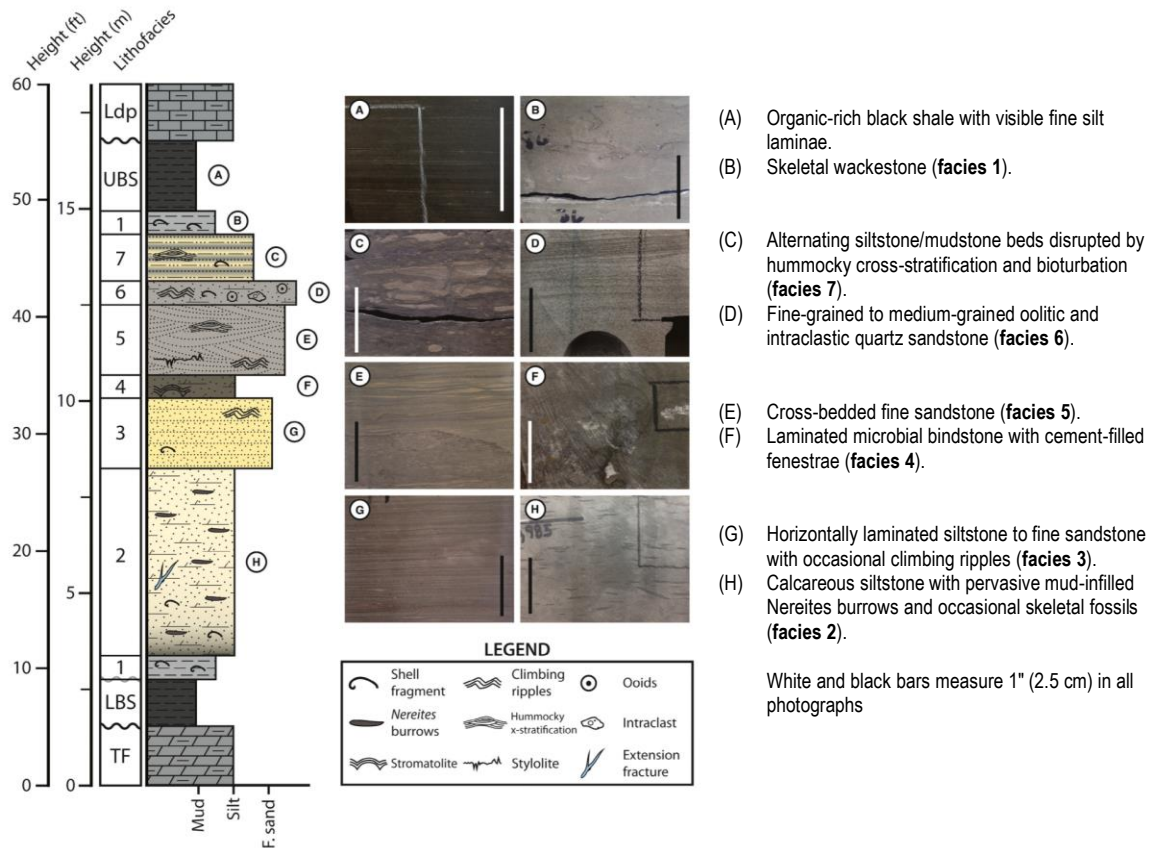


Figure 3.1. Example of generalized stratigraphy of the Bakken Formation (Modified from Barnes et al., 2020).

Figure 3.2 presents examples of the Bulk mineral chemostratigraphy and the X-ray diffraction (XRD) measurements (cumulative weight %) from two Bakken cores studied by Barnes et al., (2020). The lithofacies' colors and textures shown in this figure correspond to the general stratigraphic column in Figure 3.1. From this figure, as noted by Barnes et al. (2020) it is seen that

the Bakken black shales are mostly clay and quartz. While the UB is distinguished by higher proportions of quartz, carbonate and total organic carbon (TOC), the LB is richer in clays and potassium feldspar. Each member contains heterogeneous enrichments of carbonate (ca 9 wt.%) and pyrite (ca 6.5 wt.%). Dolomite constitutes the majority of the UB and LB shale carbonates (ca 85% of all carbonates). By contrast, the MB averages ca 47.6 wt.% carbonate mineralogy, of which ca 31% is calcite. Quartz and clays comprise the siliciclastic component, which decrease up-section as carbonate mass increases in the shallower facies towards the top of the member. Also, of note is the presence of significant pyrite and anhydrite in some cores, ranging up to 17% and 40%, respectively. Table 3.1 presents the range and mean values of different minerals in the Bakken members as reported by Barnes et al. (2020).

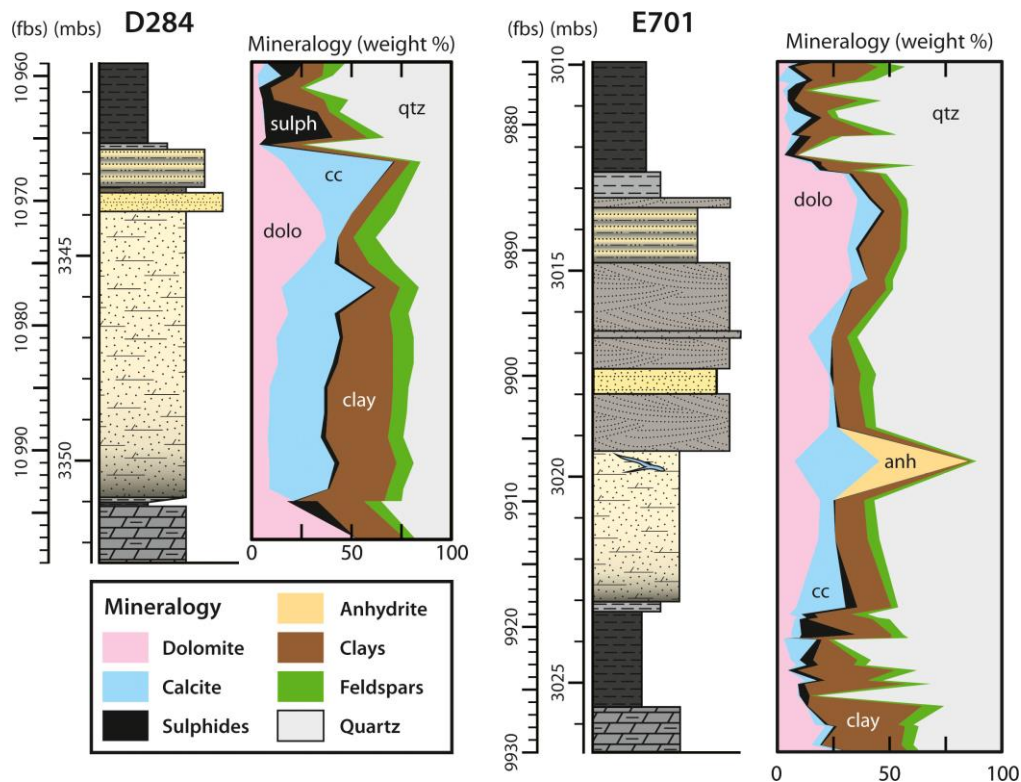
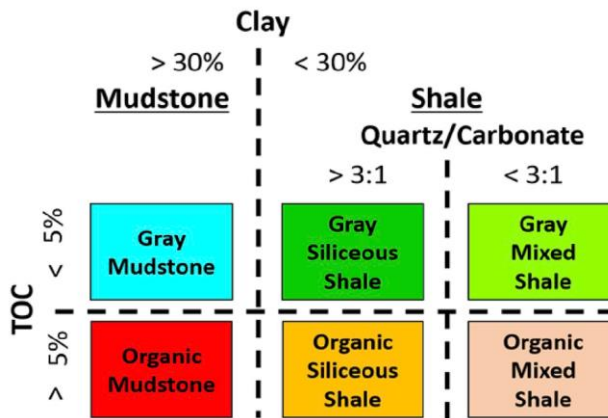


Figure 3.2. Bulk mineral chemostratigraphy through the Bakken Formation (Barnes et al., 2020).

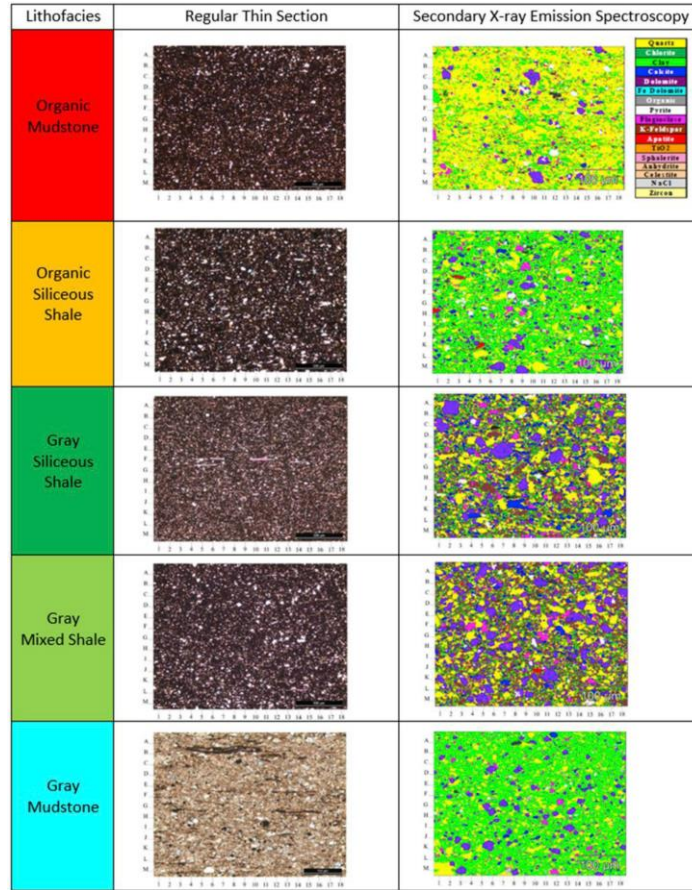
**Table 3.1.** Bulk organic carbon and mineralogical mean and range statistics for the Bakken formation members (After Barnes et al. (2020).

Formation	Wt. %	TOC	Quartz	K Feldspar	Plagioclase	Calcite	Dolomite	Pyrite	Sphalerite	Anhydrite	Clays
UBS	Mean Range	10.60	50.4	7.93	1.66	1.44	8.83	6.52	0.58	0.029	21.8
		(0.76 to 25.3)	(14.4 to 90.7)	(0 to 23)	(0 to 7)	(0 to 21)	(0 to 34)	(0 to 34)	(0 to 16)	(0 to 2)	(1.42 to 60.3)
MB	Mean Range	0.49	28.3	5.05	0.00	14.80	32.80	1.16	0.032	1.06	14.8
		(0 to 10.4)	(4 to 64.2)	(0 to 13)	-	(0 to 84)	(2 to 77)	(0 to 17)	(0 to 2.3)	(0 to 3.6)	(0 to 58)
LBS	Mean Range	9.19	44.6	9.81	0.83	1.12	5.64	6.71	0.19	0.00	29.9
		(0.45 to 23.8)	(19 to 82.4)	(2 to 25)	(0 to 5)	(0 to 16)	(1 to 21)	(1 to 24)	(0 to 5.2)	-	(0.1 to 60.7)

Bhattacharyaa and Carr (2019) proposed a schematic quantitative methodology to classify the Bakken shale lithofacies. As shown in Figure 3.3, they used three criteria to classify the Bakken shale lithofacies: TOC (cutoff 5%), clay volume (cutoff 30%) and quartz-to-carbonate ratio (cutoffs 3 and 1/3). They noted the advantage of this classification due to the fact that they observed similar facies on regular thin sections and Secondary X-ray Emission Spectroscopy images shown in Figure 3.4. Figure 3.5 shows an example of integrated well logs in one of the Bakken wells with identified lithofacies. Figure 3.6 summarizes features of different shale lithofacies in the Bakken Formation, in terms of mineralogy, TOC, and conventional well log responses that are presented by Bhattacharyaa and Carr (2019).



**Figure 3.3.** A general classification of shale lithofacies showing six different shale lithofacies (Bhattacharyaa and Carr, 2019).



**Figure 3.4.** Regular thin section and Secondary X-ray Emission Spectroscopy images showing five different shale lithofacies, corresponding to Figure 2.5 (Bhattacharyya and Carr, 2019).

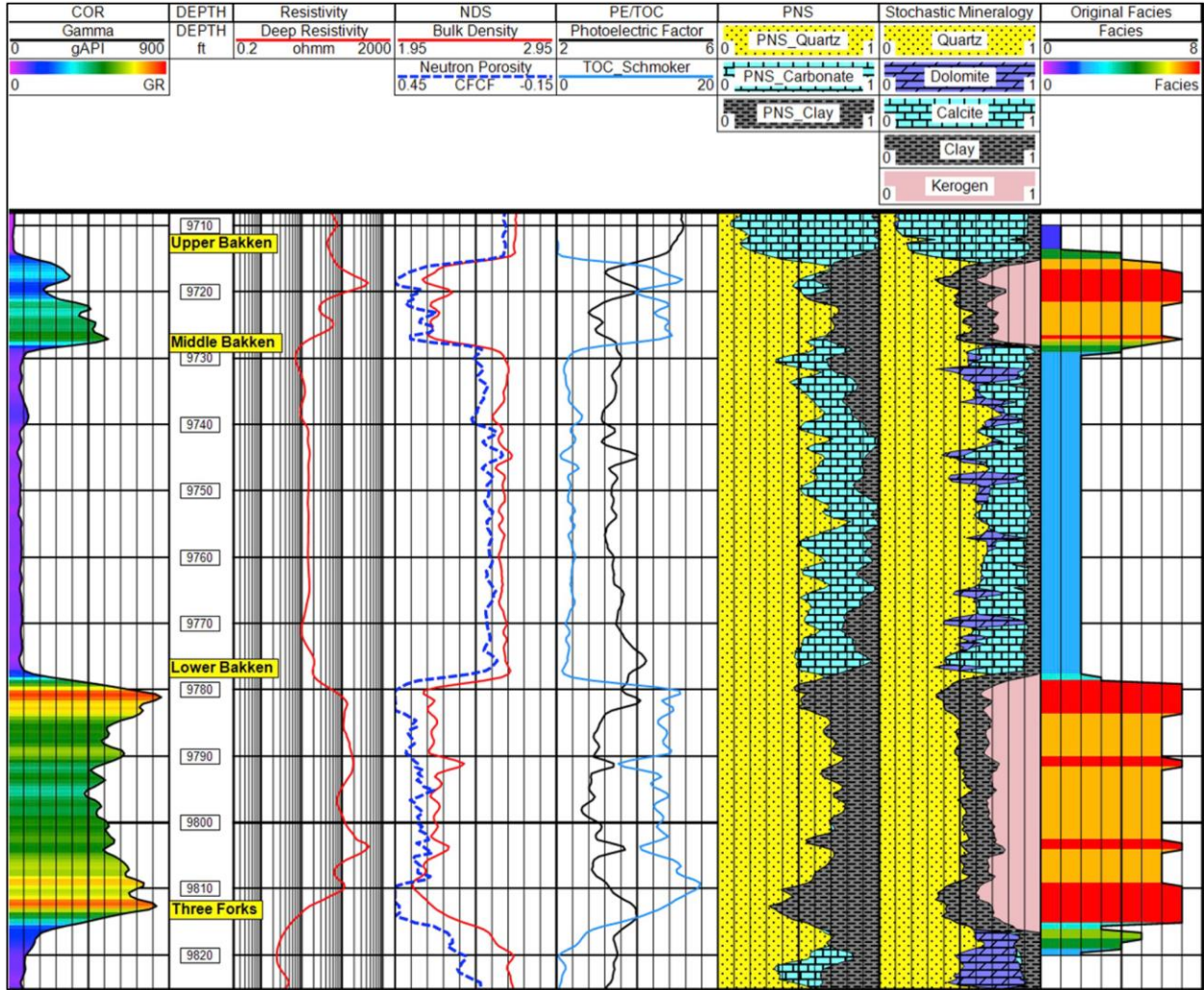
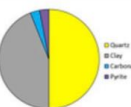
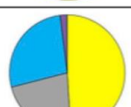
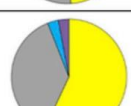


Figure 3.5. Example of integrated well logs in one of the Bakken wells with identified lithofacies (Bhattacharyaa and Carr, 2019).

Lithofacies	Pie Plot	Average Proportion (wt %)	Gamma (API)	Bulk Density (g/cc)	Neutron $\phi$ (%)	Ln (Deep Resistivity) (ohm-m)	Umaa (barns/cc)
Organic Mudstone		Quartz: 52 Carb: 3 Clay: 45 TOC: 12.5	337-873 605	2.05-2.3 2.18	30-48 39	2.1-6.56 4.33	6-9.6 7.8
Organic Siliceous Shale		Quartz: 70 Carb: 1 Clay: 29 TOC: 12.4	303-750 527	2.06-2.38 2.22	22-40 31	2.4-5.8 4.1	5.5-9.5 7.5
Gray Siliceous Shale		Quartz: 67 Carb: 5 Clay: 28 TOC: 4.2	150-347 249	2.44-2.6 2.52	18-26 22	1.03-2.3 1.67	8.3-10.6 9.45
Gray Mixed Shale		Quartz: 51 Carb: 27 Clay: 22 TOC: 2.08	101-202 152	2.55-2.68 2.62	15-27 21	1.1-3.8 2.45	8.8-12.6 10.7
Gray Mudstone		Quartz: 60 Carb: 3 Clay: 37 TOC: 3.86	238-410 324	2.43-2.5 2.47	26-36 31	1.3-3.2 2.25	8.8-9.84 9.32

**Figure 3.6.** Example mineralogical features, TOC, and conventional well log response of the five shale lithofacies of the Bakken (Bhattacharyaa and Carr, 2019).

Sorensen et al. (2010) used two wells in Dunn County (see Figure 3.7 for the location of the County) to assign lithofacies to the Bakken formation. Figure 3.8 shows the five lithofacies and corresponding GR and resistivity log responses in Well #16333 (left) and Well #16766 in Dunn County. In these wells, the top lithofacies (5) corresponds to the top of the MB and the top lithofacies (1) corresponds to the top of the LB Shale.

The above two wells were used by Sorensen et al. (2010), with the aid of the core data, to provide validation for the lithologic interpretation from the mineral solver analysis. The entire MB member was cored in the pilot hole of Well #16333. The cored interval is shown at left (core depths adjusted downward 9 feet to agree with log depths). Plugs were taken at approximately 1 ft intervals throughout the MB. Core Lab’s description of these samples indicates the MB lithology varies from shaly and commonly calcareous siltstone to very fine grained to very shaly, calcareous to very calcareous sandstone.



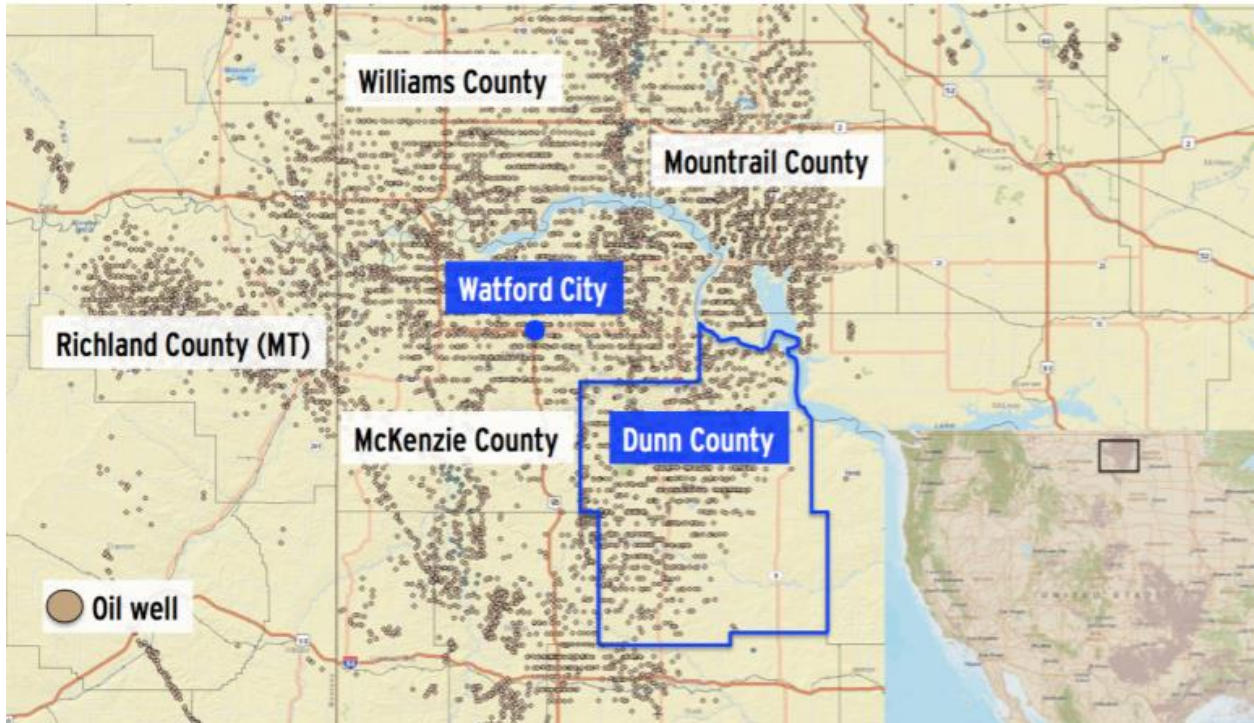


Figure 3.7. Location of Dunn County in the Williston Basin, North Dakota (Raimi and Newell, 2016).

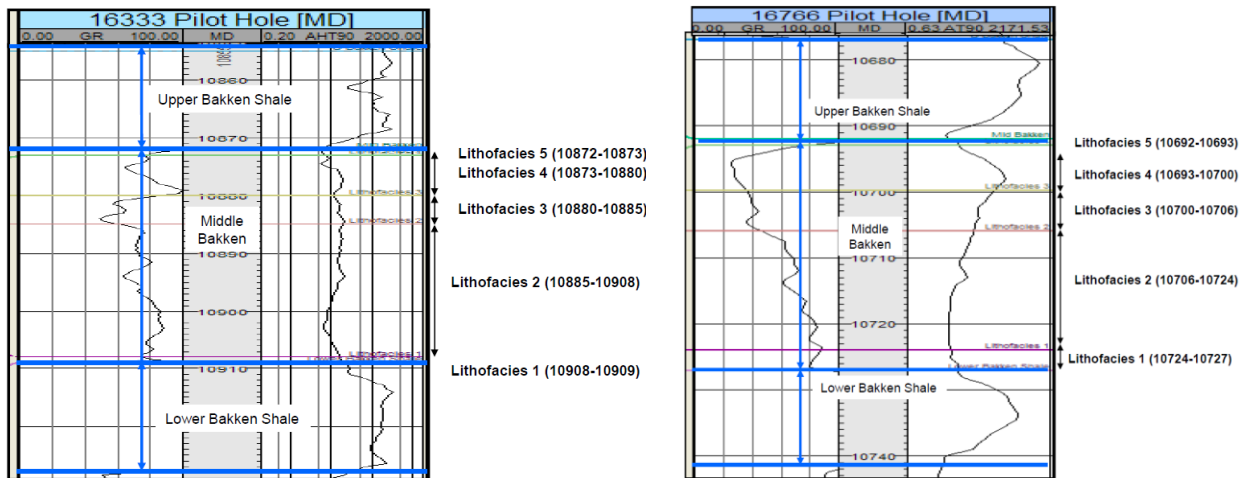


Figure 3.8. Bakken lithofacies assigned in Well #16333 (left) and Well #16766 (right) in Dunn County (Sorensen et al., 2010).

A review of this core confirmed Core Lab’s lithologic description. Mineral Solver lithology for well #16333 indicates the MB is comprised of 12% to 25% clay and about equal amounts of quartz and limestone. Based on this analysis, dolomite concentrations of 10% to 20% at isolated intervals are also present. Overall, Mineral Solver results are in complete agreement with the core data.

The same five lithofacies in the previous well were assigned for Well #16766 as seen in Figure 39 (right). In this figure, the cored interval is shown at left with core depths adjusted downward 20 feet to agree with log depths (top of core at 10610' log depth). One plug was taken from the MB and one at the transitional zone between the MB and Lower Bakken Shale. The results of the omni Laboratories XRD report for these samples indicated that the MB lithology consists of quartz, dolomite, clays, and calcite with minor amounts of feldspars and pyrite in order of abundance. Mineral Solver lithology for well 16766, as shown at left of Figure 3.9, indicates the MB at 10710 ft log depth (10690 ft core plug depth) is comprised of about 20% clay, 40% quartz and 40% limestone. Based on the Mineral Solver results, dolomite is not present at this depth but about 2% dolomite is seen lower in the well at 10712 ft and 10714 ft.

Even with the benefit of core data determining Middle Bakken lithology in the Dunn County study area is very difficult due to its gradational nature from a very fine grained, silty, calcite cemented sandstone and siltstone to very fine grained silty and argillaceous limestone. In the two Bakken cores from the study area the clastic component of the MB consists of siltstone to very fine-grained sandstone, commonly very shaly and very calcareous. This sandstone is very gradational to what can be described as a very finely crystalline to microcrystalline packstone. In summary, Bakken core from Well #16766 appears to be consistent with the Mineral Solver results.

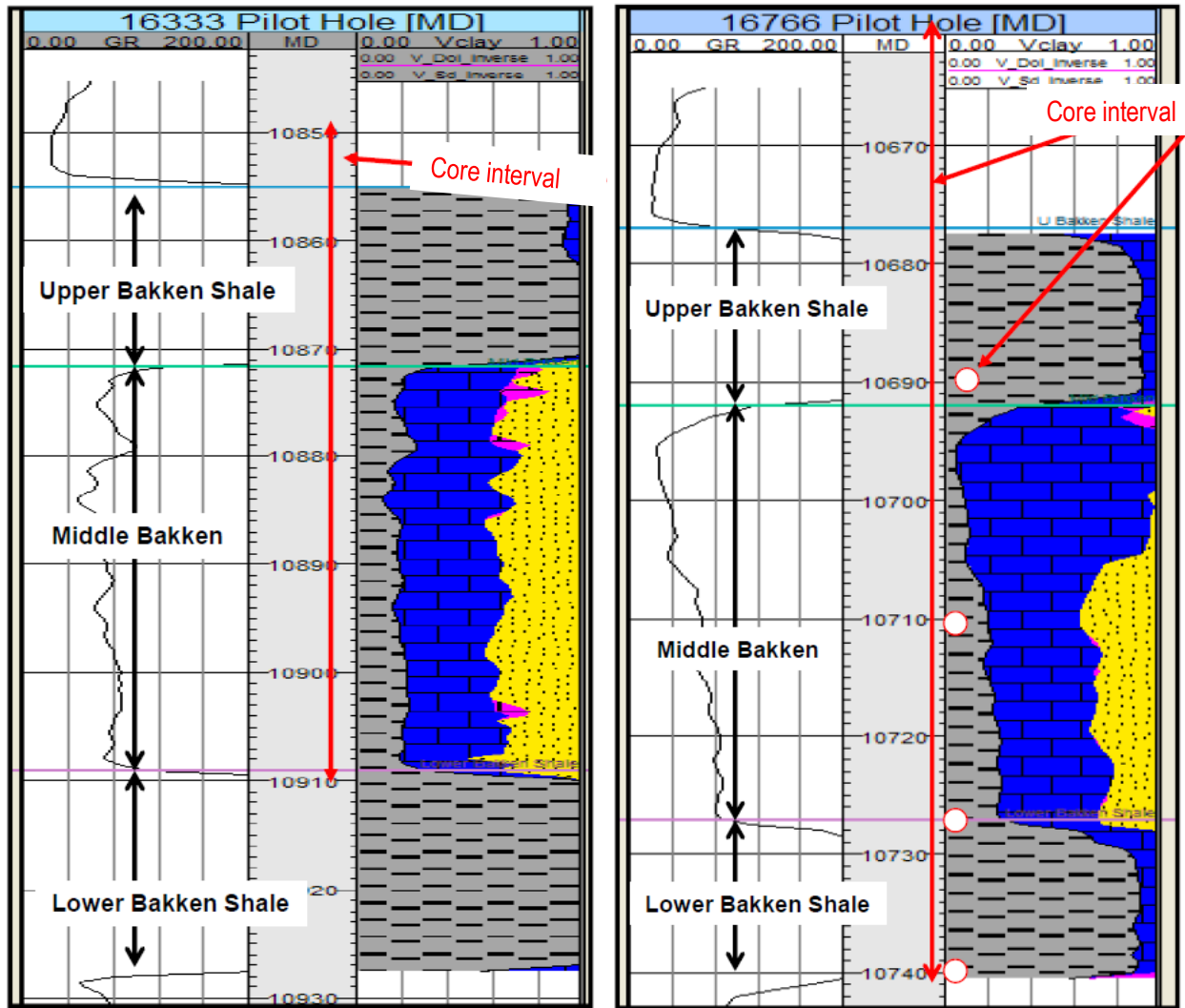


Figure 3.9. Bakken lithofacies assigned in Well #16766 in Dunn County (Sorensen et al., 2010).

### 3.2 Rock Physics Models

In this Section, a brief overview of rock physics models is presented with a focus on two specific models which will be used in the next Chapters.

Rock physics models provide a better understanding of the reservoir rock properties and the fluid contents in pore spaces in terms of velocity variation which is linked to the elastic variations. As there are many parameters affecting the velocity and attenuation of reservoir rocks (e.g. pore shape and size, fluid type, cementation and lithology, temperature, pore pressure, confining pressure),

interpretation of subsurface formations is very complex. Saberi (2017) divided rock physics models into four categories of pore fluid models, theoretical models, empirical and heuristics models, and hybrid models. Table 3.2 shows a list of some of these models. Also, in the following sub-sections, a brief review of some of these models which will be referred to and used in this thesis will be given. For more detailed information about these models, the reader is referred to Harju (2022).

**Table 3.2.** Rock Physics Classifications (After Saberi, 2017).

<b>Pore Fluid Models</b>	Brie et al. (1995) Model. Patchy vs homogeneous fluids.
<b>Theoretical Models</b>	<ol style="list-style-type: none"> <li>1- <b>Bound Models:</b> Voigt (1928), Reuss (1929), Hill (1952), Hashin–Shtrikman (1963).</li> <li>2- <b>Inclusion-Based Theories:</b> Kuster and Toksöz (1974), differential effective medium, DEM (Nishizawa, 1982), self-consistent approximation, SCA (Berryman, 1980a,b), T-matrix (Jakobsen et al., 2003a,b),</li> <li>3- <b>Contact Theories:</b> Hertz and Mindlin (Mindlin, 1949), Digby (1981), Walton (1987)</li> <li>4- <b>Transformation Models:</b> Gassmann Equation (), Brown &amp; Korringa (1975), generalized Gassman’s (1951) model, Shapiro (2007)</li> <li>5- <b>Computational Models:</b> Digital imaging</li> </ol>
<b>Empirical and heuristic models</b>	Examples: Time Average Model (Wyllie et al., 1956), Raymer et al. (1980), Eberhart Phillips (1989), Marion (1990), Sams & Andera (2001), Castagna et al. (1985), Krief et al. (1990), Greenberg & Castagna (1992)
<b>Hybrid Models</b>	Examples: Xu & White model (1995), Xu and Payne model (2009)  <b>Note:</b> Backus (1962) & Hudson (1980) models are respectively the common models used for upscaling and crack induced anisotropy modeling.

### 3.2.1 Pore Fluid Models

In practice, rock physics models usually mix the pore fluids first and then combine them with the rock texture to create a porous rock. In most cases, the pores are filled with more than one fluid, which is known as partial saturation, either as a homogenous or a nonhomogeneous (patchy)

saturation. This depends on the frequency at which the elastic waves were measured, i.e. ultrasonic, sonic or seismic measurements (Saber, 2017).

Brie et al. (1995) proposed the following empirical fluid mixing law:

$$K_{\text{fluid mix}} = (K_{\text{liquid}} - K_{\text{gas}})(1 - S_{\text{gas}})^e + K_{\text{gas}} \quad (3.1)$$

$$K_{\text{liquid}} = \frac{(S_{\text{water}} + S_{\text{oil}})}{S_{\text{water}}/K_{\text{water}} + S_{\text{oil}}/K_{\text{oil}}} \quad (3.2)$$

When the mixing coefficient  $e$  is -1 it yields the Reuss lower limit (i.e. equivalent to the homogeneous saturation), whereas, it converges to the Voigt upper limit when  $e=1$ . Field data suggest an average value of  $e$  between 3 and 5.

### 3.2.2 Voigt-Reuss-Hill Model

Voigt (1910) assumed an iso-strain model where the loading is along the parallel layers, whereas Reuss (1929) considered an iso-stress model where the load is applied perpendicular to the layers. In Voigt's model, the stress transferred into each layer is constant while the strains in each layer may differ. In Reuss model, due to the axial load, the strains in all layers will be constant while the local stresses in each layer may differ. The Hill average (Hill, 1963) is the arithmetic average of the Voigt and Reuss models.

### 3.2.3 Hashin-Shtrikman Model

The Hashin-Shtrikman (H-S) model provides a narrower bound than the Voigt and Reuss upper and lower bounds (1962, 1963). If one phase is fluid, then the lower bound of H-S shear moduli will be zero, similar to the Reuss model. It is also shown that the HS upper bound curve fits with moldic pores and HS lower bound fits with cracks (Kumar and Han, 2005).

### 3.2.4 Kuster and Toksoz (K-T) Inclusion Model

The inclusion models are popular in use as inclusions can be introduced into a solid medium to simulate the pores or cracks with different shapes such as spheres, ellipses with different aspect ratios (i.e. height to base axis length), needles and disks. The inclusions may be empty or filled with gas, fluid or solid. For example, in shale formations, the inclusion may consist of kerogen as a solid phase and gas/oil as the fluid phase. Thin section or SEM data and/or image logs are needed to determine the density, distribution, and shape of the pores and/or fractures.

Assuming that the effect of the randomly oriented inclusions is isotropic, the equivalent bulk ( $K_{KT}$ ) and shear ( $\mu_{KT}$ ) moduli based on the K-T model are:

$$(K_{KT} - K_s) \frac{K_s + 4\mu_s/3}{K_{KT}^* + 4\mu_s/3} = \sum_{i=1}^N x_i (K_i - K_s) P^i \quad (3.3)$$

$$(\mu_{KT} - \mu_s) \frac{\mu_s + \zeta_s}{\mu_{KT} + \zeta_s} = \sum_{i=1}^N x_i (\mu_i - \mu_s) Q^i \quad (3.4)$$

Here, subscript  $s$  stands for the solid or host material and the subscript  $i$  stands for the inclusion.  $P^i$  and  $Q^i$  are the shape factors that can be calculated, for examples, for sphere and penny shape inclusions from Table 3.3. In this Table,  $\alpha$  is the aspect ratio of the ellipsoid, which is the ratio of the height ( $c$ ) to the base of the ellipsoid assuming the base is a circle ( $a=b$ ).

**Table 3.3.** Shape factors for sphere and penny shaped cracks (Schon, 2011).

Inclusion	$P^{si}$	$Q^{si}$
Sphere: general	$\frac{K_s + \frac{4}{3}\mu_s}{K_i + \frac{4}{3}\mu_s}$	$\frac{\mu_s + \zeta_s}{\mu_i + \zeta_s}$
Sphere: fluid filled	$\frac{K_s + \frac{4}{3}\mu_s}{K_i + \frac{4}{3}\mu_s}$	$\frac{\mu_s}{\zeta_s} + 1$

Penny-shaped crack: general	$\frac{K_s + \frac{4}{3}\mu_i}{K_i + \frac{4}{3}\mu_i + \pi \cdot \alpha \cdot \beta_s}$	$\frac{1}{5} \left( 1 + \frac{8 \cdot \mu_s}{4 \cdot \mu_i + \pi \cdot \alpha (\mu_s + 2 \cdot \beta_s)} + 2 \frac{K_i + \frac{2}{3}(\mu_i + \mu_s)}{K_i + \frac{4}{3}\mu_i + \pi \cdot \alpha \cdot \beta_s} \right)$
Penny-shaped crack: fluid filled	$\frac{K_s}{K_i + \pi \cdot \alpha \cdot \beta_s}$	$\frac{1}{5} \left( 1 + \frac{8 \cdot \mu_s}{\pi \cdot \alpha (\mu_s + 2 \beta_s)} + 2 \frac{K_i + \frac{2}{3}\mu_s}{K_i + \pi \cdot \alpha \cdot \beta_s} \right)$
where	$\beta_s = \mu \frac{3K_s + \mu_s}{3K_s + 4\mu_s}$	and $\zeta_s = \frac{\mu_s}{6} \frac{9K_s + 8\mu_s}{K_s + 2\mu_s}$

The main considerations of the K-T model include:

- It is applicable only for small porosity ranges. Also, it does not consider the interaction between different pores and the ratio of porosity to pore aspect ratio should be much smaller than 1 (Bing and Jia, 2014).
- It violates the upper and lower Hashin-Shtrikman bounds, in particular at low porosity range (Bing and Jia, 2014).
- For a given porosity, regardless of the number of inclusions the results are the same, as pores are assumed to be disconnected.
- Compressional and shear velocities are more influenced by thinner pores than by thicker pores.
- Compressional velocities are affected more than shear velocities due to the saturation and the effect of the fluid is closely related to the aspect ratio of the inclusion.

### 3.2.5 Differential Effective Medium (DEM)

DEM theory (Bruggeman, 1935) models two-phase composites by incrementally adding inclusions to the matrix phase. Calculations of DEM requires numerical solution of differential equations.

In a two-phase composite, where phase 1, with volume fraction  $x_1$ , is the matrix phase, and phase 2, with volume fraction  $x_2$ , is the included phase. Assume that the effective bulk and shear moduli

$K^*(x_2)$  and  $\mu^*(x_2)$  at one value of  $x_2$  is known, treat  $K^*(x_2)$  and  $\mu^*(x_2)$  as the composite host bulk and shear moduli, and let  $K^*(x_2+\Delta x_2)$  and  $\mu^*(x_2+\Delta x_2)$  represent the effective bulk and shear moduli after a small fraction  $\Delta x_2/(1-x_2)$  of composite host has been replaced by inclusions of phase 2. The following equations are used to solve numerically to calculate bulk and shear moduli of the effective medium:

$$(1 - x_2) \frac{dK^*(x_2)}{dx_2} = (K_2 - K^*)P^{*2}(x_2) \quad (3.5)$$

$$(1 - x_2) \frac{d\mu^*(x_2)}{dx_2} = (\mu_2 - \mu^*)Q^{*2}(x_2) \quad (3.6)$$

Here, initial conditions  $K^*(0) = K_1$ ,  $\mu^*(0) = \mu_1$ ,  $K_1$  and  $\mu_1$  are the bulk and shear moduli of the initial host material and  $K_2$  and  $\mu_2$  are the bulk and shear moduli of the incrementally added inclusions.

The followings are some of the main features of the DEM for modeling the effective elastic medium of rocks (Bing and Jia, 2014):

- It can never violate rigorous bounds compared with the K-T theory.
- As the ordinary differential equations for bulk and shear moduli are coupled, it is not straight forward to integrate them to obtain accurate analytical formulae for the bulk and shear moduli. This means numerical solutions of differential equations must be developed in order to obtain accurate estimation of the bulk and shear moduli.
- The order by which different inclusions (i.e. pores or cracks) with different aspect ratios are added has a major impact on the effective elasticities of the porous medium.

### 3.2.6 Backus Averaging Theory

The Backus averaging method (1962) presents analytical expressions for equivalent elastic properties of a stack of thin layers. the individual layers may be isotropic, TIV, TIH, Orthorhombic, or monoclinic (Kumar, 2013). The Backus and Hudson (1980) models are, respectively, the



common models used for upscaling and for crack induced anisotropy modeling. As stated by Saberi (2017) “Backus showed that at the long wavelength limit, a stratified medium composed of isotropic layers will behave like a transverse isotropic (TI) medium, and derived the effective elastic constants for such a medium. Hudson (1980) derived the effective elastic constants of a cracked medium by modeling an isotropic background superimposed with oriented cracks. This model is quite commonly used in carbonates for modeling fracture effects on velocities and also modeling azimuthal inversion studies for fracture characterization”.

In Backus averaging, in order to include the lenticular fabric of Illite, instead of being a continuous sheet, the stiffness coefficients  $C_{11}$  and  $C_{66}$ , i.e. corresponding to properties along the lamination were modified by Vernik and Landis (1996).

### **3.3 Example Rock Physics Models of the Bakken**

Harju (2022) conducted rock physics modeling of the three Bakken members using different algorithms and based on some of the models listed in Table 3.2. Tables 3.4 to 3.6 present the volume fraction of the minerals that he used based on the available XRD data from a certain depth, for UB and LB shales and the MB clastic and carbonate members, respectively. In his study, both homogeneous and patchy fluids were considered as pore fluids and the fluid saturation was performed using the Gassmann and K-T model. In general, the workflow consisted of mixing the non-clay minerals first using the Hill averaging and then adding in the clay minerals, and Kerogen, in case of shale, using K-T or DEM models. The fluid mixing used the Brie model assuming two phase fluids of water and oil at 50% saturation for each phase and then adding the fluid to the rock matrix using the K-T or DEM models. For UB and LB shales, the Backus averaging was also applied to capture the anisotropy. Also, the anisotropy was modeled using the K-T model by performing two sets of models: velocities parallel and perpendicular to the layering. The Wiley

model was used as a reference corresponding to an average pore aspect ratio of approximately 0.1.

In addition, the HS bounds were calculated in some cases.

From Tables 3.4 to 3.6 it is observed that the major clay mineral in shale formation is Illite (47.5% out of total of 53.8%) and quartz and dolomite are the major non-clay minerals. It is therefore, reasonable, for simplicity, to consider one phase of clay minerals (53.8%) as Illite and two phases of non-clay minerals as quartz and dolomite (total of 46.2%). The same approach was used in the work done by Harju (2022) for the clastic and carbonated sections in the MB member for calculation of the average velocities and moduli.

**Table 3.4.** Summary of UB and LB Shale Mineralogy (wt%) (Sorensen, et al., 2010). Clay minerals are bolded.

Minerals	Calcite	Chlorite	Dolomite	Pyrite	Cristobalite	Illite	Quartz	Smectite	TC
<b>Wt%</b>	0.8	<b>4.7</b>	11.6	2.5	1.2	<b>47.5</b>	30.2	<b>1.6</b>	53.8

**Table 3.5.** Summary of MB clastic Mineralogy (wt%) (Sorensen, et al., 2010). Clay minerals are bolded.

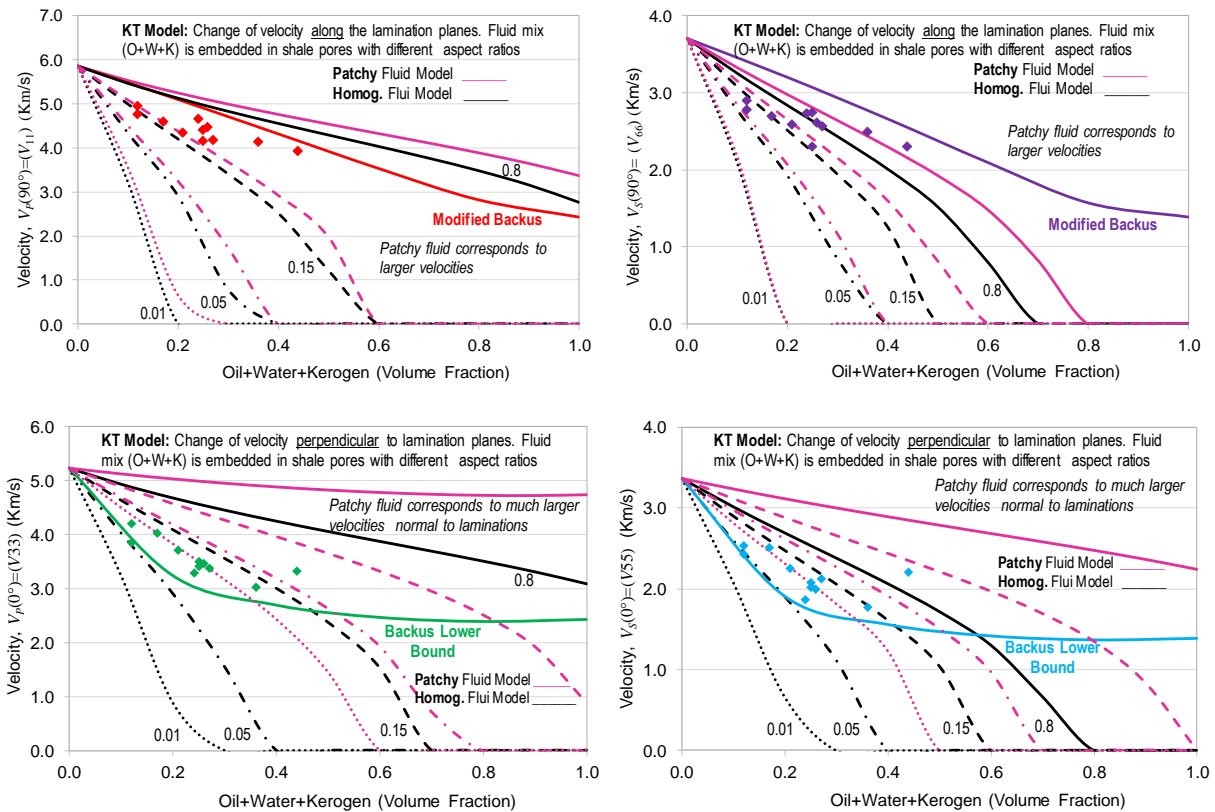
Calcite	Chlorite	Dolomite	Pyrite	Cristobalite	Illite	Quartz	Smectite	TC
4.7	<b>2.7</b>	10.2	3.3	1.3	<b>21.4</b>	53.7	<b>2.7</b>	26.7

**Table 3.6.** Summary of MB carbonate Mineralogy (wt%) (Sorensen, et al., 2010). Clay minerals are bolded.

Calcite	Chlorite	Dolomite	Pyrite	Cristobalite	Illite	Quartz	Smectite	TC
36.3	<b>1.0</b>	23.0	0.6	0.8	<b>10.2</b>	26.9	<b>1.1</b>	12.4

Figure 3.10 shows the results of compressional (left) and shear (right) velocities parallel (top) and perpendicular (bottom) to the shale laminations for patchy versus homogeneous fluid. Here, the shale anisotropy was modeled using the K-T model. In this figure, the lower Backus bound for velocities perpendicular to the lamination and the modified Backus plot in case of velocities parallel to the laminations are presented. As stated by Harju (2022): “patchy fluid increases both compressional and shear velocities, as compared to homogeneous fluid. However, this increase is much more significant in case of velocities perpendicular to the laminations as opposed to along

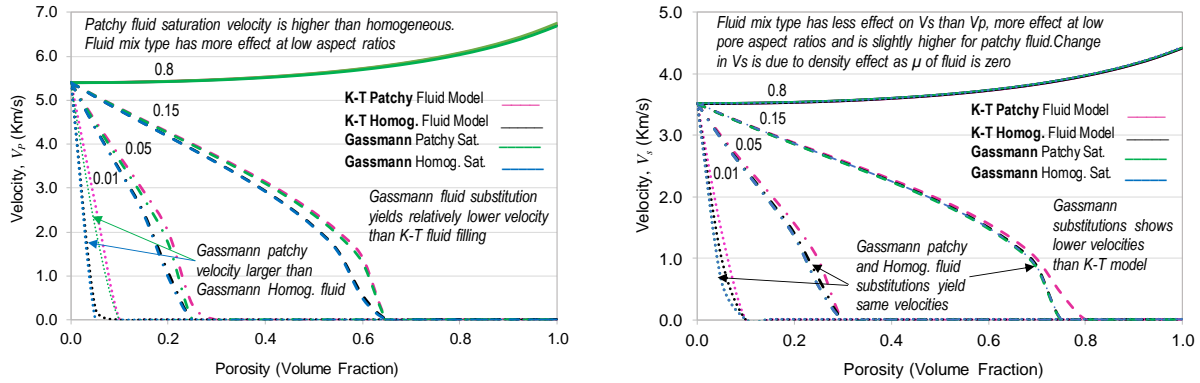
the shale layering. We have reported earlier that fluid shear moduli are not affected by the fluid model regardless of being patchy or homogeneous. However, shear moduli of the entire rock (i.e. rock matrix + saturated pores) is slightly affected by the fluid model, which is explained by the implication of the inclusion's bulk moduli in the formula of shear moduli calculation of K-T model, while density is not affected by fluid mixing method". The lab data of Figure 3.10 belong to the Bakken formation taken from Carcione et al. (2011).



**Figure 3.10.** Comparison of compressional (left) and shear (right) velocities parallel (top) and perpendicular (bottom) to the shale laminations for patchy versus homogeneous fluid (Harju, 2022).

Figure 3.11 presents the results of velocity calculations using the K-T model for MB clastic formation for both patchy and homogeneous fluids. Also, the results of Gassmann equation for fluid substitution are presented for comparison purposes. From this figure, according to Harju (2022), the main findings are:

- The effect of the fluid mix type is more pronounced at low pore aspect ratios (i.e. cracks).
- Patchy fluid saturation velocity is higher than that of homogeneous fluid, due to the assumption of connectivity of the fluid in the latter case.
- Gassmann fluid substitution (with assumption of connected pores) yields relatively lower velocity than K-T fluid filling (isolated pores assumption) for cracks.
- Fluid mix type has less effect on shear than compressional velocity and it is more pronounced at lower pore aspect ratios. Also, the K-T model shows slightly larger velocities at low pore aspect ratios for patchy compared to homogeneous fluids.
- Fluid mix type has less noticeable effect on shear moduli than bulk moduli for the K-T model. However, for Gassmann, the shear velocity is the same regardless of fluid type.
- Change in shear velocity is due to change of density at different rock porosity, as shear velocity for fluid is zero.
- Shear velocity for dry and saturated rocks are the same ( $\mu_{\text{sat}} = \mu_{\text{dry}}$ ) for Gassmann.
- Gassmann's equation results in similar velocities for patchy and homogeneous fluids as the shear velocity in Gassmann's equation is a function of density and shear moduli. As Gassmann assumes no change in porosity of the rock due to the fluid substitution (i.e. no change in density), and also referring to the second assumption in Gassmann's equation, i.e.  $\mu_{\text{sat}} = \mu_{\text{dry}}$ , shear velocity will be similar regardless of the fluid type.

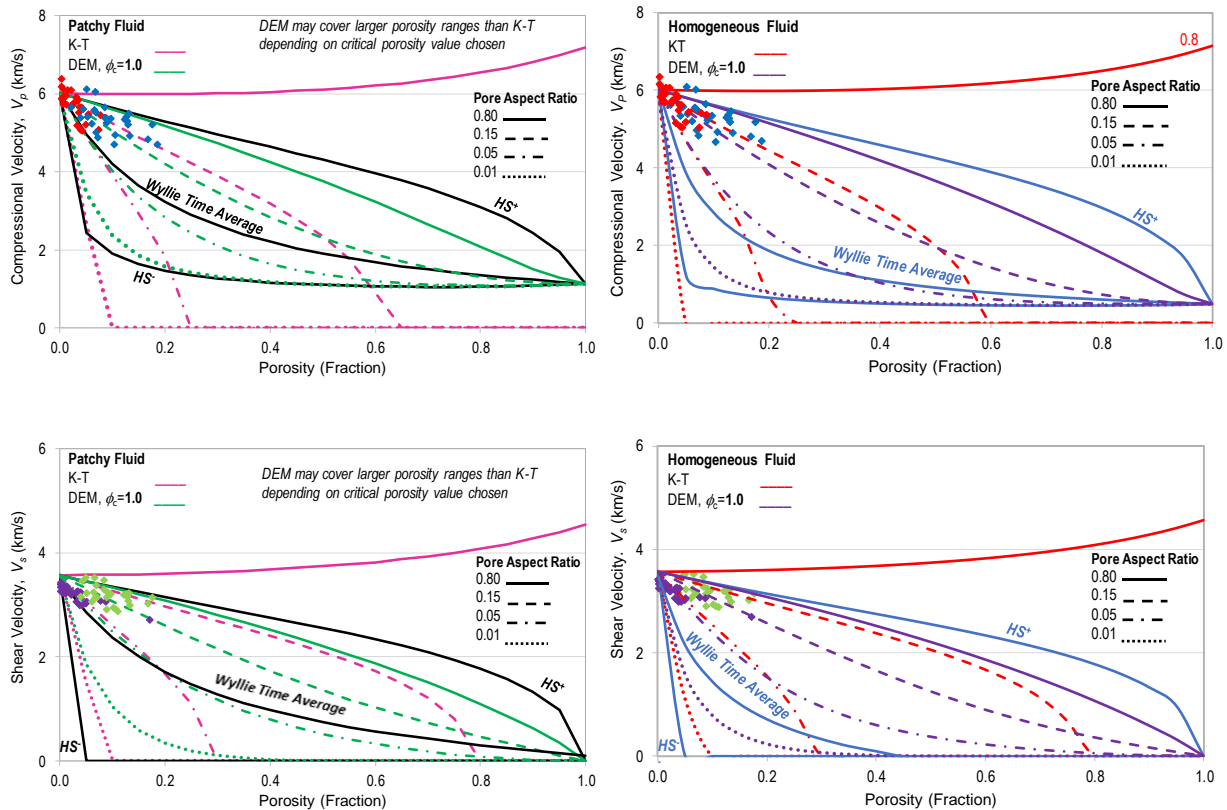


**Figure 3.11.** Compressional (left) and shear (right) velocities models for MB clastic formation (Harju, 2022).

The results corresponding to the MB carbonate formation are presented in Figures 3.12 for K-T and DEM model, assuming critical porosity of 1.0. The critical porosity ( $\phi_c$ ) is the porosity beyond which the grains lose their contacts and instead of the grains, the fluid will be the load bearing medium. In practice, the critical porosity is between 35-45% (Schon, 2011). The HS upper and lower bounds, as well as Wyllie time averaging are also shown on these plots. From this figure the following conclusions were drawn by Harju (2022):

- The results of DEM are within the HS upper and lower bounds for all different aspect ratios whereas, as expected this is not the case for the K-T model.
- The DEM and K-T models for cracks converge to the HS lower bound, indicating weakest case, whereas larger aspect ratios, or more of spherical pores, converges to the HS upper bound, representing the strongest case.
- Assuming critical porosities, the primary porosity (corresponding to  $\alpha=0.1$ ) will be closer to the Wyllie time average results.
- In general, DEM covers a larger range of porosities for different pore types, whereas the K-T model is limited to small porosity ranges for simulation of crack dominated pore types.

- DEM shows a better match to the data than the K-T model. Yet, it suggests more of intraparticle pores for carbonate, especially for dolomite (blue dots), while we expect more cracks in MB carbonate formation. This discrepancy could be due to the difference in mineralogy of the samples in the two cases and conditions of the experiments



**Figure 3.12.** Compressional (top) and shear (bottom) velocities of MB carbonates based on DEM critical porosity of 1.0 and K-T model for patchy (left) and homogeneous fluid (right), Harju (2022). Red and blue dots are, respectively, lab data corresponding to limestone and dolomite from Bakken reported by Sayers (2008).

### **3.4 Summary**

In this Chapter, after reviewing the geology and stratigraphic characteristics of the Bakken formation with references to different past studies, a summary of the mineralogy and log properties of the Bakken members were presented. This was followed by a summary of the main rock physics models, with a focus on the inclusion-based theories of the DEM model. An example of the applications of these models for the Bakken members done by Harju (2022) was presented.

The DEM rock physics models will be used in the next Chapter to develop correlations for estimating velocity and elastic properties of the Bakken formations instead of using the cumbersome rock physics models such as the K-T and especially the DEM model.

# CHAPTER 4

## DEM-Based Velocity-Porosity Correlations

As explained in the previous Chapters, the members of the Bakken formation are constituted of different minerals with different volume fractions. In this Chapter, we use a superimposed approach in order to estimate the velocity, or equivalently, the elastic properties of the Bakken formation, based on the velocity and volume fraction of the minerals. The mineralogy of the formation is taken from the XRD data or ECS logs. This Chapter is focused on the lab scale (macro) data analysis. The DEM inclusion-based rock physics model will be applied to develop generic correlations for formations with low to large porosities.

### 4.1 Superimposed Modeling

The rock physics models provide relationships between velocity and porosity, as discussed in the previous Chapter. The inclusion-based models also include the impact of pore aspect ratio ( $AR$ ) in the models. However, the use of these models is not simple and requires a series of calculations and sometimes requires numerical modeling such as DEM.

In this study the basic idea is to establish velocity-porosity correlations as a function of pore  $AR$  as alternatives to the rock physics models. However, these correlations will be developed based on the results of rock physics modeling. To propose more generalized correlations applicable to



formations constituted of different minerals in different percentages and filled with different fluids, we use a superimposed approach. The workflow that is used includes the following steps:

1. Define the main mineral constituents of the formation members under study. With special focus on the Bakken formation, we consider calcite (limestone), dolomite, clay, quartz, feldspar and anhydrite as the main minerals for the UB and LB shales and Middle Bakken clastic and carbonates formations (Harju, 2022). However, the results for other minerals will also be presented.
2. Assume the pores are filled with three phase fluids of water, oil, and gas. The water, oil and gas saturations should also be measured or calculated using different petrophysical methods and calibrated against core data. This will allow calculation of the average fluid phase velocity.
3. Apply the DEM model to calculate the average velocity of a rock which is composed of only one mineral with varying porosities filled with three-phase fluids, and different pore *ARs*.
4. Determine the volume fractions of different minerals in the formation based on the XRD or ECS analysis. The formation velocity can then be calculated as a linear average (or other functions) of each mineral velocity and volume fraction.

The above workflow allows simple calculation of the velocity of a formation with various minerals and pores with different shapes filled with different fluids, using established correlations. The calculations can be done using a calculator or by developing a simple excel spreadsheet. The input data needed in this workflow to estimate formation velocity includes porosity, pore fluid saturation, and pore *AR*. Depending on the data availability, one can perform different analysis as desired. For example, if the *AR* is not known, assuming different *ARs* as input to the correlations and comparing with the measured velocity data (from lab data or sonic logs), the pore *AR* can be estimated. Also, establishing a velocity correlation with other common logs such as GR or density,

one can replace these log values with velocity in the developed correlations. In the following sections the details of developing the correlations are explained for calcite as an example, and then the results are presented for different minerals.

## 4.2 Minerals and Fluid Properties

The bulk ( $K$ ) and shear ( $\mu$ ) moduli and density ( $\rho$ ) of minerals that were used in this study for modeling purposes are listed in Table 4.1. The data were obtained from the XRD analysis (Harju, 2022). It is important to mention that the properties listed in this table for clay minerals (Illite, chlorite, and smectite) correspond to wet clays, not dry. This was with the idea that it includes the effect of bound water in clays, so there will be no need to add bound water to the workflow, for simplification purposes. Also in this Table, the corresponding values of compressional ( $V_p$ ) and shear velocities are presented. These velocities were calculated using the isotropic equations of (Schon, 2011):

$$V_P = \sqrt{\frac{K+4/3\mu}{\rho}}, \quad V_S = \sqrt{\frac{\mu}{\rho}} \quad (4.1)$$

Table 4.2 shows the properties of the water, oil and gas that were used for modeling in this study, all of them taken from the Bakken core and log data. It is to be noted that the shear moduli and shear velocity of fluids are zero.

**Table 4.1.** Bulk moduli ( $K$ ), shear moduli ( $\mu$ ), density ( $\rho$ ) and compressional ( $V_p$ ) and shear ( $V_s$ ) velocities of minerals used in this study for modeling (Harju, 2022).

Minerals	Calcite	Chlorite	Dolomite	Pyrite	Cristobalite	Illite	Quartz	Smectite
$K$ (MPa)	76.8	95.3	94.7	158	39.1	11.7	36.6	9.3
$\mu$ (MPa)	32.0	11.4	45.0	149	16.3	16.4	45.0	6.9
$\rho$ (gr/cc)	2.71	2.69	2.87	5.02	2.32	2.60	2.65	2.20
$V_p$ (Km/s)	6.64	6.41	7.34	8.43	5.12	3.59	6.04	2.90
$V_s$ (Km/s)	3.44	2.06	3.96	5.45	2.65	2.51	4.12	1.77

**Table 4.2.** Bulk moduli ( $K$ ), density ( $\rho$ ) and equivalent velocity ( $V_p$ ) of pore fluids (Harju, 2022).

Minerals	Oil	Water	Gas
$K$ (MPa)	0.42	2.2	0.15
$\rho$ (gr/cc)	0.8	1.1	0.015
$V_p$ (Km/s)	0.725	1.414	3.162

### 4.3 Porosity-Velocity Relationship from DEM Model

As mentioned earlier, the correlations of porosity-velocity are developed based on the output of the DEM model. This is a commonly used model for determining the average properties of the formation. However, calculation of the differential equations (see equations 3.3 and 3.4 in Chapter 3) requires using specialized software. In this study we used Techlog to calculate the average velocities. To explain the process here, we present the calculation steps for calcite.

The DEM model was used to calculate the average velocities of a rock composed of only calcite mineral. The simulations were conducted assuming different porosities, fluid saturations and pore ARs. This generated a large volume of data which was used to develop correlations representing the porosity-velocity relations, as functions of fluid saturation and pore ARs.

Figure 4.1 shows the results of compressional ( $V_p$ ) and shear ( $V_s$ ) velocities for calcite as a function of porosity and ARs. This example corresponds to the case of pores fully saturated with gas ( $S_g=100\%$ ). Also, it is to mention that the calculations presented here use Brie equation (see equations 3.1 and 3.2 in the preceding Chapter) with coefficient of  $e=3$  to average fluid properties. As it will be discussed later, this is a good average value for most of the real applications.

From the results of Figure 4.1 two main observations are made. First, when the aspect ratio of the pores become larger than approximately 0.50, the velocities do not change noticeably. Second, the slope of the curves appears to be steeper when pore's aspect ratio is less than approximately 0.10. These observations were considered in developing the correlations. Figure 4.2 presents the best

fits to the curves of Figure 4.1. The correlations that were used as best fits to the velocity-porosity data for  $V_p$  (when  $AR < 0.1$ ) was the one phase exponential decay equation in the form of:

$$V_p = (V_{p,m} - C_0)e^{-C_1\phi} + C_0 \quad AR < 0.1 \quad (4.2)$$

Here,  $V_{p,m}$  is the velocity of the mineral and  $C_0$  and  $C_1$  are constants of the correlations.

Exponential equations were used for  $V_p$  (when  $AR \geq 0.1$ ) and for  $V_p$  corresponding to all  $ARs$ .

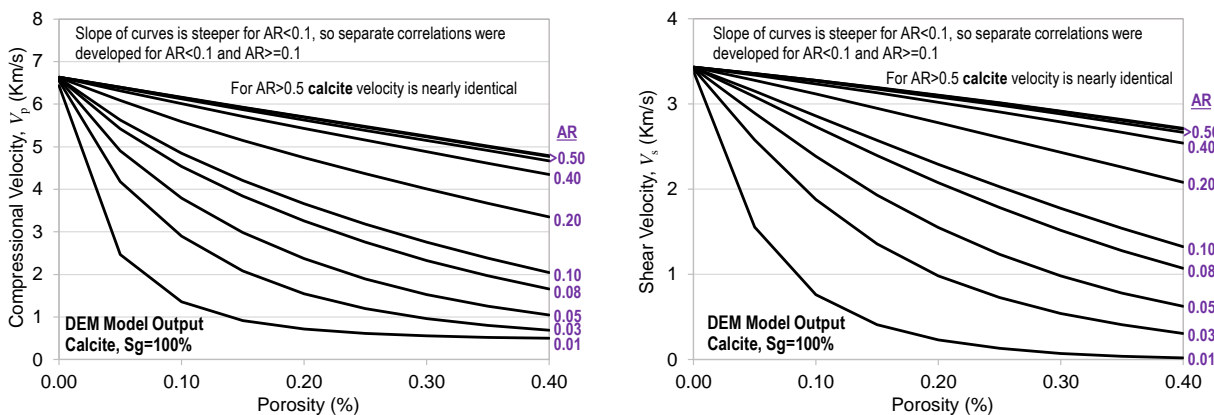
$$V_p = V_{p,m}e^{-C_0\phi} \quad AR \geq 0.1 \quad (4.3)$$

$$V_s = V_{s,m}e^{-C'_1\phi} \quad \text{All } ARs \quad (4.4)$$

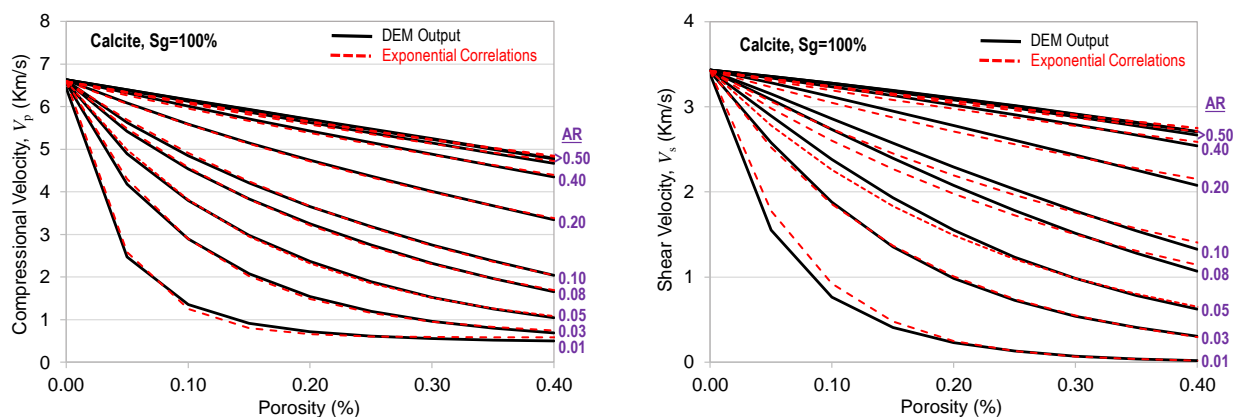
While the exponential fit was the same for all  $ARs$  for the case of  $V_p$ , based on the earlier observations from Figure 4.1 and 4.2, separate correlations were developed for two cases of  $AR \geq 0.1$  and  $AR < 0.1$  for more accurate fits. The results of Figure 4.2 show a very good agreement between the DEM model and correlations, both for compressional and shear velocities with correlation coefficients of close to 1.

The above results indicate an overall exponential trend between the velocity and porosity. This is the same observation as reported by various researchers from lab and field data analysis (e.g. Athy, 1930; Kahraman and Yeken, 2008; Kurtulus et al., 2016; Kassab and Weller, 2015).

Similar to the results of Figure 4.2, correlations were applied for the case of calcite fully saturated with oil (Figure 4.3) and with water (Figure 4.4). The results of Figures 4.2 to 4.4 imply that, as expected, moving from gas to oil and water saturated pores, at zero porosity, the velocities correspond to the velocity of calcite (i.e.  $V_{p,cal} = 6.59$  Km/s and  $V_{s,cal} = 3.42$  Km/s). However, as porosity increases, the compressional velocities tend to reach the velocity of the fluid occupying the pores, whereas, shear velocities tend towards zero, and regardless of the fluid type, the shear velocity is zero when the medium is filled with fluid.



**Figure 4.1.** DEM model compressional ( $V_p$ ), (left) and shear ( $V_s$ ), (right) velocity versus porosity for calcite fully saturated with gas with different pore's aspect ratios.



**Figure 4.2.** Exponential fits to the DEM model data (from Figure 4.1) present a good agreement for both compressional ( $V_p$ ), (left) and shear ( $V_s$ ), (right) velocity data for calcite fully saturated with gas.

The above results refer to the extreme cases where the pores are filled with a single-phase fluid, which graphically correspond to the three vertices of a triangle (see Figure 4.5). In this Figure, the edges of the triangle represent two-phase fluid with saturation of each phase corresponding to the distance from each vertex. Any point inside the triangle has three-phase fluid saturations, and the percentage of each phase is represented by the distance of the point from each vertex. For example, the fluid saturation for each phase corresponding to point  $P$  in this figure can be written as:

$$S_w = \frac{l_w}{l_w + l_o + l_g} \quad S_o = \frac{l_o}{l_w + l_o + l_g} \quad S_g = \frac{l_g}{l_w + l_o + l_g} \quad (4.5)$$

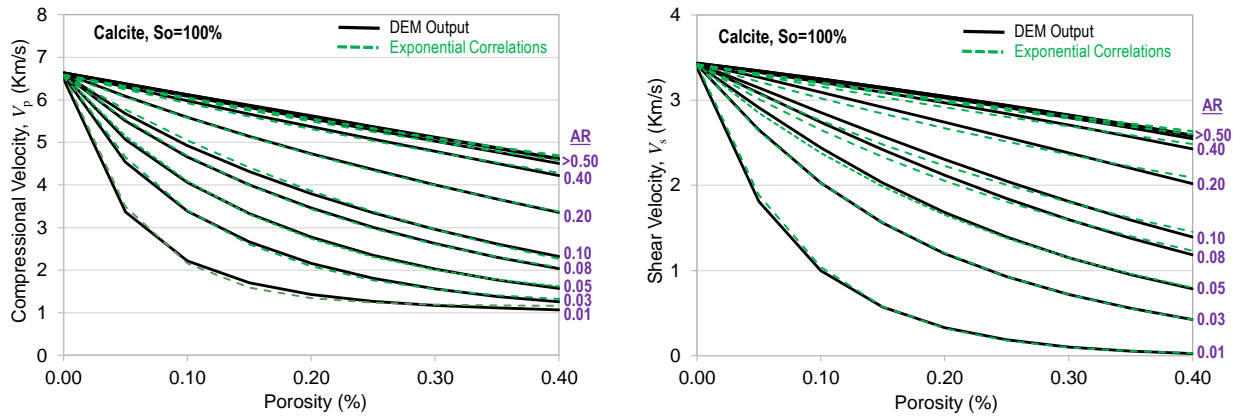


Figure 4.3. Exponential fits to the DEM model data for compressional ( $V_p$ ), (left) and shear ( $V_s$ ), (right) velocity data for calcite fully saturated with oil.

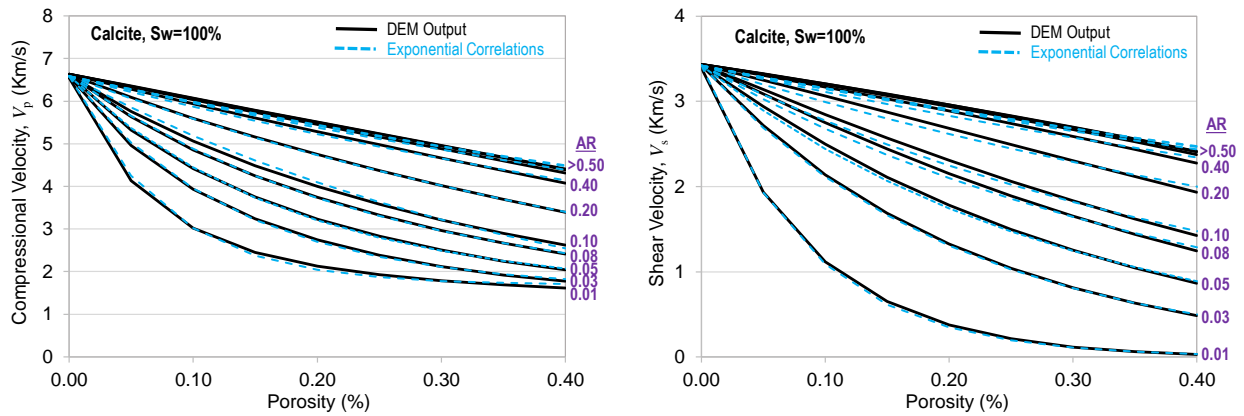


Figure 4.4. Exponential fits to the DEM model data for compressional ( $V_p$ ), (left) and shear ( $V_s$ ), (right) velocity data for calcite fully saturated with oil.

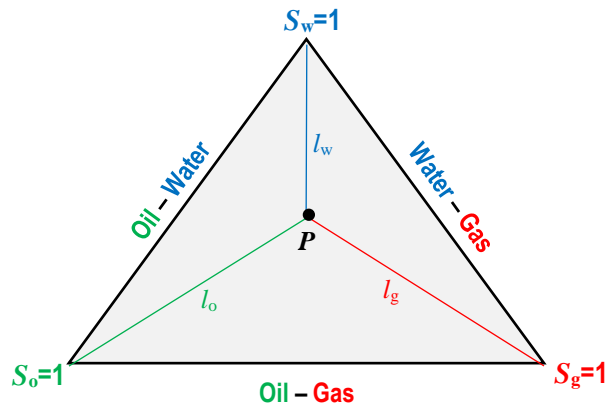
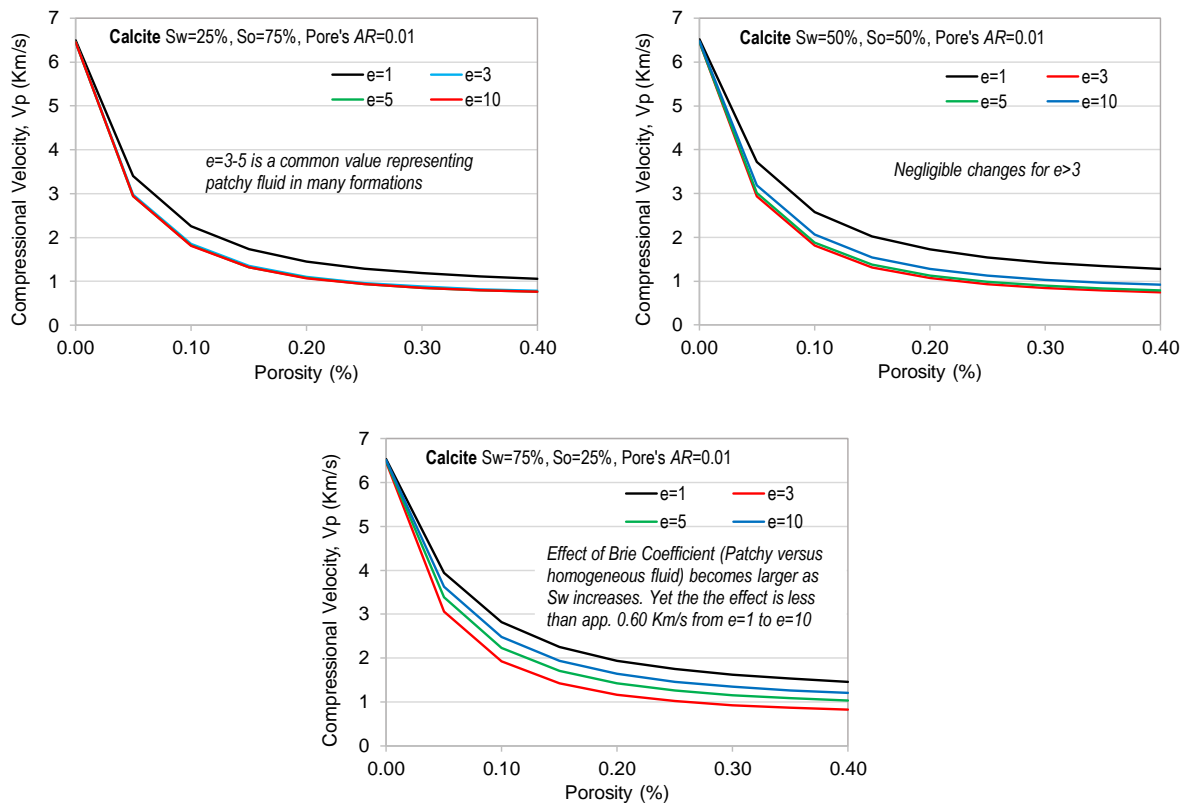


Figure 4.5. The vertices of the triangle correspond to the velocity of the rock saturated with a single-phase fluid of water, oil or gas. The edges represent the two-phase fluid saturations. Any point inside the triangle represents three-phase fluid with the saturation percentages represented by the distance to each vertex.

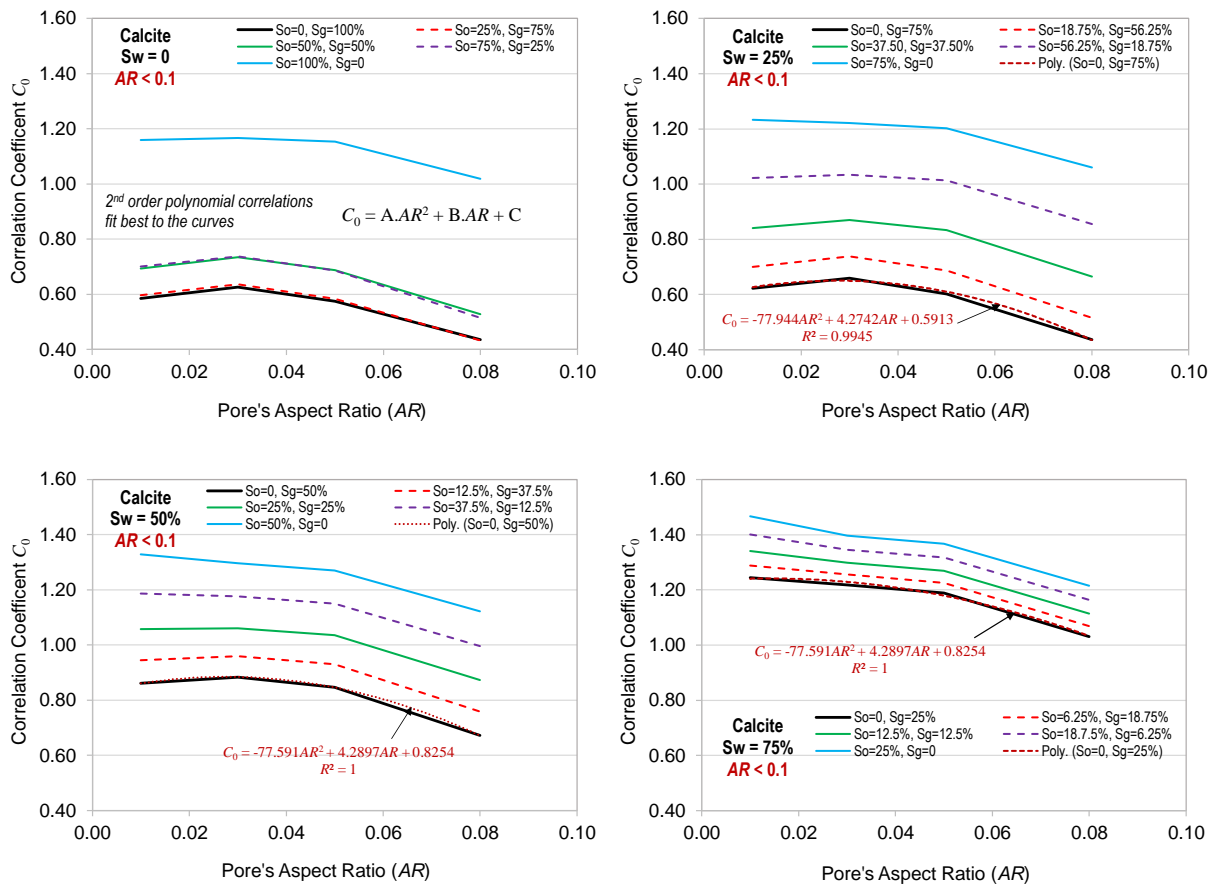
As mentioned before, in the above calculations the Brie model with coefficient  $e=3$  (see equation 3.1 and 3.2 in the preceding Chapter) was used to mix the fluid phases. This is a generally representative value of the patchy fluid type in many formations. In order to investigate the impact of the Brie coefficient on velocity changes, Figure 4.6 was constructed to show the results corresponding to two phase fluid (water and oil) for calcite having pores with an aspect ratio of 0.01 (i.e. cracks) for four Brie coefficients of  $e=1, 3, 5, 10$ . The results are presented for three cases with water saturations of  $S_w=25\%$ ,  $50\%$  and  $75\%$ . The results show that as water saturation increases, the impact of fluid type becomes more visible. However, the maximum difference from  $e=1$  to  $e=10$ , in the case of  $S_w=75\%$  does not exceed  $0.60$  Km/s. Therefore, in the following analysis, we used a value of  $e=3$  for all calculations and development of correlations.



**Figure 4.6.** The effect of fluid type mixing (Brie coefficient,  $e$ ) on velocity response for calcite with two phase fluids of water and oil with different saturations and assuming crack type pores ( $AR=0.01$ ).

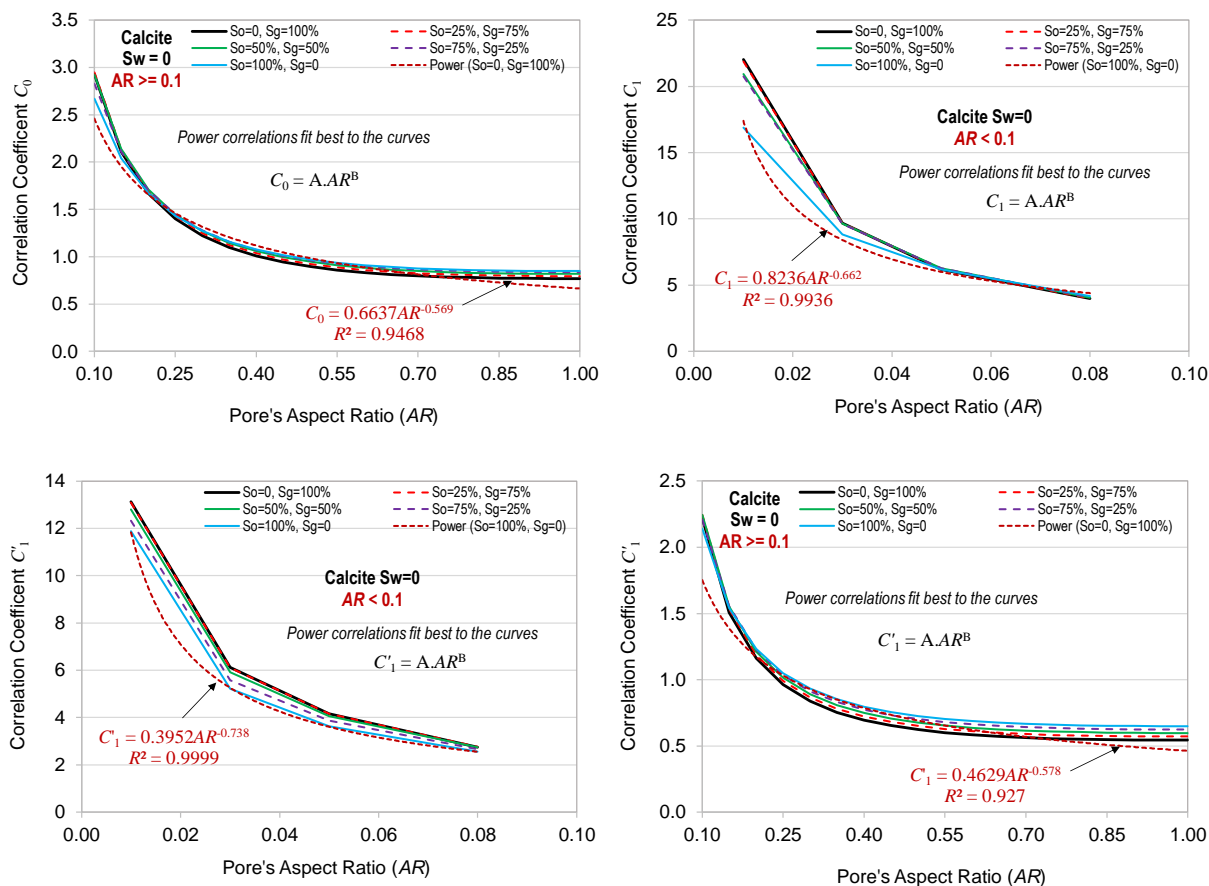
### 4.4 Relationship of Coefficients $C_s$ and ARs

In order to develop the correlations between velocity and porosity, as a function of fluid saturations and AR, we establish the trend of changes of each parameter (first derivation or slope) with respect to another one. For example, in Figure 4.7 the trend of change of coefficients  $C_0$  are plotted for the case of  $AR < 0.1$  (corresponding to  $V_p$ ) and for four cases of water saturations of  $S_w=0\%$ , 25%, 50%, 75% and different values of oil and gas saturations. As it is shown in these plots a 2<sup>nd</sup> order polynomial correlation presents a good fit to each of these curves.



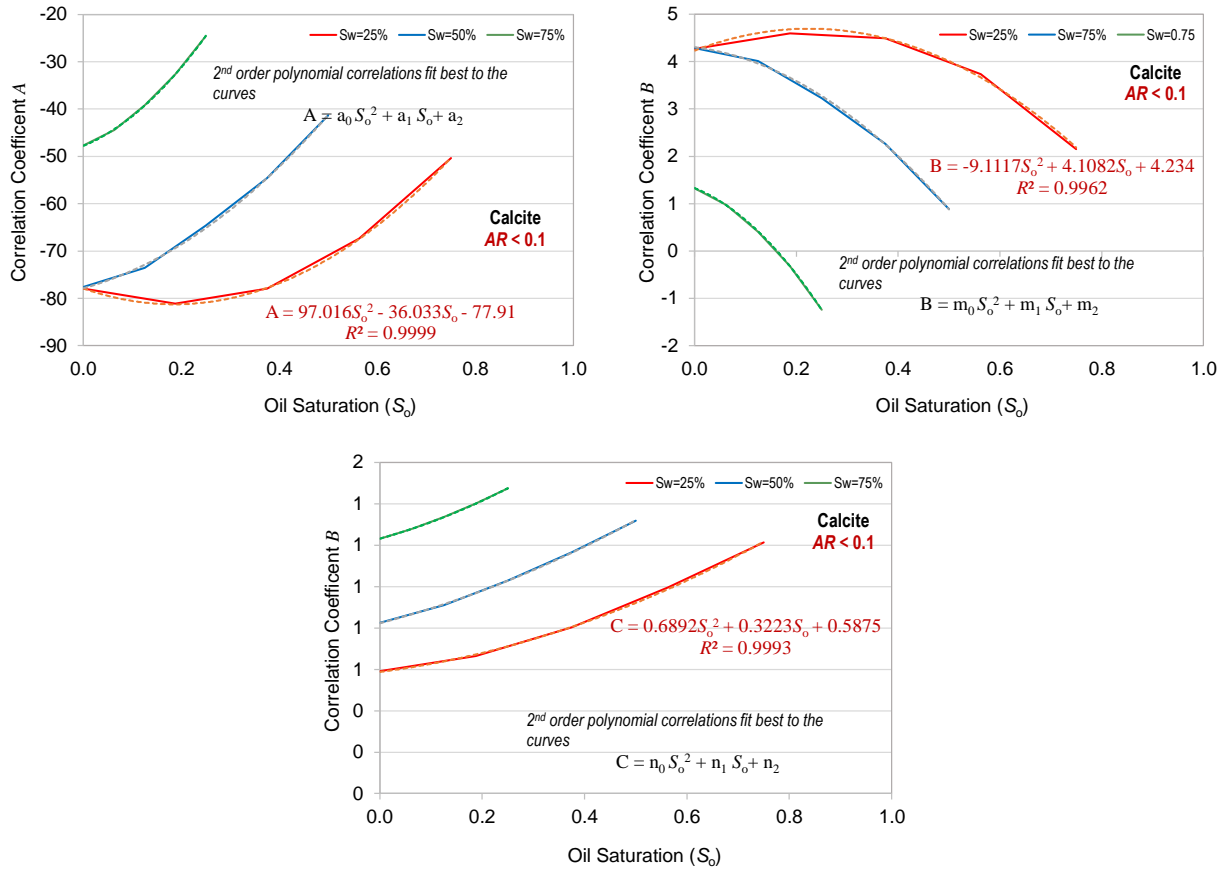
**Figure 4.7.** Second orders polynomial fits well to the coefficients  $C_0$  with respect to pore's aspect ratios (AR) as a function of water, oil and gas saturations for calcite. This is for the case of  $AR < 0.1$ .





**Figure 4.8.** Examples showing that power equations show a good fit for changes of coefficients  $C_1$ , when  $AR < 0.1$ , and coefficients  $C_0$  and  $C'_1$  for both cases of  $AR < 0.1$  and with respect to pore aspect ratios ( $AR$ ) as a function of water, oil and gas saturations for calcite.

Constants A, B and C from these correlations will be used for the next step to find their relationships with oil saturation ( $S_o$ ). The same procedure was repeated for coefficients  $C_0$  and  $C_1$  when  $AR \geq 0.1$  (corresponding to  $V_p$ ) and for  $C$  (corresponding to  $V_s$ ) when  $AR < 0.1$  and  $AR \geq 0.1$ . one example for each of these cases are presented in Figure 4.8, corresponding to  $S_w=0$ . The results show that a power equation provides the best fit to each curve for these plots and this holds true for other water saturations as well.



**Figure 4.9.** Examples of relationships between correlation constants A, B and C with oil saturation,  $S_o$ , when  $AR < 0.1$ , and for three water saturations of 25%, 50% and 75%.

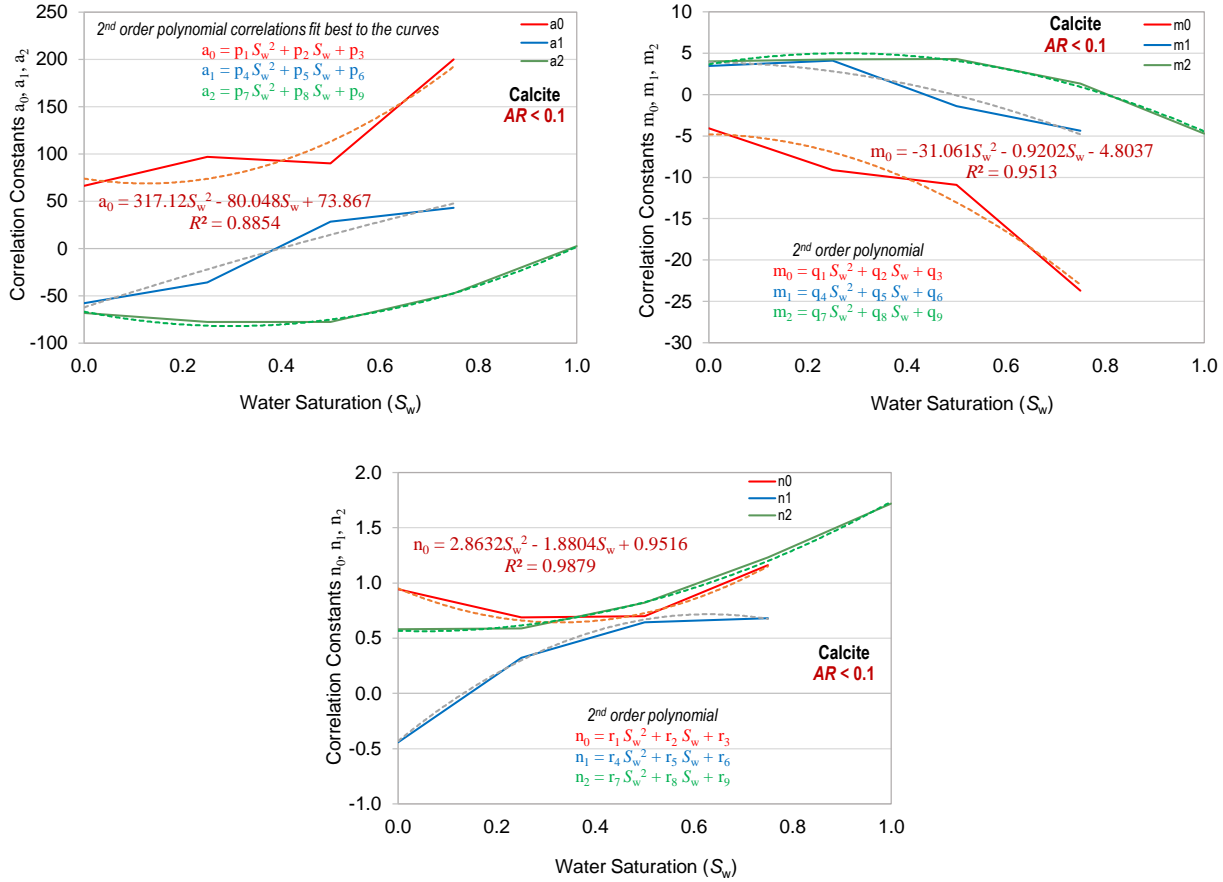
#### 4.5 Relationship of Constants A, B and C with $S_o$

Here, the relationship between constants A, B and C from the previous step with oil saturation ( $S_o$ ) is established. Examples of such relationships for calcite, corresponding to compressional velocity data, when  $AR < 0.1$  and for three water saturations of 25%, 50% and 75% are shown in Figure 4.9. The results indicate that 2<sup>nd</sup> order polynomial is the best fit to these curves.

#### 4.6 Relationship of Constants a's, m's and n's with $S_w$

The last stage requires establishment of relationships between constants a, m and n from the previous step with water saturation ( $S_w$ ). Examples of such relationships are shown in Figure 4.10

for the case of compressional velocity, when  $AR < 0.1$ . In these and all other cases, which are not shown here, polynomial relations found to be the best fit to the curves.



**Figure 4.10.** Examples of relationships between constants a's, m's and n's with water saturation,  $S_w$ , when  $AR < 0.1$ .

## 4.7 Summary of Correlations

Here, a summary of correlations that were developed in the preceding sections are presented. These correlations establish a relationship between compressional and shear velocities of a single-phase rock as a function of saturation (water, oil, gas), and pore aspect ratio ( $AR$ ).

**Case 1:** Compressional Velocity ( $V_p$ ),  $AR < 0.1$

$$V_p = (V_{p,m} - C_o)e^{-C_1\phi} + C_o \quad (4.6)$$

$$C_0 = A. AR^2 + B. AR + C \quad (4.7)$$

$$C_1 = A. AR^B \quad (4.8)$$

**Case 2:** Compressional Velocity ( $V_p$ ),  $AR \geq 0.1$

$$V_p = V_{p,m} e^{-C_0 \phi} \quad (4.9)$$

$$C_0 = A. AR^B \quad (4.10)$$

**Case 3:** Shear Velocity ( $V_s$ ),  $AR < 0.1$  and  $AR \geq 0.1$

$$V_s = V_{s,m} e^{-C'_1 \phi} \quad (4.11)$$

$$C'_1 = A. AR^B \quad (4.12)$$

where:

$$\begin{aligned} A &= a_0 S_0^2 + a_1 S_0 + a_2, & B &= m_0 S_0^2 + m_1 S_0 + m_2 & C &= n_0 S_0^2 + n_1 S_0 + n_2 \\ a_0 &= p_1 S_w^2 + p_2 S_w + p_3 & m_0 &= q_1 S_w^2 + q_2 S_w + q_3 & n_0 &= r_1 S_w^2 + r_2 S_w + r_3 \\ a_1 &= p_4 S_w^2 + p_5 S_w + p_6 & m_1 &= q_4 S_w^2 + q_5 S_w + q_6 & n_1 &= r_4 S_w^2 + r_5 S_w + r_6 \\ a_2 &= p_7 S_w^2 + p_8 S_w + p_9 & m_2 &= q_7 S_w^2 + q_8 S_w + q_9 & n_2 &= r_7 S_w^2 + r_8 S_w + r_9 \end{aligned} \quad (4.13)$$

Table 4.3 presents all the constants of the above correlations for calcite. It is important to note that, as mentioned before, these correlations will estimate the velocities for a rock which is composed of only calcite with different water, oil, and gas saturations, assuming pores with different aspect ratios, calculations done based on the DEM method, and considering a Brie coefficient of  $e=3$  for fluid mixing. Tables 4.4 to 4.8 include the constants for quartz, dolomite, illite, anhydrite and Kerogen, respectively. These are the major constituents of the Bakken formation. We have also developed these constants for several other minerals.

To check the validity of the developed correlations for calcite, Table 4.9, summarizes the results of  $V_p$  and  $V_s$  calculations based on the above correlations and the values from the DEM model. The

results are for constant porosity of 5% with two ARs of 0.01 and 0.1 and show a very good agreement in overall.

**Table 4.3.** Constants p, q and r for **calcite** to estimate velocities as function of fluid saturations and pore's aspect ratio using the DEM based developed correlations.

$V_p, AR < 0.1$			$V_p = (V_{p,m} - C_o)e^{-C_1\phi} + C_o$			$C_0 = A.AR^2 + B.AR + C$		$C_1 = A.AR^B$	
<b>p1</b>	<b>p2</b>	<b>p3</b>	<b>p4</b>	<b>p5</b>	<b>p6</b>	<b>p7</b>	<b>p8</b>	<b>p9</b>	
1261.601	-549.347	122.612	-266.118	313.338	-93.760	189.694	-115.373	-67.684	
<b>q1</b>	<b>q2</b>	<b>q3</b>	<b>q4</b>	<b>q5</b>	<b>q6</b>	<b>q7</b>	<b>q8</b>	<b>q9</b>	
-115.601	38.394	-7.773	9.075	-12.784	5.612	-18.841	10.237	3.741	
<b>r1</b>	<b>r2</b>	<b>r3</b>	<b>r4</b>	<b>r5</b>	<b>r6</b>	<b>r7</b>	<b>r8</b>	<b>r9</b>	
3.421	-2.120	0.978	-3.084	3.737	-0.450	1.307	-0.134	0.566	
$V_p, AR \geq 0.1$			$V_p = V_{p,m}e^{-C_o\phi}$			$C_0 = A.AR^B$			
<b>p1</b>	<b>p2</b>	<b>p3</b>	<b>p4</b>	<b>p5</b>	<b>p6</b>	<b>p7</b>	<b>p8</b>	<b>p9</b>	
-0.0641	-0.0227	-0.0256	-0.0598	-0.0249	0.1104	-0.0978	0.3036	0.6622	
<b>q1</b>	<b>q2</b>	<b>q3</b>	<b>q4</b>	<b>q5</b>	<b>q6</b>	<b>q7</b>	<b>q8</b>	<b>q9</b>	
0.0269	0.0146	0.0394	-0.0158	0.0748	0.0370	0.0631	0.1127	-0.5686	
$V_s, AR < 0.1$			$V_s = V_{s,m}e^{-C'_1\phi}$			$C'_1 = A.AR^B$			
<b>p1</b>	<b>p2</b>	<b>p3</b>	<b>p4</b>	<b>p5</b>	<b>p6</b>	<b>p7</b>	<b>p8</b>	<b>p9</b>	
0.054	-0.012	-0.104	0.159	-0.318	0.066	-0.178	0.103	0.435	
<b>q1</b>	<b>q2</b>	<b>q3</b>	<b>q4</b>	<b>q5</b>	<b>q6</b>	<b>q7</b>	<b>q8</b>	<b>q9</b>	
0.125	-0.114	-0.028	-0.102	-0.008	0.038	-0.082	0.083	-0.747	
$V_s, AR \geq 0.1$			$V_s = V_{s,m}e^{-C'_1\phi}$			$C'_1 = A.AR^B$			
<b>p1</b>	<b>p2</b>	<b>p3</b>	<b>p4</b>	<b>p5</b>	<b>p6</b>	<b>p7</b>	<b>p8</b>	<b>p9</b>	
11.009	-4.952	0.141	-5.585	2.514	0.029	-0.030	0.301	0.460	
<b>q1</b>	<b>q2</b>	<b>q3</b>	<b>q4</b>	<b>q5</b>	<b>q6</b>	<b>q7</b>	<b>q8</b>	<b>q9</b>	
12.810	-5.748	0.027	-6.344	2.886	-0.019	-0.010	0.209	-0.582	

**Table 4.4.** Constants p, q and r for **Quartz** to estimate velocities as function of fluid saturations and pore's aspect ratio using the DEM based developed correlations.

$V_p, AR < 0.1$		$V_p = (V_{p,m} - C_o)e^{-c_1\phi} + C_o$			$C_o = A.AR^2 + B.AR + C$		$C_1 = A.AR^B$	
<b>p1</b>	<b>p2</b>	<b>p3</b>	<b>p4</b>	<b>p5</b>	<b>p6</b>	<b>p7</b>	<b>p8</b>	<b>p9</b>
-9503.626	3458.538	155.141	894.444	530.247	-78.757	276.756	50.849	-438.981
<b>q1</b>	<b>q2</b>	<b>q3</b>	<b>q4</b>	<b>q5</b>	<b>q6</b>	<b>q7</b>	<b>q8</b>	<b>q9</b>
518.117	-194.240	-5.472	-80.509	-9.259	3.056	-22.384	4.270	10.834
<b>r1</b>	<b>r2</b>	<b>r3</b>	<b>r4</b>	<b>r5</b>	<b>r6</b>	<b>r7</b>	<b>r8</b>	<b>r9</b>
-2.423	-0.151	0.928	-2.316	3.798	-0.412	1.363	-0.127	0.505
$V_p, AR \geq 0.1$		$V_p = V_{p,m}e^{-C_o\phi}$			$C_o = A.AR^B$			
<b>p1</b>	<b>p2</b>	<b>p3</b>	<b>p4</b>	<b>p5</b>	<b>p6</b>	<b>p7</b>	<b>p8</b>	<b>p9</b>
-0.0401	-0.0103	-0.0143	-0.0341	-0.0162	0.1065	-0.0598	0.2905	0.4544
<b>q1</b>	<b>q2</b>	<b>q3</b>	<b>q4</b>	<b>q5</b>	<b>q6</b>	<b>q7</b>	<b>q8</b>	<b>q9</b>
0.0227	0.0239	0.0366	0.0005	0.0464	0.0633	0.0438	0.1784	-0.6352
$V_s, AR < 0.1$		$V_s = V_{s,m}e^{-c'_1\phi}$			$C'_1 = A.AR^B$			
<b>p1</b>	<b>p2</b>	<b>p3</b>	<b>p4</b>	<b>p5</b>	<b>p6</b>	<b>p7</b>	<b>p8</b>	<b>p9</b>
0.021	-0.030	-0.110	0.116	-0.302	0.076	-0.204	0.129	0.518
<b>q1</b>	<b>q2</b>	<b>q3</b>	<b>q4</b>	<b>q5</b>	<b>q6</b>	<b>q7</b>	<b>q8</b>	<b>q9</b>
0.077	-0.104	-0.022	-0.118	0.017	0.036	-0.076	0.083	-0.716
$V_s, AR \geq 0.1$		$V_s = V_{s,m}e^{-c'_1\phi}$			$C'_1 = A.AR^B$			
<b>p1</b>	<b>p2</b>	<b>p3</b>	<b>p4</b>	<b>p5</b>	<b>p6</b>	<b>p7</b>	<b>p8</b>	<b>p9</b>
11.808	-5.311	0.151	-5.979	2.690	0.027	-0.033	0.310	0.548
<b>q1</b>	<b>q2</b>	<b>q3</b>	<b>q4</b>	<b>q5</b>	<b>q6</b>	<b>q7</b>	<b>q8</b>	<b>q9</b>
11.949	-5.360	0.024	-5.918	2.693	-0.023	-0.004	0.181	-0.564

**Table 4.5.** Constants p, q and r for **Dolomite** to estimate velocities as function of fluid saturations and pore's aspect ratio using the DEM based developed correlations.

$V_p, AR < 0.1$		$V_p = (V_{p,m} - C_o)e^{-c_1\phi} + C_o$			$C_o = A.AR^2 + B.AR + C$		$C_1 = A.AR^B$	
<b>p1</b>	<b>p2</b>	<b>p3</b>	<b>p4</b>	<b>p5</b>	<b>p6</b>	<b>p7</b>	<b>p8</b>	<b>p9</b>
146.213	-47.732	90.555	14.224	193.615	-80.600	186.574	-117.025	-109.234
<b>q1</b>	<b>q2</b>	<b>q3</b>	<b>q4</b>	<b>q5</b>	<b>q6</b>	<b>q7</b>	<b>q8</b>	<b>q9</b>
17.860	-22.075	-4.530	-33.700	9.130	4.817	-17.126	11.144	3.226
<b>r1</b>	<b>r2</b>	<b>r3</b>	<b>r4</b>	<b>r5</b>	<b>r6</b>	<b>r7</b>	<b>r8</b>	<b>r9</b>
1.472	-1.266	0.931	-2.542	3.494	-0.439	1.291	-0.154	0.570
$V_p, AR \geq 0.1$		$V_p = V_{p,m}e^{-C_o\phi}$			$C_o = A.AR^B$			
<b>p1</b>	<b>p2</b>	<b>p3</b>	<b>p4</b>	<b>p5</b>	<b>p6</b>	<b>p7</b>	<b>p8</b>	<b>p9</b>
-0.0457	-0.0132	-0.0174	-0.0387	-0.0195	0.1011	-0.0686	0.2763	0.6124
<b>q1</b>	<b>q2</b>	<b>q3</b>	<b>q4</b>	<b>q5</b>	<b>q6</b>	<b>q7</b>	<b>q8</b>	<b>q9</b>
0.0245	0.0178	0.0312	0.0011	0.0476	0.0407	0.0499	0.1172	-0.5887
$V_s, AR < 0.1$		$V_s = V_{s,m}e^{-c'_1\phi}$			$C'_1 = A.AR^B$			
<b>p1</b>	<b>p2</b>	<b>p3</b>	<b>p4</b>	<b>p5</b>	<b>p6</b>	<b>p7</b>	<b>p8</b>	<b>p9</b>
0.076	-0.071	-0.087	0.046	-0.218	0.066	-0.175	0.121	0.445
<b>q1</b>	<b>q2</b>	<b>q3</b>	<b>q4</b>	<b>q5</b>	<b>q6</b>	<b>q7</b>	<b>q8</b>	<b>q9</b>
0.120	-0.132	-0.016	-0.147	0.043	0.035	-0.072	0.087	-0.748
$V_s, AR \geq 0.1$		$V_s = V_{s,m}e^{-c'_1\phi}$			$C'_1 = A.AR^B$			
<b>p1</b>	<b>p2</b>	<b>p3</b>	<b>p4</b>	<b>p5</b>	<b>p6</b>	<b>p7</b>	<b>p8</b>	<b>p9</b>
11.227	-5.049	0.143	-5.704	2.566	0.022	-0.030	0.286	0.468
<b>q1</b>	<b>q2</b>	<b>q3</b>	<b>q4</b>	<b>q5</b>	<b>q6</b>	<b>q7</b>	<b>q8</b>	<b>q9</b>
13.166	-5.905	0.021	-6.527	2.957	-0.024	-0.014	0.197	-0.582

**Table 4.6.** Constants p, q and r for **Illite** to estimate velocities as function of fluid saturations and pore's aspect ratio using the DEM based developed correlations.

$V_p, AR < 0.1$		$V_p = (V_{p,m} - C_o)e^{-c_1\phi} + C_o$			$C_o = A.AR^2 + B.AR + C$		$C_1 = A.AR^B$	
<b>p1</b>	<b>p2</b>	<b>p3</b>	<b>p4</b>	<b>p5</b>	<b>p6</b>	<b>p7</b>	<b>p8</b>	<b>p9</b>
2038.545	-147.875	218.529	-1540.1	1288.32	-64.604	66.823	144.823	-217.41
<b>q1</b>	<b>q2</b>	<b>q3</b>	<b>q4</b>	<b>q5</b>	<b>q6</b>	<b>q7</b>	<b>q8</b>	<b>q9</b>
-90.628	69.433	-13.248	80.189	-72.549	4.521	-6.084	-8.012	5.727
<b>r1</b>	<b>r2</b>	<b>r3</b>	<b>r4</b>	<b>r5</b>	<b>r6</b>	<b>r7</b>	<b>r8</b>	<b>r9</b>
2.496	-2.162	0.940	-3.692	4.189	-0.402	1.073	0.041	0.497
$V_p, AR \geq 0.1$		$V_p = V_{p,m}e^{-C_o\phi}$			$C_o = A.AR^B$			
<b>p1</b>	<b>p2</b>	<b>p3</b>	<b>p4</b>	<b>p5</b>	<b>p6</b>	<b>p7</b>	<b>p8</b>	<b>p9</b>
-0.0832	-0.0517	-0.0423	-0.1065	-0.0308	0.1204	-0.1510	0.3336	0.4515
<b>q1</b>	<b>q2</b>	<b>q3</b>	<b>q4</b>	<b>q5</b>	<b>q6</b>	<b>q7</b>	<b>q8</b>	<b>q9</b>
0.0317	-0.0172	0.0765	-0.1355	0.2063	0.0571	0.0848	0.1969	-0.6156
$V_s, AR < 0.1$		$V_s = V_{s,m}e^{-c'_1\phi}$			$C'_1 = A.AR^B$			
<b>p1</b>	<b>p2</b>	<b>p3</b>	<b>p4</b>	<b>p5</b>	<b>p6</b>	<b>p7</b>	<b>p8</b>	<b>p9</b>
-0.207	0.269	-0.160	0.605	-0.681	0.061	-0.183	0.031	0.507
<b>q1</b>	<b>q2</b>	<b>q3</b>	<b>q4</b>	<b>q5</b>	<b>q6</b>	<b>q7</b>	<b>q8</b>	<b>q9</b>
0.022	-0.007	-0.061	0.086	-0.176	0.038	-0.096	0.051	-0.704
$V_s, AR \geq 0.1$		$V_s = V_{s,m}e^{-c'_1\phi}$			$C'_1 = A.AR^B$			
<b>p1</b>	<b>p2</b>	<b>p3</b>	<b>p4</b>	<b>p5</b>	<b>p6</b>	<b>p7</b>	<b>p8</b>	<b>p9</b>
10.711	-4.831	0.140	-5.429	2.451	0.037	-0.035	0.320	0.563
<b>q1</b>	<b>q2</b>	<b>q3</b>	<b>q4</b>	<b>q5</b>	<b>q6</b>	<b>q7</b>	<b>q8</b>	<b>q9</b>
10.392	-4.690	0.050	-5.218	2.443	-0.017	0.022	0.188	-0.551



**Table 4.7.** Constants p, q and r for **Anhydrite** to estimate velocities as function of fluid saturations and pore's aspect ratio using the DEM based developed correlations.

$V_p, AR < 0.1$		$V_p = (V_{p,m} - C_o)e^{-c_1\phi} + C_o$			$C_o = A.AR^2 + B.AR + C$		$C_1 = A.AR^B$	
<b>p1</b>	<b>p2</b>	<b>p3</b>	<b>p4</b>	<b>p5</b>	<b>p6</b>	<b>p7</b>	<b>p8</b>	<b>p9</b>
-197.575	196.096	105.803	-59.266	253.503	-78.647	191.547	-82.758	-110.158
<b>q1</b>	<b>q2</b>	<b>q3</b>	<b>q4</b>	<b>q5</b>	<b>q6</b>	<b>q7</b>	<b>q8</b>	<b>q9</b>
24.807	-27.752	-7.068	-18.275	-5.393	5.737	-20.772	10.539	3.267
<b>r1</b>	<b>r2</b>	<b>r3</b>	<b>r4</b>	<b>r5</b>	<b>r6</b>	<b>r7</b>	<b>r8</b>	<b>r9</b>
2.144	-1.646	0.905	-3.040	3.774	-0.415	1.301	-0.167	0.530
$V_p, AR \geq 0.1$		$V_p = V_{p,m}e^{-C_o\phi}$			$C_o = A.AR^B$			
<b>p1</b>	<b>p2</b>	<b>p3</b>	<b>p4</b>	<b>p5</b>	<b>p6</b>	<b>p7</b>	<b>p8</b>	<b>p9</b>
-0.0666	-0.0255	-0.0268	-0.0645	-0.0228	0.1013	-0.0997	0.2798	0.5814
<b>q1</b>	<b>q2</b>	<b>q3</b>	<b>q4</b>	<b>q5</b>	<b>q6</b>	<b>q7</b>	<b>q8</b>	<b>q9</b>
0.0289	0.0136	0.0454	-0.0256	0.0922	0.0382	0.0724	0.1194	-0.5953
$V_s, AR < 0.1$		$V_s = V_{s,m}e^{-c'_1\phi}$			$C'_1 = A.AR^B$			
<b>p1</b>	<b>p2</b>	<b>p3</b>	<b>p4</b>	<b>p5</b>	<b>p6</b>	<b>p7</b>	<b>p8</b>	<b>p9</b>
-0.002	0.034	-0.112	0.216	-0.366	0.064	-0.181	0.088	0.446
<b>q1</b>	<b>q2</b>	<b>q3</b>	<b>q4</b>	<b>q5</b>	<b>q6</b>	<b>q7</b>	<b>q8</b>	<b>q9</b>
0.093	-0.093	-0.033	-0.080	-0.030	0.037	-0.087	0.077	-0.740
$V_s, AR \geq 0.1$		$V_s = V_{s,m}e^{-c'_1\phi}$			$C'_1 = A.AR^B$			
<b>p1</b>	<b>p2</b>	<b>p3</b>	<b>p4</b>	<b>p5</b>	<b>p6</b>	<b>p7</b>	<b>p8</b>	<b>p9</b>
10.814	-4.866	0.139	-5.479	2.469	0.022	-0.027	0.277	0.474
<b>q1</b>	<b>q2</b>	<b>q3</b>	<b>q4</b>	<b>q5</b>	<b>q6</b>	<b>q7</b>	<b>q8</b>	<b>q9</b>
12.585	-5.650	0.032	-6.243	2.857	-0.026	0.003	0.189	-0.577

**Table 4.8.** Constants p, q and r for **Kerogen** to estimate velocities as function of fluid saturations and pore's aspect ratio using the DEM based developed correlations.

$V_p, AR < 0.1$		$V_p = (V_{p,m} - C_o)e^{-C_1\phi} + C_o$			$C_0 = A. AR^2 + B. AR + C$		$C_1 = A. AR^B$	
<b>p1</b>	<b>p2</b>	<b>p3</b>	<b>p4</b>	<b>p5</b>	<b>p6</b>	<b>p7</b>	<b>p8</b>	<b>p9</b>
552.945	-606.596	67.450	-915.168	652.907	-20.438	-129.841	145.137	-20.661
<b>q1</b>	<b>q2</b>	<b>q3</b>	<b>q4</b>	<b>q5</b>	<b>q6</b>	<b>q7</b>	<b>q8</b>	<b>q9</b>
-10.829	38.838	-10.168	88.240	-73.920	3.073	7.190	-16.876	0.281
<b>r1</b>	<b>r2</b>	<b>r3</b>	<b>r4</b>	<b>r5</b>	<b>r6</b>	<b>r7</b>	<b>r8</b>	<b>r9</b>
0.201	-1.097	1.166	-2.610	3.718	-0.567	0.932	0.182	0.689
$V_p, AR \geq 0.1$		$V_p = V_{p,m}e^{-C_o\phi}$			$C_0 = A. AR^B$			
<b>p1</b>	<b>p2</b>	<b>p3</b>	<b>p4</b>	<b>p5</b>	<b>p6</b>	<b>p7</b>	<b>p8</b>	<b>p9</b>
0.0072	-0.2417	-0.2568	-0.0860	-0.5147	0.2859	-0.6340	0.6776	0.5524
<b>q1</b>	<b>q2</b>	<b>q3</b>	<b>q4</b>	<b>q5</b>	<b>q6</b>	<b>q7</b>	<b>q8</b>	<b>q9</b>
0.1078	-0.1781	0.1067	-0.4540	0.4295	0.0965	0.0305	0.3396	-0.5359
$V_s, AR < 0.1$		$V_s = V_{s,m}e^{-C'_1\phi}$			$C'_1 = A. AR^B$			
<b>p1</b>	<b>p2</b>	<b>p3</b>	<b>p4</b>	<b>p5</b>	<b>p6</b>	<b>p7</b>	<b>p8</b>	<b>p9</b>
-0.486	0.502	-0.114	0.810	-0.698	0.031	-0.068	-0.002	0.340
<b>q1</b>	<b>q2</b>	<b>q3</b>	<b>q4</b>	<b>q5</b>	<b>q6</b>	<b>q7</b>	<b>q8</b>	<b>q9</b>
-0.208	0.249	-0.081	0.447	-0.417	0.033	-0.055	0.015	-0.763
$V_s, AR \geq 0.1$		$V_s = V_{s,m}e^{-C'_1\phi}$			$C'_1 = A. AR^B$			
<b>p1</b>	<b>p2</b>	<b>p3</b>	<b>p4</b>	<b>p5</b>	<b>p6</b>	<b>p7</b>	<b>p8</b>	<b>p9</b>
10.116	-4.586	0.117	-5.277	2.334	0.137	-0.103	0.574	0.486
<b>q1</b>	<b>q2</b>	<b>q3</b>	<b>q4</b>	<b>q5</b>	<b>q6</b>	<b>q7</b>	<b>q8</b>	<b>q9</b>
8.887	-4.112	0.051	-4.712	2.192	0.067	-0.087	0.384	-0.525

**Table 4.9.** Comparison of the velocity prediction based on the DEM model and correlations for calcite for some case examples.

AR	$S_w$	$S_o$	$S_g$	$\phi$	$V_p$ (Km/s) DEM	$V_p$ (Km/s) Correlation	$V_s$ (Km/s) DEM	$V_s$ (Km/s) Correlation
0.01	0.0	0.0	1.0	0.05	2.468	<b>2.595</b>	1.551	<b>1.738</b>
	0.0	25%	75%	0.05	2.490	<b>2.576</b>	1.559	<b>1.753</b>
0.01	25%	18.75%	56.25%	0.05	2.658	<b>2.682</b>	1.615	<b>1.815</b>
0.01	50%	0.5	0	0.05	3.635	<b>3.685</b>	1.861	<b>1.920</b>
.01	1.0	0	0	0.05	4.130	<b>4.706</b>	1.934	<b>1.959</b>
0.1	0	0	1.0	0.05	5.627	<b>5.833</b>	3.148	<b>3.136</b>
0.01	0.0	0.25	75%	0.05	5.623	<b>5.824</b>	3.145	<b>3.124</b>
0.1	25%	18.75%	56.25%	0.05	5.619	<b>5.816</b>	3.139	<b>3.129</b>
0.1	50%	50%	0	0.05	5.694	<b>5.879</b>	3.139	<b>3.109</b>

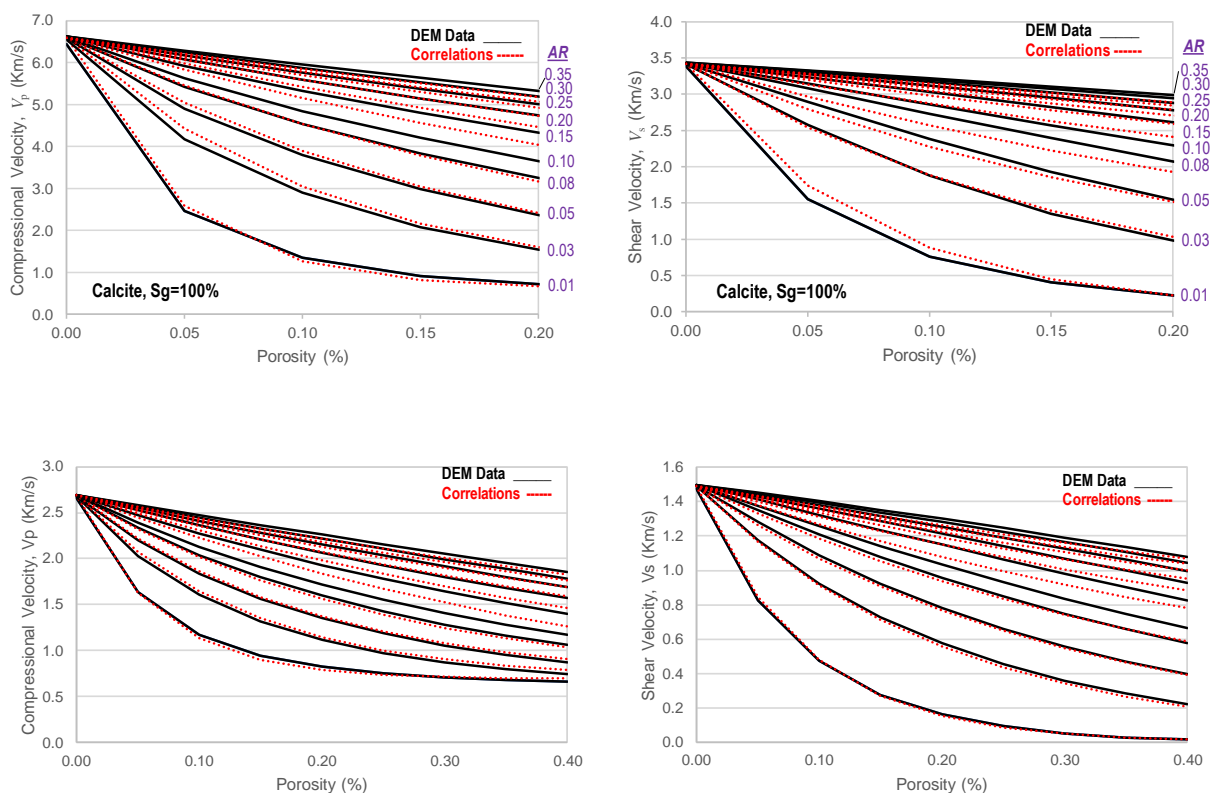
Figure 4.11 shows the results of the velocity-porosity calculations from the DEM model versus correlations for calcite and kerogen, as an example, for the case of 100% gas saturation and varying pore aspect ratios. It is seen that for both compressional and shear velocities, a very close agreement is observed between the two methods, despite some deviations at larger ARs.

In the next section we discuss on how to calculate the velocity of a rock which is constituted of several minerals.

#### 4.8 Rock Velocity Averaging

In order to determine the average velocity of a rock with different mineral constituents, we use the commonly used equivalent medium theories of rock physics. The Voigt, Reuss or Hill models (see equation 3.2.2 in the previous Chapter) are the simplest models that we can use to calculate the rock average velocity, based on the velocity of each mineral and their corresponding volume

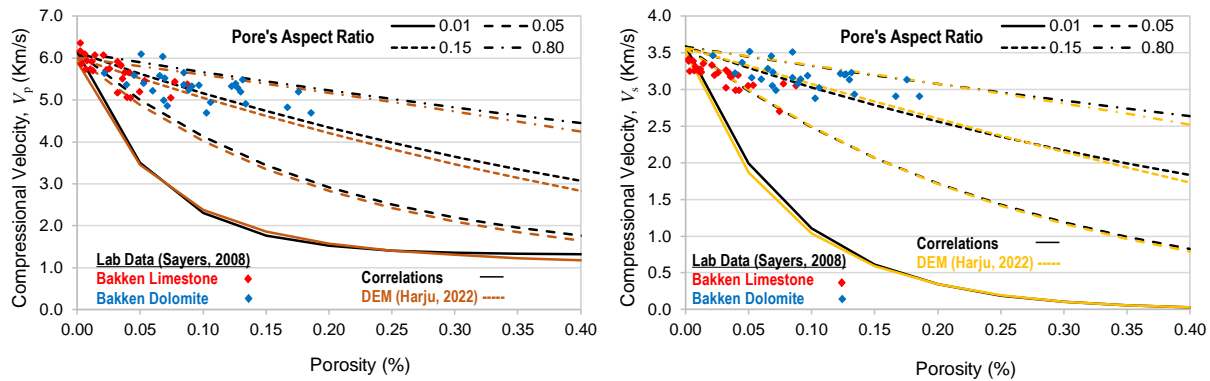
fraction, using the correlations developed in this study. The volume fraction of minerals is derived from XRD lab testing or ECS log.



**Figure 4.11.** Comparison of (compressional (left) and shear (right) velocity versus porosity relationship from DEM model versus developed correlations for calcite (top) and kerogen (bottom) fully saturated with gas and with different pore's aspect ratios.

To demonstrate the applications of this method, we used the correlations, to calculate the compressional and shear velocities of the Bakken formation. For comparison purposes, we use the same input data that was used by Harju (2022), as presented in Section 3.3 of Chapter 3. In his work, Harju (2022) presented the DEM model results for only MB carbonate formations (see Figure 3.12), with the results for MB clastic and UB and LB shales presented based on the K-T model. Figure 4.12 is the comparison of the correlations and the DEM model for patchy fluid type for four main pore types of cracks ( $AR=0.01$ ), interparticle ( $AR=0.05$ ), intraparticle or intergranular ( $AR=0.15$ ) and moldic ( $AR=0.80$ ). the results show a very good agreement for both  $V_p$  (left figure)

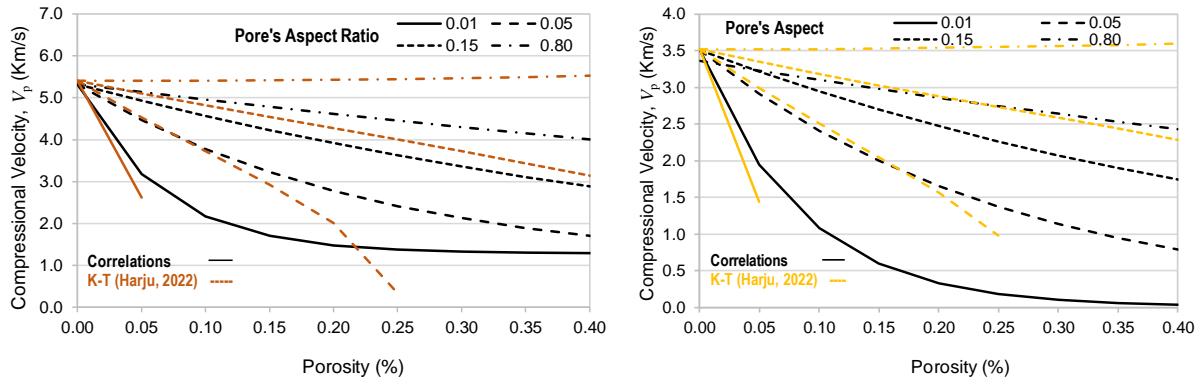
and  $V_s$  (right figure). The slightly larger velocities (which is even less for the case of shear velocity) are due to the effect of Brie coefficients and other factors. The results demonstrate the great ability of the correlations to reproduce the DEM model results very accurately. The advantage, however, is that there is no need to use different models for different formations or use any software for the calculations.



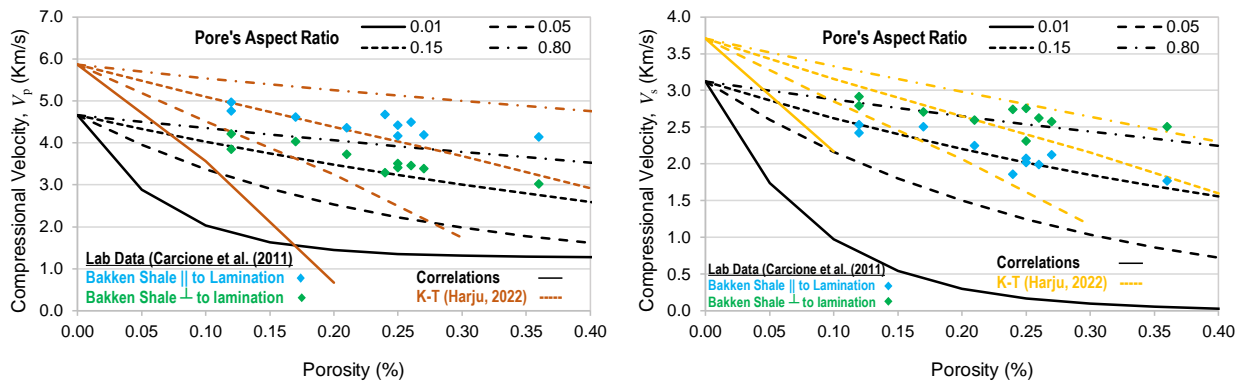
**Figure 4.12.** Comparison of velocity-porosity relationship from the DEM model (Harju, 2022) versus developed correlations for the Middle Bakken carbonate formation. Compressional (left) and shear (right) velocities.

Similar results are presented for the MB clastic and Bakken shale in Figure 4.13 and Figure 4.14, respectively. The results, clearly show that the K-T model is not a good representation of the formation properties, especially at large porosities. In the case of shale models, the K-T results correspond to the velocities assuming isotropic shale properties. The DEM model appears to underestimate the shale velocity and predict more intergranular pores as opposed to the K-T model which represents more interparticle pores.

In the next Chapter, the correlations will be applied to predict the velocities of formations, with several conclusions are drawn.



**Figure 4.13.** Comparison of velocity-porosity relationship from K-T model (Harju, 2022) versus developed correlations for the Middle Bakken clastic formation. Compressional (left) and shear (right) velocities.



**Figure 4.14.** Comparison of velocity-porosity relationship from K-T model (Harju, 2022) versus developed correlations for the Middle Bakken shale formation. Compressional (left) and shear (right) velocities.

## 4.9 Summary

DEM based correlations were developed in this Chapter to calculate the velocity-porosity relations for single mineral rocks saturated with three-phase fluid in pores with different aspect ratios. The use of these correlations can remove the tedious calculations of differential equations of the DEM models. The calculations of velocities based on these correlations can be simply developed in an excel spreadsheet. In the next Chapter, the applications of the developed correlations are demonstrated on a number of case studies from wells in the Bakken formation of the Williston Basin, North Dakota.

# CHAPTER 5

## Case Study Examples

In this Chapter, the developed correlations of the previous Chapter will be applied to predict the velocity and elastic parameters of formations in Well #17015 in Mountrail County and wells in the Grenora area in North Dakota. The results will be compared with DEM models to evaluate the accuracy of the correlations output and also with log and lab data in order to draw some conclusions.

### 5.1 Well #17015, Nesson State

#### 5.1.1. Input Data

Figure 5.1 shows the location of Well #17015 and five other wells in Mountrail and Dunn Counties, which were used for a study carried out by the EERC (Sorensen et al., 2010) and the rock physics models for Well #17015 developed by Harju (2022), (Section 3.3, Chapter 3).

Figure 5.2 presents some of the petrophysical logs of Well #17015 corresponding to the upper and lower Bakken (UB, LB) shale and the middle Bakken (MB). These include density (RHOZ) and neutron porosity (NPHI) logs, photoelectric factor (PEFZ), shallow (AT10) and deep (AT90) resistivity logs, shale volume (Vsh), and the calculated effective (PHIE) and total (PHIT) porosities. In general, shales have lower density and slower velocities than MB due to the presence of kerogen and higher shale volume. In the MB, the existence of carbonate in the upper part, results

in higher velocity compared to the lower clastic part. The results of Figure 5.2 will be used later in the rock physics modeling.

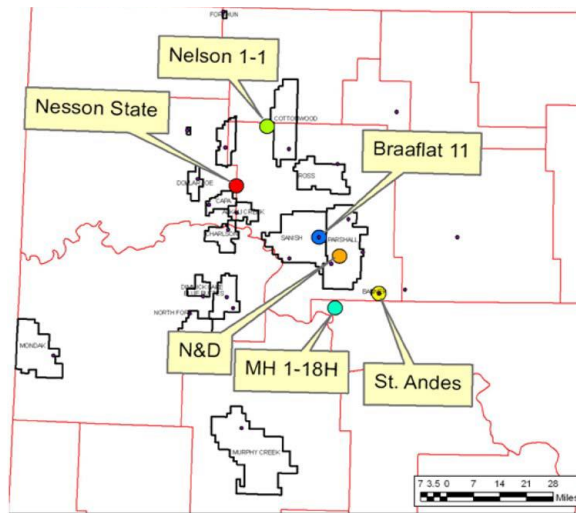


Figure 5.1. Location of Well #17015, Nesson State (Sorensen et al., 2011).

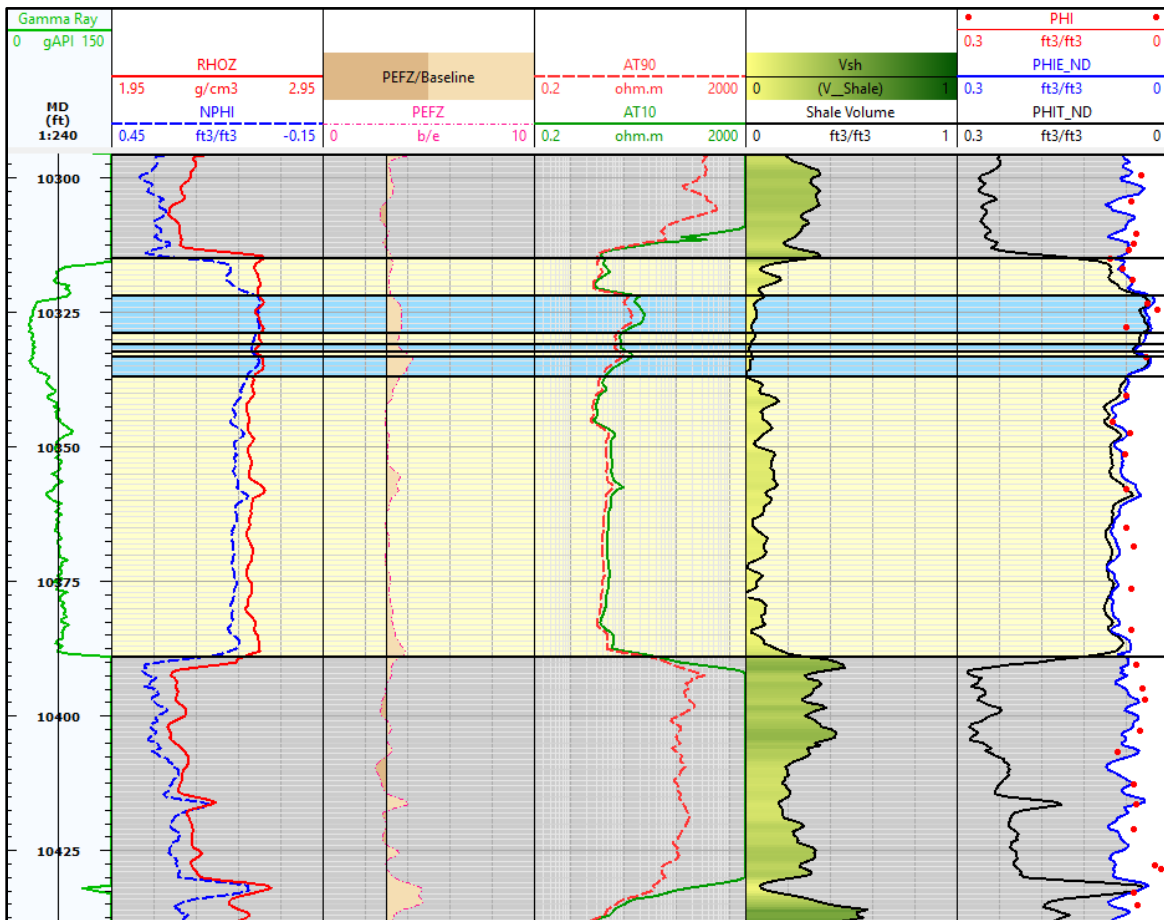


Figure 5.2. Petrophysical logs of Well #17015, Nesson State.



Looking at Figure 5.2, it can be seen that the MB formation can be distinguished from the UB and LB based on the gamma ray log. The carbonate section in the MB can be differentiated from the clastic zone from other logs. In the carbonate intervals, the density and neutron porosity logs are overlapping while the increase of clastic abundance separates these two logs. Similarly, the PEZF response varies based on lithological characteristics of the rock. In the carbonate zones of the MB, shale is less abundant compared to in the clastic zones. The porosities were calculated from the neutron-density and the effective porosity shows a good match with core data.

Figure 5.3 shows the volume fractions of primary minerals in this Well from the ECS log, which were used to calculate the velocity values at different depths. It is to be noted that the ECS log provided the cumulative fraction of calcite and dolomite (carbonate). However, it is possible to decompose and estimate the fraction of each of these minerals (Harju, 2022).

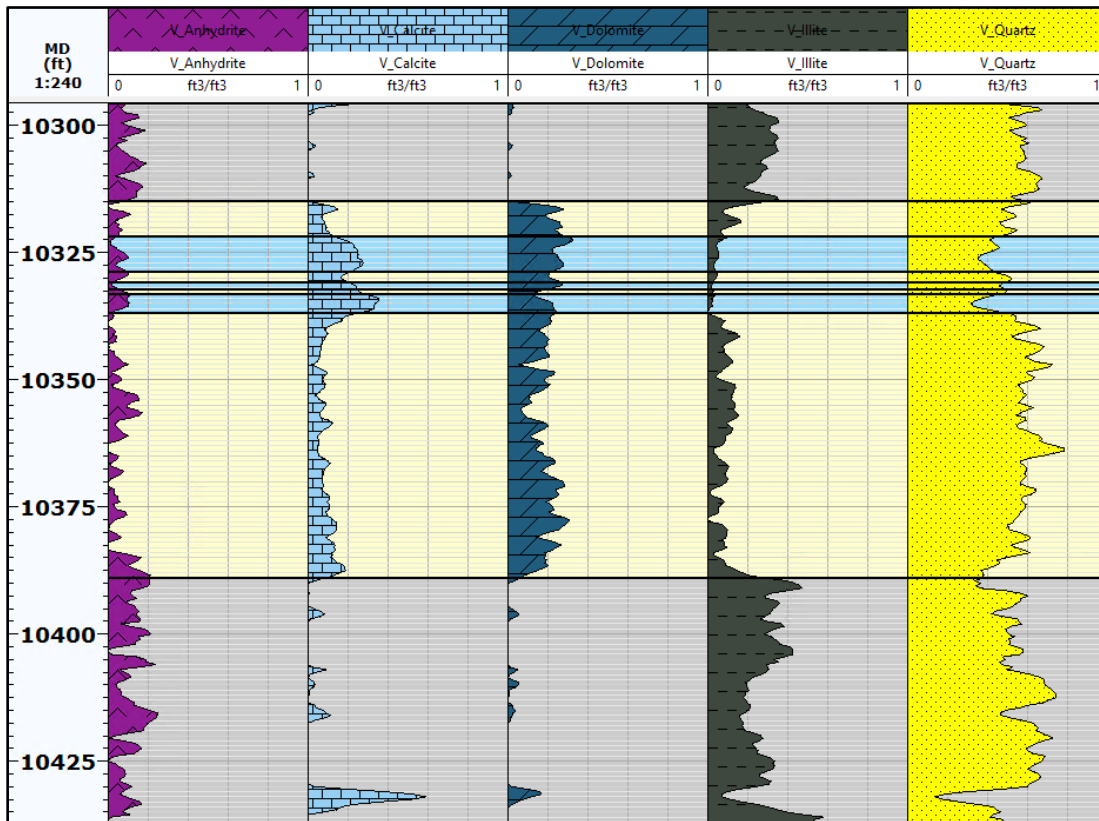
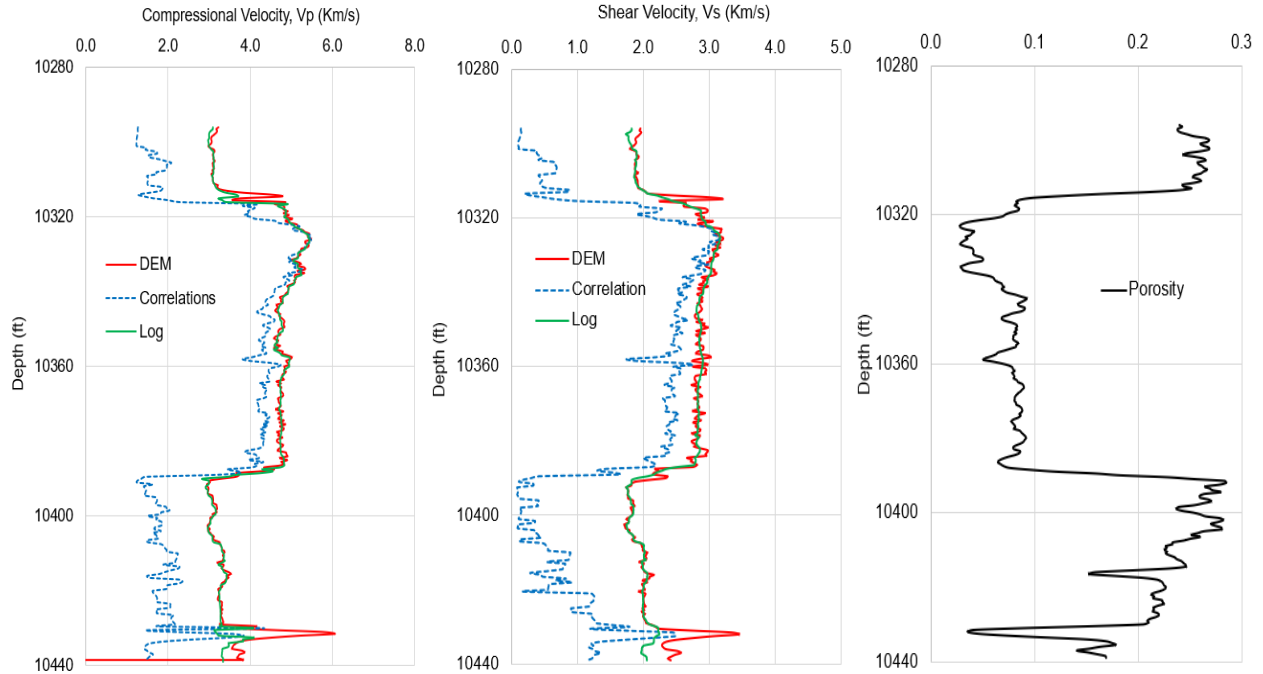


Figure 5.3. Volume fractions of minerals in Well #17015 from ECS log.

### 5.1.2. Previous Studies

Harju (2022) developed DEM models for the Bakken members. In his study, the objective was to compare the results with the lab-scale modeling based on existing average XRD lab data representing the overall lithology in the Bakken. Therefore, he used constant values of  $S_w=40\%$ ,  $S_o=50\%$  and  $S_g=10\%$  in the three Bakken members to be comparable with the lab-scale modeling. The fluids were then mixed using the Brie model, assuming  $e=1$  (i.e. fully patchy fluid). This assumption, while it may be acceptable at lab scale, is not applicable in field conditions and corresponding to log scale. From previous studies, at log scale  $e=3$  is a better representation of the fluid response to the waves and at even lower frequencies corresponding to the seismic scale, the fluid response will be even more homogeneous with  $e$  tending toward larger values of 10 and above. For the UB and LB shales, the average fluid mix property was embedded in Kerogen at 50% volume fraction, following the work by Carcione (2011). This means that Kerogen was considered as a part of the infill material (inclusions), which increases the fluid properties and the overall rock velocity.

In the current study, we calculated the  $V_p$  and  $V_s$  for the Bakken members using the developed correlations. In order to make equivalent comparison to Harju's (2022) study, we used the same constant fluid saturations and pore ARs that he obtained for the best match between the DEM model prediction and log measurements. However, Kerogen was not included when establishing the correlation. The results shown in Figure 5.4 represent a comparison between measured and Harju's (2022) velocity profiles, in addition to the velocity predicted from correlations.



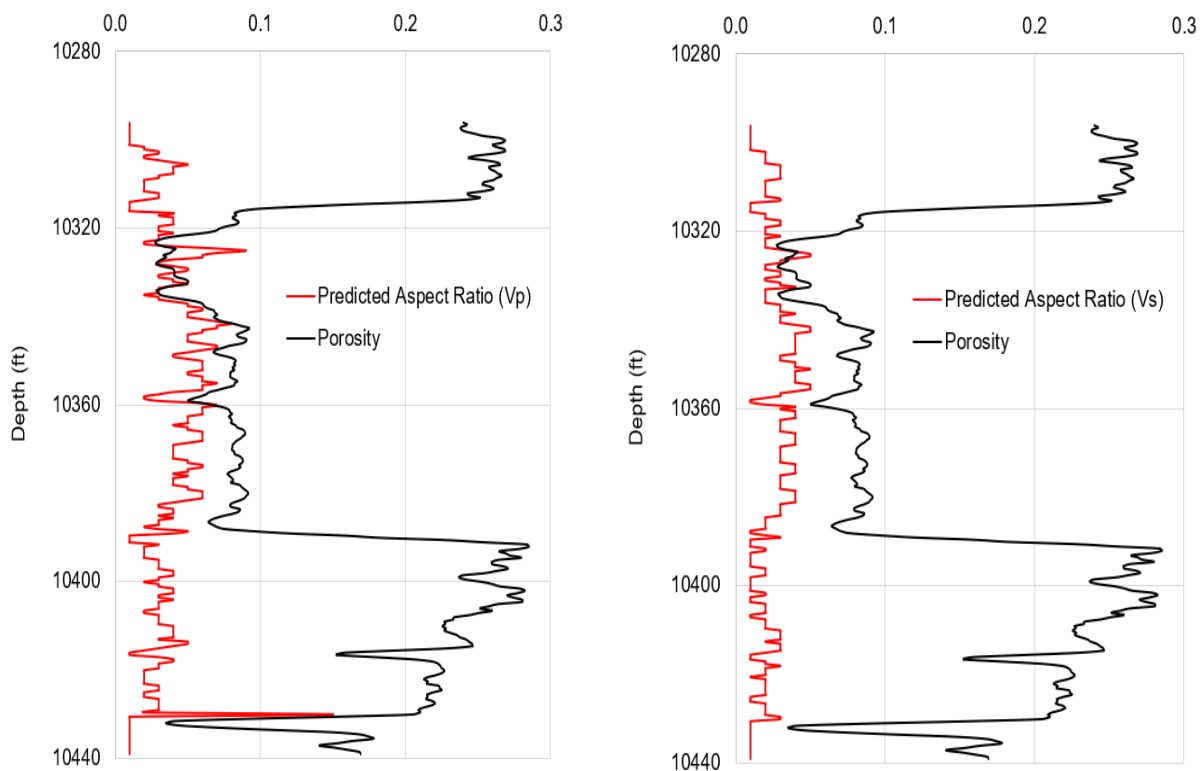
**Figure 5.4.** Velocity prediction for Well #17015. DEM model versus correlations, based on Harju's (2022) assumptions.

From this figure, it is seen that the difference between the correlations and DEM model predictions is much greater in UB and LB shales, than in the MB. This difference, is mainly due to the fact that in developing the correlations, as mentioned earlier, Kerogen was not considered as part of the fluid phase. However, it can be introduced as a new mineral and mixed with the other minerals. The correlation results shown in Figure 5.4 do not include the effect of Kerogen, therefore, it shows a much lower velocity than the DEM model, as the Kerogen portion is filled with a fluid with lower stiffness. Obviously, as the Kerogen is mainly present in UB and LB shales, it affects the difference in velocities more in these zones compared to the MB. The second reason for the correlations showing lower velocities is that Harju (2022) assumed fully patchy fluid ( $e=1$ ), whereas the correlations were developed based on the assumption of  $e=3$ , which as mentioned earlier, is a more representative value in real conditions. In the MB, only fluid mixing effect causes the deviation of velocity estimated from correlations. The correlation shows closer results to the

DEM model in the Carbonate section (upper part of the MB) than in the Clastic section (lower part of MB) due to relatively lower porosity, causing the fluid mixture effect to become less dominant in the rock's velocity.

Harju (2022) predicted the range of pore ARs at different depths by changing it to obtain the best match between the predicted velocity and the measured log velocities. From this perspective, a lower kerogen content than that assumed by Harju (2022) results in decreasing the estimated velocity in all AR ranges (predicted velocities shift to the left). Therefore, the corresponding estimated AR, compared to measured velocity, increases due to softening in the estimated velocities.

Figure 5.5 shows the AR predictions corresponding to the  $V_p$  and  $V_s$  based on Harju's (2022) work and all of his assumptions.



**Figure 5.5.** Pore's aspect ratios (AR) estimated corresponding to  $V_p$  (left) and  $V_s$  (right) and total porosity (from Harju, 2022).

The results of Figure 5.5 show mostly crack/intraparticle (crack dominated) pore types in the UB and LB shales as well as the carbonate section of MB. However, intraparticle/crack (intraparticle dominated) pore types are mostly observed in the MB clastic zone. These results are reasonable, in general, based on the assumptions made (see detailed discussions in Harju, 2022). However, in absence of any thin section and SEM images, it was not possible to confirm the pore types in different formations as predicted in Figure 5.5.

The following statements present some of the possible reasons for the real pore types being different from the above prediction due to various factors, which will lead into the necessity of performing some additional studies that are done in this research work.

- Harju (2022) considered constant fluid saturations as explained earlier. However, in real conditions, fluid saturations ( $S_w$ ,  $S_o$ , and  $S_g$ ) vary with depth and have significant effect on rock stiffness. For instance, lower water saturation at some depth intervals results in lower velocities compared to those predicted by Harju (2022) who considered constant  $S_w=40\%$ .
- Considering  $e=1$  may lead to a small overprediction of rock velocity, compared to  $e=3$ , which is more representative at log-scale.
- Kerogen is also not constant in the UB and LB shales as assumed by Harju (2022). Furthermore, due to the solid nature of Kerogen, considering it as part of the matrix is more reasonable.
- Harju (2022) considered total porosity in his work because of Kerogen, that was considered as a part of the inclusions. However, the effective pores do not contain Kerogen.
- Harju (2022) considered wet illite instead of dry illite in his studies, because, as mentioned earlier, he wanted to compare the log-scale modeling to lab-scale. In lab-scale modeling, Harju (2022) compared the DEM model to Gassmann's model for fluid substitution. It would be

wrong to assume the bound water is connected (as assumed by Gassmann's relation). Therefore, he used wet clay to include the bound water effect first, and then modeled Kerogen and effective pores assuming isolated and connected pores to show the difference on rock stiffness.

- Assumption of wet illite by Harju (2022), lowers the illite density, resulting in an increase of the estimated velocity (corresponding to higher *AR* prediction, as mentioned earlier). Because the total porosity used for the inclusion material already includes bound water, it is more appropriate to consider dry illite properties when using total porosity instead of effective porosity.

The above assumptions by Harju (2022) deviates the prediction of the pore *ARs* from field scale values. This becomes more important when there are no thin sections and SEM images to calibrate the results. Therefore, in this study, we attempt to redo the DEM modeling using the developed correlations and by changing the above assumptions at different steps, estimate the pore *ARs* and interpret the results. This is discussed in the following subsections.

### 5.1.3. Variable Fluid Saturation

In order to apply the correlations for velocity calculations, the values of water, oil and gas saturations should be estimated. The modified-Simandoux (1963) resistivity-based equation was applied to predict water saturation. This equation is presented as:

$$\left(\frac{\phi^m}{a.R_w}\right) S_w^n + \left(\frac{V_{sh}}{R_{sh}}\right) S_w - \frac{1}{R_t} = 0 \quad (5.1)$$

In this equation  $R_t$  is the formation resistivity,  $R_w$  is the formation water resistivity,  $R_{sh}$  is the shale resistivity,  $\phi$  is the porosity,  $a$ ,  $m$ , and  $n$  are the Archie equation constants, and  $V_{sh}$  is the fraction of shale.

This equation is an extension of the equation for shaly rocks for the cases where exponent  $n \neq 2$ . The Simandoux equation of 1963 was one of the first models to successfully incorporate and correct the excess conductivity in the rock matrix due to the presence of dispersed clays. The input data to calculate the water saturation in Well #17015 is shown in Table 5.1. In this Table, the constants  $m$  and  $n$  in the MB member are 1.6 in carbonate and 1.75 in clastic formations. Similarly, the water resistivity changes from 0.016 ohm-m in carbonate to 0.01 ohm-m in clastic. This is due to the fact that MB1 to MB7 represent different lithofacies as reviewed in Chapter 2 (see Figure 5.6).

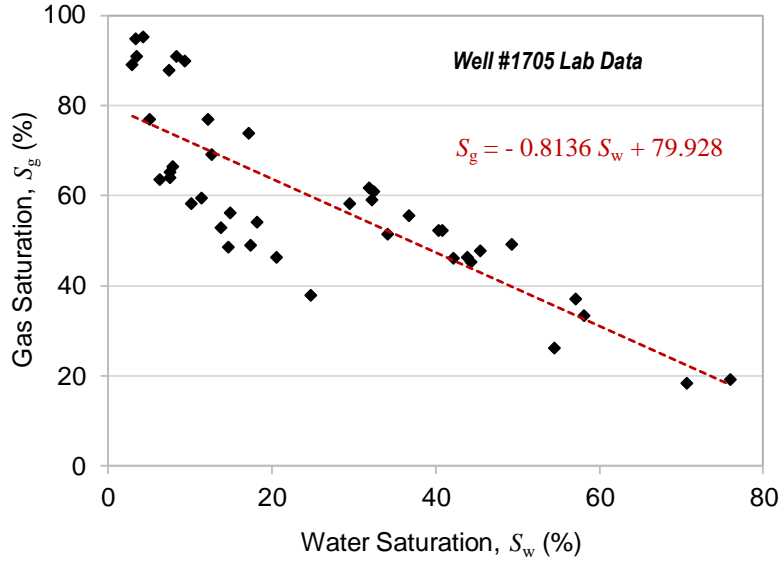
**Table 5.1.** modified Simendoux input parameter to predict water saturation.

Workflow Table Parameters					
Zone	a	m	n	Rw (ohm.m)	Res_shale (ohm.m)
UB	0.6	2	2	0.03	10
MB1	0.6	1.75	1.75	0.016	5
MB2	0.6	1.6	1.6	0.01	5
MB3	0.6	1.75	1.75	0.016	5
MB4	0.6	1.6	1.6	0.01	5
MB5	0.6	1.75	1.75	0.016	5
MB6	0.6	1.6	1.6	0.01	5
MB7	0.6	1.7	1.7	0.016	5
LB	0.6	2	2	0.03	10

Figure 5.3 shows the relationship between the water and gas saturation from lab data in Well #17015. The linear correlation shown in this Figure in the form of:

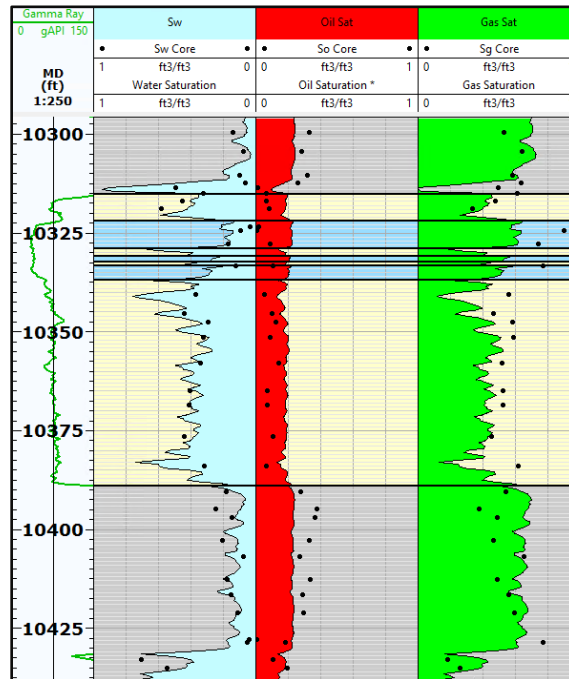
$$S_g = -0.8136S_w + 79.928 \tag{5.2}$$

was used to estimate the gas saturation.



**Figure 5.6.** Lab data from Well #17015, showing a linear correlation between water and gas saturation.

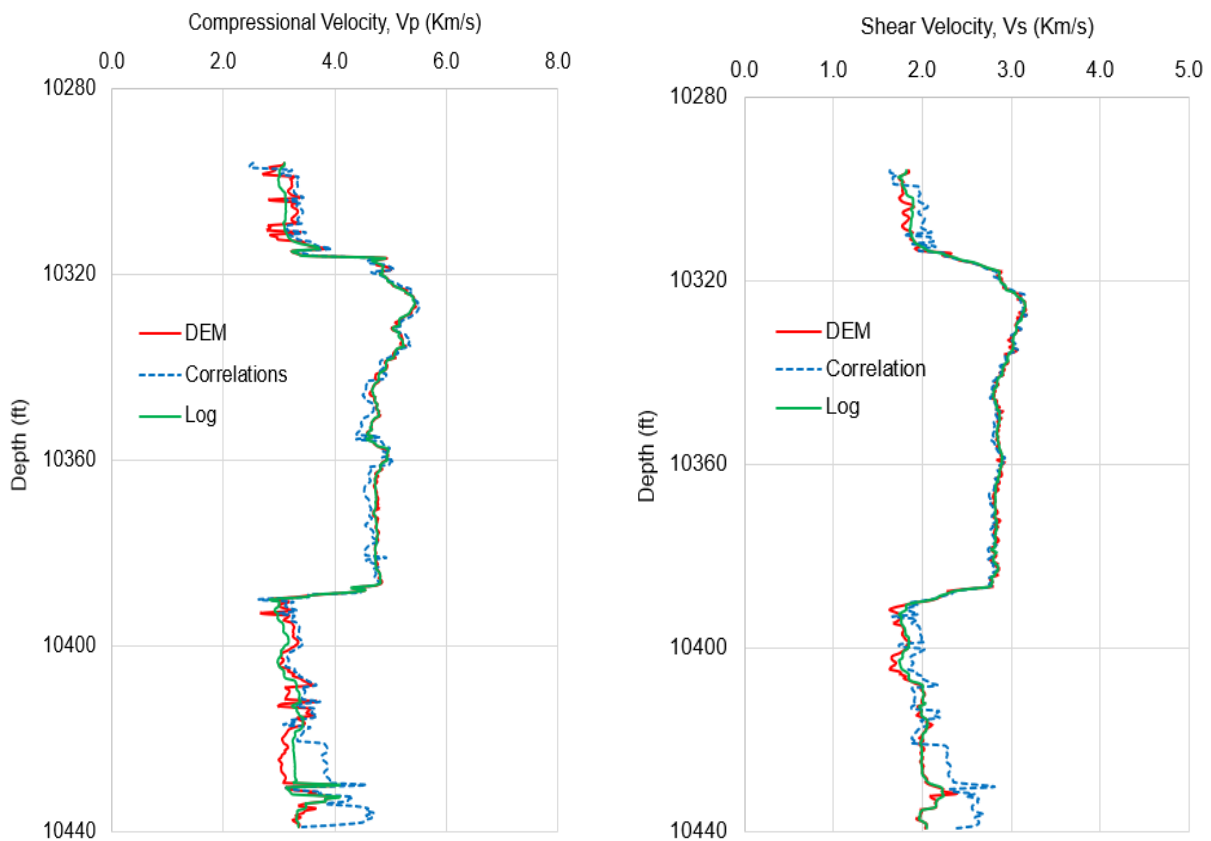
The oil saturation was calculated as the remainder of water and gas saturation (i.e.  $S_o = 1 - S_w - S_g$ ): Figure 5.7 shows the plots of water, oil and gas saturations with some core data for calibration purposes, which show good agreement. It is seen that this is mainly a gas dominated area with a large volume of gas fraction.



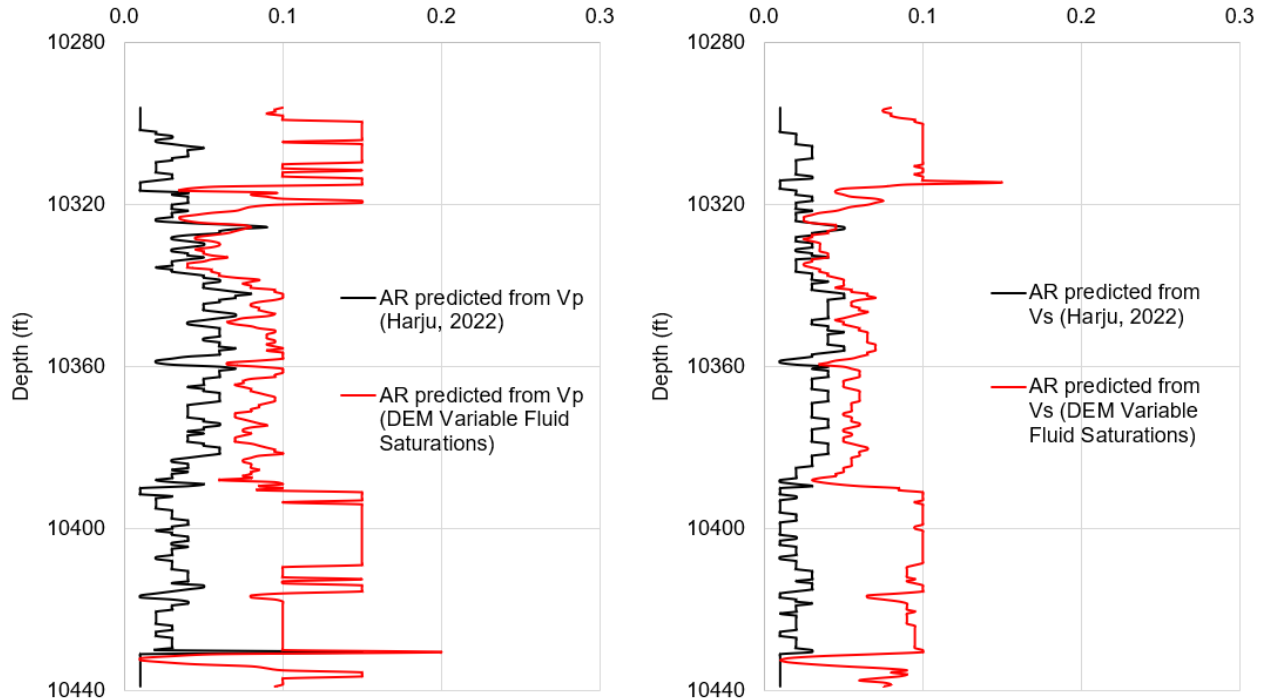
**Figure 5.7.** Water, oil and gas saturation predicted for Well #17015, Nesson State.



Considering variable water saturation, the results of the DEM model and correlations for estimation of  $V_p$  and  $V_s$  are shown in Figure 5.8, which show a good match, especially in the MB member. Considering the predicted velocities, the pore ARs were estimated in such a way to minimize the difference between predicted velocities and the measured log values. The results are presented in Figure 5.9 together with predictions of Harju (2022) where constant fluid saturations were assumed. It is seen that the results look different, and it is to be noted that the effect of Kerogen is not included yet in the DEM model and correlations results of Figure 5.8 and 5.9.



**Figure 5.8.**  $V_p$  (left) and  $V_s$  (right) velocity estimation from DEM model and correlations considering variable water saturations.



**Figure 5.9.** Pores' aspects ratio ( $AR$ ) prediction from Harju (2022) (blue) with constant fluid saturations assumption versus developed correlations with varying fluid saturations (black), corresponding to  $V_p$  (left) and  $V_s$  (right).

In the UB and LB shales, due to the lower estimated water saturation (stiffer fluid) compared to that assumed by Harju (2022) (40%) the estimated velocity from the new DEM model decreased. As a result, the measured velocity fits the estimated velocities with higher  $AR$ s. Therefore, the  $AR$  prediction changed from crack to intraparticle dominated. In the absence of thin sections or SEM images, the results cannot be quantitatively validated. However, as shown from the mineral composition given by ECS logs (see Figure 5.3), the UB and LB are mostly clay and quartz with no presence of carbonate and are well-known for their brittle nature and their heterogeneity (cracks are more likely to be present in Carbonate). Siliciclastic pore geometry is most-likely intraparticle (Xu & White, 1996). However, with the presence of anhydrite and the lenticular texture of clays, we expect a small amount of crack type pores in the UB and LB shales. This can probably be adjusted by including the effect of Kerogen or by considering dry illite properties. In the MB formation, the deviation of the  $AR$  from the different models is reduced, especially in the Carbonate

portion, because of the low porosity making fluid less significant compared to UB and LB where total porosity is high.

#### 5.1.4. Variable Kerogen

In order to include the effect of Kerogen in shale layers, one approach is to consider Kerogen as part of the fluid and integrate its effect during the fluid mixing, similar to the approach that was taken in the DEM model. The alternative approach is to consider Kerogen as one of the minerals and add its effect during the mineral mixing phase. The earlier approach will increase the velocity of the pores, whereas the latter one will reduce the velocity of the matrix. Considering the process of developing the correlations, it is simpler to use the latter approach to include the effect of Kerogen in the UB and LB shales.

As the kerogen volume was not available, we estimated it using the Passey method (1990). This method combines the resistivity log (which responds to the fluid phase) and porosity log (which responds to both fluid and matrix/kerogen phases) to estimate the TOC in organic rich rocks. In organic-rich rocks, porosity and deep resistivity readings are separated, whereas in organic-lean rocks, the two curves overlies. The separation between the two curves or the scaled difference ( $\Delta \log R$ ) between them is related to the TOC content throughout the level of organic maturity (LOM) as:

$$\Delta \log R = \log_{10} \frac{RT}{RT_{\text{baseline}}} - [SF(PHI - PHI_{\text{baseline}})] \quad (5.3)$$

Here,  $RT$  is the deep resistivity log (ohm/m),  $RT_{\text{baseline}}$  is the resistivity in the organic-lean zone (ohm/m),  $PHI$  is porosity log (sonic, density or neutron logs), and  $PHI_{\text{baseline}}$  is the porosity log reading in the organic-lean zone. The scaling factor (SF) is calculated after baselining the two

curves in the organic-lean zone. Table 5.2 presents the workflow for TOC estimation using Passey's method in the Bakken shale.

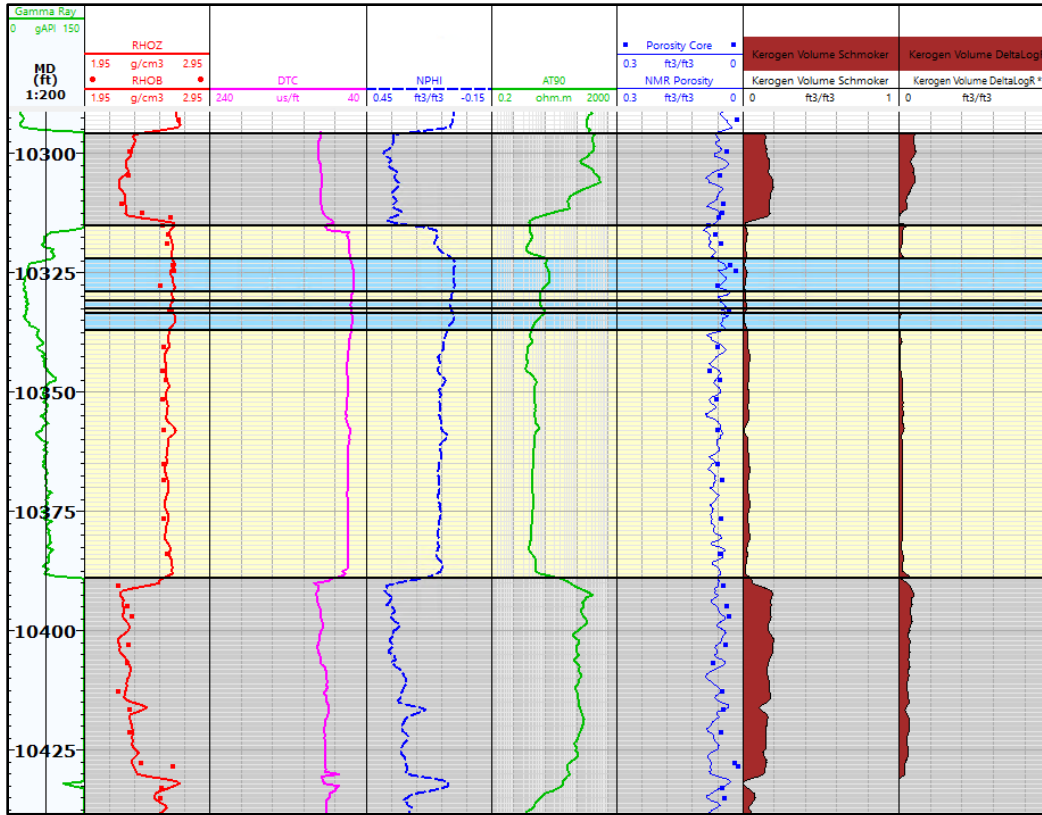
**Table 5.2.** Workflow of estimating kerogen level in the Bakken shale using Passey method.

Zone	Vitrinite Reflectance	Resistivity Baseline (ohm.m)	NPHI Baseline	TOC Type
UB	0.9	10.0	0.3	III
MB1	0.9	2.5	0.08	III
MB2	0.9	10.5	0.08	III
MB3	0.9	7.0	0.08	III
MB4	0.9	7.0	0.08	III
MB5	0.9	9.5	0.08	III
MB6	0.9	4.0	0.08	III
MB7	0.9	2.5	0.08	III
LB	0.9	10.0	0.3	III

For comparison purposes, the TOC level was also estimated using the Schmoker (1979) method. This method relies on the density to determine the TOC level and is an empirical method developed to quantitatively estimate TOC in Devonian shales from log data. The method was later applied to the Bakken black shales consisting of rock matrix, interstitial pores, pyrite, and organic matter. Schmoker's (1979) empirical model is presented as:

$$TOC(wt\%) = \frac{154.497}{\rho} - 57.261 \quad (5.4)$$

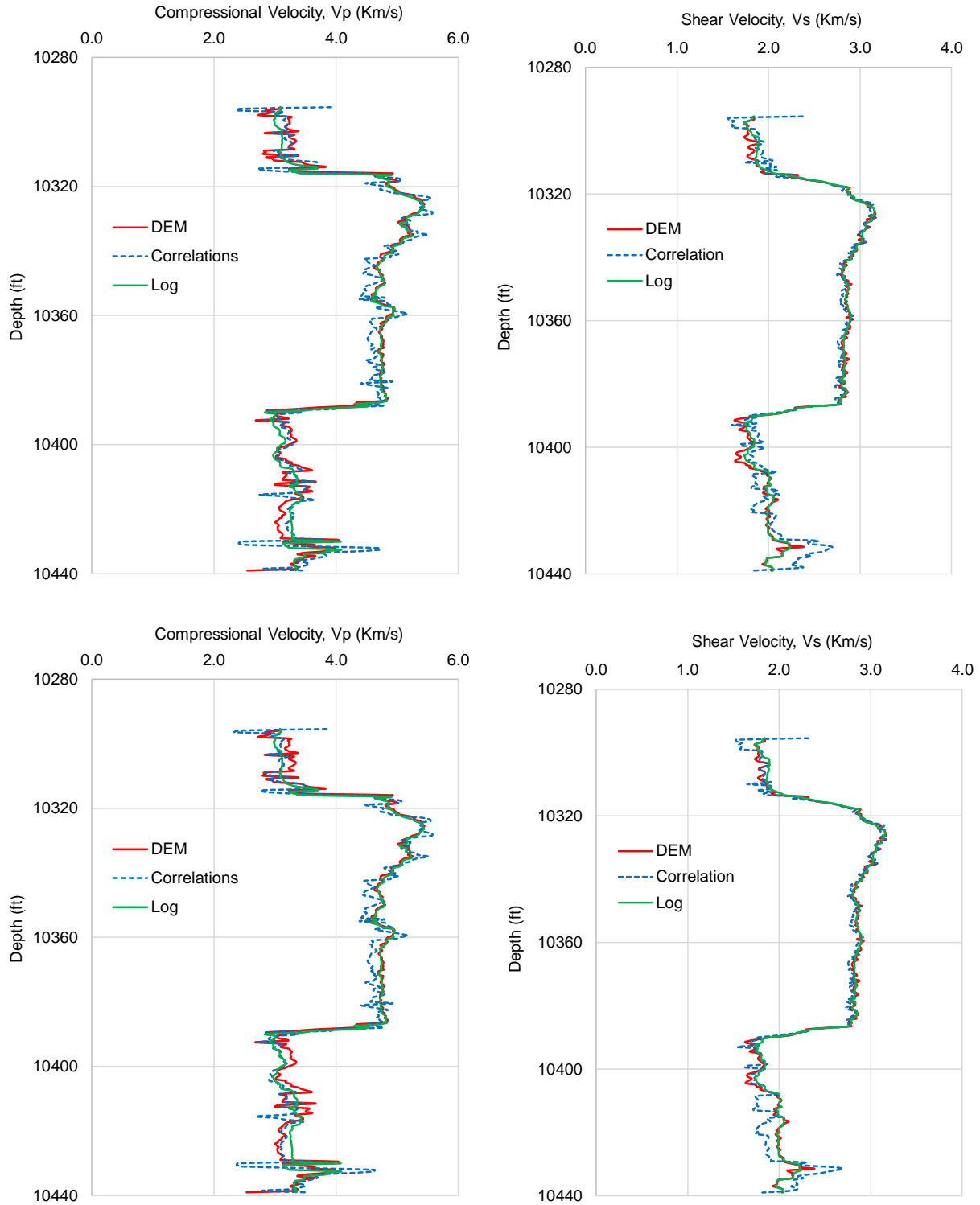
Here,  $\rho$  is the bulk density (g/cc), and the constants were specifically calculated for the upper and lower shale members of the Bakken Formation based on an organic matter density of 1.01 g/cc, a matrix density of 2.68 g/cc, and a ratio between weight percent of organic matter and organic carbon of 1.3. The study reported an average organic-carbon content in the upper and lower shale members of 12.1 wt.% and 11.5 wt.% respectively, calculated at 159 locations in North Dakota and 107 in Montana (from Wiki).



**Figure 5.10.** Estimation of TOC level in UB and LB shale in Well #17015 using Passey, Schmoker, and Hester method.

The results of TOC estimations are shown in Figure 5.10, which show that the Passey method results in a lower level of TOC. Due to the lack of Rock-Eval pyrolysis analysis lab data, it was not possible to calibrate the log estimations. However, based on the match of the results with the existing rock physics models in this study it was seen that the Passey method provides a better estimate of TOC.

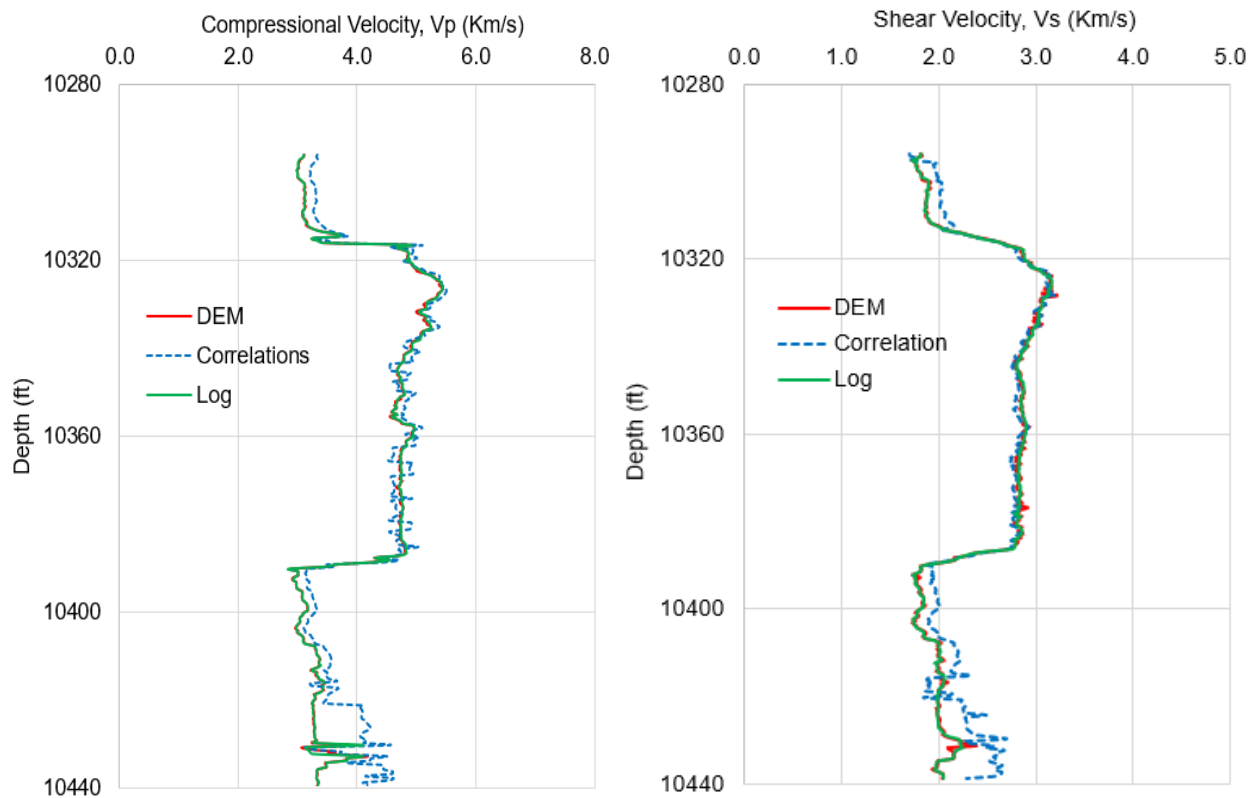
To do this, we added kerogen, as one of the minerals in the shale sections and used developed correlation constants for Kerogen (see Table 4.8) to include its impact on total velocity. The results are shown in Figure 5.11 for both the Passey and Schmoker methods, which indicate that the Passey method presents a closer agreement with the DEM model and log data.



**Figure 5.11.** Impact of adding kerogen in UB and LB shale on velocity prediction from correlations for Well #17015 using Passey (top) and Schmoker (bottom) methods.

### 5.1.5. Dry Illite properties

Here, we continue on the previous step of considering variable fluid saturation and Kerogen, and consider dry illite properties and total porosity as inclusion volumes to estimate velocities of the Bakken members from the DEM model and correlations. The results are presented in Figure 5.12. Although the MB shows a pretty good match, the UB and LB shales are slightly overestimating the DEM model values.



**Figure 5.12.**  $V_p$  (left) and  $V_s$  (right) velocity estimation from DEM model and correlations versus measured log data considering variable water saturations and variable Kerogen fraction, dry illite and total porosity as the inclusion volume.

Estimation of density is also sensitive to the parameters mentioned earlier. Figure 5.14 shows different estimated densities versus measured density logs (red). The estimations include modeled density considering only fluid saturation, without accounting for the presence of Kerogen or

adjusting the illite properties (black), density estimation by including the effect of dry clay properties (green), and the modeled density by adding the kerogen effect (blue).

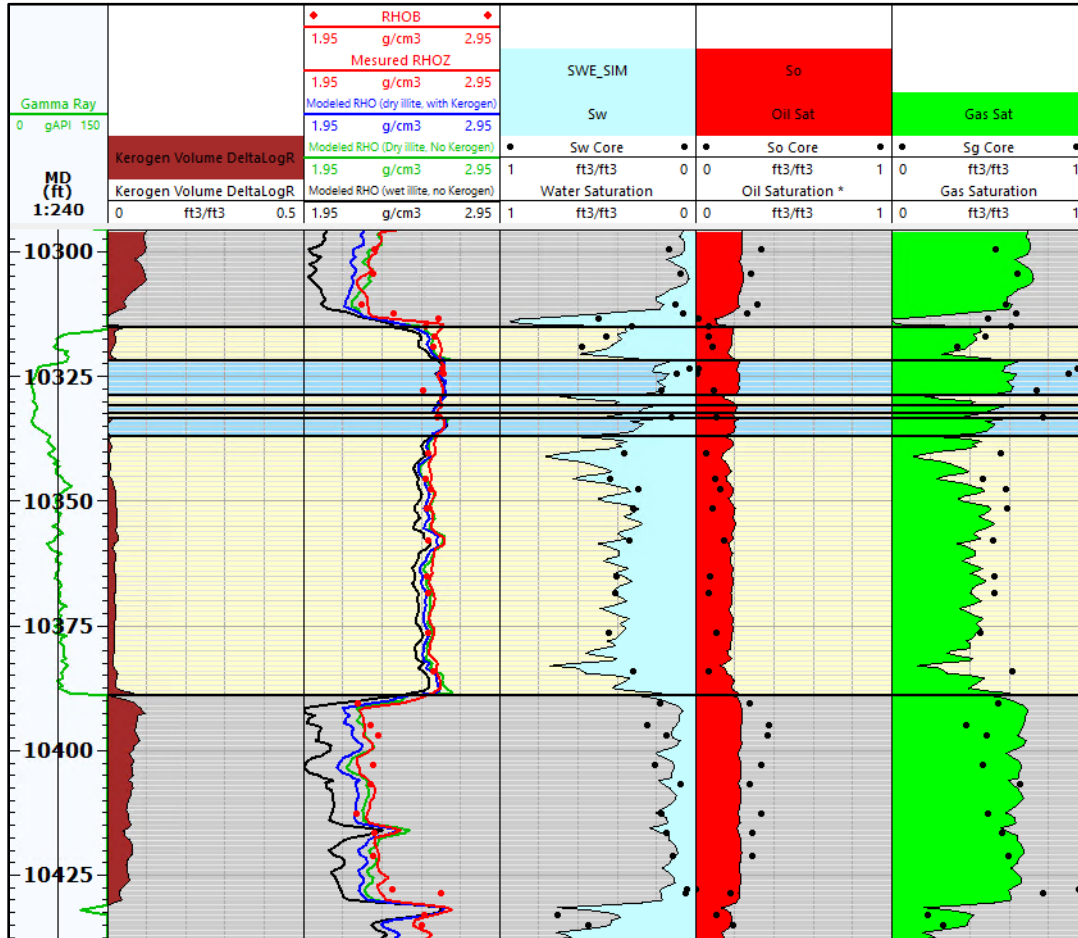


Figure 5.13. Modeled densities for the Bakken assuming dry and wet illite and with and without addition of Kerogen.

From this figure, the following observations can be made:

- Modeled density considering dry, instead of wet density, gives a better match with measured density and core data.
- Considering Kerogen as part of matrix lowers the density.
- The difference between measured (red) and modeled densities, considering kerogen effect (blue) may be due to some uncertainties in mineralogy, such as considering all clays as illite



type where chlorite can be present in the Bakken formation. Also, in UB and LB, we can find small amounts of pyrite, which can increase density.

- There can be also some range of error in carbonate log decomposition. However, looking at the good match in the carbonate section of MB, where clay is small and there is no Kerogen, this effect should be minimal.

The prediction of pore *AR* across the different Bakken members was done at this last stage, and compared to the previous prediction that considers only the variation of fluid saturations filling the pores, to show the effect of considering Kerogen volume as part of the rock matrix and dry illite, as presented in Figure 5.14.

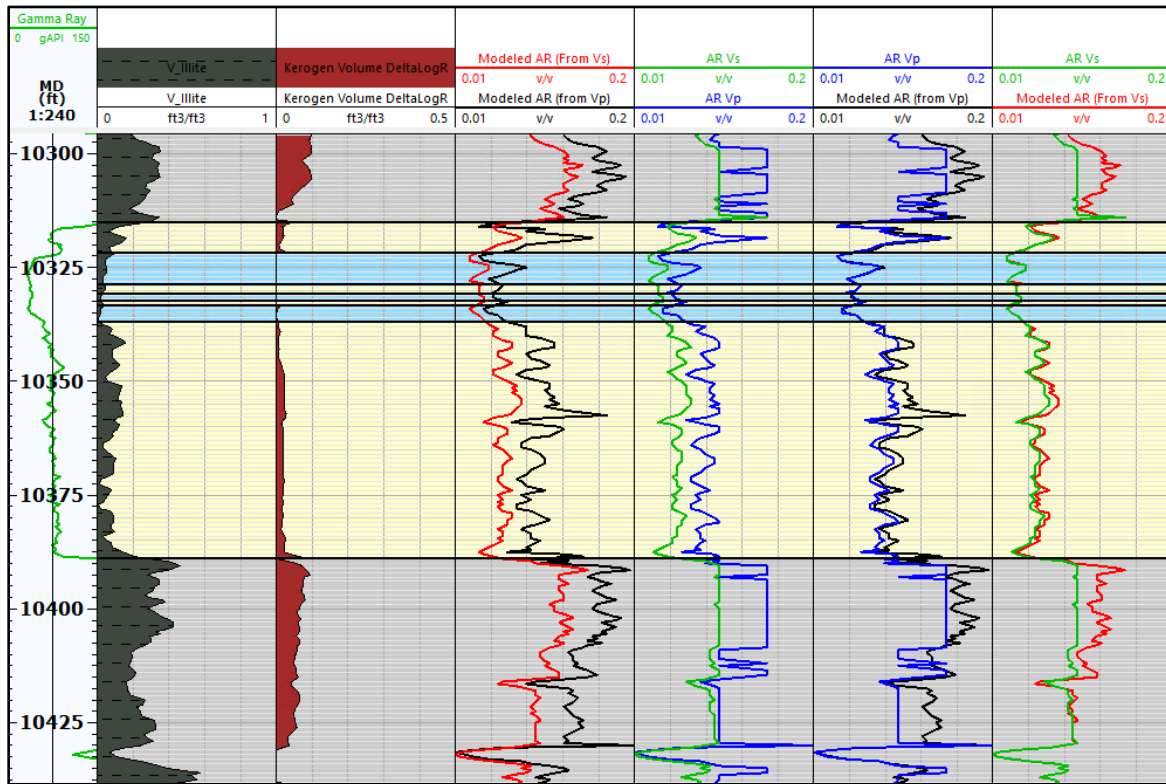


Figure 5.14. Pore’s aspect ratios corresponding to  $V_p$  and  $V_s$ , estimated from new DEM (black and red curves) and previous (blue and green curves) modeling.

From this figure, the following statements may be made:

- The pore aspect ratio predicted from S- wave velocity, after considering the above mentioned parameters, was not much affected by this modification due to the low illite and kerogen abundance, especially in the carbonate portion, where a similar prediction was observed, compared to the previous model (no kerogen and dry illite effect).
- In UB and LB shales, the predicted  $AR$  was affected by the presence of illite and Kerogen from both  $V_p$  and  $V_s$ , where a small presence of stiff pores is observed.
- In UB and LB, the predicted  $AR$  from  $V_p$  was less affected compared to the previous model (due to kerogen and dry illite effect), because of the relatively higher bulk moduli of kerogen (6 GPa) compared to its lower shear moduli (3.15 GPa), and considering Kerogen density of 1.4 g/cc.
- The increase in predicted  $AR$  in the new model is reasonable because of the presence of the organic matter that has a geometry greater than interparticle of around 0.4 (Xu & ` , 2017).

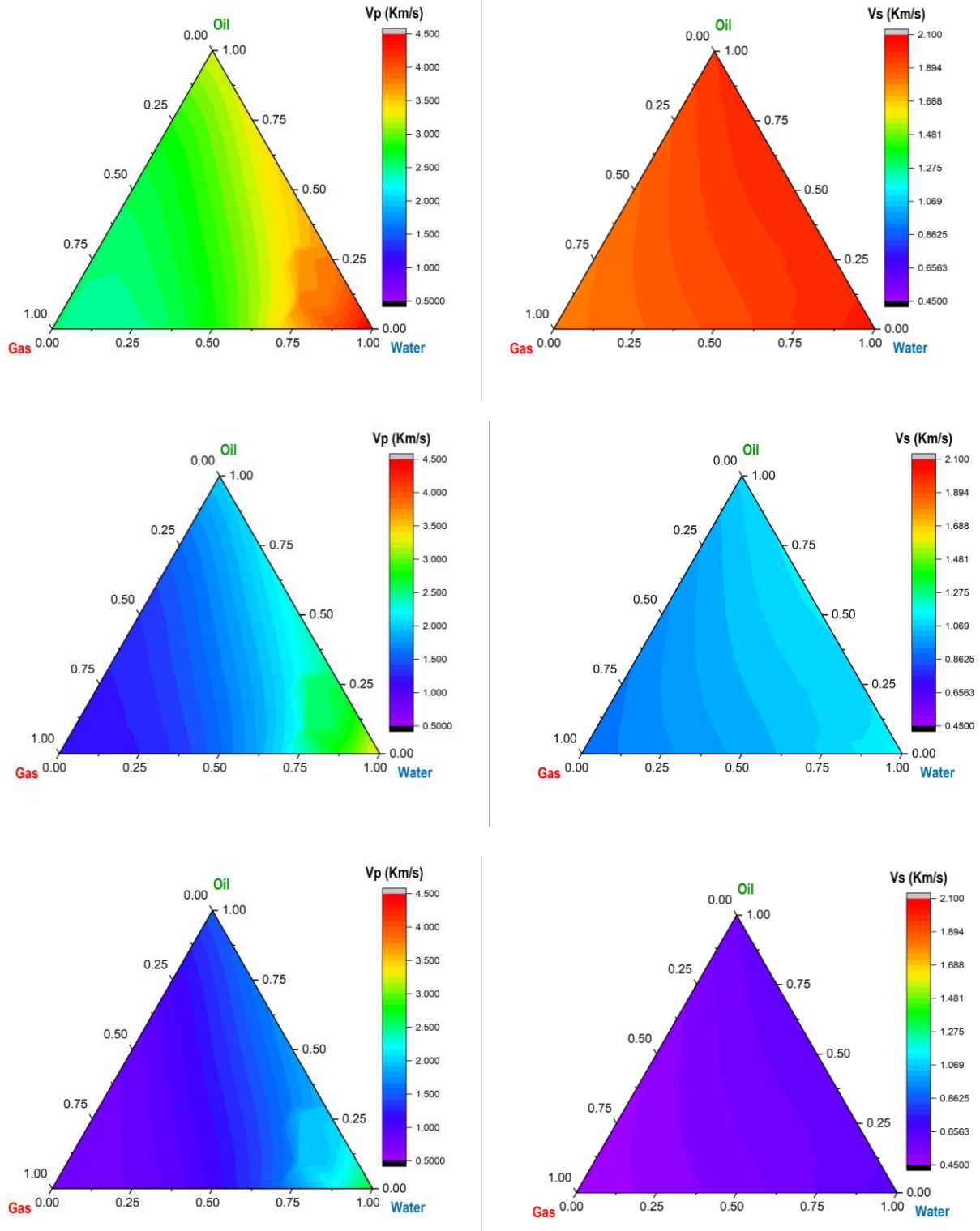
Unfortunately, in this well there are no thin sections or SEM images to validate these predictions. Further example case studies are carried out in wells from Grenora field to examine the applicability of these correlations, and predicting the pore aspect ratios following the same procedure, in wells that contain data to validate the outcomes.

#### 5.1.6. Ternary Plots

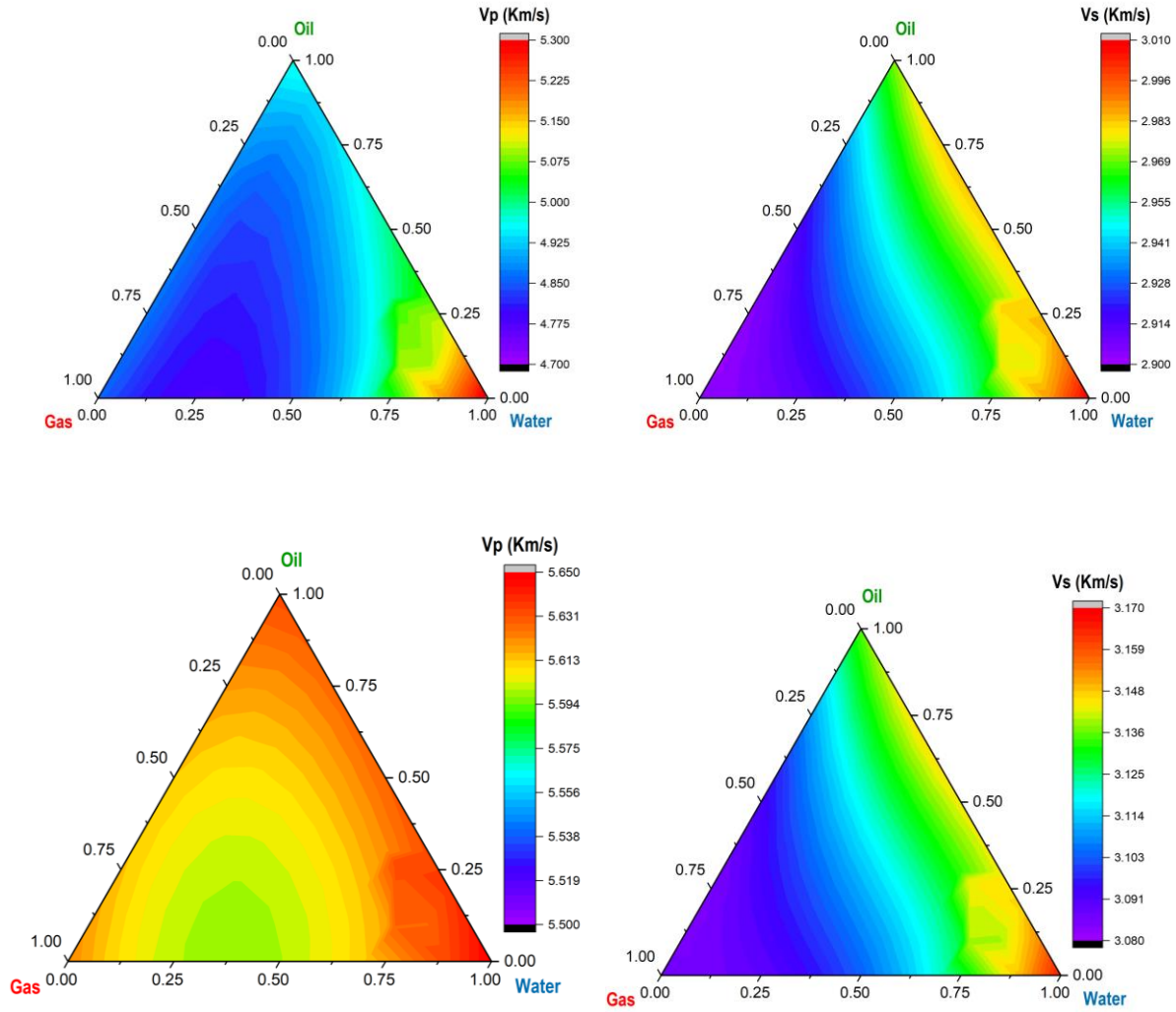
Figure 5.15 presents the ternary plots corresponding to  $V_p$  and  $V_s$  for the MB carbonates to visualize the impact of different fluid saturations. The results show that, while the pore aspect ratio is constant at 0.01 (crack), by increasing the porosity in total and reducing the velocity the maximum value corresponds to when pores are fully saturated with water. Also, as expected, in the case of two-phase flow, the change of velocity from water to gas saturated pores is larger than the change from oil saturated to gas saturated pores. The results show that, for  $V_p$ , the largest velocity

( $S_w=100\%$ ) when porosity is 5% is 4.5 Km/s, which changes to approximately 3.5 Km/s and 2.5 Km/s as porosity increases to 10% and 15%, respectively. Corresponding values for  $V_s$  change from 2.1 Km/s to 1.1 Km/s and 0.6 Km/s, respectively.

Figure 5.16 shows the ternary plots when porosity is kept constant at 5% and the pore aspect ratio is changed from 0.05 (intraparticle) to 0.15 (intergranular). The results for aspect ratio of 0.01 (crack) are same as the top row images of Figure 5.10. The results of Figure 5.16 show that in general, by increasing the pore aspect ratio (i.e. changing the pore shape from crack to more circular or moldic), the formation becomes stronger and velocities become faster, as one would expect. Also, a lower range of velocity values is observed as the pore aspect ratios increase. Changing the AR from 0.05 to 0.15 corresponds to a range of change of  $V_p$  from 4.7-5.3 Km/s to 5.50-5.65 Km/s and for  $V_s$  from 2.90-3.01 Km/s to 3.08-3.17 Km/s. This suggests that the crack type pores can influence the formation elastic properties much more than pores with higher aspect ratios.



**Figure 5.15.** Ternary plots of change of  $V_p$  (left column) and  $V_s$  (right column) for the Middle Bakken carbonate formation as a function of three-phase fluid saturation, due to change of porosity from 5% to 10% and 15%, from top to the bottom. Pore aspect ratio is  $AR=0.01$ .



**Figure 5.16.** Ternary plots of change of  $V_p$  (left column) and  $V_s$  (right column) for the Middle Bakken carbonate formation as a function of three-phase fluid saturation, due to change of pore aspect ratio from 0.05 (interparticle), (top) to 0.15 (intergranular), (bottom). Porosity is 5%.

## 5.2 Case Studies from Grenora Oilfield, Williams County

The three wells from Grenora field, reviewed in Chapter 3, were used in this study for rock physics modeling using the developed correlations. These wells are Rasmussen 1-21-16H (NDIC Well #20844), Muller 1-21-16H (NDIC Well #20552) and Trigger 1-31H (NDIC Well #17946).

### 5.2.1 Petrophysical ELAN for Wells from Grenora Oilfield, Williams County

The input data that was required for the rock physics modeling for these wells was not available, hence, the typical petrophysical elemental analysis (ELAN) was performed to obtain the necessary data. The outputs of the ELAN that was needed in this study include:

#### **Mineral volumes:**

Volume fractions of each mineral.

#### **Effective and total porosity (PHIT and PHIE):**

Total porosity = Effective porosity + Clay bound. Total porosity does not account for kerogen porosity.

#### **Effective water saturation (SWE):**

Effective water saturation corresponds to the effective porosity. Clay-bound porosity is completely water-saturated. Water saturation was estimated using the modified-Simandoux model with the input data listed in Table 5.3.

#### **Total organic carbon (TOC) and kerogen volume:**

TOC and kerogen volumes are calculated only in UB and LB.

This Section summarizes the results of the ELAN for these three wells. The minerals to consider in each formation for the mineralogical model were selected based on the XRD lab as well as cuttings data and reports. In general, minerals with less than 2% of volume fraction were

disregarded. In well Trigger 1-31H, only basic logs were available, hence only dominant minerals were considered for evaluation. Also, kerogen was not considered for the MB.

**Table 5.3.** Input data to calculate water saturation using Simandoux model in 3 wells of Grenora field.

$\phi_e$	Computed from QELAN
$R_w$	0.017 to 0.02 ohm.m @210 degF
$a$	1.0
$m$	1.75 to 1.8
$n$	2.0
$V_{sh}$	Computed from QELAN
$R_{sh}$	5 ohm.m for MB (varied in UB and LB)
$R_t$	Deep Resistivity Log

Resistivity-based models have limitations in evaluating the organic-rich shales because of the presence of high resistivity Kerogen. In this study, to obtain consistent results with available core data,  $R_{sh}$  values were varied.

The TOC was calculated using Passey’s (1990) model that can be represented in terms of compressional slowness and resistivity as:

$$\Delta \log R = \log_{10} \frac{RT}{RT_{baseline}} + 0.02[S F(DTC - DTC_{baseline})] \quad (5.5)$$

$$W_{TOC} = D \log_{10} RT \times 10^{0.297 - 1.688 LOM} \quad (5.6)$$

$$W_{TOC} \% = 100 W_{TOC} \quad (5.7)$$

In the above equations  $DTC$  is the compressional sonic log reading in any zone ( $\mu\text{sec}/\text{ft}$ ),  $DTC_{baseline}$  is the sonic baseline in non-source rock ( $\mu\text{sec}/\text{ft}$ ),  $\Delta \log R$  is the Passey’s number (fractional),  $LOM$  is the level of organic maturity (unitless),  $W_{TOC}$  is the total organic carbon (weight fraction) and  $W_{TOC} \%$  is the total organic carbon (weight percent).

In the present study  $RT_{baseline} = 0.2 \text{ ohm.m}$ ,  $DTC_{baseline} = 60 \mu\text{s}/\text{ft}$  and Vitrinite reflectance value  $VR = 0.76$  were used. The latter value is taken from the core studies of well 20884.

The absolute value of the sonic and resistivity log values in the low-resistivity shale is called baselines. These baselines are generally attributed to the shales that do not contain kerogen. They will vary with the depth of burial and geologic age. Therefore, finding a correct baseline requires non-source rock shales. However, there are no sections of the UB and LB that do not display non-source rock characteristics. In this study, these baseline values are chosen as initial numbers and iterated until a good match between the estimated TOC and the core data is obtained.

It is to be noted that only the Rasmussen 1-21-16H well has core derived TOC data. Hence,  $R_t$  and  $DTC$  baselines are obtained in this well by matching with the core data. The same baselines were used to estimate the TOC and kerogen volumes in the Muller 1-21-16H and Trigger 1-31H wells. Kerogen volume can be estimated from the following relationship:

$$K_{vol} = TOC * CONV * \frac{RHOB}{RHOK} \quad (5.8)$$

where,  $RHOB$  is the bulk density and  $TOC$  is computed from equations 5.4 to 5.6. In this study, conversion factor of  $CONV=1.2$  Kerogen density of  $RHOK = 1.7$  g/cc were used. Figures 5.17 to 5.19 present the output of the ELAN for the three study wells.



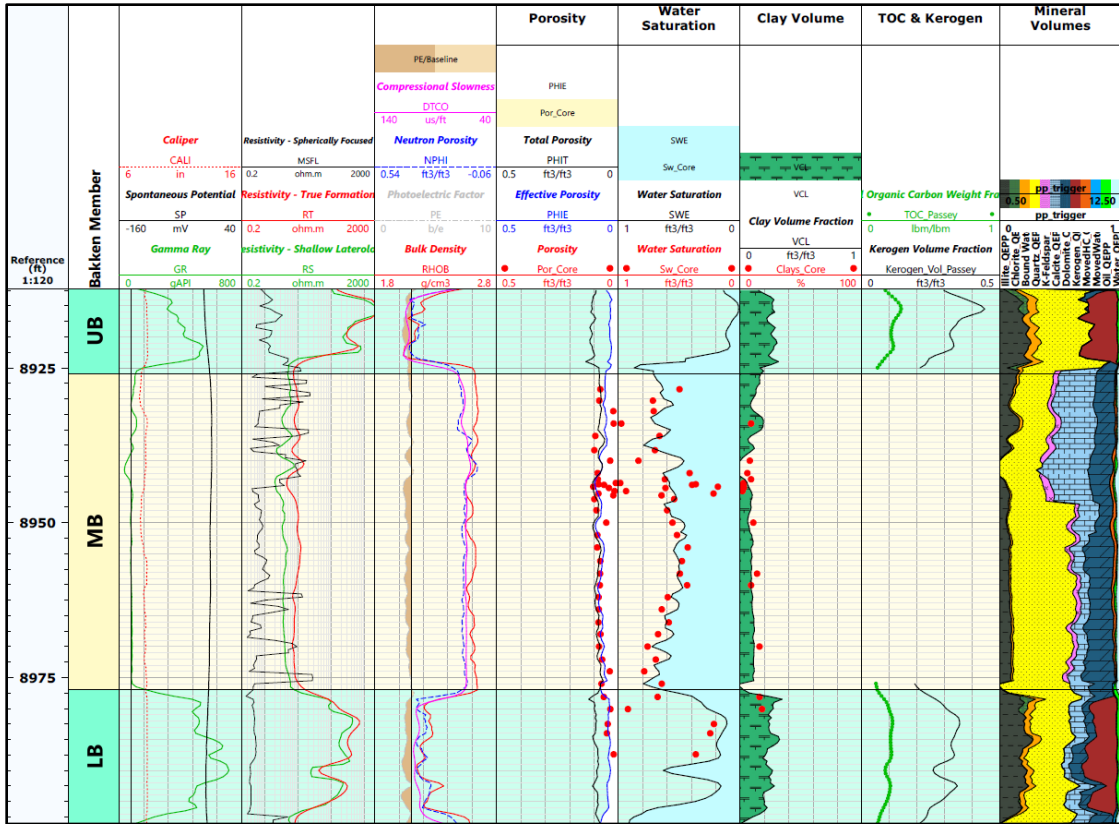


Figure 5.17. The output of the Petrophysical ELAN for Well #17946 in Grenora field.

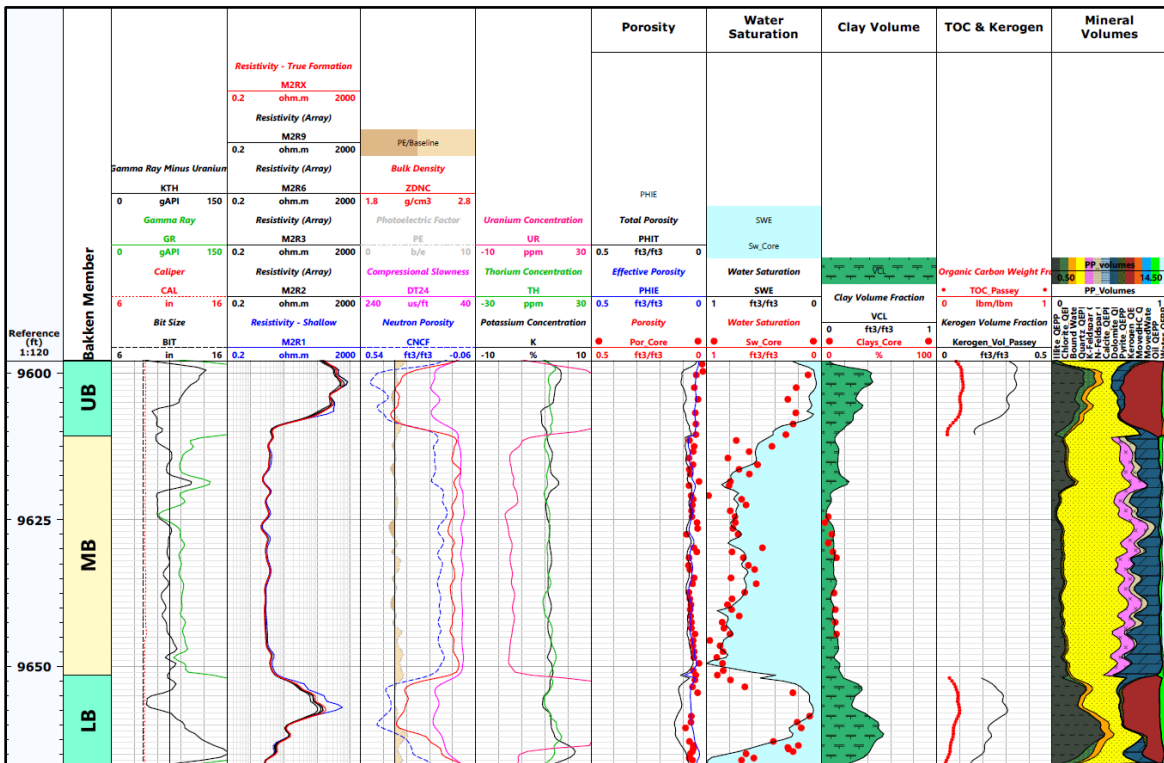


Figure 5.18. The output of the Petrophysical ELAN for Well #20552 in Grenora field.

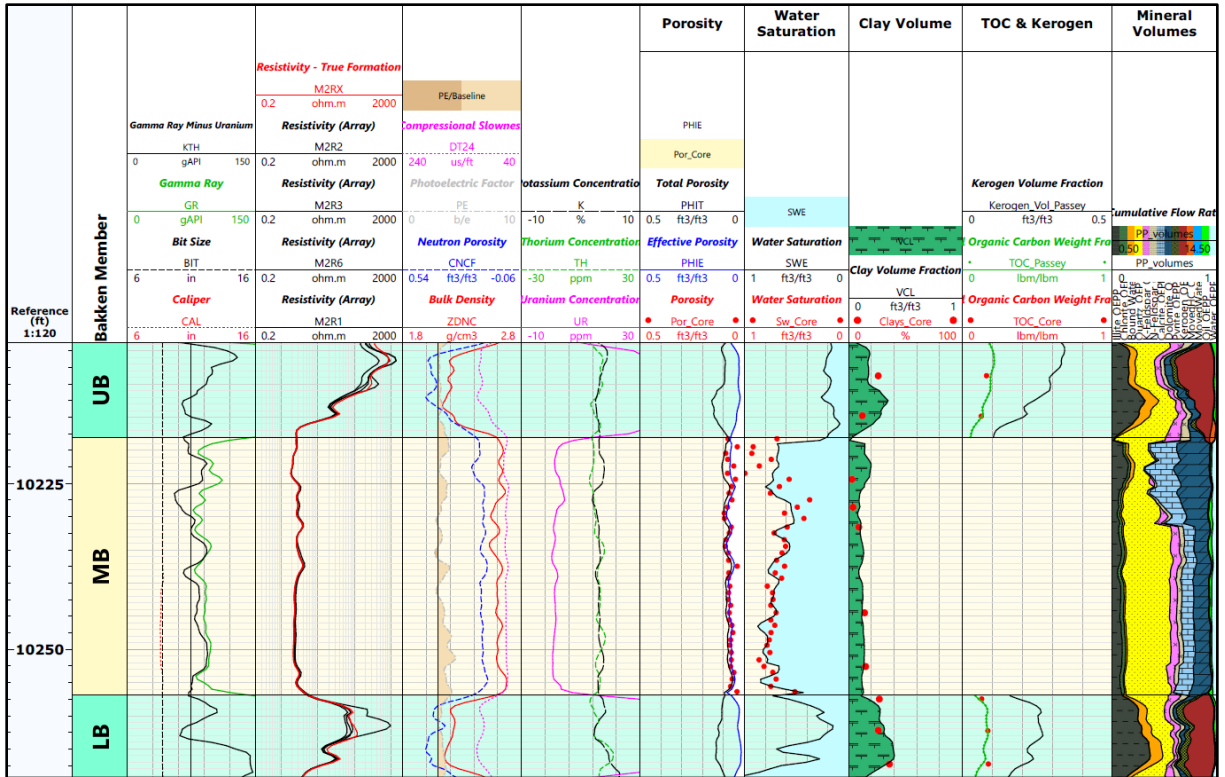


Figure 5.19. The output of the Petrophysical ELAN for Well #20844 in Grenora field.

### 5.2.2 Shear Velocity ( $V_s$ ) Estimation

In the three study wells, only compressional sonic ( $DTC$ ) data was available. However, the shear sonic ( $DTS$ ) data is also needed for the rock physics modeling. In order to estimate the shear velocity ( $V_s$ ) from the available  $V_p$  data, empirical correlations were used. As the Bakken formation has complex lithology, Greenberg and Castagna (1992) which is a commonly used correlation in multimineral formations was used. The method is based on deriving polynomial  $V_p - V_s$  relations in pure lithologies (limestone, dolomite, sandstone, and shale), then  $V_s$  in the multimineral lithology formation is estimated by averaging the arithmetic and harmonic means of the shear velocities of the pure lithologies.

$$V_s(Km/s) = \frac{1}{2} \left\{ \left[ \sum_{i=1}^L X_i \sum_{j=1}^{N_i} a_{ij} V_p^j \right] + \left[ \sum_{i=1}^L X_i \left( \sum_{j=1}^{N_i} a_{ij} V_p^j \right)^{-1} \right]^{-1} \right\} \quad (5.9)$$

where  $X_i$ ,  $L$ ,  $a_{ij}$ , and  $N_i$  are the volume of minerals constituents, the number of pure mineral constituents, the empirical regression coefficients, and the order of polynomial of constituent  $i$ , respectively.

Table 5.4 summarizes the polynomial regression coefficients, and correlation coefficients, for pure minerals (sandstone, limestone, dolomite, and shale) from which the  $V_p - V_s$  relation in the multimineral composite was derived.

**Table 5.4.** Regression coefficients for pure lithologies (Castagna et al., 1993).

Lithology	$a_{i2}$	$a_{i1}$	$a_{i0}$	$R^2$
Sandstone	0	0.80416	-0.85588	0.98352
Limestone	-0.05508	1.01677	-1.03049	0.99096
Dolomite	0	0.58321	-0.07775	0.87444
Shale	0	0.76969	-0.86735	0.97939

The preceding relations are designed for fully brine-saturated rocks. Therefore, transformation to the actual fluid saturation is required in order to obtain an accurate  $V_s$  prediction. The method consists of estimating the brine-saturated  $V_p$  and  $V_s$  values, then transforming to the measured  $V_p$  and the corresponding  $V_s$  of the new fluid saturation using Gassmann’s fluid substitution relation. Equation 5.9 describes the transformation of bulk modulus ( $K$ ) estimation of initial fluid-saturation to new fluid-saturation, without passing through the dry state:

$$\frac{K_{Sat1}}{K_0 - K_{Sat1}} - \frac{K_{fl1}}{\phi(K_0 - K_{fl1})} = \frac{K_{Sat2}}{K_0 - K_{Sat2}} - \frac{K_{fl2}}{\phi(K_0 - K_{fl2})} \quad (5.10)$$

In the following Sections, detailed discussion of the rock physics modeling results will be presented for each of the three Wells in the Grenora field.

### 5.2.3 Well #17946, Trigger 1-31H

#### 5.2.3.1 Minerals Composition in Well #17946

Figure 5.20 shows the variation of minerals volume fractions across the three Bakken members of well #17946 derived from the ELAN. The results were validated with XRD data.

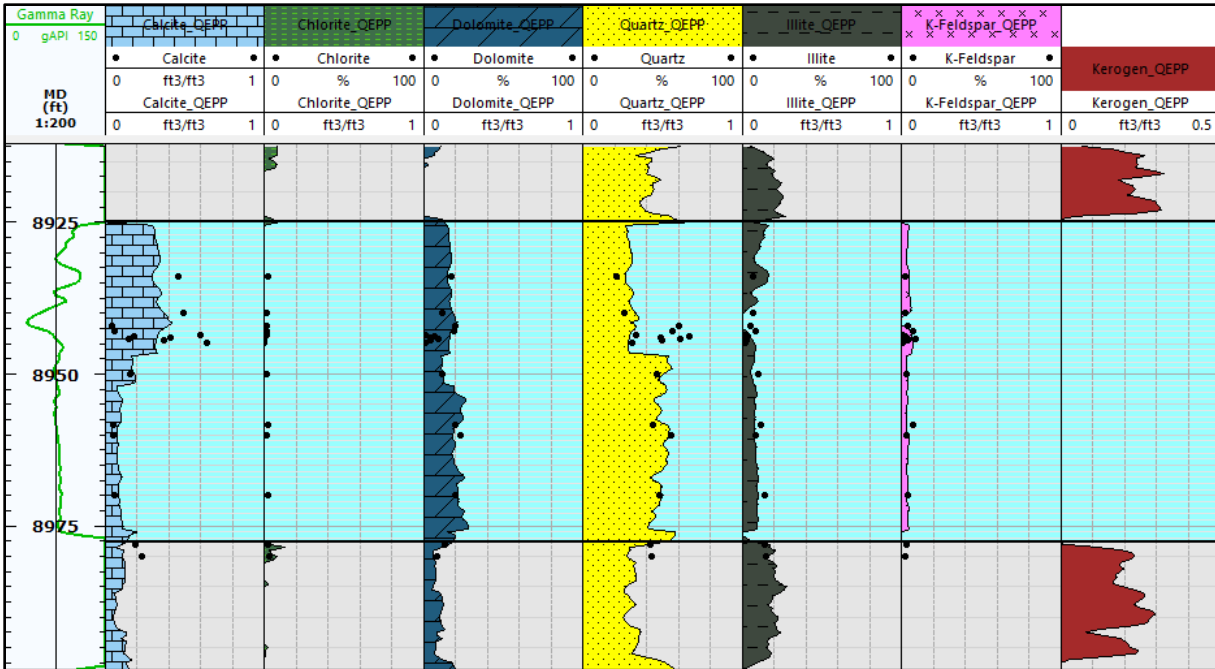


Figure 5.20. Minerals composition of Well #17946 in Grenora field, calibrated with XRD data.

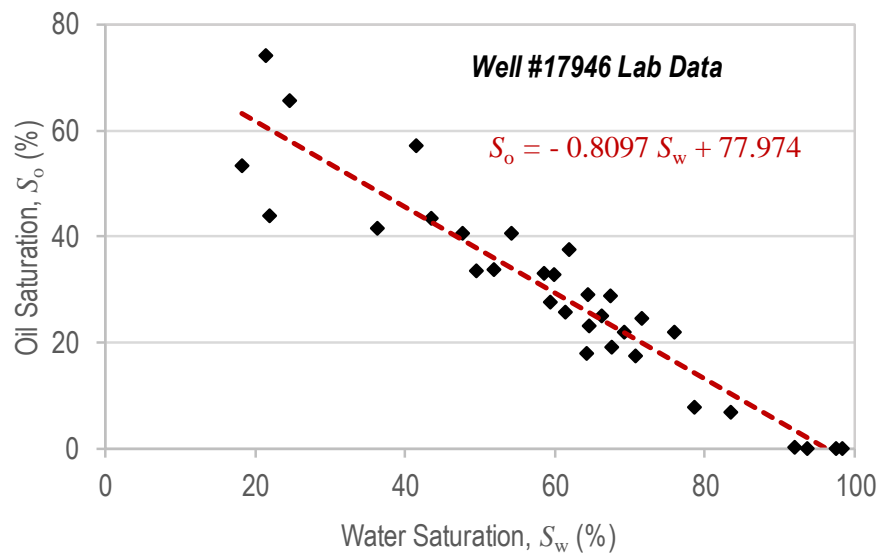
The results of Figure 5.20 show a good match between ELAN and XRD data. Regarding the lithology, UB and LB are mainly composed of clays and quartz minerals. Although carbonates are almost absent from the UB, the LB exhibits the presence of carbonate. As discussed in detail in Chapter 3 (see for example Figure 3.9), the MB is divided into two subzones. The upper part is mainly carbonate with an abundance of calcite minerals. In the lower part of the MB clastic and quartz are the most abundant minerals. The total amount of carbonate reduces due to reduction in calcite whereas the dolomite content remains almost the same as in the carbonate section. Kerogen volume was included in the ELAN mineralogy workflow, and the results were compared to the TOC computation obtained from Passey’s (1990) method. A good match between both methods was found. The mineral composition was used to obtain the rock matrix properties required during the rock physics modeling.

### 5.2.3.2 Fluids Saturation in Well #17946

We followed a similar approach to well #17015, where water saturation was calculated from the Modified-Simandoux method and calibrated with core data. Oil versus water saturation data from core analysis shows a linear trend in the form of:

$$S_o = -0.8097S_w + 77.974 \quad (5.11)$$

This relation, as shown in Figure 21, was used to estimate oil saturation.



**Figure 5.21.** Lab data from Well #17946, showing a linear correlation between water and oil saturation.

The gas saturation was estimated as  $S_g = 1 - S_w - S_o$ . Figure 5.22 shows the water, oil, and gas saturation profiles, in addition to the equivalent fluid properties, including fluid density and bulk modulus. The results in the MB, where core data is available, show good agreement.

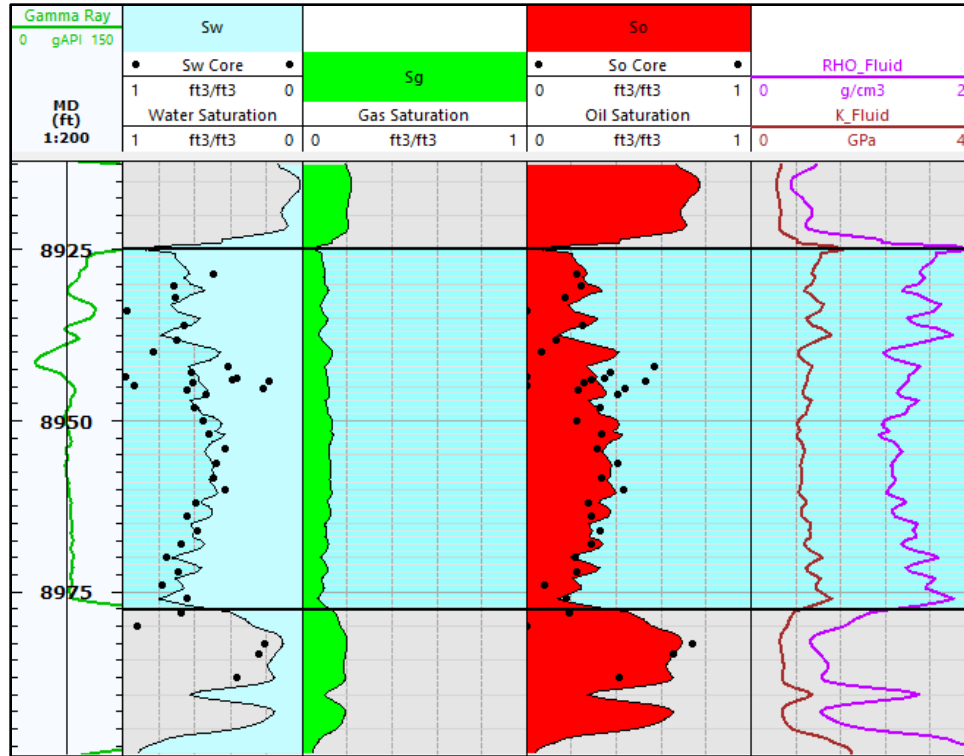


Figure 5.22. Water, oil, and gas saturation predicted for well #17946.

Figure 5.22 shows that, unlike well #17015 in Mountrail County, well #17946 is mainly oil dominated. This explains why the kerogen content in this well is relatively higher, compared to well #17015. The Rock-Eval pyrolysis data in some wells from Grenora field show that the area is less mature compared to Mountrail County. Therefore, Kerogen content is higher with higher potential of cracking and conversion into hydrocarbon (Kerogen is in late phase of type II). In contrast, the Rock-Eval data from wells in Mountrail County show that, in overall, Kerogen is type II/III and type III at some points. This also explains the reason for lower total porosity, as early mature wells do not generate any maturity-induced porosity, which is usually generated from the cracking of Kerogen and conversion into bitumen.

### 5.2.3.3 Shear Velocity Estimation in Well #17946

Figure 5.23 shows the results of shear wave velocity prediction from the compressional velocity. The process consists of estimating brine-saturated compressional velocity ( $V_{p,b}$ ), calculating brine-

saturated shear velocity ( $V_{s,b}$ ) from  $V_{p,b}$ , and applying Gassmann’s relation for fluid substitution to obtain shear velocity of the new fluid (water, oil, and gas), respectively. After that, the measured  $V_p$  and the estimated  $V_s$ , corresponding to the actual fluid saturations were reused in Gassmann’s transformation into brine-saturated velocities ( $V_{p,b}$  and  $V_{s,b}$ ) to check the convergence with the previous brine-saturated estimations.

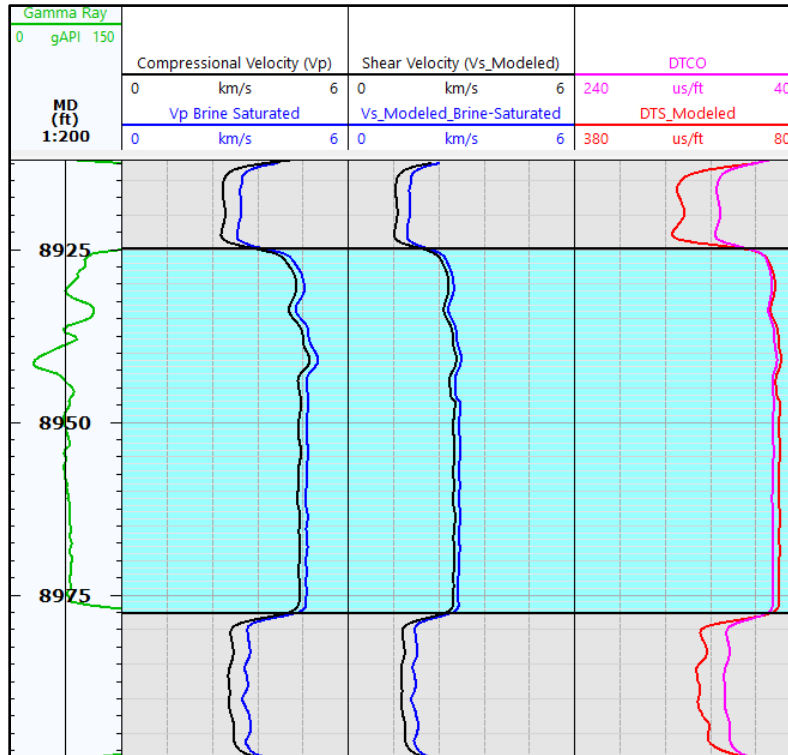


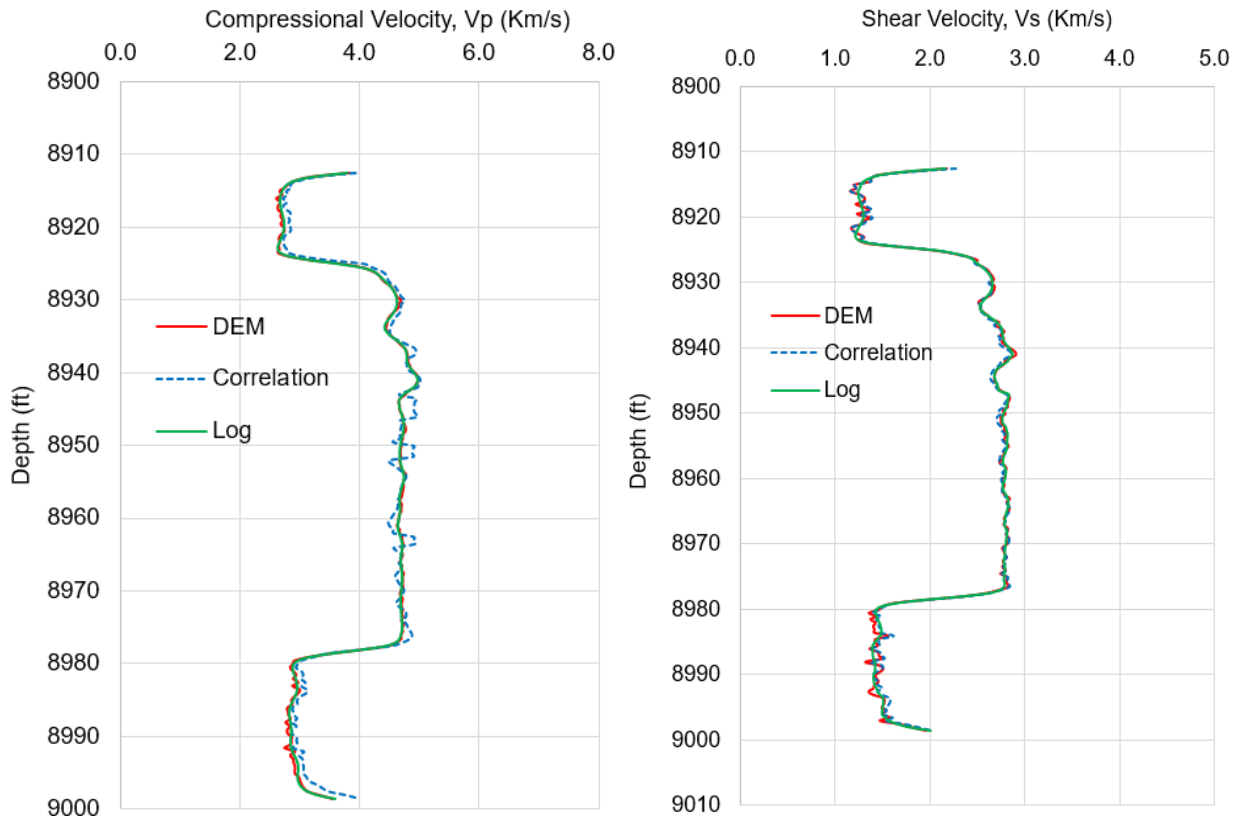
Figure 5.23. Shear velocity ( $V_s$ ) prediction from compressional velocity using Greenberg-Castagna relation, in well #17946.

The results in Figure 5.23 show that, due to their lower water saturations, the UB and LB brine-saturated velocities have large deviation from the velocities with the actual fluid saturation. This large saturation induced deviation is not observed in the MB.

#### 5.2.3.4 Density, Velocities, and Pore’s AR prediction in Well #17946

After obtaining the rock matrix properties, fluid properties, and estimating shear velocity, the DEM model was applied to estimate compressional and shear velocities and match them to the measured

values to obtain the optimum pores aspect's ratio prediction in the Bakken formation of well #17946, following the work by Harju (2022). The results were compared with the output from correlations and the results are shown in Figure 5.24.

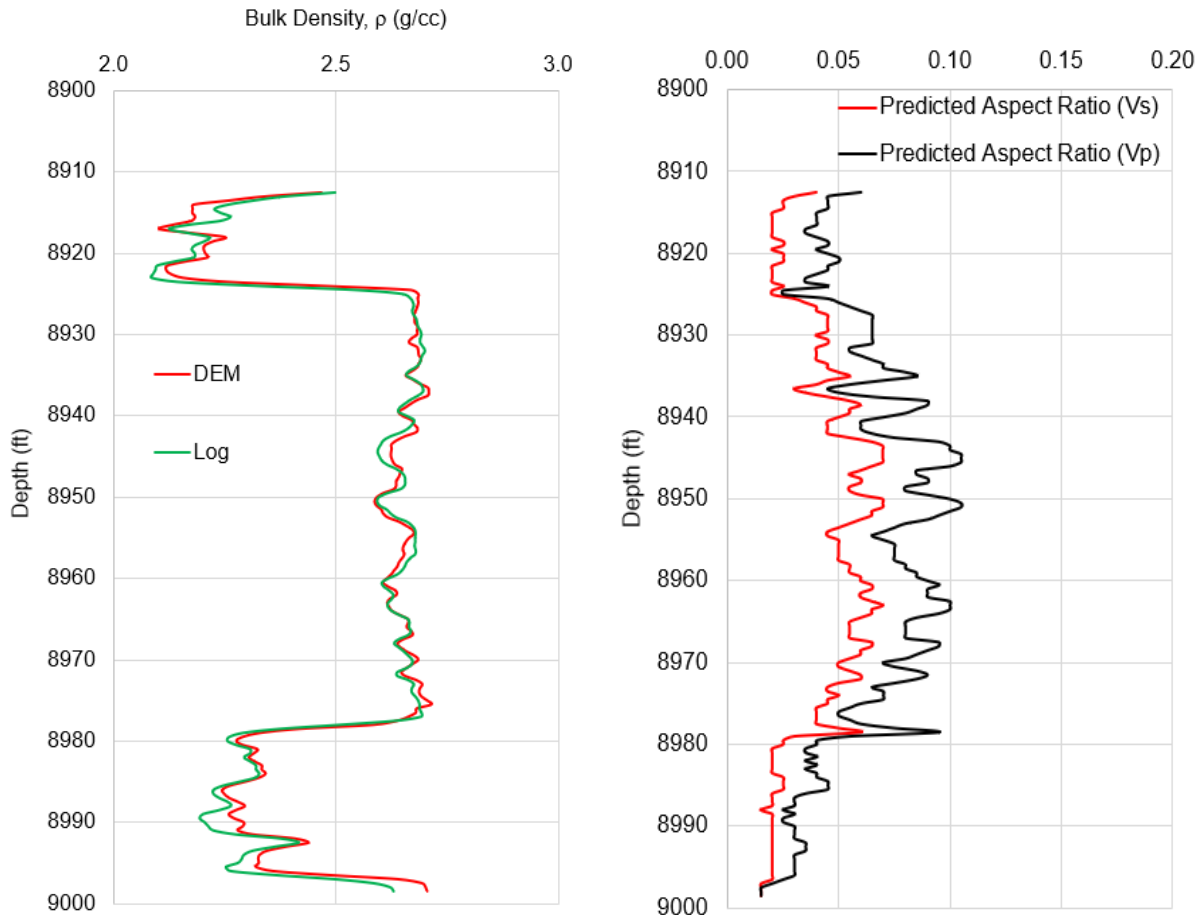


**Figure 5.24.**  $V_p$  (left) and  $V_s$  (right) velocity estimation from DEM model and correlations versus measured log data in well #17946.

The results show a very close match between the correlations, the DEM model, and measured values, especially for the  $V_s$  prediction. The correlations in the UB and LB show better fits to the DEM model results than what were observed in Well #17015 due to lower total porosity (~12%) which reduces the range of deviation due to a reduced porosity effect. This demonstrates the applicability of these correlations, especially at low and medium porosity ranges, for which the correlations were initially developed.



Accurate estimation of the bulk density has a significant effect on the accuracy of predictions of the dominant pore ARs across the Bakken members. Underestimating the density leads to inaccurate prediction of pore AR. Figure 5.25 shows the comparison between the estimated density and the measured bulk density (left) and the predicted pore ARs from both  $V_p$  and  $V_s$  (right) predictions.



**Figure 5.25.** Estimated (red) versus measured (green) bulk density ( $\rho_b$ ) (left) and AR's prediction from both  $V_p$  (black) and  $V_s$  (red) (right) in Well #17946.

The results of Figure 5.25 show a very good estimation of the bulk density when compared with log data. This is due to the accurate estimation of the different elements that contribute to the rock's density, including dry-clay properties (both illite and chlorite), as well as fluid saturations and Kerogen prediction as part of the matrix instead of inclusions (see Section 5.1 and Figure 5.13).

As expected, pore  $AR$ s predicted from  $V_p$  appear to be higher than from  $V_s$ , due to the effect of fluid and several other factors (Harju, 2022). The prediction shows that the LB has a lower  $AR$  compared to UB, which is due to the presence of more cracks in the LB and its brittle nature. This claim agrees with the presence of carbonate minerals in the LB, especially calcite, compared to the UB which has more quartz with mostly intraparticle pore types ( $AR= 0.1$ ). In the upper part of the MB, the presence of carbonates tends to lower the pore  $AR$  compared to the clastic lithology in the lower part of this member.

The above findings are in overall agreement with the thin Section, petrographic description, XRD, and SEM analysis results of core samples of Well #17946 (see Tables 2.8 in Chapter 2 and Appendix B.1).

#### **5.2.4 Well #20552, Muller 1-21-16H**

##### **5.2.4.1 Mineral Composition in Well #20552**

Figure 5.26 shows the variation of mineral volume fractions across the Bakken formation for Well #20552 derived from the ELAN. The results were validated with XRD data and a good match is observed between the mineralogical model and the XRD data.

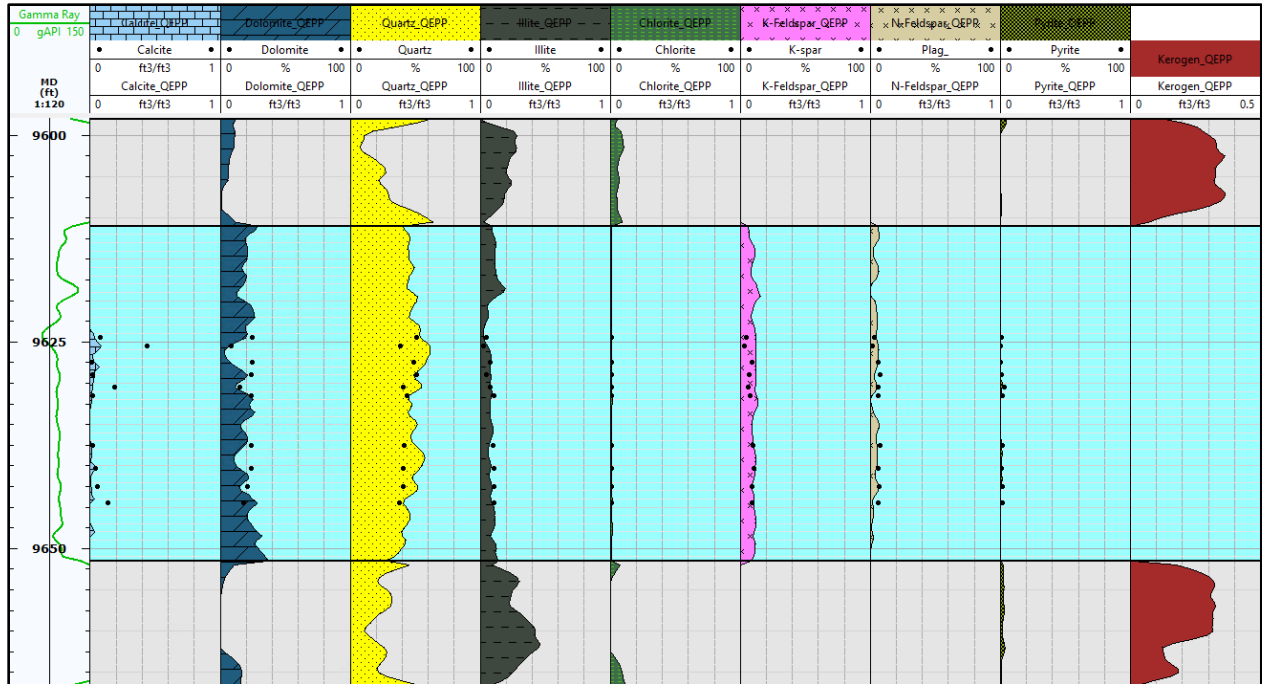


Figure 5.26. Minerals composition of Well #17946 in Grenora field, calibrated with XRD data.

Figure 2.26 shows that this well, compared to Well #17946, exhibits some differences in mineralogy. This well has some dolomite in the UB, much less carbonate (either calcite or dolomite) in LB, and both UB and LB show less quartz content compared to well #17946. The mineralogy information provides valuable information for prediction of the pore ARs in this well and compare with Well #17946. The higher carbonate content (i.e. dolomite) and lower quartz content in the UB will lead to a lower AR in this well. In addition, the Kerogen volume in this well is higher than in Well #17946. This can be an indication of higher oil saturation, lower gas saturation, and the presence of less hydrocarbon in the MB formation (as the main reservoir), as the Bakken members are considered less mature than in Well #17946.

In the MB, this well has less carbonate than Well #17946. In addition, it is seen that, in this well, the carbonates are dominated by dolomite with absence of calcite. Furthermore, this well exhibits larger feldspar content and it is represented by not only potassium-rich, but also sodium-rich

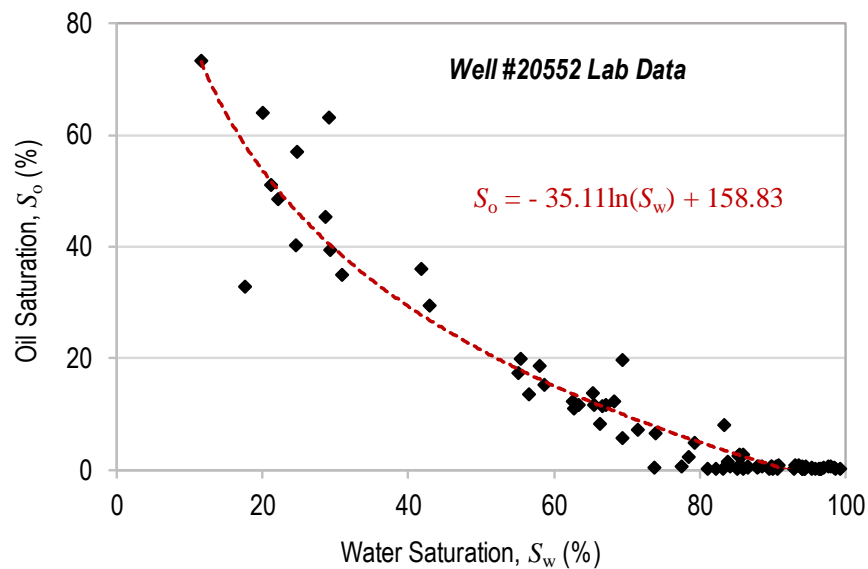
feldspar, which increases the rock's stiffness. Finally, unlike Well #17946, this well shows pyrite traces.

#### 5.2.4.2 Fluids Saturation in Well #20552

Following the workflow for the previous wells, the water saturation was estimated for this well using the modified-Simandoux model. Oil saturation was estimated from its correlation trend with water saturation, which follows a logarithmic function as (also see Figure 5.27):

$$S_o = -35.11 \ln(S_w) + 158.83 \quad (5.12)$$

It is to be noted that the core water and oil saturation data in this well were available for UB and LB as wells as the MB, contrary to well #17946. From Figure 5.27 it is seen that at low water saturation ( $S_w < 5\%$ ), the logarithmic correlation gives abnormal oil saturation values. Therefore, in this case, for simplicity, we assume the hydrocarbon portion as fully-oil saturated.



**Figure 5.27.** Lab data from Well #20552 shows a logarithmic relation between water and oil saturations.

Figure 5.28 presents the water, oil, and gas saturations, fluid density, and bulk modulus from logs. The results show good agreement with core data in all Bakken members.

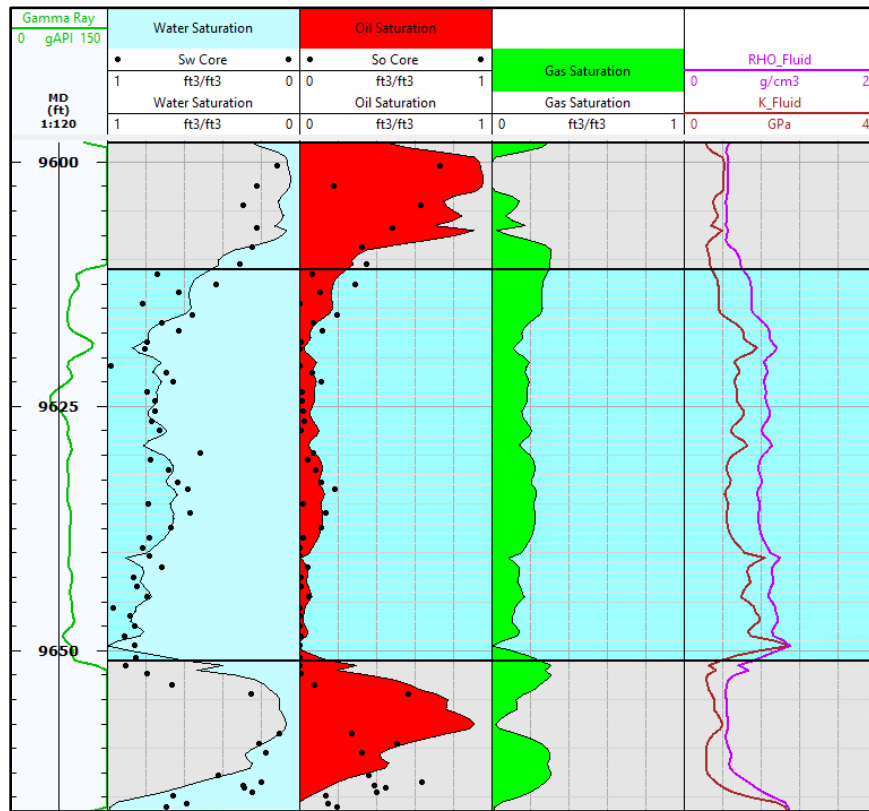


Figure 5.28. Water, oil, and gas saturation predicted for well #20552.

As expected, this well has higher oil saturation in the UB and LB shales than Well #17946 due to relatively lower maturity. Moreover, the water saturation in the reservoir section (MB) is higher which suggests the potential of generating more hydrocarbons after the conversion of Kerogen, as the source-rock (i.e. UB and LB) become more matured.

### 5.2.4.3 Shear Velocity Estimation in Well #20552

There is no shear data available in this well, hence, similar to Well #17946, we used the Greenberg and Castagna (1992) polynomial relation (see equation 5.8) to predict shear velocity ( $V_s$ ) log. In this well, sonic velocity from core data was available and was used to calibrate the predicted log

data. Figure 5.29 shows the compressional velocity log, the predicted shear velocity log and the brine-saturation compressional and shear velocities, calibrated with core data for this well.

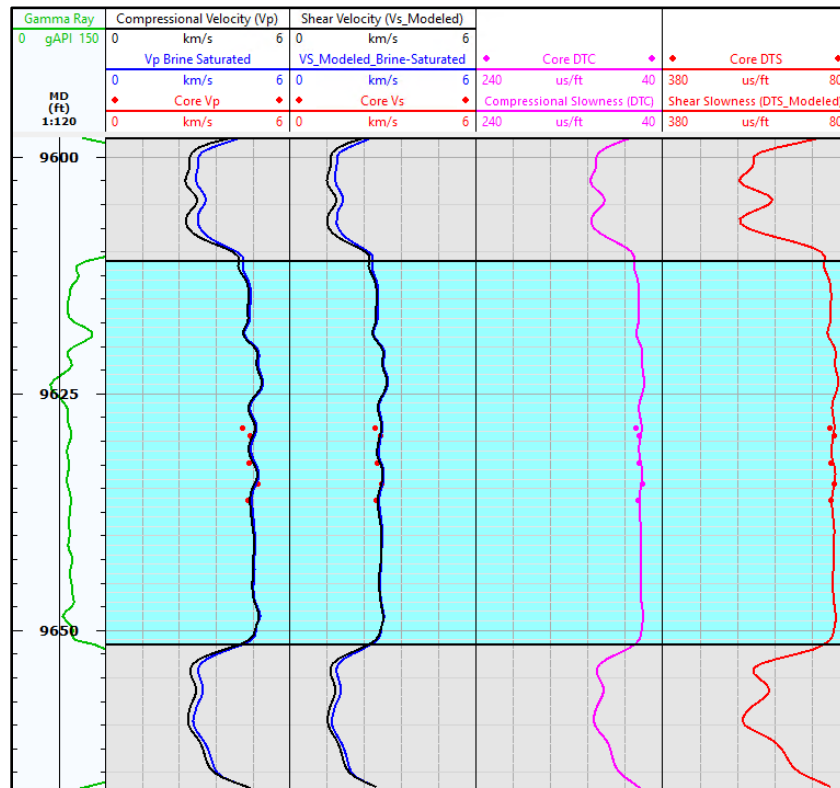
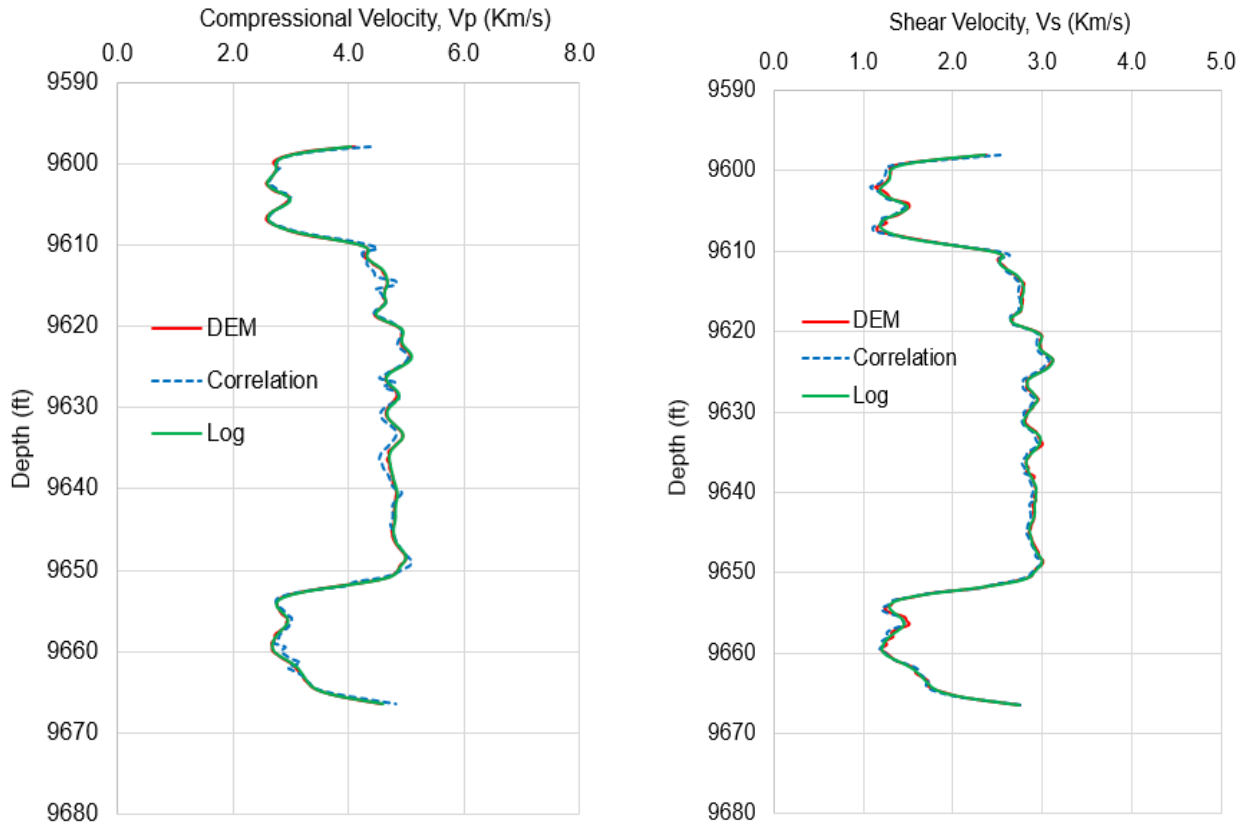


Figure 5.29. Shear velocity (Vs) prediction from compressional velocity using Greenberg-Castagna relation, in well #20552.

The results in Figure 5.29 show a very close match between the predicted shear velocity and core data. Furthermore, it is observed that the difference between brine-saturated and fluid-saturated predictions is very small in the MB formation due to the higher water saturation compared to Well #17946, where the difference between brine and fluid saturated velocities are significant. The difference is similarly smaller in the UB and LB because of relatively higher water content and hydrocarbon is oil dominated in this well.

5.2.4.4 Density, Velocities, and Pore AR Prediction in Well #20552

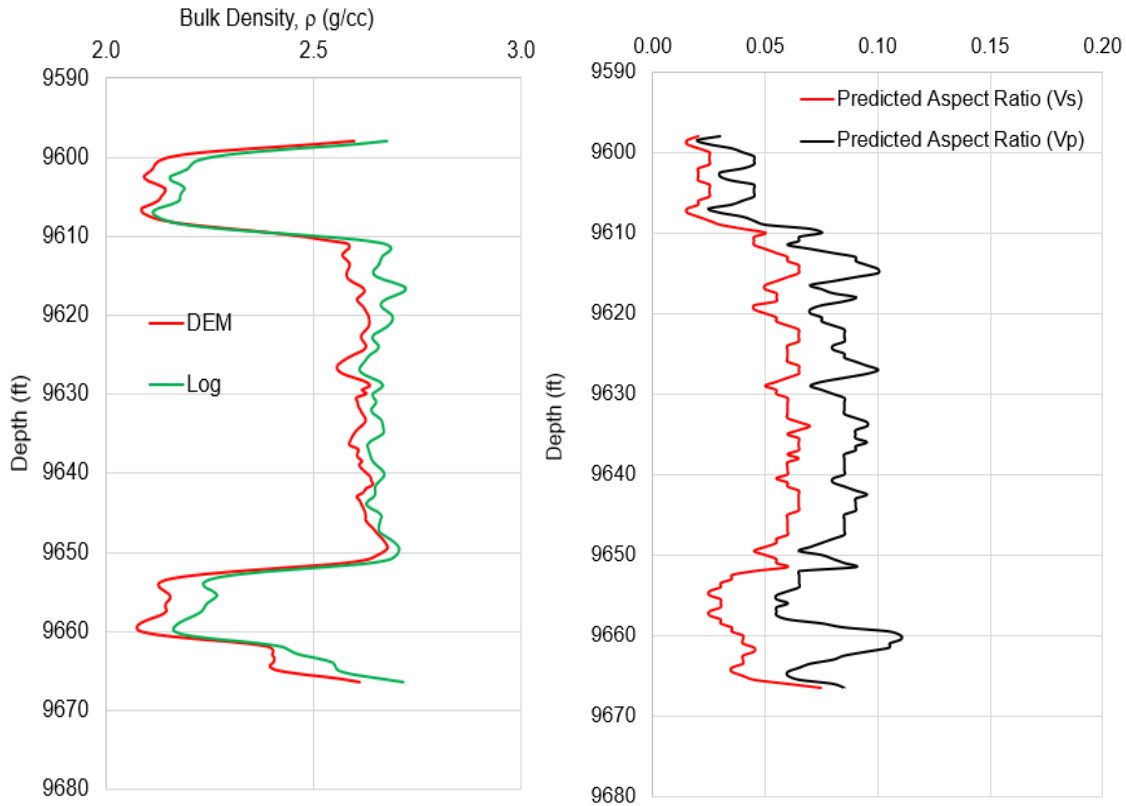
Similar to the previous wells, the velocity profiles for Well #20552 were predicted from the DEM model and developed correlations. The results, together with measured  $V_p$  and  $V_s$  logs are presented in Figure 5.30.



**Figure 5.30.**  $V_p$  (left) and  $V_s$  (right) velocity estimation from DEM model and correlations versus measured log data in well #20552.

The results show a good match between the DEM model and correlations across all the Bakken members, demonstrating the accuracy of the correlations to predict velocities in different type of formations.

The predicted bulk density and ARs for this well are shown in Figure 5.31. The difference in the pore geometry when compared to the previous well is affected by lithology, fluid properties, and maturity level.



**Figure 5.31.** Estimated (red) versus measured (green) bulk density ( $\rho_b$ ) (left) and ARs prediction for both  $V_p$  (black) and  $V_s$  (red) (right) in well #20552.

The results in this Figure show some deviations in the estimated bulk density when compared to the measured values (left), however the overall match is good. The observed discrepancy in some intervals is, partially, due to eliminating some minerals with small volume fractions (less than 2%) in the ELAN workflow. The uncertainties related to the fluid estimation may also contribute to this difference.

In the MB formation, the upper portion of Well #17946 has a very high-volume fraction of carbonate and lower quartz content compared to this well. The abundance of quartz leads to dominance of intraparticle pores ( $AR=0.1$ ) which results in the increase of pore  $AR$ . In addition, dolomite is dominant in the carbonate content of Well #20552. The dolomitization of carbonate minerals means its recrystallization, resulting in larger crystals (oid), but stiffer minerals



(cementation effect). Lower carbonate and dolomitization are the reasons for higher pore *ARs* predicted in this well compared to Well #17946. The high presence of feldspars in this well compared to Well #17946 also led to larger pore *AR* prediction. In short, the upper intervals of the MB formation in Well #20552 exhibit larger pore *ARs* than well #17946 with higher presence of intraparticle porosity replacing the intergranular or crack pores. Moreover, there are some differences in the middle and bottom parts of the MB due to lithology and fluid effects.

In both wells, the UB shows some similarities in the pore morphology due to close mineral composition represented by the absence of carbonate. However, Well #20552 has slightly smaller pore *ARs* in the UB formation due to the Kerogen effect and low presence of brittle minerals (i.e. dolomite) compared to Well #17946, which does not have any dolomite.

The above findings are in overall agreements with the thin Section, petrographic description, XRD and SEM analysis results of core samples of Well #20552 (see Tables 2.9 in Chapter 2 and Appendix B.2).

## **5.2.5 Well #20844, Rasmussen 1-21-16H**

### **5.2.5.1 Minerals Composition in Well #20844**

Figure 5.32 shows the variation of mineral volume fractions across the Bakken formation in well #20844 derived from the ELAN workflow. The mineralogy is compared to the XRD data and the results show a good match between the developed mineralogical model and the XRD data. The Kerogen volume computed from the ELAN shows a good fit to the computed TOC content using Passey's (1990) method. The available TOC lab data in this well also shows a similar trend to the Kerogen volume.

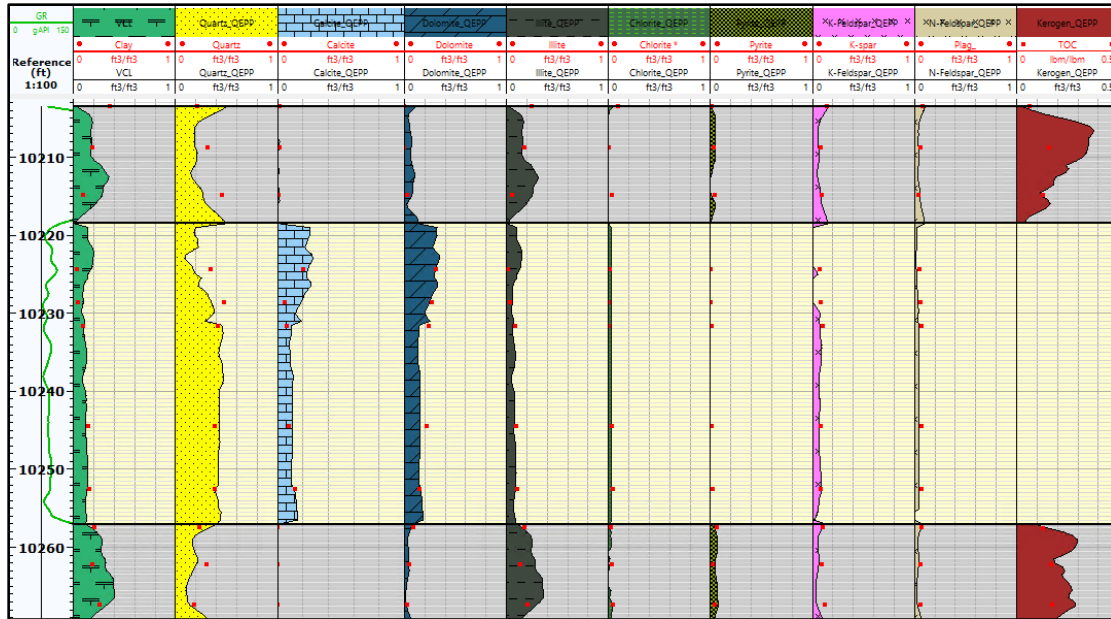


Figure 5.32. Mineral composition of Well #20844, calibrated with XRD and TOC data.

From Figure 5.32, it is seen that the computed mineralogical model provides a good match with the XRD data in the MB. However, there are some uncertainties in the UB and LB shales that can potentially affect the accuracy of the final results. For example, and as will be discussed later, shale was overestimated at some intervals of the Bakken while the quartz volume fraction is underestimated versus the lab data. Alternatively, the estimated Kerogen volume may be slightly overestimated when compared to TOC data.

Overall, the UB and LB shales are dominated by clay minerals, or more precisely, by illite and quartz. Carbonate abundance is very small in both UB and LB, with slightly higher content in the UB compared to the LB. These carbonates are represented by dolomite mineral with a total absence of calcite. Well #20844 also has a considerable amount of feldspars and more traces of pyrite.

Regarding the MB formation, similar to most wells in the Bakken, the top part is dominated by carbonates while higher quartz volume is observed in the middle and bottom intervals of the MB formation.

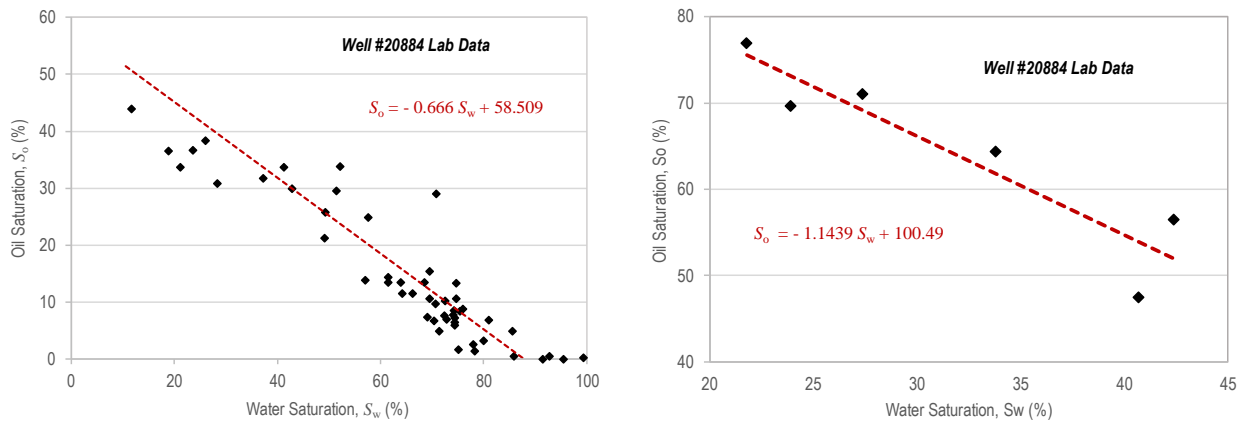
5.2.5.2 Fluids Saturation in Well #20844

A similar workflow to the one used for the previous wells was adopted here to estimate different fluid saturations. However, in this well, two different linear correlations were established to better characterize the fluid fractions. The following relationship between water and oil saturation was observed for the MB formation (see Figure 5.33, left):

$$S_o = -0.6609 S_w + 59.063 \tag{5.13}$$

The second correlation showed a good fit to the UB and LB formations based on the core data (see Figure 5.33, right):

$$S_o = -1.1439 S_w + 100.49 \tag{5.14}$$



**Figure 5.33.** Lab data from Well #20844, showing linear relationships between water and oil saturation in the MB (left) and UB and LB shales (right).

Gas saturation was calculated as  $S_g = 1 - S_w - S_o$ . Figure 5.34 shows the water, oil, and gas saturation profiles and the total and effective porosities, in addition to the fluid properties (density and bulk modulus). The results show good agreement with the core data.

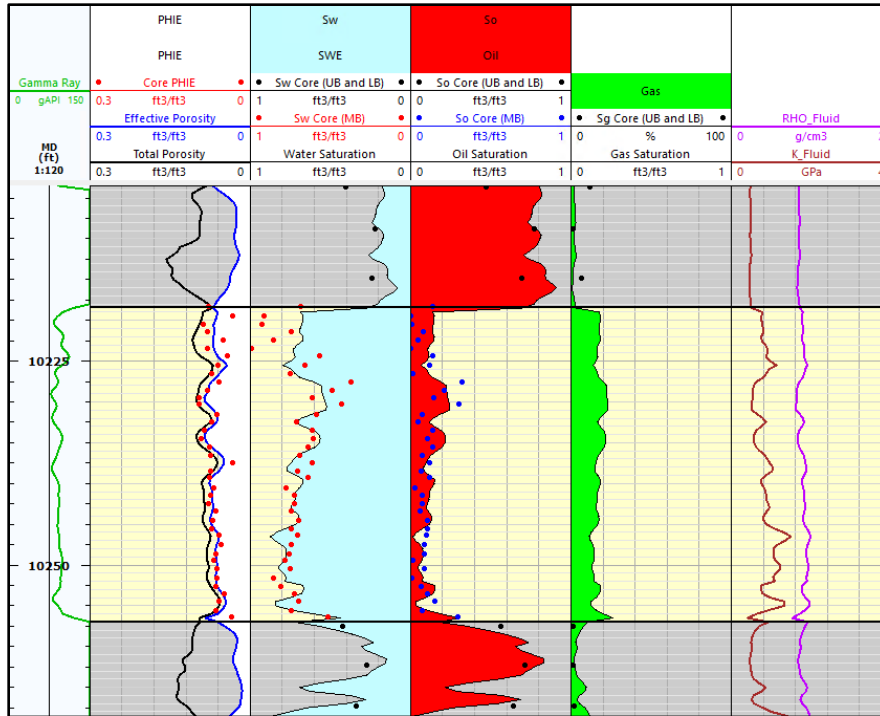
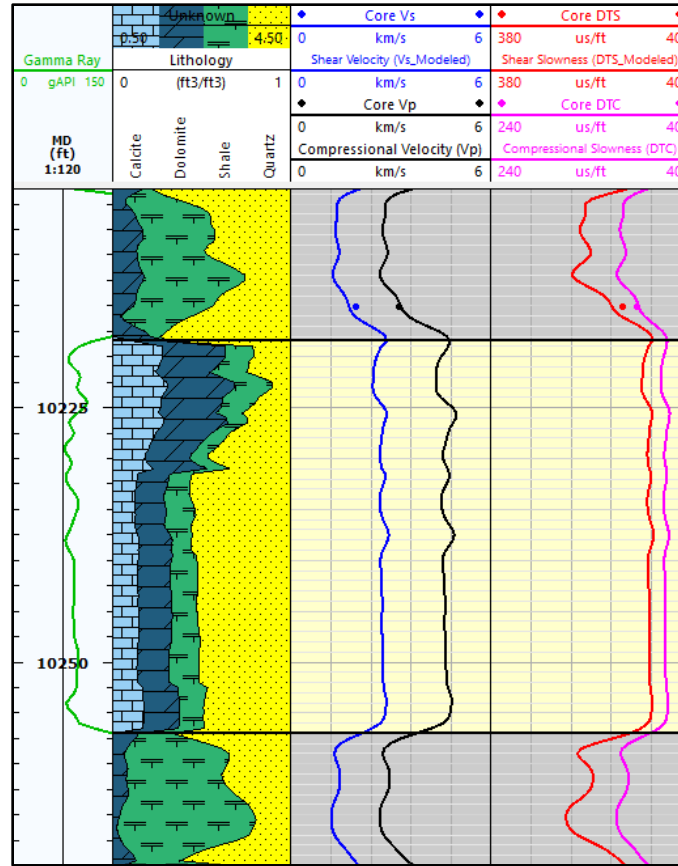


Figure 5.34. Water, oil, and gas saturation predicted for well #20844.

In this well, the bound water (difference between total and effective porosities) in the UB and LB members may be overestimated due to overprediction of shale content. This can slightly affect the fluid properties, as well as bulk density, in the shale members. Furthermore, similar to Well #20552, the water saturation in this well is relatively higher than that of Well #17946, while the Kerogen volume is higher (less mature). This explains the reason for low hydrocarbon content, in general, and the small gas content, in particular.

### 5.2.5.3 Shear Velocity Estimation in Well #20844

Similar to the previous two wells, the Greenberg-Castagna model was applied in this well to estimate shear velocity as a function of compressional velocity. The existing sonic core data in this well was used to calibrate the model. The measured compressional and shear velocities and slownesses are illustrated in Figure 5.35.

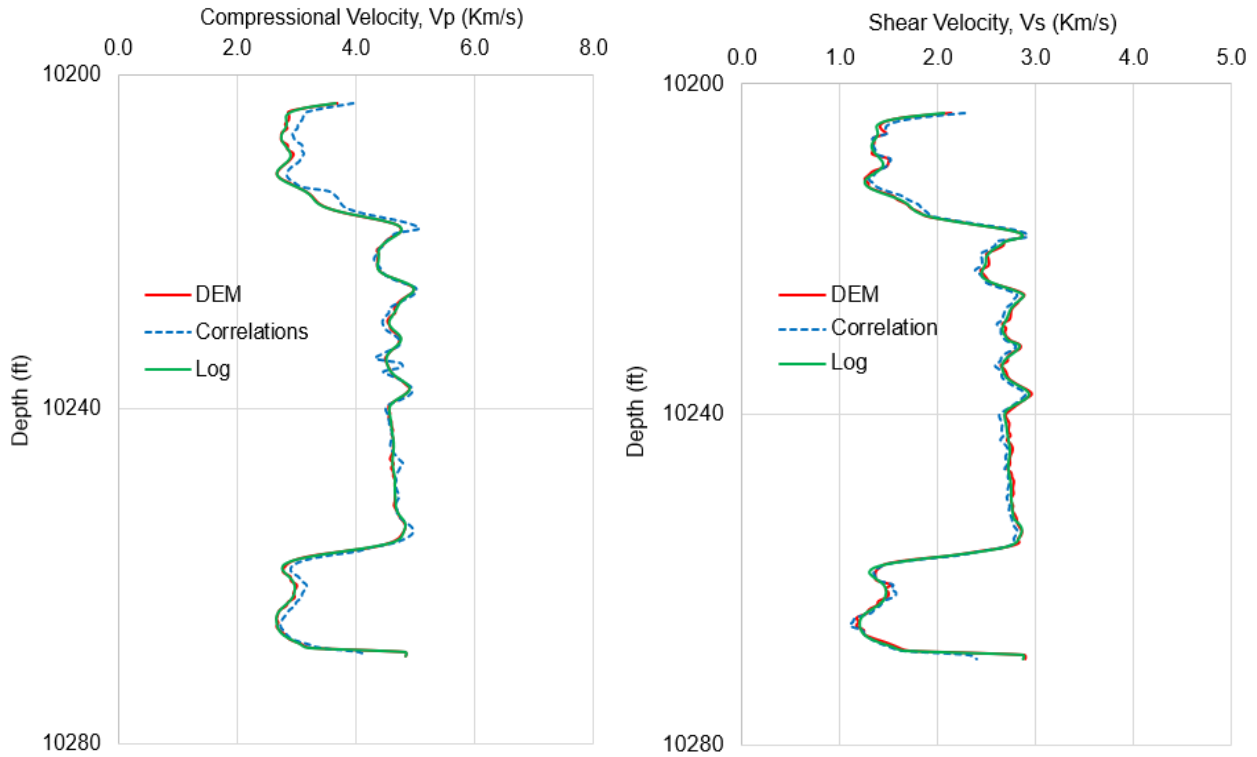


**Figure 5.35.** Shear velocity ( $V_s$ ) prediction from compressional velocity using Greenberg-Castagna relation, in Well #20844.

The shear velocity is well-predicted in the MB formation, but slightly underestimated in the the UB and LB. This is potentially caused by the overestimation of shale and underestimation of quartz, respectively, that may affect the lithology concentration which, in turn, will contribute to some uncertainties in the pure mineral regression coefficients. This justifies the small deviation from the core data shown in the UB member.

#### 5.2.5.4 Density, Velocities, and Pore's AR Prediction in Well #20844

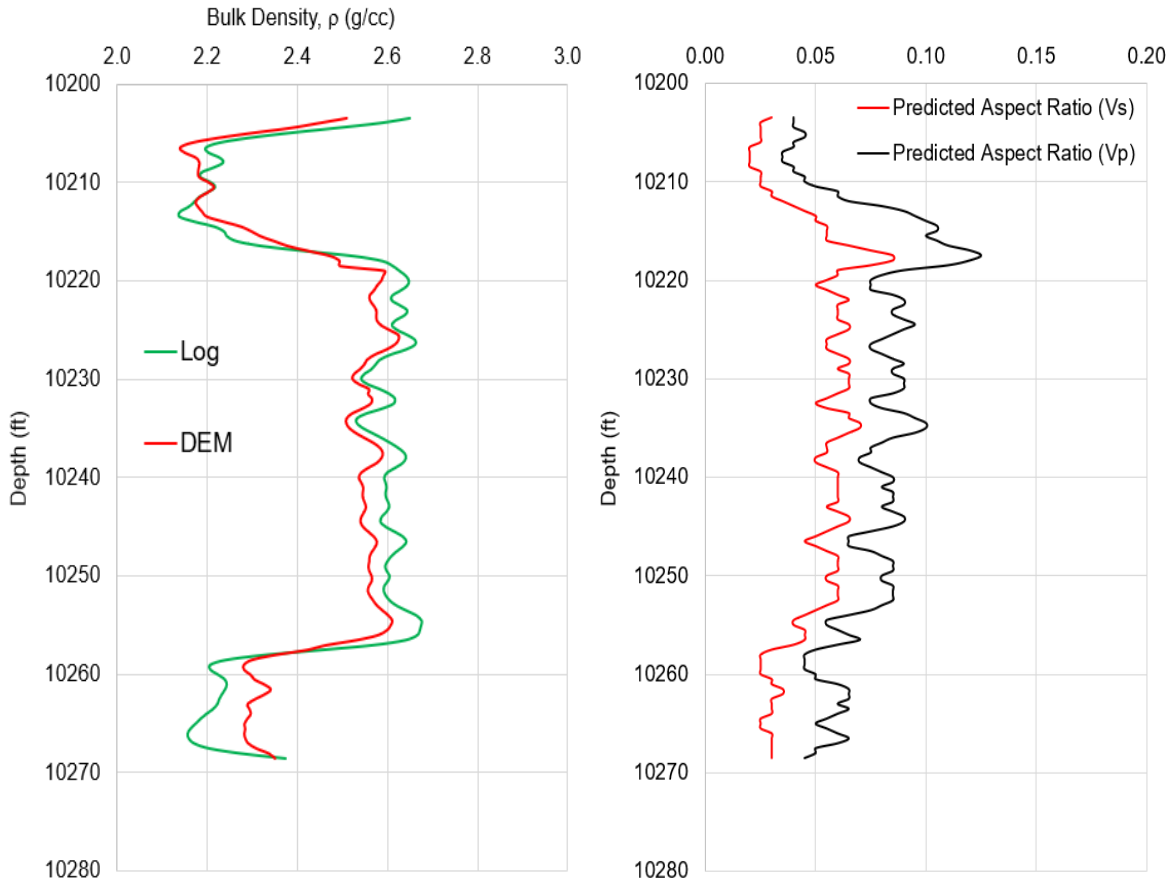
Similar to previous case studies, the velocities were predicted from the DEM model and developed correlations and compared with the measured  $V_p$  and  $V_s$  logs. The results are shown in Figure 5.36.



**Figure 5.36.**  $V_p$  (left) and  $V_s$  (right) velocity estimation from DEM model and correlations versus measured log data in Well #205844.

The results again demonstrate the efficacy of the developed correlations to reproduce the DEM model results at any given porosity, fluid saturation, and pore's  $AR$ .

The predicted bulk density and pore  $AR$ s in this well are illustrated in Figure 5.37. The difference in the pore geometry when compared to the previous well is due to differences in lithology, fluid properties, and maturity.



**Figure 5.37.** Estimated (red) versus measured (green) bulk density ( $\rho_b$ ) (left) and pore AR prediction from both  $V_p$  (black) and  $V_p$  (red) (right) in Well #20844.

As expected, the estimated bulk density shown in this Figure (left) overestimates the measured density in the LB due to the uncertainties in mineralogy. Overestimation of illite and underestimation of quartz led to the density differences as the dry illite density is around 2.75 g/cc compared to the density of quartz which is 2.65 g/cc. Except for these outliers, the density prediction shows an acceptable match to the measured values.

AR predictions in the UB shale member show that the estimated pore geometry corresponds to a mixture of intergranular, intraparticle, and to a lower extent it contains cracks. Interestingly, it can be seen that the pore AR increases with depth in the UB and the pore geometry becomes intraparticle dominated. This can be related to the increase of quartz and feldspar volumes in the

lower part of the UB and the decrease in Kerogen content that leads to the stiffening of the estimated velocity. The pore morphology in the MB is a mixture of intergranular and intraparticle pore types. The LB shows mainly intergranular pores with an *AR* of close to 0.5. The pore *AR* shows some intraparticle pores ( $AR=0.1$ ) and this trend follows the quartz and feldspar abundance.

The above findings are in overall agreement with the thin Section, petrographic description, XRD and SEM analysis results of core samples of Well #20844 (see Tables 2.10 in Chapter 2 and Appendix B.3).

### **5.3 Summary**

In this Chapter, we presented the results of four case studies. The first well, is located in Mountrail County and the other three wells located in the Grenora field. The results demonstrated overall that the developed correlations can provide a close estimation of velocity to the DEM model. The estimations are better for lower pore aspect ratios, as the initial Bakken data which was used to develop these correlations represent low pore aspect ratios. Also, the interpretation of the results indicates the importance of having a good knowledge of the mineralogy, fluid saturation, Kerogen content and volume fraction of different minerals in order to make more reliable and accurate predictions of density and velocity.



# CHAPTER 6

## Conclusions and Recommendations

In this research study, velocity-porosity correlations were developed for the Bakken formation members as a function of fluid saturation and pore geometry. The correlations were developed from numerous simulation data of the Differential Effective Medium (DEM) model, an inclusion-based rock physics model.

The first Section of this Chapter lists the main conclusions drawn from this work and the second Section presents some recommendations for future work as a continuation of this study.

### 6.1 Conclusions

From this study the following general conclusions are drawn:

- Rock physics models can provide an estimate of formations elastic properties based on physics-based theories. The estimations are based on the velocity measurements at different scales.
- Several empirical based velocity-porosity correlations have been proposed for different types of formations as function of various parameters. However, these correlations are specific to a specific field and conditions. In contrast, the rock physics models have been developed based

on fundamental concepts such as the interaction of rock and fluid and they integrate the rock physics into the calculations. This makes them more reliable and generalizable.

- Inclusion-based rock physics models have gained recognitions in the oil and gas industry due to the fact that they include the effect of pore geometry and fluid type in their workflow. Among different models, the differential effective medium (DEM) theory has a wider range of applications and was used in this study for the purpose of developing velocity-porosity correlations for the Bakken formation.
- The velocity-porosity correlations developed in this study, which are based on the data from several DEM based models, show a close agreement with the DEM model. The correlations include the effect of fluid saturation (water, oil and gas) as well as pore aspect ratio ( $AR$ ). It was observed that the trend of change of porosity versus velocities are different for pore aspect ratios of less than 0.1 than for larger aspect ratios. Therefore, the correlations were presented separately for  $AR < 0.1$  and  $AR \geq 0.1$ .
- It was shown that the velocity-porosity relations from the DEM model follow in general an exponential trend. For lower  $AR$  values, the slope is steep and it gradually reduces to the point that for  $AR$ s larger than approximately 0.5, the plots become linear. The exponential trend of velocity-porosity has been reported from lab and field data and is frequently used in the Petroleum Engineering applications.
- It was discussed that changing the Brie coefficient ( $e$ ) to calculate fluid mixing, makes it possible to capture the effect of patchy (heterogeneous) and homogeneous fluids. The closer the Brie coefficient is to 1, the more homogeneous the fluid and more representative of higher frequencies, corresponding to the log scales. Larger values of  $e$  represent more patchy fluids, corresponding to lower frequencies and seismic scale. In practice, and as was demonstrated in

this work,  $e=3$  maybe a good average number to represent field scale applications and changing  $e$  from this value will not affect the results significantly. Therefore, in this study, Brie coefficient was set to 3 to simplify the correlations.

- In order to estimate the velocity from the developed correlations, similar to any other studies, the quality and reliability of the input data are very important. The water, oil and gas saturation, as well as the kerogen volume in shale formations should be calculated using the most applicable petrophysical methods. Also, access to XRD lab data and ECS logs are important to determine the mineral volume fractions. If required, the petrophysical elemental analysis (ELAN) needs to be conducted to estimate the mineral composition.
- The results of different case studies presented in Chapter 5 showed the importance of considering variable fluid saturations at different depths for calculating the velocity and elastic properties of formations. The ternary plots visually present the change of properties as a result of changing the fluid saturations.
- It is very important to distinguish between wet-illite and dry-illite in modeling. The results of this study showed that the type of illite assumed affects illite density, which can result in an increase in estimated velocity, which corresponds to higher  $AR$  prediction. If the total porosity is used for the inclusion material, it already includes bound water. Therefore, it is more appropriate to consider dry-illite properties in modeling if using the total porosity instead of effective porosity. Also, modeled density considering dry, instead of wet illite, gives a better match with measured density and core data.
- To include the effect of Kerogen, in this study, we treated it as one of the minerals in the shale sections of the UB and MB members and used the developed correlation constants for Kerogen to include its impact on total velocity. The results indicate that the Passey method presents a

closer agreement with the DEM model and log data. Considering Kerogen as part of the matrix lowers the density, as opposed to adding its effect as a mix to the fluid phase.

- From the results of studies of Well #17015, it was found that crack/intraparticle (crack dominated) pore types are expected in the UB and LB shales as well as the carbonate section of MB. However, intraparticle/crack (intraparticle dominated) pore types are mostly observed in the MB clastic zone. While there were no thin sections or SEM images to validate these findings, the mineral composition from the ECS logs shows that the UB and LB, that are well-known for their brittle nature and their heterogeneity, are mostly clay and quartz with no presence of carbonate. Siliciclastic pore geometry is most likely intraparticle. However, with the presence of anhydrite and the lenticular texture of clays, we expect a minor presence of crack type pores in the UB and LB shales. This can probably be adjusted by including the effect of Kerogen or by utilizing dry-illite properties. In the MB formation, the deviation of the *AR* from the different models is reduced, especially in the Carbonate portion, because of the low porosity which makes the fluid less significant compared to UB and LB where total porosity is high.
- In cases where shear velocity logs are not available, in complex lithologies such as the Bakken formation, the use of the Greenberg and Castagna (1992) correlation is a commonly used model. The method is based on deriving polynomial  $V_p - V_s$  relations in pure lithologies (limestone, dolomite, sandstone, and shale), then  $V_s$  in the multimineral lithology formation is estimated by averaging the arithmetic and harmonic means of the shear velocities of the pure lithologies.
- From the results of the four studied wells, it is seen that, in general, UB and LB are mainly composed of clays and quartz minerals. Although carbonates are almost absent from the UB,

the LB exhibits the presence of some carbonate. The MB can be divided into two subzones. The upper part is mainly carbonate with an abundance of calcite minerals, whereas, the lower part is rich in clastic and quartz minerals. The total amount of carbonate in the lower part is reduced due to reduction in calcite whereas dolomite content remains almost the same as in the upper carbonate section.

- The fluid saturation calculations showed that well #17015 in Mountrail County is gas dominated. The Rock-Eval pyrolysis data in some wells from Grenora field showed that the area is less mature compared to Mountrail County. Therefore, Kerogen content is higher with higher potential of cracking and conversion into hydrocarbon (Kerogen is in late phase of type II), as opposed to Kerogen of type II/III and type III in Mountrail County. This also explains the reason for lower total porosity, as early mature wells do not generate any maturity-induced porosity, which is usually generated from the cracking of Kerogen and conversion into bitumen.
- Pore  $AR$ s predicted from  $V_p$  appear to be higher than  $V_s$ , due to primarily to the effect of fluid along with several other minor factors.
- For the studied wells, prediction of pore  $AR$ s showed that the LB has lower  $AR$ s compared to UB, which is due to the presence of more cracks in the LB and its brittle nature. This claim agrees with the presence of carbonate minerals in the LB, especially calcite, while the UB has more quartz with mostly intraparticle pore types ( $AR= 0.1$ ). In the upper part of the MB, the presence of carbonates tends to lower the pore  $AR$  compared to the clastic lithology in the lower part of this member.
- Predicted pore  $AR$  in the UB shale member shows that the estimated pore geometry corresponds to a mixture of intergranular, intraparticle, and to a lower extent, cracks.

Interestingly, it can be seen that the pore  $AR$  increases with depth in the UB and the pore geometry becomes intraparticle dominated. This can be related to the increase of quartz and feldspars volumes in the lower part of the UB and the decrease in Kerogen content that leads to the stiffening of the estimated velocity. The pore morphology in the MB is a mixture of intergranular and intraparticle pore types. The LB shows mainly intergranular pores with an  $AR$  close to 0.5. The pore  $AR$  shows some intraparticle pores ( $AR=0.1$ ) as this trend follows the quartz and feldspar abundance.

## 6.2 Recommendations

There are several lines of new research ideas that can be followed as the continuation of this research study. Some of these ideas are presented here.

- This study was mainly focused on correlation applications for the Bakken shale formation. The correlations were developed based on the mineral properties of the Bakken. While we expect that the range of properties should not deviate significantly in other formations, it would be interesting to test the accuracy and applicability of the correlations in other formations.
- To calculate the average rock velocity in this study, we used the simple averaging method, equivalent to the Hill model. This seemed to provide a reasonable match when compared to the lab and log data. However, it would be a good project to explore the use of different averaging methods, especially in cases where the results are not in reasonable agreement with lab or log data.
- While we used a constant Brie coefficient of  $e=3$  in this study with some reasonable justifications, a good project would be to use different values to investigate in further detail the effect of fluid type (i.e. homogeneous versus patchy) on rock properties, especially in higher porosities where it is considered to be an important factor in a given formation.



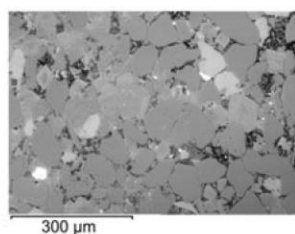

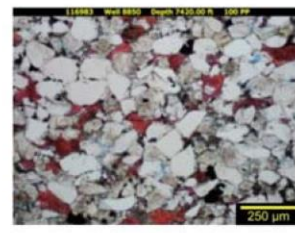
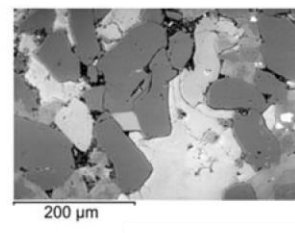

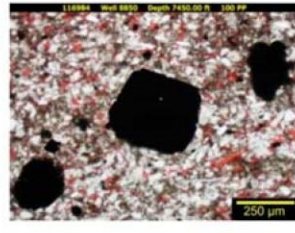
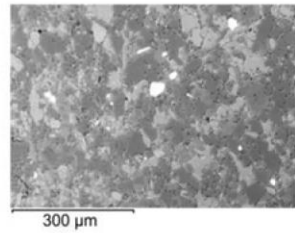
- Replacing the Brie fluid mixing model with Gassmann's fluid substitution and comparing the results of correlations, is another potential continuation of this study.

APPENDIX A



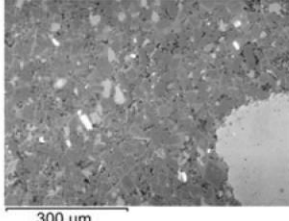

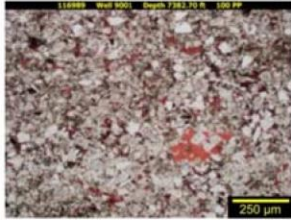
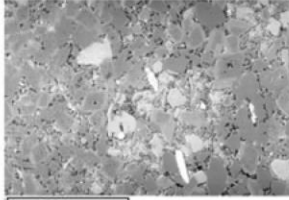

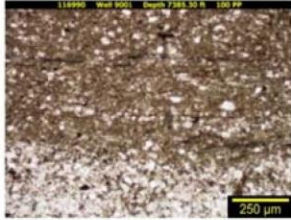
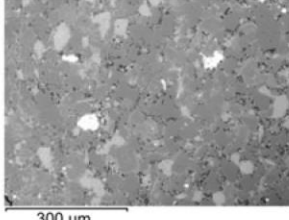
Depth, ft	Core Sample	Thin Section, 100x PP	SEM Image	Lithofacie/ Lithology
7397.5				L7 Silty Dolostone
7400.8				L6 Silty Dolostone
7407.3				L5 Dolomitic Siltstone
7410.0				L4 Dolomitic, Argillaceous Siltstone

Figure A.1. Images and brief description for Lithofacies L1 to L7 in NDIC Well No. 8850. Depths shown indicate the depth from which each sample was obtained (continued).



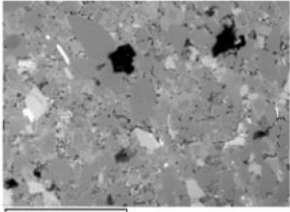


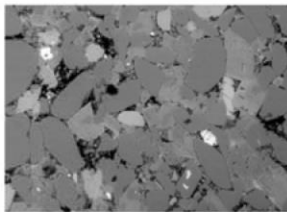

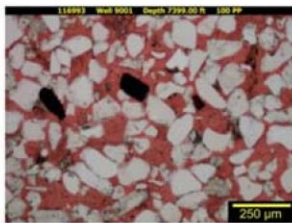
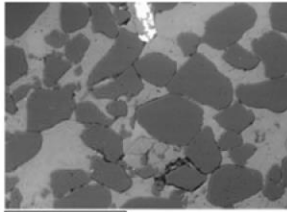

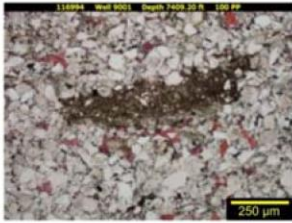
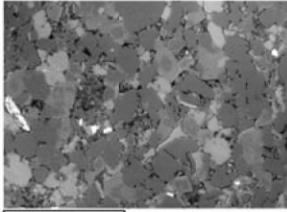


Depth, ft	Core Sample	Thin Section, 100x PP	SEM Image	Lithofacie/ Lithology
7412.5				L3 Dolomitic Siltstone
7420.0				L2 Calcareous to Dolostone Siltstone
7450.0				L1 Calcareous, Argillaceous Siltstone



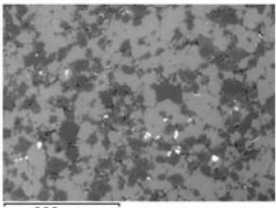
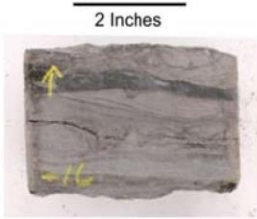

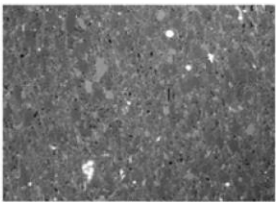

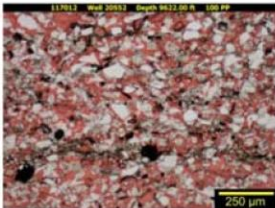
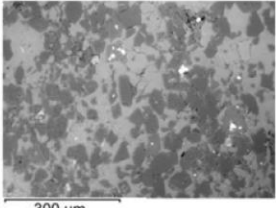

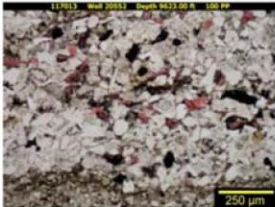
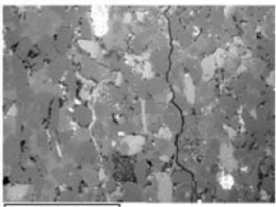
**Figure A.1.** (continued). Images and brief description for Lithofacies L1 to L7 in NDIC Well No. 8850. Depths shown indicate the depth from which each sample was obtained.

Depth, ft	Core Sample	Thin Section, 100x PP	SEM Image	Lithofacie/ Lithology
7381.0				L7 Silty, Argillaceous Dolostone
7382.7				L6 Argillaceous, Silty Dolostone
7385.3				L5 Argillaceous, Dolomitic Siltstone


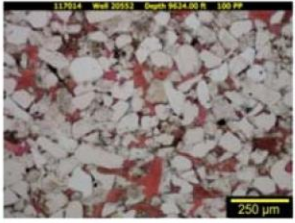
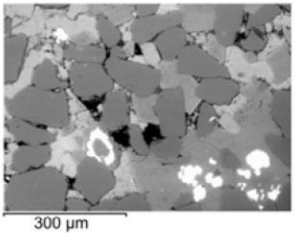

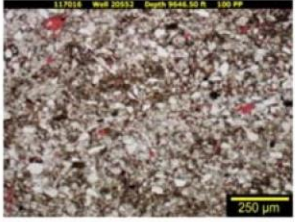
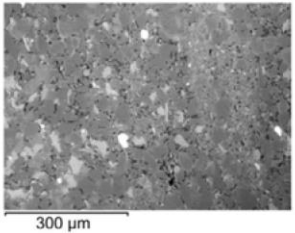
**Figure A.2.** Images and brief description for Lithofacies L1 to L7 in NDIC Well No. 9001. Depths shown indicate the depth from which each sample was obtained (continued).

Depth, ft	Core Sample	Thin Section, 100x PP	SEM Image	Lithofacie/ Lithology
7392.4				L4 Argillaceous, Dolomitic Siltstone
7394.8				L3 Dolomitic Siltstone
7399.0				L2 Calcareous Siltstone
7409.2				L1 Argillaceous, Dolomitic Siltstone

**Figure A.2.** (continued). Images and brief description for Lithofacies L1 to L7 in NDIC Well No. 9001. Depths shown indicate the depth from which each sample was obtained.


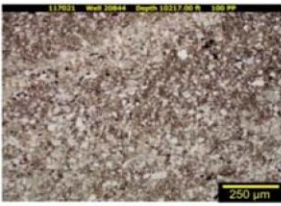
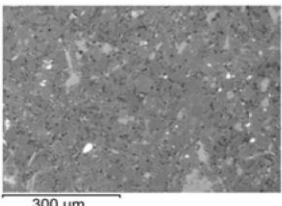

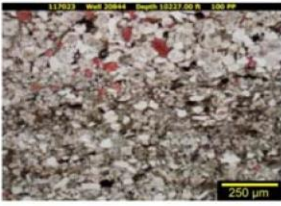
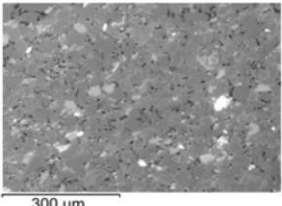


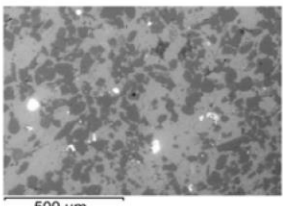
Depth, ft	Core Sample	Thin Section, 100x PP	SEM Image	Lithofacie/ Lithology
9613.0				L8 Slightly Silty, Argillaceous Limestone
9616.0				L8 Silty, Argillaceous Dolostone
9622.0				L5 Argillaceous, Silty Limestone
9623.0				L5 Silty, Dolostone

**Figure A.3.** Images and a brief description of lithofacies characterized by the EERC in NDIC Well No. 20552. Depths shown indicate the depth from which each sample was obtained (continued).

Depth, ft	Core Sample	Thin Section, 100x PP	SEM Image	Lithofacie/ Lithology
9624.0				L4 Calcareous Siltstone
9646.5				L1 Calcareous, Argillaceous Siltstone


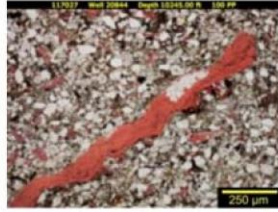
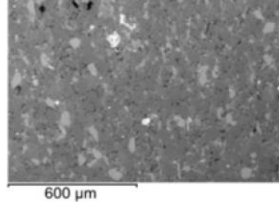


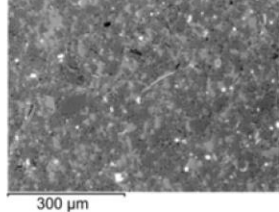
**Figure A.3.** (continued). Images and a brief description of lithofacies characterized by the EERC in NDIC Well No. 20552. Depths shown indicate the depth from which each sample was obtained.

EERC JS47792.CDR

Depth, ft	Core Sample	Thin Section, 100x PP	SEM Image	Lithofacie/ Lithology
10217.0				L7 Silty Dolostone
10227.0				L5 Argillaceous, Dolomitic Siltstone
10237.0				L3 Calcareous Siltstone

**Figure A.4.** Images and a brief description of lithofacies characterized by the EERC in NDIC Well No. 20844. Depths shown indicate the depth from which each sample was obtained (continued).

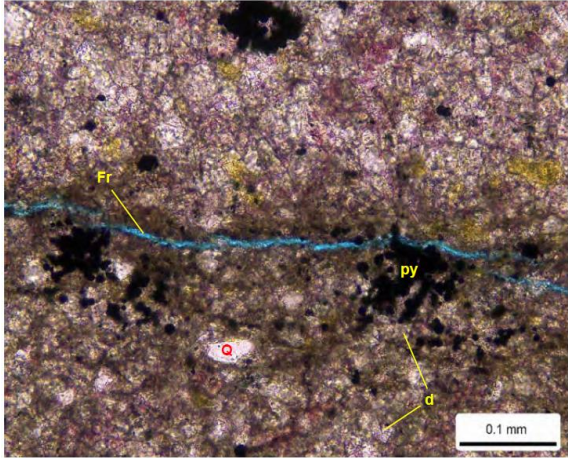
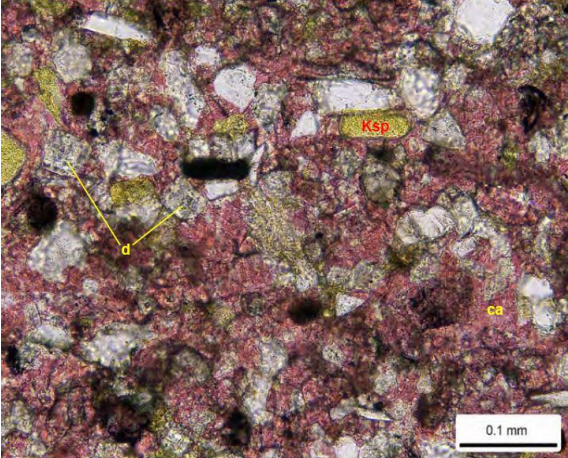
EERC JS47793.CDR

Depth, ft	Core Sample	Thin Section, 100x PP	SEM Image	Lithofacie/ Lithology
10245.0				<p>L2 Slightly Calcareous, Dolomitic Siltstone</p>
10256.0				<p>L1 Silty, Calcareous Mudstone</p>

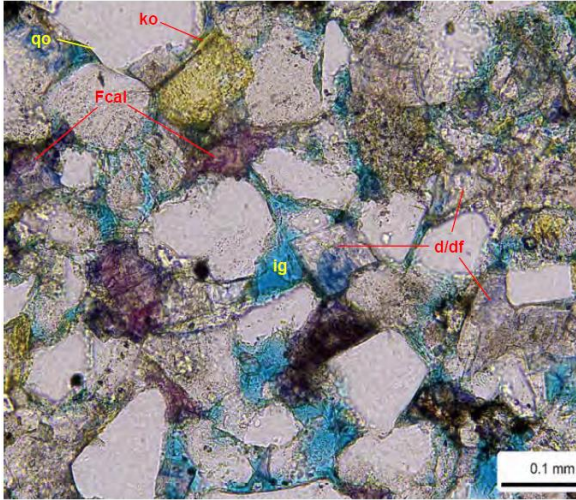
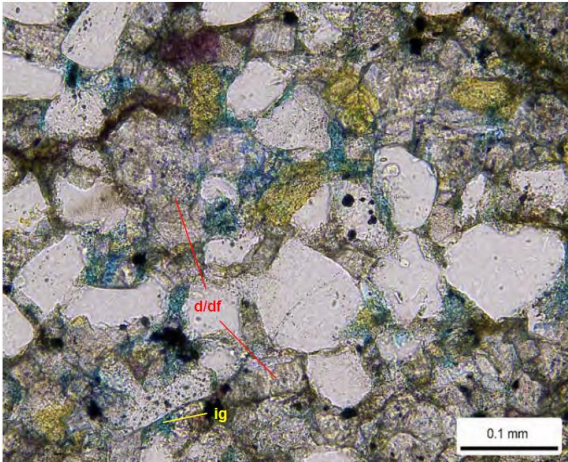
**Figure A.4.** (continued). Images and a brief description of lithofacies characterized by the EERC in NDIC Well No. 20844. Depths shown indicate the depth from which each sample was obtained.

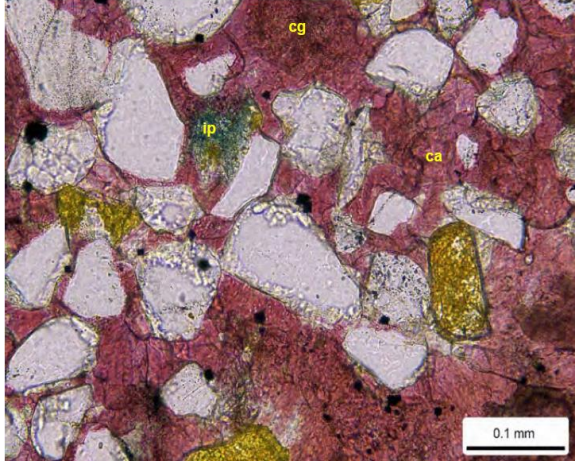
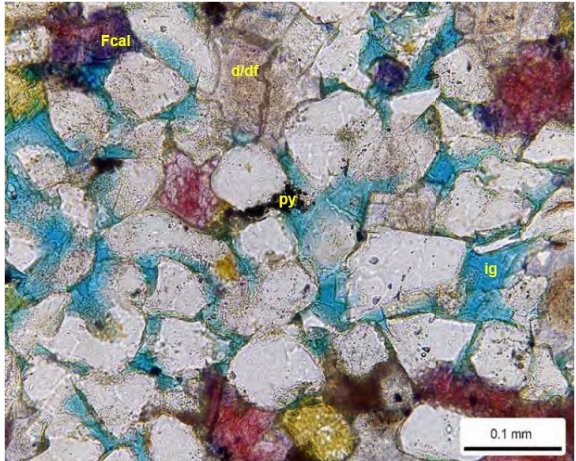
## APPENDIX B

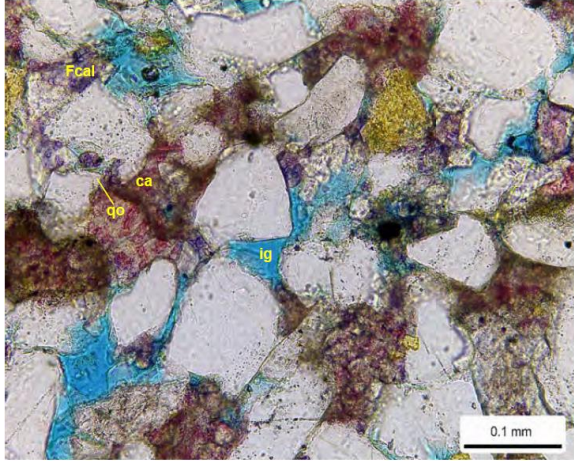
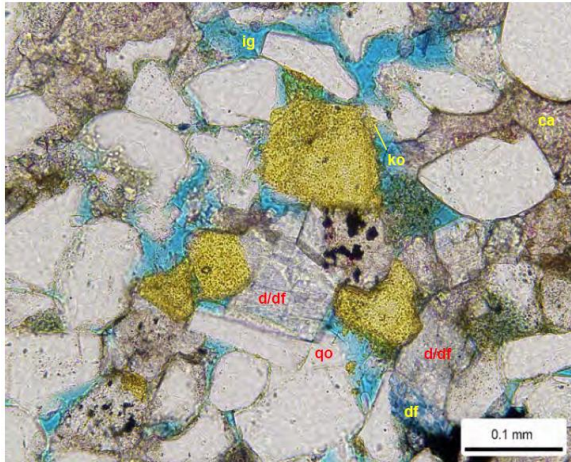
Table B.1. Trigger No. 1-31H, NDIC Well #17946 (Regenerated from NDIC Well report, 2019)

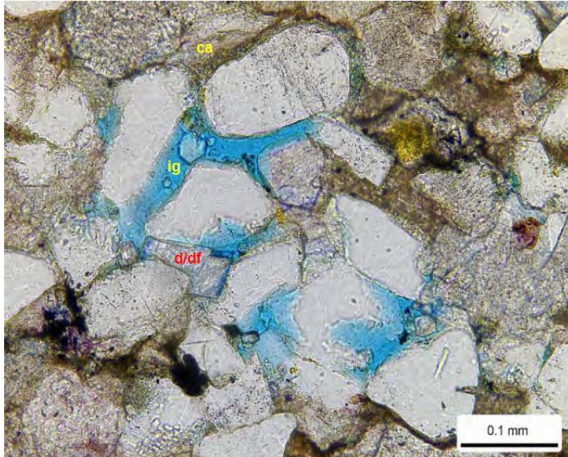
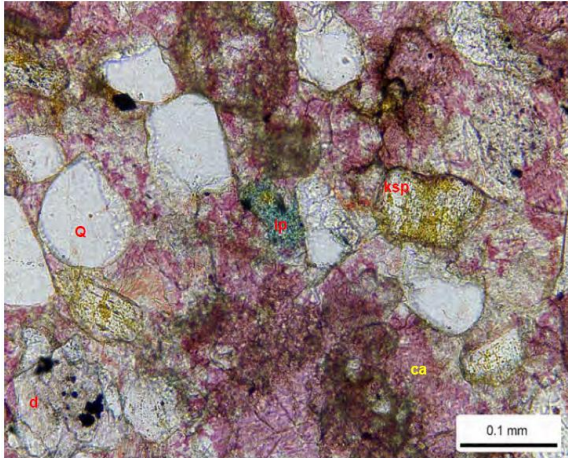
Sample Number	Sample Depth (ft)	Porosity (%)	Permeability (md)
4	8934.00	1.9	0.0003
<b>Lithology:</b> Calcareous Silty Shale			
<b>Petrographic Description</b> This silty shale is heavily burrowed. Silt grains are mostly monocrystalline quartz (Q), but minor to trace amounts of feldspars, calcareous grains, and muscovite are also observed. A large portion of the matrix has been cemented/replaced by calcite. Finely crystalline dolomite (d) is also observed replacing grains and matrix. Thin syntaxial quartz overgrowths have developed on several detrital quartz grains. Pyrite (py) has a patchy distribution. It is unclear if the fracture (Fr) in photo is natural or induced.			
Sample Number	Sample Depth (ft)	Porosity (%)	Permeability (md)
7	8940.00	3.3	0.0005
<b>Lithology:</b> Argillaceous Sandstone			
<b>Petrographic Description</b> This very-fine grained argillaceous sandstone is faintly laminated. Most of the grains are monocrystalline quartz. Less common grains include potassium feldspar (Ksp), plagioclase, volcanic rock fragments, argillaceous rock fragments, calcareous grains, and muscovite. Detrital matrix is common and consists of clay that has been partially cemented/replaced by calcite. Calcite cement (ca) is abundant and fills all of the intergranular pore space. Cementation/replacement by dolomite (d) is common. Other less common authigenic cements include syntaxial quartz overgrowths and pyrite. Visible pores are absent.			



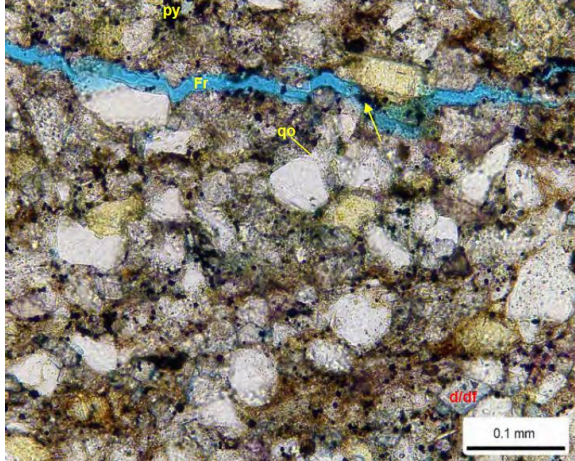
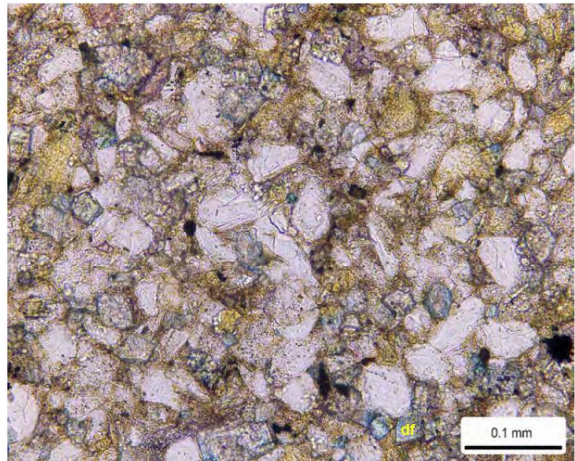
Sample Number	Sample Depth (ft)	Porosity (%)	Permeability (md)
8	8942.00	8.5	0.060
<b>Lithology:</b> Slightly Argillaceous Sandstone			
<b>Petrographic Description</b> <p>This very fine-grained slightly argillaceous sandstone contains size-sorted laminae and isolated burrows. Monocrystalline quartz grains are abundant. Less common grains include potassium feldspar, plagioclase, igneous rock fragments, argillaceous rock fragments, and calcareous grains. A minor amount of detrital clay matrix is observed in some of the finer-grained lamina. Dolomite/ferroan dolomite (d/df) is abundant and is found mostly replacing grains and less commonly as pore-filling cement. A minor amount of ferroan calcite (Fcal) is also found replacing grains and as pore-filling cement. Other minor cements include quartz overgrowths (qo), potassium feldspar overgrowths (ko), and pyrite. Intergranular pores are minor in abundance and concentrated in the coarser lamina. Secondary intragranular pores are rare.</p>			
Sample Number	Sample Depth (ft)	Porosity (%)	Permeability (md)
9	8943.00	8.4	0.004
<b>Lithology:</b> Argillaceous Sandstone			
<b>Petrographic Description</b> <p>This very fine-grained argillaceous sandstone is moderately sorted. Monocrystalline quartz grains are abundant and potassium feldspar is observed in moderate amounts. Plagioclase, volcanic rock fragments, argillaceous rock fragments, heavy minerals, muscovite, and calcareous grains are found in minor to trace amounts. Detrital clay matrix is common. Dolomite (d/df) is common. Some of the dolomite is slightly ferroan or has ferroan rims around non-ferroan dolomite cores. A minor amount of calcite and ferroan calcite is observed as intergranular cement and replacing grains. Other cements found in minor to trace amounts include pyrite, syntaxial quartz overgrowths, and potassium feldspar overgrowths. Intergranular pores (ig) are minor in abundance; intragranular pores are rare.</p>			

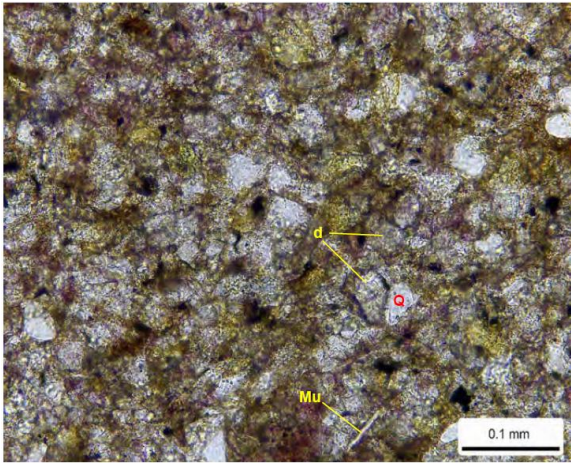
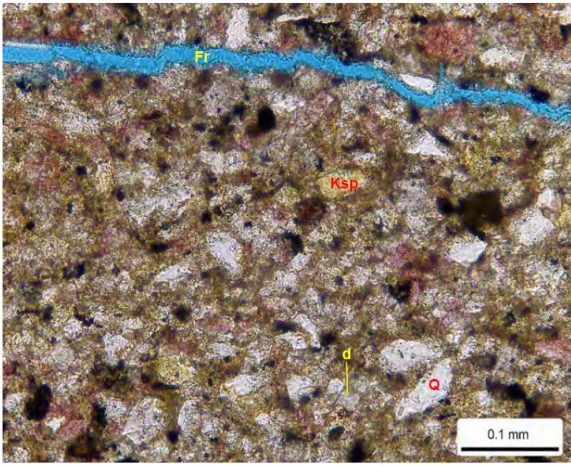
Sample Number	Sample Depth (ft)	Porosity (%)	Permeability (md)
10	8943.60	1.1	0.001
<b>Lithology:</b> Sandstone			
<b>Petrographic Description</b> All of the pore space in this very fine-grained sandstone has been filled with calcite cement (ca). Monocrystalline quartz grains are abundant and calcareous grains (cg) are common. Other grains found in minor to trace amounts include feldspars, argillaceous rock fragments, volcanic rock fragments, argillaceous rock fragments, chert, ooids, and skeletal fragments (brachiopods, echinoderms). Cements other than calcite found in minor to trace amounts include dolomite, pyrite, and syntaxial quartz overgrowths. Rare intragranular pores (ip) have formed by the partial dissolution of feldspar grains.			
Sample Number	Sample Depth (ft)	Porosity (%)	Permeability (md)
11	8943.80	8.1	1.55
<b>Lithology:</b> Sandstone			
<b>Petrographic Description</b> This very fine-grained sandstone is moderately well sorted. Monocrystalline quartz grains are abundant and calcareous grains are common. Other grains found in minor to trace amounts include potassium feldspar, plagioclase, argillaceous rock fragments, muscovite, and brachiopod fragments. Dolomite (d/df) is found in moderate amounts as replaced grains and as intergranular cement. The intergranular cement has a patchy distribution. Some of the dolomite is slightly ferroan. Other minor cements include pyrite (py), calcite, ferroan calcite (Fcal), and syntaxial quartz overgrowths. Intergranular pores (ig) are observed in moderate amounts.			

Sample Number	Sample Depth (ft)	Porosity (%)	Permeability (md)
12	8943.90	5.9	0.32
<b>Lithology:</b> Slightly Argillaceous Sandstone			
<b>Petrographic Description</b> <p>This fine-grained slightly argillaceous sandstone is moderately well sorted. Most of the framework grains are monocrystalline quartz. Calcareous grains, potassium feldspar, volcanic rock fragments, argillaceous rock fragments, ooids, brachiopods, and echinoderm fragments are much less common. Detrital clay matrix is observed in minor amounts. Calcite cement (ca) is abundant, but has a patchy distribution. A moderate amount of dolomite cement/replacement is observed; some of the dolomite is slightly ferroan. Syntaxial quartz overgrowths (qo), potassium feldspar overgrowths, ferroan calcite cement/replacement (Fcal), and pyrite are also observed in minor to trace amounts. Intergranular pores (ig) are concentrated in areas with less calcite cement.</p>			
Sample Number	Sample Depth (ft)	Porosity (%)	Permeability (md)
13	8944.20	10.2	2.15
<b>Lithology:</b> Slightly Argillaceous Sandstone			
<b>Petrographic Description</b> <p>This sample is a very fine-grained, moderately well sorted slightly argillaceous sandstone. Monocrystalline quartz is abundant and calcareous grains and potassium feldspar are observed in moderate amounts. Other rare grains include plagioclase, volcanic rock fragments, metamorphic rock fragments, argillaceous rock fragments, and brachiopod fragments. Detrital clay matrix is found in minor amounts. Dolomite/ferroan dolomite cement/replacement (d/df) is common. A ferroan dolomite rim (df) is noted around a less-ferroan dolomite core. Calcite cement (ca) is moderate in abundance and locally fills intergranular pores. Other cements found in minor to trace amounts include syntaxial quartz overgrowths (qo), potassium feldspar overgrowths (ko), pyrite, and rare anhydrite. Intergranular pores (ig) are moderate in abundance with less calcite cement.</p>			

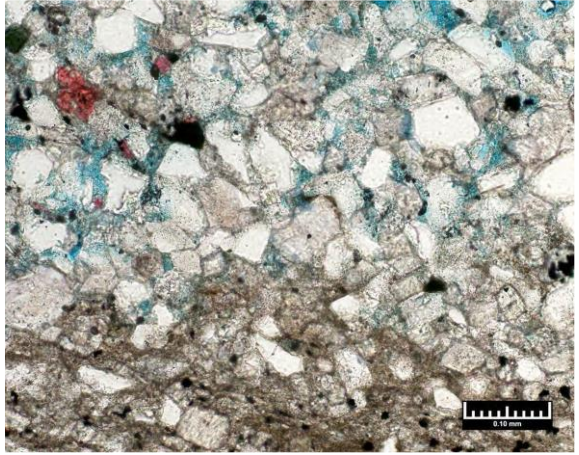
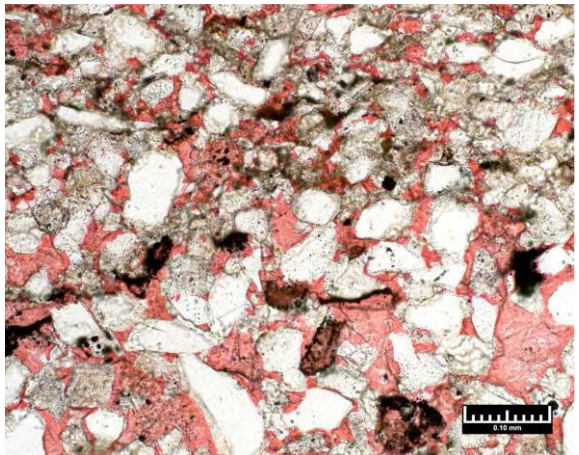
Sample Number	Sample Depth (ft)	Porosity (%)	Permeability (md)
14	8944.40	3.8	0.004
<b>Lithology:</b> Slightly Argillaceous Sandstone			
<b>Petrographic Description</b> This fine-grained sandstone is well sorted. Monocrystalline quartz grains are abundant and calcareous grains are observed in moderate amounts. Other grains found in minor to trace amounts include polycrystalline quartz, potassium feldspar, plagioclase, argillaceous rock fragments, heavy minerals, ooids, and skeletal fragments (echinoderms, brachiopods). Detrital clay matrix is minor in abundance. Calcite cement (ca) is abundant and has a patchy distribution. Other cements found in minor to trace amounts include dolomite/ferroan dolomite (d/df), pyrite, and syntaxial quartz overgrowths. Intergranular pores (ig) are minor in abundance and concentrated in areas that have not been cemented by calcite.			
Sample Number	Sample Depth (ft)	Porosity (%)	Permeability (md)
15	8944.90	1.5	0.001
<b>Lithology:</b> Sandstone			
<b>Petrographic Description</b> This very fine grained, moderately well sorted sandstone has been extensively cemented by calcite (ca). Monocrystalline quartz grains (Q) are abundant, non-skeletal calcareous grains are common, and skeletal grains (bryozoans, brachiopods, and echinoderms) are observed in moderate amounts. Other grains found in minor to trace amounts include potassium feldspar (Ksp), volcanic rock fragments, argillaceous rock fragments, and ooids. Dolomite cement and replaced grains (d), pyrite, and syntaxial quartz overgrowths are found in minor to trace amounts. Rare intragranular pores (ip) found within partially dissolved feldspar grains and lithic fragments are the only pore type observed in thin section.			

Sample Number	Sample Depth (ft)	Porosity (%)	Permeability (md)
20	8950.00	5.0	0.048
<b>Lithology:</b> Argillaceous Siltstone			
<b>Petrographic Description</b> This argillaceous siltstone contains clay-rich laminations. Monocrystalline quartz grains are abundant. Other less common grains include potassium feldspar, plagioclase, volcanic rock fragments, argillaceous rock fragments, muscovite, and calcareous grains. Detrital clay matrix is common. Calcite cement is abundant and fills virtually all of the primary intergranular pore space. Dolomite/ferroan dolomite (d/df) is common. Pyrite and syntaxial quartz overgrowths (qo) are observed in minor to trace amounts. It is unclear if the fracture (Fr) in photo A is natural or induced.			
Sample Number	Sample Depth (ft)	Porosity (%)	Permeability (md)
24	8958.25	7.5	0.002
<b>Lithology:</b> Argillaceous Siltstone			
<b>Petrographic Description</b> This argillaceous siltstone contains faint clay-rich laminations (not observed in this field of view). Monocrystalline quartz grains are abundant. Other grains found in minor to trace amounts include potassium feldspar, plagioclase, volcanic rock fragments, muscovite, calcareous grains, and skeletal fragments. Detrital clay matrix is common. Dolomite/ferroan dolomite cement/replacement (d/df) is abundant. Ferroan dolomite (df) is occasionally found as rims around non-ferroan dolomite cores. Pyrite (py) and syntaxial quartz overgrowths are observed in moderate amounts. Thin, discontinuous parallel fractures (Fr) are observed in thin section but it is unclear if they are natural or drilling-induced.			

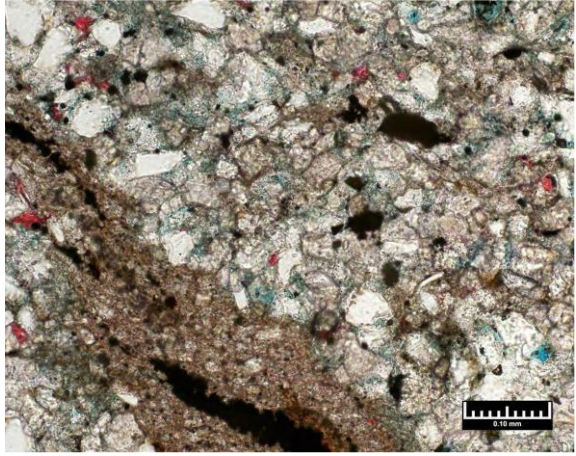
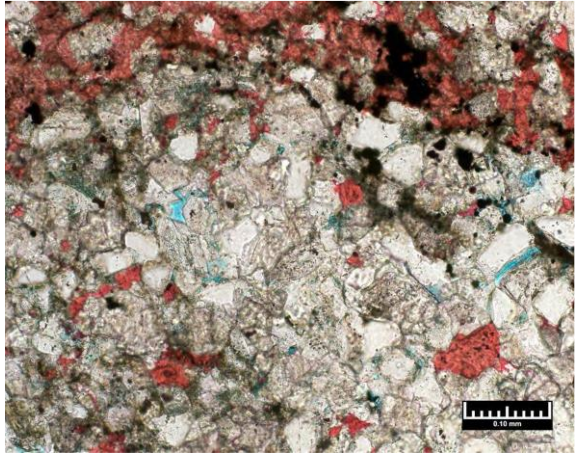
Sample Number	Sample Depth (ft)	Porosity (%)	Permeability (md)
25	8960.10	7.6	0.003
<b>Lithology:</b> Argillaceous Siltstone			
<b>Petrographic Description</b> This argillaceous siltstone contains faint clay-rich laminations. Monocrystalline quartz grains are abundant. Other grains found in minor to trace amounts include potassium feldspar, plagioclase, volcanic rock fragments, chert, muscovite, and calcareous grains. Detrital clay matrix is abundant. Dolomite cement/replacement (d/df) is abundant. Much of the dolomite is slightly ferroan. Syntaxial quartz overgrowths (qo) are observed in moderate amounts. Pyrite framboids (py) are dispersed throughout the matrix. Potassium feldspar overgrowths are rare. Tiny intergranular pores are found in trace amounts. Secondary intragranular pores are rare. Pyrite (arrow) appears to have precipitated in the fracture (Fr), suggesting the fracture may be natural.			
Sample Number	Sample Depth (ft)	Porosity (%)	Permeability (md)
30	8970.00	7.9	0.004
<b>Lithology:</b> Argillaceous Siltstone			
<b>Petrographic Description</b> Faint outlines of burrows (bu) are observed in this argillaceous siltstone. Most of the framework grains are monocrystalline quartz. Less common grains include potassium feldspar, plagioclase, volcanic rock fragments, heavy minerals, muscovite, calcareous grains, and skeletal fragments (brachiopod spine, Br). Detrital clay matrix is abundant. Much of the sample has been replaced by finely crystalline dolomite and ferroan dolomite (df). Syntaxial quartz overgrowths are moderate in abundance. Pyrite and calcite cements are rare. Tiny intergranular pores are observed in trace amounts.			

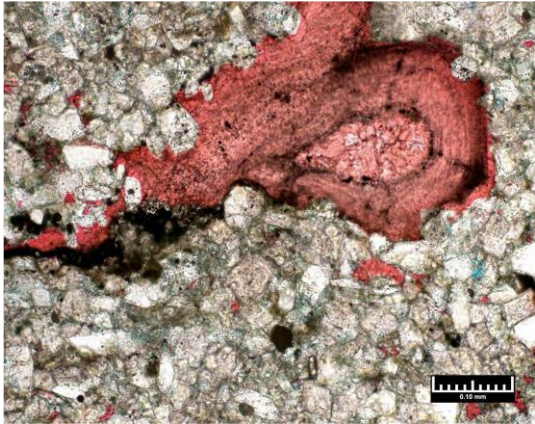

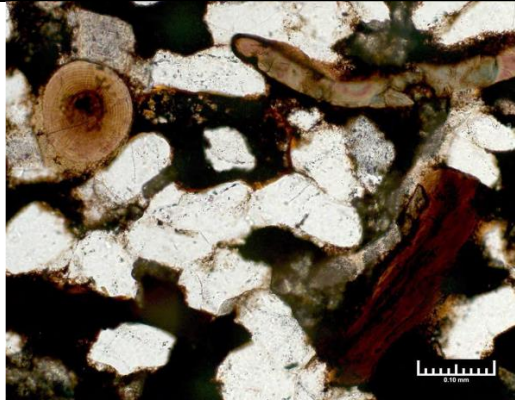
Sample Number	Sample Depth (ft)	Porosity (%)	Permeability (md)
34	8978.15	5.9	0.343
<b>Lithology:</b> Argillaceous Siltstone			
<b>Petrographic Description</b> This argillaceous siltstone is burrowed (bu). Silt size quartz grains (Q) are abundant. Potassium feldspar, plagioclase, heavy minerals, muscovite (Mu), calcareous grains, and skeletal fragments (brachiopods and echinoderms-E) are observed in minor to trace amounts. Most of the matrix consists of detrital clay, but a minor amount has been cemented/replaced by calcite. Finely crystalline dolomite (d) commonly replaces grains and matrix. Other authigenic cements found in minor to trace amounts include calcite, pyrite, and syntaxial quartz overgrowths. Visible pores are absent.			
Sample Number	Sample Depth (ft)	Porosity (%)	Permeability (md)
35	8980.10	3.2	0.0003
<b>Lithology</b> Argillaceous Siltstone			
<b>Petrographic Description</b> Most of the detrital grains in this argillaceous siltstone are monocrystalline quartz (Q). Other grains found in minor to trace amounts include potassium feldspar (Ksp), plagioclase, volcanic rock fragments, muscovite, calcareous grains, and skeletal fragments (brachiopods and echinoderms-E). The matrix is mostly detrital clay but a large portion of the matrix has been cemented/replaced by calcite. Finely crystalline dolomite (d) commonly replaces grains and matrix. Other cements found in minor to trace amounts include calcite, pyrite, and quartz overgrowths. A discontinuous fracture (Fr) is noted in these images; it is unclear if the fracture is natural or drilling-induced.			

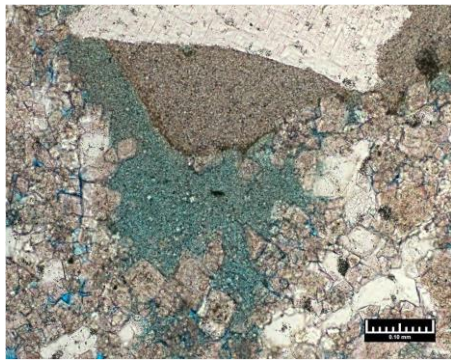
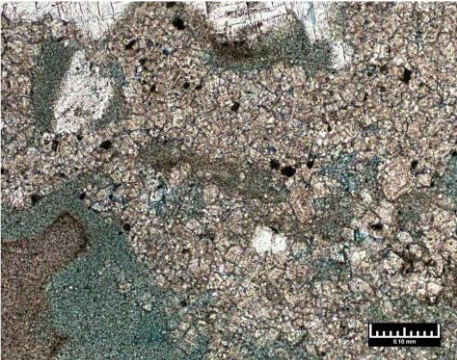
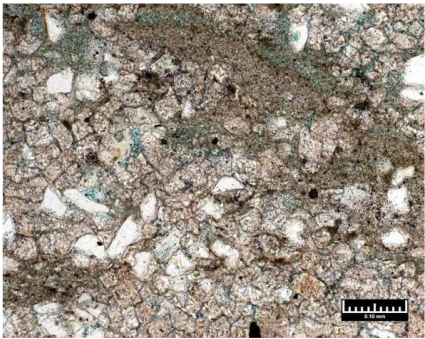
**Table B.2.** Muller No. 1-21-16H, NDIC Well #20552 (Regenerated from NDIC Well report, 2021a)

Sample Number	Sample Depth (ft)	Porosity (%)	Klink. Perm. @ 2600 psi (md)
1-47	9627.50	8.4	0.308
<p><b>Lithology:</b> Dolomitic, silty, very fine-grained sandstone to argillaceous, silty/sandy dolostone</p>			
<p><b>Pore System</b> Dominantly erratically distributed intergranular/intercrystalline pores that occur in matrix-poor laminations/areas; a subordinate amount of secondary pores have resulted from partial to complete grain dissolution (including feldspars); micropores associated with authigenic clays and altered/partially leached grains significantly contribute to the pore volume</p>			
Sample Number	Sample Depth (ft)	Porosity (%)	Klink. Perm. @ 2600 psi (md)
1-50	9630.50	4%	<0.0001
<p><b>Lithology:</b> Calcareous, dolomitic, silty, very fine-grained sandstone and slightly argillaceous, calcareous, dolomitic, sandy siltstone to silty/sandy dolostone</p>			
<p><b>Pore System</b> Trace amounts of remnant intergranular pores and secondary grain dissolution pores resulting from dissolution of siliciclastic grains (feldspar); calcite cement has greatly reduced intergranular porosity; traces of micropores are visible within altered/partially leached grains and between crystals of authigenic clays</p>			

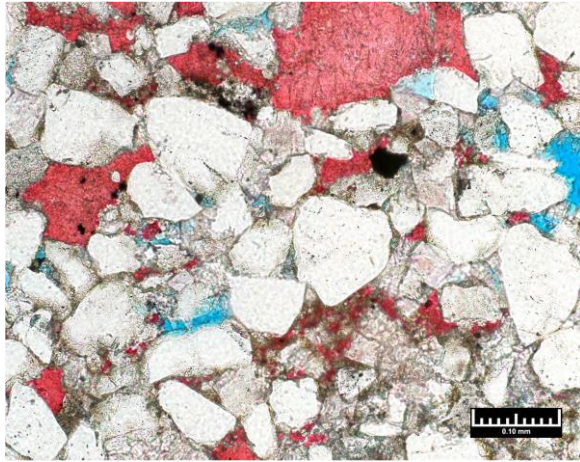
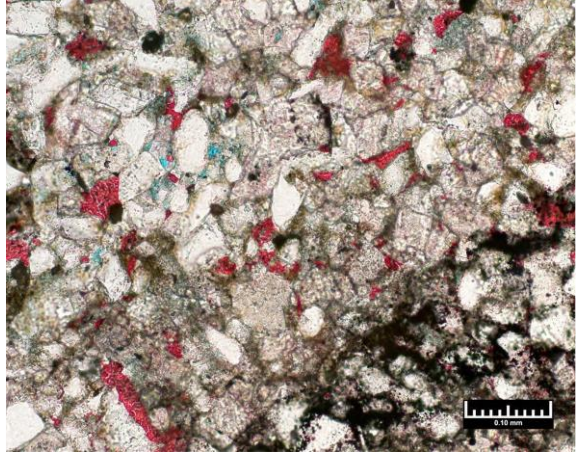


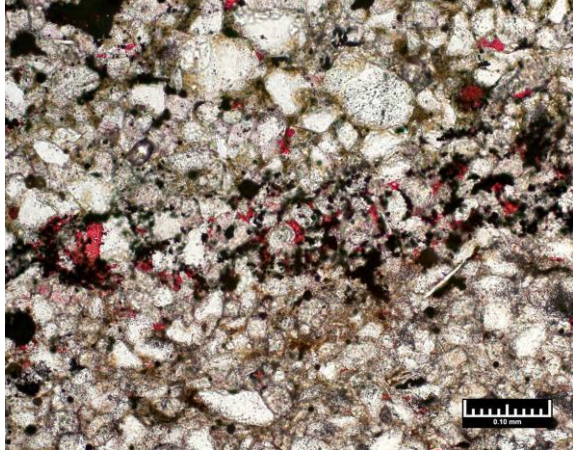
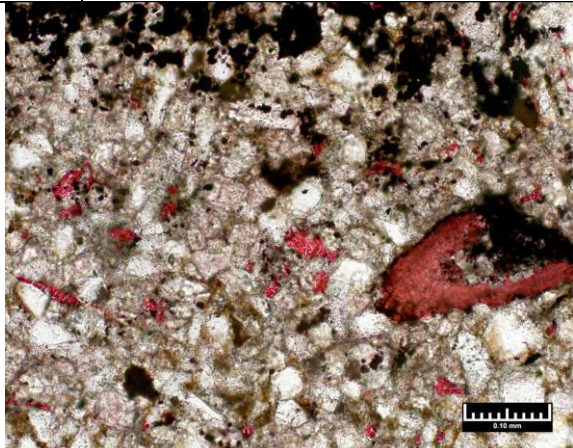
Sample Number	Sample Depth (ft)	Porosity (%)	Klink. Perm. @ 2600 psi (md)
1-53	9633.60	7.1%	0.017
<p><b>Lithology:</b> Slightly calcareous, argillaceous, silty/sandy dolostone to dolomitic, silty, very fine-grained sandstone</p>			
<p><b>Pore System</b> Dominantly micropores that occur between crystals of authigenic clays and within altered/partially leached grains; very minor amount of isolated intergranular pores is locally preserved in matrix-poor areas; very minor secondary grain dissolution pores resulting from dissolution of siliciclastic grains (including feldspar)</p>			
Sample Number	Sample Depth (ft)	Porosity (%)	Klink. Perm. @ 2600 psi (md)
1-55	9635.95	5.8%	0.072 (fractures)
<p><b>Lithology:</b> Calcareous, dolomitic, silty, very fine-grained sandstone to slightly calcareous, slightly argillaceous, silty/sandy dolostone</p>			
<p><b>Pore System</b> Erratically distributed pores are most common in portions of sandstone laminations lacking matrix; dominantly micropores that occur between crystals of authigenic clays and detrital grains, as well as within altered/partially leached grains; small intergranular/intercrystalline pores are locally preserved in matrix-poor areas; very minor secondary grain dissolution pores resulting from dissolution of siliciclastic grains)</p>			

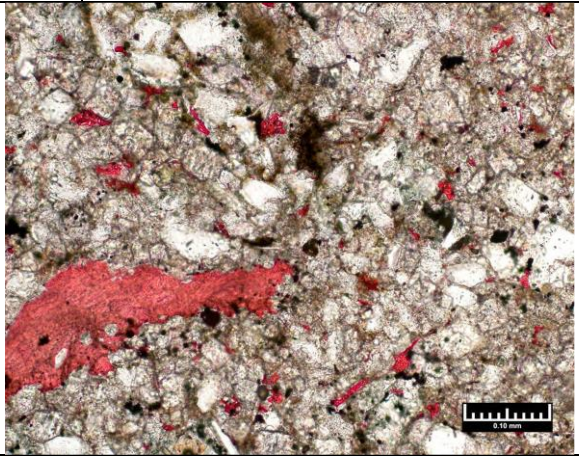
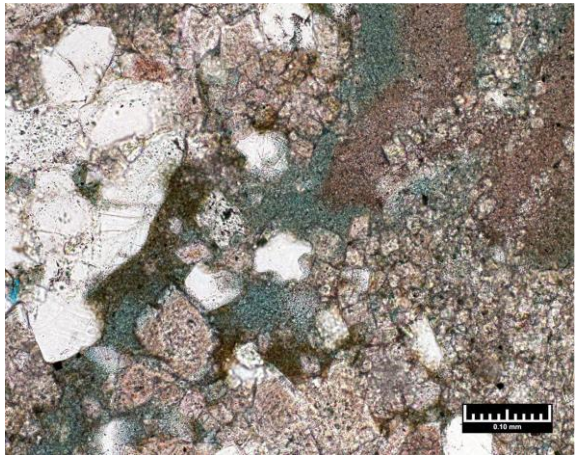
Sample Number	Sample Depth (ft)	Porosity (%)	Klink. Perm. @ 2600 psi (md)
1-59	9639.50	6.6%	0.0019
<p><b>Lithology:</b> Slightly calcareous, slightly argillaceous, silty/sandy dolostone to dolomitic, sandy siltstone</p>			
<p><b>Pore System</b> Dominantly micropores that are present within intergranular detrital and authigenic clays; widely scattered, very small intergranular pores occur in matrix poor portions of the sample; very minor secondary grain dissolution pores resulting from dissolution of siliciclastic grains (including feldspar)</p>			
Sample Number	Sample Depth (ft)	Porosity (%)	Klink. Perm. @ 2600 psi (md)
1-80	9660.50	8.9%	NA
<p><b>Lithology:</b> Organic-rich, silty shale</p>			
<p><b>Pore System</b> No visible pores using standard petrographic techniques</p>			
Sample Number	Sample Depth (ft)	Porosity (%)	Klink. Perm. @ 2600 psi (md)
1-83	9663.50	5.5%	NA (fractured)
<p><b>Lithology:</b> Organic-rich, phosphatic, dolomitic, pyritic, argillaceous, very fine-grained sandstone to sandy dolostone, with thin silty/sandy shale laminations</p>			
<p><b>Pore System</b> Trace intraparticle pores within phosphatic fragments</p>			

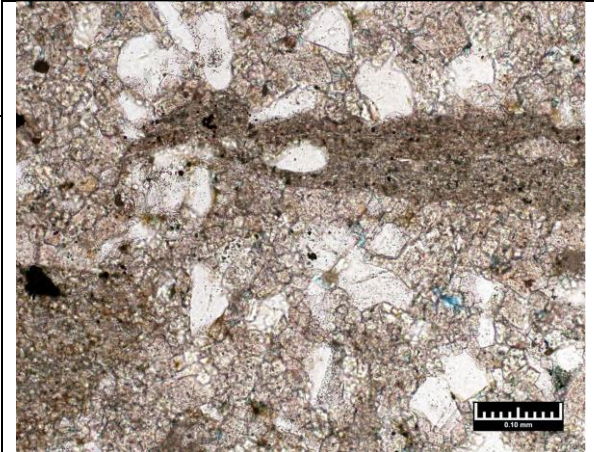
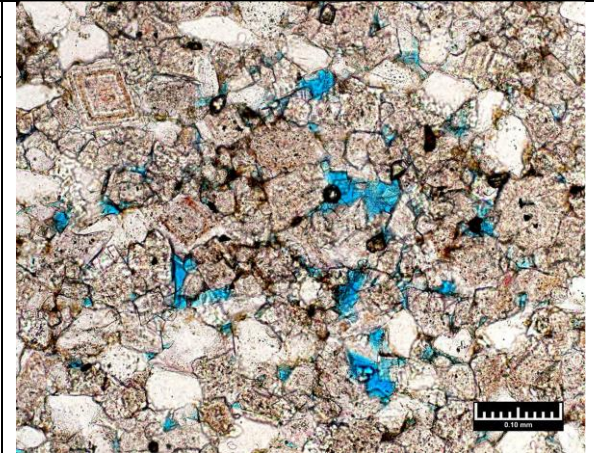
Sample Number	Sample Depth (ft)	Porosity (%)	Klink. Perm. @ 2600 psi (md)
1-83	9669.30	8.0%	0.458 md (fractured)
<p><b>Lithology:</b> Slightly silty, argillaceous dolostone to silty/sandy dolostone</p>			
<p><b>Pore System</b> Irregularly distributed pores; dominantly small intercrystalline pores that occur between replacement dolomite crystals in clay-poor areas, and micropores that are present in altered argillaceous clasts and remnant detrital clay matrix; rare small grainmoldic pores; trace secondary dissolution pores in partially leached feldspar grains</p>			
Sample Number	Sample Depth (ft)	Porosity (%)	Klink. Perm. @ 2600 psi (md)
1-90	9670.55	8.5%	N/A (fractured)
<p><b>Lithology:</b> Slightly silty dolostone and slightly silty, argillaceous dolostone to dolomitic shale</p>			
<p><b>Pore System</b> Dominantly irregularly distributed pores micropores that occur within altered/partially leached argillaceous rip-up clasts and within clays present in dolomite intercrystalline areas; a subequal quantity of very small intercrystalline pores that occur within grain-rich; rare grain moldic pores</p>			
Sample Number	Sample Depth (ft)	Porosity (%)	Klink. Perm. @ 2600 psi (md)
1-96	9676.50	3.9%	0.0017
<p><b>Lithology:</b> Slightly argillaceous, silty/sandy dolos.</p>			
<p><b>Pore System</b> Dominantly subequal amounts of poorly developed very small intercrystalline/intergranular pores that are erratically distributed, occurring between dolomite crystals and/or siliciclastic grains, and micropores that mostly occur within altered/partially leached argillaceous rip-up clasts and also within clays present in dolomite intercrystalline areas and small dolomitic grains; a very minor amount of small secondary intraparticle pores result from the partial leaching of siliciclastic grains (mostly feldspar)</p>			

**Table B.3.** Rasmussen No. 1-21-16H, NDIC Well #20844 (Reproduced from NDIC Well report, 2021b)

Sample Number	Sample Depth (ft)	Porosity (%)	Klink. Perm. @ 2600 psi (md)
1-55	10227.50	5.9	0.0033
<p><b>Lithology:</b> Slightly argillaceous, calcareous, dolomitic, very fine-grained sandstone to siltstone; locally grades to slightly argillaceous, silt dolostone</p> <p><b>Pore System</b> Intergranular pores have an irregular or patchy distribution, mostly occurring in coarser sandstone laminations that lack or have limited depositional matrix; much smaller amounts of secondary pores resulting from the dissolution of siliciclastic grains (including feldspar) and micropores that are associated with authigenic and detrital clays, as well as altered grains</p>			
Sample Number	Sample Depth (ft)	Porosity (%)	
1-63	10235.50	7.5	0.033
<p><b>Lithology:</b> Slightly calcareous, argillaceous, dolomitic sandy siltstone to silty, very fine-grained sandstone (~95% of sample; locally grades to dolostone) and slightly argillaceous, calcareous, dolomitic, silty, very fine-grained sandstone (~5%)</p> <p><b>Pore System</b> Minor intergranular pores mostly occur in coarser laminations/areas that lack or have limited depositional matrix and appear isolated by surrounding matrix-rich rock; micropores associated with authigenic and detrital clays, as well as altered grains form a significant portion of the pore volume; trace secondary pores resulting from the dissolution of siliciclastic grains</p>			

Sample Number	Sample Depth (ft)	Porosity (%)	Klink. Perm. @ 2600 psi (md)
1-66	10238.50	7.3	0.032
<p><b>Lithology:</b> Slightly calcareous, argillaceous, dolomitic sandy siltstone to silty/sandy dolostone; locally grades to argillaceous, dolomitic, silty, very fine-grained sandstone</p>			
<p><b>Pore System</b> Very minor amount of isolated intergranular pores that mostly occur in coarser laminations/areas that lack or have limited depositional matrix; very minor amounts of micropores occur within altered/partially leached grains (mostly altered argillaceous fragments) and between crystals of authigenic and detrital clays; trace secondary pores resulting from the dissolution of siliciclastic grains (including feldspar)</p>			
Sample Number	Sample Depth (ft)	Porosity (%)	Klink. Perm. @ 2600 psi (md)
1-68	10240.50	6.8	0.0037
<p><b>Lithology:</b> Slightly calcareous to calcareous, argillaceous, dolomitic, sandy siltstone to silty/sandy dolostone</p>			
<p><b>Pore System</b> minor amount of micropores are observed within argillaceous grains, altered siliciclastic grains, and the detrital clays; trace amounts of very small intergranular pores and secondary intraparticle pores resulting from the partial leaching of feldspar grains; pore system limited by abundance of matrix and locally common calcite cement</p>			

Sample Number	Sample Depth (ft)	Porosity (%)	Klink. Perm. @ 2600 psi (md)
1-72	10244.50	7.1	0.0072
<p><b>Lithology:</b> lightly calcareous, argillaceous, dolomitic, sandy siltstone to silty/sandy dolostone</p> <p><b>Pore System</b> Localized traces of micropores visible within argillaceous grains, altered grains, authigenic clays, and the detrital clay matrix; trace intraparticle pores within a compacted phosphatic vertebrate fragment and very small intergranular pores; limited reservoir quality is due to abundance of depositional matrix</p>			
Sample Number	Sample Depth (ft)	Porosity (%)	
1-105	10277.40	8.1	4.8 (fractured)
<p><b>Lithology:</b> Interbedded/interlaminated dolomitic, very fine-grained sandstone, silty/sandy dolostone, and slightly dolomitic mudstone to silty/sandy mudstone</p> <p><b>Pore System</b> Erratically distributed pores that generally appear isolated; the sandstone contains minor intergranular/intercrystalline pores are very sparsely scattered, and micropores the occur within compacted argillaceous clasts; dolostones contain micropores in argillaceous clasts and in remnant detrital clays that occur between replacement dolomite crystals, as well as rare intercrystalline pores</p>			
Sample Number	Sample Depth (ft)	Porosity (%)	
1-107	10279.40	5.4	0.049

<p><b>Lithology:</b> Sandy/silty dolostone to dolomitic, very fine-grained sandstone</p>			
<p><b>Pore System</b> Erratically distributed small intercrystalline/intergranular pores occur between dolomite crystals or between dolomite crystals and siliciclastic grain; a minor amount of micropores are observed within some argillaceous intraclasts; trace amounts of small pores resulting from the dissolution of dolomite crystals and small grain moldic pores</p>			
Sample Number	Sample Depth (ft)	Porosity (%)	Klink. Perm. @ 2600 psi (md)
1-115	10287.50	4.5	0.0020
<p><b>Lithology:</b> Sandy dolostone</p>			
<p><b>Pore System</b> Dominantly erratically small intercrystalline/intergranular pores occur between dolomite crystals or between dolomite crystals and siliciclastic grains; a minor amount of micropores are observed within some argillaceous intraclasts; rare secondary pores that appear to result from the dissolution of feldspar grains</p>			

## REFERENCES

- Athy, L.F. (1930) Density, Porosity and Compaction of Sedimentary Rocks. *Bulletin of the American Association of Petroleum Geologists (AAPG Bulletin)*, 14, 1-24.
- Backus, G., E., 1962. Long wave elastic anisotropy produced by horizontal layering. *Journal of geophysics research*. Vol. 67, No. 11.
- Barnes, B. D., Husson, J. M., and Peters, S. E., 2020. Authigenic carbonate burial in the Late Devonian–Early Mississippian Bakken Formation (Williston Basin, USA). *Sedimentology Volume 67*, Pages 2065–2094.
- Bhattacharyaa, S., and Carr, T. R., 2019. Integrated data-driven 3D shale lithofacies modeling of the Bakken Formation in the Williston basin, North Dakota, United States. *Journal of Petroleum Science and Engineering Volume 177*, Pages 1072-1086.
- Brie, A., Pampuri, F., Marsala, A.F., and Meazza, O., 1995, Shear sonic interpretation in gas-bearing sands: SPE 30595, 701-710.
- Bing, L. H., and Jia, Z. J., 2014. A differential effective medium model of multiple porosity rock and its analytical approximations for dry rock. *Chinese journal of Geophysics*, 57(6): 835-845.
- Bruggeman D.A.G., 1935. Berechnung verschiedener physikalischer Konstanten von heterogenen Substanzen, *Ann. Phys., Lpz*, 24, 636–679.
- Carcione, J. M., Helle, H. B., and Avseth, P., 2011. Source-rock seismic-velocity models: Gassmann versus Backus. *Geophysics Vol. 76*, No. 5, P 37-45.
- Egenhoff, S. O., 2017. The lost Devonian sequence - Sequence stratigraphy of the middle Bakken member, and the importance of clastic dykes in the lower Bakken member shale, North Dakota, USA. *Marine and Petroleum Geology. Volume 81*, March 2017, Pages 278-293.
- Greenberg, M.L. and Castagna, J.P., 1992. Shear-Wave Velocity Estimation in Porous Rocks: Theoretical Formulation, Preliminary Verification and Applications. *Geophysical Prospecting*, 40, 195-209.
- Harju, J. A., 2022. Effect of Mineralogy on Elastic Properties of the Bakken Formation. Ph.D. Thesis, University of North Dakota.
- Hill, R., 1963. Elastic properties of reinforced solids: some theoretical principles. *Journal of the Mechanics and Physics of Solids*. 11(5): p. 357-372.
- Hudson, J.A., 1981, Wave speeds and attenuation of elastic waves in material containing cracks: *Geophys.*
- Kahraman S, Yeken T (2008) Determination of physical properties of carbonate rocks from P-wave velocity. *Bull Eng Geol Environ* 67:277–281
- Kassab MA, Weller A (2015) Study on P-wave and S-wave velocity in dry and wet sandstones of Tushka region, Egypt. *Egypt J Pet* 24(1):1–11
- Kumar, D., 2013. Applying Backus averaging for deriving seismic anisotropy of a long-wavelength equivalent medium from well-log data. *Journal of Geophysics and Engineering, Volume 10*, Issue 5.



- Kumar, M., and Han, D., 2005. Pore shape effect on elastic properties of carbonate rocks. SEG. P. 1477-1480.
- Kurtulus C, Cakir S, Yogurtcuoglu AC (2016) Ultrasound study of limestone rock physical and mechanical properties. Soil Mech Found Eng 52(6):27–31
- NDIC Well #17946 Report, 2019. North Dakota Industrial Commission (NDIC). <https://www.dmr.nd.gov/oilgas/>.
- NDIC Well #20552 Report, 2021a. North Dakota Industrial Commission (NDIC). <https://www.dmr.nd.gov/oilgas/>.
- NDIC Well #20844 Report, 2021b. North Dakota Industrial Commission (NDIC). <https://www.dmr.nd.gov/oilgas/>.
- Passey, Q. R., Creaney, S., Kulla, J.B., Moretti, F.J., and Stroud, J.D., 1990, A practical model for organic richness from porosity and resistivity logs: AAPG Bulletin, 74, 1777-1794.
- Polzin., P., 2017. The Economic Impact of the Bakken. Montana Business Quarterly.
- Raimi, D., and R. G., Newell, 2016. Dunn County and Watford City, North Dakota: A case study of the fiscal effects of Bakken shale development.
- Saberi, M. R., 2017. A closer look at rock physics models and their assisted interpretation in seismic exploration. Iranian Journal of Geophysics, Pages 71 – 84.
- Sayers, C. M., 2010. Geophysics Under Stress: Geomechanical Applications of Seismic and Borehole Acoustic Waves, SEG.
- Schmoker, J., 1979, Determination of organic content of Appalachian Devonian shales from formation-density logs: AAPG Bulletin, 63, no. 9, 1504-1537.
- Schon, J. H., 2011. Physical Properties of Rocks, A Workbook. Handbook of Petroleum Exploration and Production, 8. Elsevier.
- Simandoux, P., 1963, Dielectric measurements on porous media application to the measurement of water saturations: study of the behavior of argillaceous formations: Revue de l'Institut Francais du Petrole 18, Supplementary Issue, p. 193-215.
- Sorensen, J., Hawthorne, S. B., Smith, S. A., Braunberger, J. R., Liu, G., Klenner, R. C. L., Botnen, L. S., Steadman, E. L., Harju, J. A., Doll, T. E., 2014. Subtask 1.10 – CO<sub>2</sub> Storage and Enhanced Bakken Recovery Research Program. Final report, DE-FC26-08NT43291.
- Sorensen, J., Schmidt, D. D., Smith, S. A., Bailey, T. P., Mibeck B. A. F. and Harju, J. A., 2010. Subtask 1.2 – Evaluation of key factors affecting successful oil production in the Bakken formation, North Dakota. DOE Award No.: DE-FC26-08NT43291.
- Reuss, A., 1929, Berechnung der fließgrenze von mischkristallen aufgrund der plastizitatbedingung fur einkristalle. Zeitschrift fur Ange-wandte Mathematikaus Mechnik, 9, 49–58.
- Vernik, L., and C. Landis, 1996, Elastic anisotropy of source rocks: Implications for hydrocarbon generation and primary migration, AAPG Bulletin, 80, 531–544.

Voigt, Woldemar. 1910. Lehrbuch der Kristallphysik. Leipzig: B.G. Teubner, p. 67.

Xu, J., and Sonnenberg, S. A., 2017. An SEM Study of Porosity in the Organic-rich Lower Bakken Member and Pronghorn Member, Bakken Formation, Williston Basin. Unconventional Resources Technology Conference (URTEC) DOI 10.15530-urtec-2017-2697215.